



**HAL**  
open science

# Theory and ab-initio calculations of collective excitations in nanostructures: towards spatially-resolved EELS

Ralf Hambach

## ► To cite this version:

Ralf Hambach. Theory and ab-initio calculations of collective excitations in nanostructures: towards spatially-resolved EELS. Materials Science [cond-mat.mtrl-sci]. Ecole Polytechnique X, 2010. English. NNT : . pastel-00587080

**HAL Id: pastel-00587080**

**<https://pastel.hal.science/pastel-00587080>**

Submitted on 19 Apr 2011

**HAL** is a multi-disciplinary open access archive for the deposit and dissemination of scientific research documents, whether they are published or not. The documents may come from teaching and research institutions in France or abroad, or from public or private research centers.

L'archive ouverte pluridisciplinaire **HAL**, est destinée au dépôt et à la diffusion de documents scientifiques de niveau recherche, publiés ou non, émanant des établissements d'enseignement et de recherche français ou étrangers, des laboratoires publics ou privés.

Thèse présentée pour obtenir le grade de  
DOCTEUR DE L'ÉCOLE POLYTECHNIQUE

par

RALF HAMBACH

---

**Theory and *ab-initio* calculations  
of collective excitations in nanostructures :  
towards spatially-resolved EELS**

---

Soutenue le 19 Novembre 2010 devant le jury composé de :

Prof. Peter SCHATTSCHEIDER	Rapporteur
Prof. Luc HENRARD	Rapporteur
Prof. Stefan BLÜGEL	Examinateur
Prof. Emmanuel ROSENCHER	Examinateur
Dr. Odile STEPHAN	Examinatrice
Dr. Christine GIORGETTI	Co-Directrice
Dr. Lucia REINING	Directrice



# Contents

<b>Preface</b>	<b>v</b>
<b>I Background</b>	<b>1</b>
<b>1 Introduction</b>	<b>3</b>
1.1 Electron Microscopy . . . . .	3
1.2 Macroscopic Dielectric Theory . . . . .	8
1.3 Microscopic Dielectric Theory . . . . .	12
<b>2 Scattering Theory</b>	<b>17</b>
2.1 General Formalism . . . . .	17
2.2 Angular-Resolved Electron Energy-Loss Spectroscopy . . . . .	19
2.3 Spatially-Resolved Electron Energy-Loss Spectroscopy . . . . .	22
2.4 Inelastic X-Ray Scattering . . . . .	26
2.5 Connection with Dielectric Theory . . . . .	28
<b>3 The Many-Body Problem</b>	<b>35</b>
3.1 Density-Functional Theory . . . . .	35
3.2 Time-Dependent Density-Functional Theory . . . . .	39
3.3 Numerical Details . . . . .	43
<b>II Developments and Applications</b>	<b>51</b>
<b>4 Anisotropy of the Mixed Dynamic Form Factor</b>	<b>53</b>
4.1 Discontinuity in the MDFF: an Overview of our Results . . . . .	53
4.2 Dielectric Properties of Crystals . . . . .	55
4.3 Graphite . . . . .	60
4.4 Silicon . . . . .	67
4.5 Conclusions . . . . .	74
<b>5 Polarisability of Two-Dimensional Systems</b>	<b>75</b>
5.1 Graphene . . . . .	75
5.2 Models for the Dielectric Properties . . . . .	78
5.3 Ab-Initio Calculations . . . . .	84
5.4 Local-Response Approximation . . . . .	93

5.5	Beyond the Local-Response Approximation . . . . .	99
5.6	Building-Block Approach . . . . .	104
5.7	Further Studies . . . . .	106
<b>6</b>	<b>Polarisability of Carbon Nanotubes</b>	<b>113</b>
6.1	Single-Wall Carbon Nanotubes . . . . .	113
6.2	Model Calculations . . . . .	119
6.3	Zone-folding for Excitations . . . . .	121
6.4	Anisotropic Excitations in SWCNTs . . . . .	132
6.5	Zone-Folding for the Microscopic Dielectric Function . . . . .	138
<b>7</b>	<b>Towards Spatially-Resolved EELS</b>	<b>143</b>
7.1	Near-Field EELS for a Graphene Layer . . . . .	143
7.2	Near-Field EELS for Carbon Nanotubes . . . . .	150
7.3	Microscopic Charge Oscillations . . . . .	153
7.4	Open Questions and Outlook . . . . .	154
<b>III</b>	<b>Appendices</b>	<b>159</b>
<b>A</b>	<b>Theoretical Supplements</b>	<b>161</b>
A.1	Time-Dependent Perturbation Theory . . . . .	161
A.2	Continuous Fourier Transformation . . . . .	164
A.3	Discrete Fourier Series . . . . .	166
A.4	Response in Cylindrical Systems . . . . .	168
A.5	Algebra of the Dielectric Matrix . . . . .	174
<b>B</b>	<b>Microscopic Dielectric Theory</b>	<b>175</b>
B.1	Dielectric Theory . . . . .	175
B.2	Ambiguity of the Microscopic Dielectric Function . . . . .	179
B.3	Connecting Microscopic and Macroscopic Quantities . . . . .	182
<b>C</b>	<b>Code Development</b>	<b>185</b>
C.1	Tight-Binding for Carbon Materials . . . . .	185
C.2	Local-Response Approximation . . . . .	188
C.3	AR-EELS for SWCNT . . . . .	189
C.4	From Graphite to Graphene . . . . .	190
	<b>Acknowledgements</b>	<b>195</b>
	<b>Bibliography</b>	<b>197</b>

# Nomenclature

$\chi^0$	Independent-particle polarisability, eq. 3.14
$\pi$	Polarisability, eq. (3.17)
$\chi$	Susceptibility, or density response function, eq. (2.43)
$\bar{\pi}, \bar{\chi}$	Slab polarisation function / slab susceptibility, eq. (5.31)
$\bar{\pi}_{\text{CNT}}, \bar{\chi}_{\text{CNT}}$	Cylinder polarisation function / cylinder susceptibility, eq. (6.16)
$\varepsilon, \varepsilon_M$	Microscopic / macroscopic dielectric function, eq. (1.9) / (1.15)
$\bar{\varepsilon}$	Two-dimensional dielectric function, eq. (5.33)
$\bar{\varepsilon}_{\text{CNT}}$	Dielectric function of the Cylinder, eq. (6.18)
$v, v_{3D}$	Coulomb potential, eq. (A.27)
$\bar{v}, v_{\text{CNT}}$	Coulomb potential for sheet / cylinder, eq. (5.28) / (6.17)
$\mathbf{q}, \mathbf{q}_r$	Momentum transfer / reduced momentum transfer
$q_{\perp}, q_{\parallel}$	Momentum transfer perpendicular / parallel to the tube axis
$\mathbf{G}, \mathbf{K}, \mathbf{Q}$	Reciprocal lattice vectors
$\bar{\mathbf{r}}, \bar{\mathbf{q}}, \bar{\mathbf{k}}$	In-plane vectors (position, wave vectors)
$\varrho$	Cylindrical coordinates $(\varrho, \varphi, \mathfrak{z})$ , eq. (A.49)
$\xi$	Helical momentum $(lp)$ , eq. (6.12)
$d, d_0$	Interlayer distance in graphene stacks and graphite ( $d_0 = 3.33 \text{ \AA}$ )
BZ	Brillouin zone
DP	Dielectric Properties
DSF	Dynamic Structure Factor
FT	Fourier Transform
gcd	Greatest Common Divisor
KS	Kohn-Sham
(A)LDA	(Adiabatic) Local-Density Approximation
LRA	Local-Response Approximation
MDFF	Mixed Dynamic Form Factor
RPA	Random Phase Approximation
SWCNT	Single-Wall Carbon Nanotube
TB	Tight Binding
ZF	Zone folding
(TD)DFT	(Time-Dependent) Density-Functional Theory

If not stated differently, SI-units are used throughout this thesis.



# Preface

“Was man in einem Mikroskop bei hoher Vergrößerung sieht, was Teleskope, Spektroskope und die mannigfachen Vergrößerungsapparate der Elektronik enthüllen, ist nicht ohne Theorie verständlich, es muss gedeutet werden.”

*(Max Born: Symbol und Wirklichkeit, 1964 [1])*

It is a dream of the materials scientist to understand the properties of matter from its microscopic structure at the atomic level—to understand, for example, the origin of the very different characteristics of water, salt, diamond, iron, or any other material. It is our dream, because this understanding allows us to design new substances and to predict their properties. Few examples from the long list of man-made materials are plastics, photonic crystals [2], and nanostructures [3] like quantum-dots, carbon nanotubes [4], or graphene [5].

The first step in this process is clearly a minute investigation of prototype materials. Two techniques are most important for the experimental analysis at the microscopic level, namely spectroscopy and microscopy: In spectroscopy, the system under study is exposed to an external perturbation and its response is measured. In optical absorption experiments, for example, the system is illuminated with light and one measures the probability that a photon of a certain wavelength is absorbed by the material. The resulting spectra contain direct information about the electronic structure.

Microscopy, on the other hand, allows one to access spatial informations. For example, far-field optical microscopes have contributed a lot to our present understanding of biological systems. But due to the diffraction limit, their application is limited to objects larger than the wave length of light ( $\approx 0.5 \mu\text{m}$ ). In electron microscopes this restriction is much less important because electrons with a kinetic energy of more than 20 keV have a de Broglie wavelength well below  $0.1 \text{ \AA}^{-1}$  [6]. The resolving power is mainly limited by the accuracy of the electromagnetic lenses. It has been continuously improved over the last decades (see fig. 1.1a) and electron microscopes became a standard tool to investigate nanostructures at the nanometre scale. For instance, the water-repellent surface of the leaves of the lotus flower and the bright colours of the butterfly have been explained with the microstructure of the surface [7]. Very recently, important progress was made and aberration-corrected microscopes with sub-atomic resolution became available [8].

If one is interested in the excitation properties at the nanometre scale, for instance, to study the excitations of individual nanoparticles, one can combine the principles of spectroscopy and microscopy. In a scanning transmission electron microscope (STEM) [9], the electron beam is focussed to a spot size of the order of  $1 \text{ \AA}$  and the detector analyses

the energy of the arriving electrons. On their way through the specimen, the electrons in the beam can be scattered inelastically and transfer energy to the sample, e. g., by inducing electron-hole transitions or exciting collective charge oscillations, the so-called plasmons. Measuring the energy distribution of the scattered electrons, one can obtain local informations about the electronic excitations of the system. By virtue of these *spatially-resolved electron-energy loss measurements* it is now possible to investigate both localised and extended excitations on a sub-nanometre scale with high energy resolution for any type of material [10].

With the new generation of microscopes it is now possible to achieve a spot size even below one Ångström. These important instrumental improvements give rise to new fundamental questions on the image formation and the spatial distribution of the involved excitations. At the atomic length scale, one clearly enters the quantum world where the intuitive classical picture is no longer valid. A detailed theoretical understanding of both the imaging process and the response of the target in the framework of quantum mechanics is thus essential for the interpretation of measurements in electron microscopy. The aim of this thesis is to contribute to this microscopic understanding and to prepare the theoretical tools to accompany modern microscopy experiments.

Within non-relativistic quantum mechanics, all microscopic properties of the target are determined by the Schrödinger equation for the constituting particles. But already for three interacting particles, an exact solution of this equation becomes impossible. In order to describe the response of the many-body system it is therefore necessary to decrease the complexity using physically motivated approximations or to reformulate the problem. In particular, dielectric theory has been successfully applied for macroscopic systems and even for rather small nanoparticles [10]. The response of the target to an external perturbation is then described within classical electrodynamics [11], whereas all quantum-mechanical effects are incorporated into the dielectric function  $\varepsilon$  that describes the bulk material. The latter is *a priori* unknown and has to be determined, e. g., from experiment or model calculations. However, this macroscopic approach cannot be applied to describe the response of individual atoms.

*Ab-initio* calculations, instead, are especially suited for a reliable quantum-mechanical description of the material at the atomic level. In the framework of (time-dependent) density-functional theory [12, 13] it is now possible to calculate the geometry, the electronic structure, and the excitations of systems with hundreds of electrons starting from first principles. No empirical parameters have to be included, in principle, in these numerical simulations and the results can be directly compared with experiment.

Unfortunately, there is a gap between the size of systems that can be described with dielectric theory and those accessible to *ab-initio* calculations. Important examples are atomically thin nanostructures like single-wall carbon nanotubes with diameters of a few nanometres. Such structures are particularly interesting for spatially-resolved electron energy-loss measurements. Several fundamental questions can be studied which concern, e. g., the properties of plasmons in low-dimensional systems, the delocalisation of the energy-loss signal, and the question which information is actually probed in atomically

resolved experiments. In this thesis, I develop and implement a method to overcome this problem by means of a building-block approach: Combining dielectric theory and *ab-initio* calculations, I describe the collective excitations in nanostructures (like carbon nanotubes) starting from the microscopic polarisability of their building blocks (bulk graphite). On the one hand, this considerably reduces the computational cost and opens the way to study electronic excitations for systems which are too large for a full *ab-initio* treatment, and too small for a reasonable description within the dielectric formalism. On the other hand, it allows us to analyse the loss spectra of nanostructures in terms of their normal-mode excitations which considerably simplifies the interpretation of the energy-loss spectra.

In this thesis I focus on the range of low energy losses  $E < 40$  eV, where only valence electrons contribute to the response of the system and collective electron oscillations can be excited. Using *ab-initio* calculations and the methods that I have developed, I study the collective electronic excitations in different carbon systems, namely graphite, graphene sheets, and single-wall carbon nanotubes. They are prototypes for three-, two-, and one-dimensional systems, respectively. Apart from this very fundamental interest, these materials have outstanding properties and many potential applications [5, 14]. This is a further motivation to study and understand the properties of carbon materials.

This thesis is organised in three parts:

- In the first part, the theoretical background for angular- and spatially-resolved electron-energy loss spectroscopy is presented. In the first two chapters, I discuss the theory of image formation in the electron microscope. The differential cross section measured in experiment is derived for the case of low energy losses using a semi-classical approach (chapter 1) and quantum-mechanical scattering theory (chapter 2). It can be divided into a geometry dependent probe factor  $C(\mathbf{q}, \mathbf{q}')$  and the mixed dynamic form factor  $S(\mathbf{q}, \mathbf{q}', \omega)$  which describes the response of the target. In this thesis, the form factor is obtained from *ab-initio* calculations using a plane-wave pseudopotential code. Therefore, the fundamentals of (time-dependent) density-functional theory and the basic workflow of the numerical simulations are outlined in chapter 3.
- The main results of this thesis are contained in the second part. It is concerned with the quantum-mechanical description of the target. To this end, I have studied the properties of the mixed dynamic form factor  $S$  for carbon systems with different dimensions, as well as bulk silicon.

In chapter 4, the response of three-dimensional crystals, namely graphite and silicon, is studied using *ab-initio* calculations. I predict for the first time an angular anomaly in the mixed dynamic form factor  $S(\mathbf{q}, \mathbf{q})$  for momentum transfers  $\mathbf{q}$  in the vicinity of certain reciprocal lattice vectors  $\mathbf{G}$ . Using a two-plasmon-band model, I can explain this effect in terms of induced microscopic charge oscillations, namely the crystal local-field effects. The anomaly was confirmed by the inelastic X-ray scattering experiments of our collaborators for graphite and silicon.

In chapter 5, I consider the response of a (quasi) two-dimensional system. First, the collective excitations in graphene and, in particular, the  $\pi$  plasmon is studied using *ab-initio* calculations. Second, I develop and implement several methods that considerably reduce the computational costs of these calculations using an interpolation method in reciprocal space (p. 92) or a cutoff method for the Coulomb potential in real space (p. 102). Third, I study the response of two-dimensional systems in the limit of ideal localisation on the sheet. The resulting analytic expression relates the in-plane response in graphite with the two-dimensional response function in graphene. I study the validity of this local-response approximation—which is also the basis of local dielectric theory—by comparison with the full *ab-initio* results. Finally, a building-block approach is presented which allows us to calculate the full quantum-mechanical response of assembled systems, like multilayer graphene, starting from the isolated sheet.

In chapter 6, the methods developed for two dimensions are finally applied to (quasi) one-dimensional single-wall carbon nanotubes. First, I extend the building-block approach in order to describe the microscopic response of the tube starting from an *ab-initio* calculation of graphene. This corresponds to an extension of the well-known zone-folding model for collective excitations. I implement this method and compare the results with full *ab-initio* calculations of the angular-resolved energy-loss spectra of single-wall carbon nanotubes. Second, the local-response approximation is applied for the case of cylindrical systems and the range of validity is discussed. Third, I study the angular-resolved loss spectra in single-wall carbon nanotubes. In particular, the dependence of the plasmon dispersion on the orientation of the momentum transfer is considered.

- In the last part, I show how the methods described above can be potentially applied for an efficient theoretical description of spatially-resolved electron energy-loss experiments starting from *ab-initio* calculations. As a first model system, I consider the movement of a classical electron parallel to a single graphene layer. Depending on the imaging parameters, one can make use of the local-response approximation in the calculation of the energy-loss probability and eventually also in the description of the target system. I discuss the influence of non-local corrections and the possibility of atomic resolution for valence-electron energy-loss spectroscopy. Finally an outlook is given for the simulation of spatially-resolved electron energy-loss measurements on isolated single-wall carbon nanotubes.

**Part I**

**Background**



# 1 Introduction

## 1.1 Electron Microscopy

In this section, some of the recent experimental achievements in atomically-resolved electron microscopy are reviewed. According to the subject of this thesis, we will focus on angular- and spatially-resolved valence-electron energy-loss spectroscopy. For a general introduction to the broad topic of electron microscopy see, e. g. [9, 17].

### 1.1.1 Transmission Electron Microscope

In a transmission electron microscope (TEM), the sample is generally illuminated by a broad beam of electrons which are accelerated to energies of about 200 keV. Behind the object, the transmitted electrons are focussed to the image plane by a system of electromagnetic lenses. Although this basic principle is analogous to optical microscopy, the images cannot be simply understood as a shadow-cast of the atomic structure. Instead one has to consider the propagation of the electron wave function through the sample which leads to interference patterns in the image plane.

Already 50 years ago, images of these interference patterns have been published that showed intensity modulations at the atomic scale. In the 1980ies, high resolution images have been obtained by a reconstruction of the exit-plane wave function of the probing electron from a series of images with varying objective lens focus. Afterwards, the spatial informations of the object can be extracted from this exit-plane wave function [18].

Approximately ten years ago, aberration-corrected electron microscopes became available. With this new generation of electron microscopes, local informations about individual atoms, like shifts in the atomic positions, can be measured with an unmatched precision (see fig. 1.1a). It is now possible to study defects, dislocations, stress, and local physical properties like the dipole moment at the atomic level (see fig. 1.1b). This opens the way to understand the macroscopic properties of materials from the microscopic atomic arrangements.

### 1.1.2 Electron Energy-Loss Spectroscopy

Electron energy-loss spectroscopy (EELS), instead, gives access to the excitation properties of the system with high energy resolution. To this end, the detector does not only count the number of transmitted electrons, but also analyses their kinetic energy. The resulting energy-loss spectrum, i. e., the probability to detect a scattered electron which has lost a certain energy, contains valuable information about the excitations of the target. Depending on the imaging mode, we can distinguish between angular- and spatially-resolved EELS.

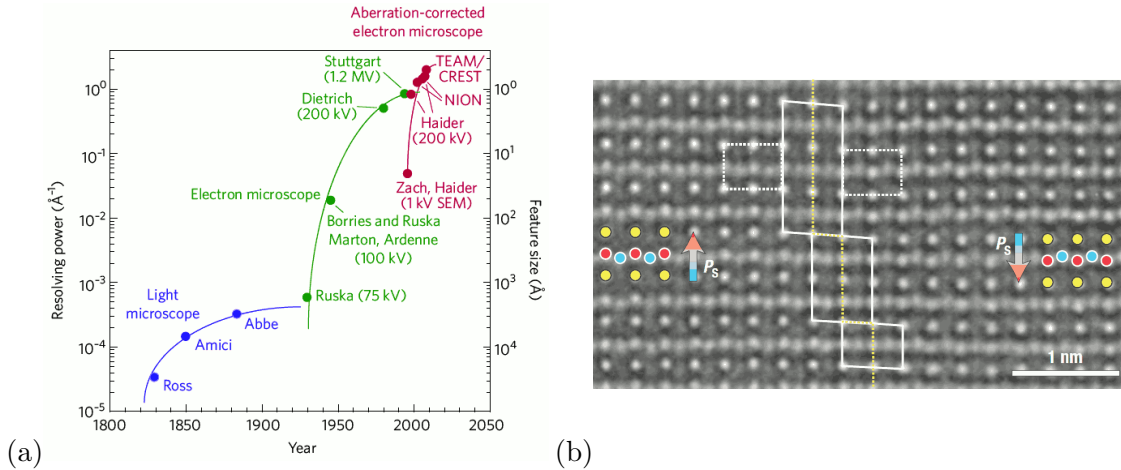


**Fig. 1.1:** Spatial resolution in transmission electron microscopy. (a) Advances in the resolving power of electron microscopes (Reprinted by permission from Macmillan Publishers Ltd: [Nature Materials](#) [15], © 2009). (b) Experimental observation of a polarisation domain wall in a ferroelectric material. Arrows give the direction of spontaneous polarisation as inferred from the local atom displacements (Reprinted by permission from Macmillan Publishers Ltd: [Nature Materials](#) [16], © 2008).

### Angular-Resolved EELS

In angular-resolved EELS, one considers the diffraction of an incoming plane electron wave. The detector collects only electrons which are scattered into a small solid-angle element  $d\Omega$  (see fig. 1.2a). As the scattering angle  $\vartheta$  is directly related to the momentum transfer  $\mathbf{q}$  of the electron to the target, one can measure the momentum dependence of the excitations by collecting several energy-loss spectra for different angles  $\vartheta$ . For instance, the plasmon dispersion in bulk materials and nanostructures can be studied using AR-EELS measurements. We will see in section 2.4 that the same information can be obtained from inelastic X-ray scattering experiments.

### Spatially-Resolved EELS

The combination of energy-loss spectroscopy and transmission electron microscopes provides access to the local excitation properties of the system with very high spectral and *spatial resolution* [10]. One of the possible experimental realisations is the energy-filtered transmission electron microscope (EFTEM). Compared to the standard TEM geometry, an energy filter is introduced behind the object to select electrons with a certain kinetic energy. As a result, one obtains a spatially-resolved image of the target which is only formed by electrons that have suffered a certain energy loss.

A complementary approach is used in scanning transmission electron microscopes (STEM) [20]. In this case, the sample is illuminated with a highly focussed electron beam that is used to scan over the sample area (see fig. 1.2b). Additionally, the detector is equipped with an energy analyser in order to measure the electron energy-loss spectrum originating from a very small region in space.

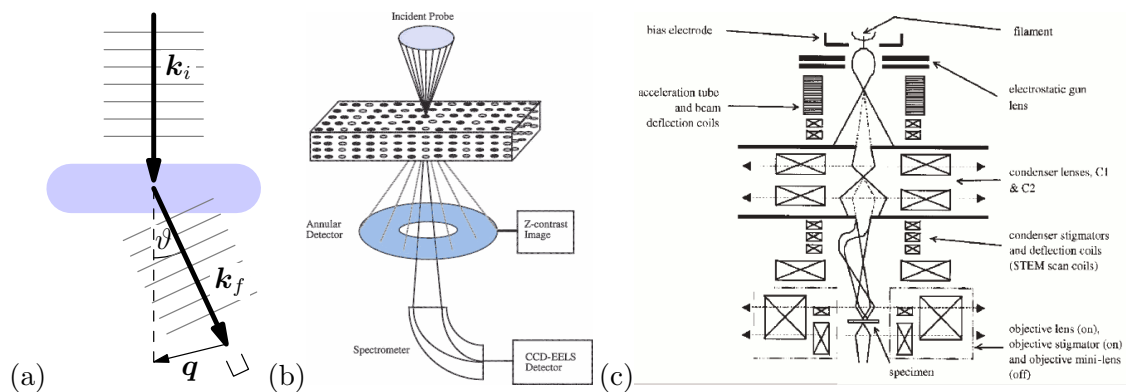


**Fig. 1.2:** (a) Geometry of an angular-resolved EELS experiment, (b) a scanning transmission electron microscope (STEM) and (c) a sketch of its experimental realisation. (Reprinted from [19] with permission from John Wiley & Sons Inc. © 2006).

### Core Loss

A typical energy-loss spectrum is shown in fig. 1.3a. At large energy transfers, one observes characteristic edges that are directly related to the discrete energy levels of the inner-shell electrons of the atom. Because the tightly bound core electrons are rather unaffected by the chemical environment, these edges are a unique signature of the atom species. They can be used to construct *elemental maps* from the spatially-resolved EELS data. These images show the spatial distribution of a certain element.

Using an aberration-corrected STEM, it has been even possible to measure elemental maps with atomic resolution (see fig. 1.3b). If one analyses also the near-edge features (which are related to the final valence states) one can also access information about chemical bonding [21].

### Valence Loss

For low energy loss, the spectrum contains informations about the band structure of the system and the collective electronic excitations. For example, it has been possible to measure the band gap of thin dielectric films with an energy resolution of few 100 meV and a spatial resolution of few nanometre using STEM valence EELS measurements [22]. Another interesting application is the investigation of surface plasmons at interfaces and small particles [23]. For example, fig. 1.4b shows the valence-loss signal for different positions across an thin layer of silicon-dioxide of 2 nm thickness. Compared to the core-loss signal (see fig. 1.4a), the spatial resolution is reduced in valence EELS measurements.

In this thesis we will investigate both the momentum dependence (chapter 4-6) and the spatial dependence (chapter 7) of the valence loss excitations in different carbon systems.

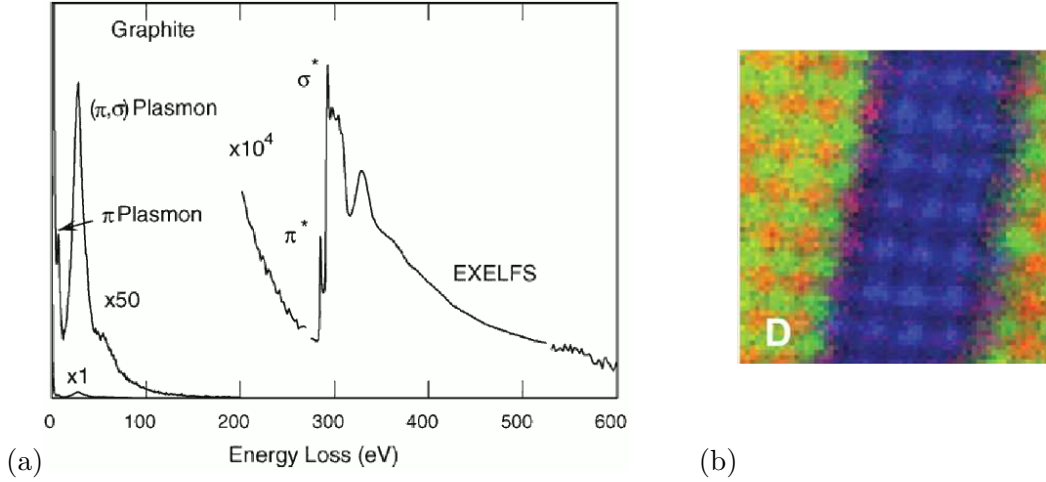


**Fig. 1.3:** STEM measurements. (a) Electron energy-loss spectrum for graphite in the valence- and core-loss region (Reprinted from [24], Micron © 2008, with permission from Elsevier). (b) An atomic-resolution elemental map of a multilayer system. Colours indicate different edge signals attributed to La (green), Ti (blue), and Mn (red) atoms (Reprinted by permission from Macmillan Publishers Ltd: [Nature Materials](#) [15], © 2009).

### 1.1.3 Some Fundamental Questions

Due to the enormous improvements in instrumentation technology, it is now possible to probe local excitation properties at the sub-Ångström level. This gives rise to several fundamental questions. Some of them shall be briefly presented in the following.

**Delocalisation of the energy-loss signal:** One might wonder which spatial resolving power can be actually obtained in spatially-resolved EELS measurements. Indeed, there are several reasons for the *delocalisation* of the EELS signal [10]: First, in a STEM the incident beam is focussed only to a finite width. This lens delocalisation can be now reduced to values below 1 Å using aberration-corrected microscopes. Second, the Coulomb field which is generated by the fast electrons has a finite extent. This Coulomb delocalisation depends on the experimental parameters like the velocity  $v$  of the impinging electrons and the energy loss  $\hbar\omega$ . Third, the excitations in the target itself have a different spatial extent. Core excitations which are excited at large energy transfers are typically localised at the atomic length scale, while valence-loss excitations like (surface) plasmons may be very extended.

As a rough estimate for the delocalisation length, one often uses Bohr’s adiabatic parameter  $b_{\max} = \omega/v$  which has been derived within classical theory [11]. Using a quantum mechanical approach, Muller and Silcox [25] show that  $b_{\max}$  should be considered as a ‘dynamic’ screening length which describes the exponential decay of the inelastic scattering signal. Using a full width at half maximum criterion, the delocalisation length for low energy losses ( $\approx 10$  eV) is then found to be of the order of a few nanometres [25].

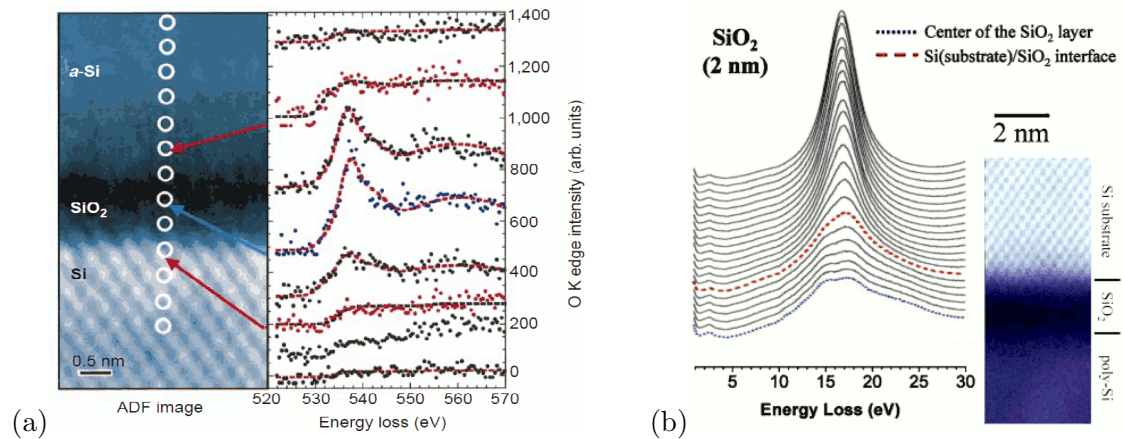


**Fig. 1.4:** Experimental EEL spectra from a STEM measurement scanning across a Si/SiO<sub>2</sub> interface. (a) The background-corrected oxygen K-edge (Reprinted by permission from Macmillan Publishers Ltd: [Nature](#) [31], © 1999) and (b) the valence-loss signal are shown for different positions across the interface (Reprinted from [32], © 2008 by The American Physical Society).

**Subsequent elastic and inelastic scattering:** Generally, the incident electrons in a focussed electron beam can be scattered several times on their way through the sample. For example, in a crystal, they can be *channeled* along the rows of atoms due to elastic scattering events. Either, one has to use very thin targets in order to avoid such *multiple-scattering effects*. Or one has to include the subsequent elastic and inelastic scattering events in a theoretical description. For example, one can consider the propagation of the density matrix of the external electron through the system using a multi-slice approach (see, e. g., [26, 27]).

**Excitations in valence EELS:** The valence-loss signals involve spatially more extended informations and are therefore less simple to interpret than core-loss spectra. For instance, Nelayah *et al.* [23] have recently reported spatially-resolved plasmon maps on small nanoparticles which have been obtained from STEM measurements. One might wonder which physical quantity is actually measured in such an experiment. García de Abajo and Kociak [28] have shown that the signal can be interpreted in terms of the photonic local-density of states of the system.

Already this short overview shows that there is an important interest in a theoretical understanding of spatially-resolved electron energy-loss spectra. In the following part of the introduction, we will briefly review the (non-relativistic) dielectric formalism which has been successfully applied for energy losses at small spheres, cylinders, and many other geometries [29, 30].

## 1.2 Macroscopic Dielectric Theory

The interaction of a swift electron with matter is generally described in the semi-classical theory. One starts from the Maxwell equations of classical electrodynamics to calculate the perturbation of the target due to the external electron. The response of the material is characterised by the dielectric function  $\varepsilon$ . It can be either determined from experiments, approximated by simple models like the Drude model for free electrons, or obtained from a quantum-mechanical calculation.

Depending on the geometry of the target system and the complexity of the dielectric function  $\varepsilon$ , the solution of the Maxwell equations can be rather complicated. In the following, we will briefly review some of the numerous approaches to this problem. For a recent overview, see e. g., [10, 33].

### 1.2.1 Dielectric Theory for Simple Geometries

For simple geometries, the Maxwell equations can be solved analytically. Assuming a frequency dependent response of the material  $\varepsilon(\omega)$ , the energy loss in planar surfaces, spheres, cylinders, and several assemblies of these objects has been calculated [30].

For instance, consider an interface between two materials  $A$  and  $B$  with a dielectric function  $\varepsilon_A$  and  $\varepsilon_B$ . The energy-loss probability of an electron travelling inside the medium  $A$  parallel to the interface at a distance  $b$  is found to be [30]

$$P \propto \ln\left(\frac{2\pi q_c v}{\omega}\right) \operatorname{Im}\left\{-\frac{1}{\varepsilon_A}\right\} - K_0\left(\frac{2b\omega}{v}\right) \operatorname{Im}\left\{-\frac{1}{\varepsilon_A}\right\} + K_0\left(\frac{2b\omega}{v}\right) \operatorname{Im}\left\{-\frac{2}{\varepsilon_A + \varepsilon_B}\right\}, \quad (1.1)$$

where  $v$  denotes the velocity of the electron,  $q_c$  the plasmon cutoff wave vector, and  $K_0$  is the zeroth-order modified Bessel function. The first term can be associated with the *volume loss*. Indeed, the other two terms compensate each other when  $\varepsilon_A = \varepsilon_B$ , i. e., when the system is homogeneous. In this case, the loss spectrum shows characteristic peaks, whenever  $\varepsilon_A(\omega) \approx 0$ . They correspond to the longitudinal normal modes of the system and can be associated with collective oscillations of the electrons, the so-called *volume plasmons*.

The other two terms are due to the interface and vanish exponentially with increasing distance  $b$  (see appendix A.4.3). The second is known as *begrenzungsterm* and accounts for the reduction of the bulk losses due to the interface. The third term contributes strong peaks, when  $\varepsilon_A(\omega) + \varepsilon_B(\omega) \approx 0$ . They are associated to electromagnetic normal modes located at the interface, the so-called *surface plasmons*. Since the discovery of these surface modes, a new field of physics has emerged which is known as *plasmonics* [34].

### Surface Plasmons

These surface modes have been first described by Ritchie [35], who studied the energy loss of a fast electron transmitted through thin foils. In such systems, the valence loss spectra show peaks at energies that differ from the expected bulk plasmon energies.

In order to understand this point, we consider the model system discussed above for the case of an electron moving parallel to a metal surface.<sup>1</sup> The dielectric function of the metal can be approximated by the Drude function which is derived from a purely classical model for the electrons in the metal. Drude considered a homogeneous gas of free electrons which move ballistically until they lose all their energy in a collision after an average time  $\tau = \eta^{-1}$ . The dielectric function then reads

$$\varepsilon_D(\omega) = 1 - \frac{\omega_p^2}{\omega^2 + i\omega\eta}, \quad \omega_p^2 = \frac{e^2 n}{m\varepsilon_0}, \quad (1.2)$$

where  $n$  is the average electron density and  $\omega_p$  denotes the *plasma frequency*. If the electron moves inside the metal ( $\varepsilon_A = \varepsilon_D$ ) parallel to the interface to vacuum ( $\varepsilon_B = 1$ ), the surface and the volume term in the loss function (1.1) become

$$\text{Im}\left\{-\frac{1}{\varepsilon_D(\omega) + \alpha}\right\} = \frac{\omega_p^2 \omega \eta}{[(\alpha + 1)\omega^2 - \omega_p^2]^2 + [(\alpha + 1)\omega\eta]^2}, \quad \alpha = \begin{cases} 0 & \text{volume} \\ 1 & \text{surface} \end{cases} \quad (1.3)$$

For small damping  $\eta$ , we find a strong peak at  $\omega_p$  in the case of volume loss and at  $\omega_p/\sqrt{2}$  for the surface-loss term.

A very similar result is obtained for insulators. In the Lorentz model, the electrons are no longer free but harmonically bound to the atom cores. The dielectric function resulting from this model then reads

$$\varepsilon_L(\omega) = 1 - \frac{\omega_p^2}{\omega^2 - \omega_0^2 + i\omega\eta}, \quad (1.4)$$

where  $\omega_0$  denotes the resonance frequency of the bound electrons. Consequently, the bulk-plasmon frequency is given by  $(\omega_p^2 + \omega_0^2)^{1/2}$ , while the surface plasmon is shifted to lower frequencies  $(\omega_p^2/2 + \omega_0^2)^{1/2}$ . This general trend is found for many different geometries and materials.

## Near-Field Electron Energy-Loss Spectroscopy

In *near-field electron energy-loss spectroscopy*, the electron travels in vacuum and does not even intersect the sample. In this case ( $\varepsilon_A = 1$ ), only the third term in eq. (1.1) contributes to the loss signal. Contributions from the volume plasmon excitation completely vanish and only the surface plasmons can be excited. As the Bessel function  $K_0(\frac{2b\omega}{v})$  vanishes exponentially, low frequency modes  $\omega$  are favoured in this aloof configuration.

In chapter 7, we will calculate the valence-loss probability of a fast electron travelling parallel to an isolated graphene sheet. Instead of using a model for the dielectric function  $\varepsilon$ , we will determine the response of the material from an *ab-initio* calculation.

---

<sup>1</sup>Ritchie [35] originally calculated the energy-loss for an electron moving perpendicular to the thin film. In the limit of sufficiently thick films, the formula assumes a form similar to that of eq. (1.1), where the prefactors  $K_0$  of the surface terms have to be replaced by an arctan-function [30].

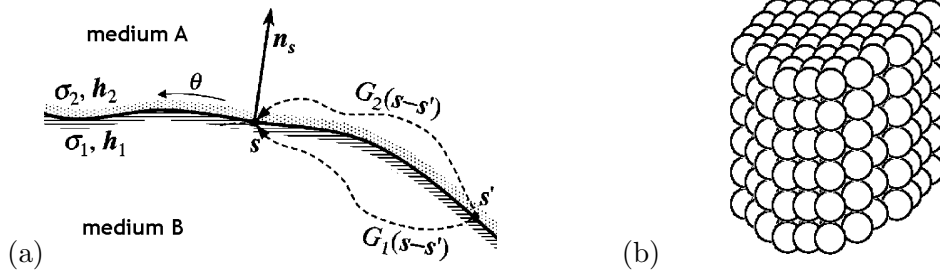


**Fig. 1.5:** (a) Boundary-element method (Reproduced from [41], © 2002 by The American Physical Society) and (b) discrete-dipole approximation. The balls indicate a single dipole.

## 1.2.2 Extensions

Numerous extensions of the previous theory have been given: First, the description of the material response has been improved. For instance, Gumbs and Horing [36] have included non-local corrections, i. e., the wave-vector dependence of the dielectric function  $\varepsilon(\mathbf{q}, \omega)$ . Stöckli *et al.* [37] have used an anisotropic dielectric function in order to describe the response of multi-wall carbon nanotubes.

Second, relativistic effects have been included in the description of the probe electron [38–40]. Indeed, the probe electrons have typically an energy of more than 100 keV and retardation effects can become important. For example, Kröger [38] has described the Čerenkov radiation that can be excited by a fast electron traversing a thin foil.

And third, the theory has been extended for arbitrary geometries. In this case, numerical simulations become necessary. They are based on either the Poisson equation in the non-retarded case or the full Maxwell equations if relativistic corrections are included. Two examples are the boundary-element method and the discrete-dipole approximation. For a more detailed list see, e. g. [10, 33].

### Boundary-Element Method

The boundary-element method (BEM) has been introduced by Fuchs [42]. He considered a system of small particles with arbitrary shape, composed of a homogeneous material which is described by the local dielectric constant  $\varepsilon_A(\omega)$ . The response of this inhomogeneous system to an external perturbation  $\varphi^e$  is associated with an induced surface charge  $\sigma$  which gives rise to an induced potential  $\varphi^i$ . Taking into account the continuity of the field components at the boundary of the particles (see fig. 1.5a), one obtains a self-consistent relation for the induced boundary charge [10]:

$$2\pi \frac{\varepsilon_A + \varepsilon_B}{\varepsilon_A - \varepsilon_B} \sigma(\mathbf{s}, \omega) = \mathbf{n}_s \cdot \nabla \varphi^e(\mathbf{s}, \omega) - \int d^2 s' \frac{\mathbf{s} - \mathbf{s}'}{|\mathbf{s} - \mathbf{s}'|^3} \cdot \mathbf{n}_s \sigma(\mathbf{s}', \omega), \quad (1.5)$$

where  $\varepsilon_B$  is the dielectric constant of the host material and  $\mathbf{n}_s$  the normal vector of the interface. The numerical solution of this equation can be very efficient, because the variable  $\mathbf{s}$  is restricted to the surface of the particles. The outlined procedure has been also generalised for the nonretarded case [40, 41].

## Discrete-Dipole Approximation

The basic idea of the discrete-dipole approximation (DDA) is to replace the homogeneous system of arbitrary shape by a finite array of polarisable dipoles (see fig. 1.5b). These dipoles will react to an external potential, but also to the fields of the other dipoles that interact with each other. For a finite set of dipoles, the Maxwell equations can be solved numerically. The polarisability  $\alpha$  of a single dipole is obtained by inverting the Clausius-Mosotti relation for a given material. Note that in contrast to the boundary-element method, the entire volume of the particles has to be considered.

The discrete-dipole approximation closely resembles the theory of Lorentz [43], who derived the dielectric properties of a crystal from the polarisability of the constituting atoms. It has been successfully applied to describe the dielectric response of nanoparticles [44] and has been also extended for periodic systems [45].

The dielectric approach described above has proven to be very valuable for the description of macroscopic and mesoscopic systems with dimensions down to several 10 nm. However, this description will fail at the atomic level. We cannot approximate the response of a single atom by a dipole, if we are interested in atomic resolution. Or even identify it with a small sphere of bulk material. Nevertheless, the semi-classical dielectric approach can be even extended to the atomic level, as we will see in the next section.

## 1.3 Microscopic Dielectric Theory

Looking back in history, the concept of the dielectric function  $\varepsilon$  was continuously extended in order to describe the response of a material more and more accurately [46]:

In optics, the complex dielectric constant  $\varepsilon_M = (n + i\kappa)^2$  reflects two important properties of the material: (i) the refraction index  $n$  that defines the speed of light  $c/n$  and determines the refraction at the boundary between two different media, and (ii) the absorption coefficient  $\kappa$  that describes the exponential loss of intensity  $I(d) = I_0 e^{-\kappa d}$  inside a material (Beer's law). It is easily understood that a single constant is generally not sufficient to describe the optical properties of a material. Already Newton [47] had found that the light of the sun could be split into the colours of the rainbow when it is diffracted by a glass prism. The refraction index  $n$  and thus the dielectric function must be a function of the frequency  $\omega$  of the light, i. e.,  $\varepsilon_M = \varepsilon_M(\omega)$ . Later on, also the optical activity and birefringence in certain crystals could be explained by the dependence of the refraction index on the polarisation direction. As a consequence, the dielectric function should be a tensor  $\varepsilon_M^{\alpha\beta}(\omega)$ , where  $\alpha$  and  $\beta$  run over the three vector components  $x$ ,  $y$ , and  $z$  [48]. And finally, one has discovered that the nonlocal contributions to the response of the material give rise to surprising behaviours like the negative refraction in certain materials. This nonlocal behaviour, which is also known as spatial dispersion, corresponds to a wave-vector dependence of the dielectric function  $\varepsilon_M(\mathbf{q}, \omega)$  [46].

All these different cases can in principle be derived from a microscopic description of the elementary excitations of the medium using the *microscopic dielectric tensor*  $\varepsilon^{\alpha\beta}$

$$E_\alpha^e(\mathbf{r}, t) = \int d\mathbf{r}' \int dt' \varepsilon^{\alpha\beta}(\mathbf{r}, \mathbf{r}', t-t') E_\beta^t(\mathbf{r}', t'), \quad (1.6)$$

which relates the external perturbation  $\mathbf{E}^e$  to the total microscopic field  $\mathbf{E}^t$ , i. e., the response of the material. It can be determined by a quantum mechanical calculation, e. g., in the framework of time-dependent perturbation theory (see chapter 3). The connection between the microscopic response  $\varepsilon$  and the macroscopic quantity  $\varepsilon_M$  can be rather complicated (see section 1.3.2 and appendix B for details).

In the following, we start from this microscopic description of the material in order to derive the energy-loss of a fast electron. This corresponds to a *semi-classical approach*: The external perturbation due to the electron is considered to be purely classical and will be derived from the microscopic Maxwell equations. The target, instead, is described by the microscopic dielectric function which is calculated in the framework of quantum mechanics. In particular, the nonlocal, frequency- and spatially dependent response is considered, i. e., no further assumptions are made *a priori* except for the linearity of the response and the neglect of relativistic effects.

### 1.3.1 Microscopic Response

Consider the perturbation of a system by an external potential  $\varphi^e(\mathbf{r}, t)$ . For example, this might be the potential induced by a fast electron in a microscope. We neglect any relativistic effects, such as transverse components of the fields or longitudinal-transverse

couplings in the material (see appendix B for details). This perturbation will polarise the material and thus induce a change  $\rho^i$  in the charge density of the system. This response should be described in the framework of quantum mechanics. In chapter 3, we will derive an approximation for the density response function or *susceptibility* which describes the *linear response* to the external potential (we use SI units)<sup>2</sup>

$$\rho^i(\mathbf{r}, t) = \int d\mathbf{r}' \int dt' e^2 \chi(\mathbf{r}, \mathbf{r}', t - t') \varphi^e(\mathbf{r}', t'), \quad \text{or shorter: } \rho^i = e^2 \chi \varphi^e. \quad (1.7)$$

This additional charge will induce a potential  $\varphi^i$  that screens the external perturbation. It can be calculated from the Poisson equation

$$\Delta \varphi^i(\mathbf{r}, t) = -\frac{1}{\epsilon_0} \rho^i(\mathbf{r}, t), \quad \varphi^i(\mathbf{r}, t) = \int d\mathbf{r}' \frac{1}{\epsilon^2} v(\mathbf{r} - \mathbf{r}') \rho^i(\mathbf{r}', t). \quad (1.8)$$

The inhomogeneous solution is given in terms of the Coulomb potential  $v$  [see eq. (A.27)], while the homogeneous part is assumed to vanish at every point due to the boundary conditions at infinity. The (*inverse*) *microscopic dielectric function* connects the external potential  $\varphi^e$  and the total potential  $\varphi^t = \varphi^e + \varphi^i$  and is defined as (in short-hand notation)

$$\varphi^t = \epsilon^{-1} \varphi^e, \quad \varphi^e = \epsilon \varphi^t. \quad (1.9)$$

It is a scalar function  $\epsilon(\mathbf{r}, \mathbf{r}', t - t')$  and not a tensor  $\epsilon^{\alpha\beta}(\mathbf{r}, \mathbf{r}', t - t')$  as in eq. (1.6), because  $\epsilon$  relates only the longitudinal (rotation-free) part  $\mathbf{E}_L = -\nabla\varphi$  of the vector fields. The connection between  $\epsilon^{\alpha\beta}$  and  $\epsilon$  is derived in appendix B. Introducing the *polarisability* as the response to the total potential, i. e.,  $\rho^i = e^2 \pi \varphi^t$ , we find from the equations above

$$\epsilon^{-1} = 1 + v\chi, \quad \epsilon = 1 - v\pi, \quad \chi = \pi + \pi v\chi. \quad (1.10)$$

The last equation is known as the *Dyson equation* and explicitly reads:

$$\chi(\mathbf{r}, \mathbf{r}', t - t') = \pi(\mathbf{r}, \mathbf{r}', t - t') + \iint d\mathbf{r}_1 d\mathbf{r}_2 \int dt_1 \pi(\mathbf{r}, \mathbf{r}_1, t - t_1) \cdot v(\mathbf{r}_1 - \mathbf{r}_2) \chi(\mathbf{r}_2, \mathbf{r}', t_1 - t'), \quad (1.11)$$

because the Coulomb potential  $v(\mathbf{r}, \mathbf{r}', t - t') = v(\mathbf{r} - \mathbf{r}')\delta(t - t')$  acts instantaneously in time (non-retarded limit). The solution of this equation will be a central part of chapter 5 and 6. Indeed, the polarisability  $\pi$ , which gives the response to the total potential  $\varphi^t$ , is found to be very local in space and is therefore a transferable quantity. The susceptibility  $\chi$ , instead, has to describe the full self-consistent screening of the external potential  $\varphi^e$ . Due to the long-range behaviour of the Coulomb potential, it generally strongly depends on the surface geometry of the system. We will discuss this important difference more precisely in section 5.4.1.

---

<sup>2</sup>The charge  $e$  appears in the definition, as we will later use the density  $n$ , not the charge density  $\rho$ .

### 1.3.2 Crystal Local-Field Effects

In a crystal, any single-point function  $f$  can be written as the following Fourier expansion

$$f(\mathbf{r}, t) = \sum_{\mathbf{G}} \int d\mathbf{q}_r \int d\omega f_{\mathbf{G}}(\mathbf{q}_r, \omega) e^{-i[\omega t - (\mathbf{q}_r + \mathbf{G})\mathbf{r}]}, \quad (1.12)$$

where the summation runs over all reciprocal lattice vectors  $\mathbf{G}$  and the reduced momentum  $\mathbf{q}_r$  is restricted to the first Brillouin zone of the crystal. The coefficient  $f_{\mathbf{0}}$  can be understood as the *macroscopic* component of the field. Indeed, by averaging the function  $f$  over the unit cell of the crystal, all terms with  $\mathbf{G} \neq \mathbf{0}$  vanish due to the high-frequency spatial oscillation of the exponential inside the unit cell.

Similarly, any response function  $\mathfrak{R} = \mathfrak{R}_{\mathbf{G}\mathbf{G}'}(\mathbf{q}_r, \omega)$  becomes a matrix in  $\mathbf{G}$ , and a function of  $\mathbf{q}_r$  and  $\omega$  in reciprocal space. For example, the Dyson eq. (1.11) then reads:

$$\chi_{\mathbf{G}\mathbf{G}'}(\mathbf{q}_r, \omega) = \pi_{\mathbf{G}\mathbf{G}'}(\mathbf{q}_r, \omega) + \sum_{\mathbf{G}''} \pi_{\mathbf{G}\mathbf{G}''}(\mathbf{q}_r, \omega) v(\mathbf{q}_r + \mathbf{G}'') \chi_{\mathbf{G}''\mathbf{G}'}(\mathbf{q}_r, \omega). \quad (1.13)$$

Physically, this means that only charge oscillations with the same reduced momentum  $\mathbf{q}_r$  are coupled inside the crystal. If the system is homogeneous, the response function becomes completely diagonal  $\mathfrak{R}_{\mathbf{G}\mathbf{G}'} = \mathfrak{R}_{\mathbf{G}\mathbf{G}} \delta_{\mathbf{G},\mathbf{G}'}$  (see appendix A.2.2). The off-diagonal elements are therefore directly related to the inhomogeneity of the system.

#### Connection with Macroscopic Quantities

We are now able to connect the microscopic dielectric function  $\varepsilon$  and the macroscopic one  $\varepsilon_M$  mentioned in the introduction of this section. The latter is defined for the macroscopic Maxwell equations, where all fields are averaged over a mesoscopic volume which is much larger than the size of the unit cell (see appendix B.1.4). The macroscopic response function  $\mathfrak{R}_M$  connects only the  $\mathbf{G} = \mathbf{0}$  components of the fields, say  $f_{\mathbf{0}}$  and  $g_{\mathbf{0}}$ . We can derive such a connection from the corresponding microscopic equation

$$g_{\mathbf{0}}(\mathbf{q}_r, \omega) = \sum_{\mathbf{G}'} \mathfrak{R}_{\mathbf{0}\mathbf{G}'}(\mathbf{q}_r, \omega) f_{\mathbf{G}'}(\mathbf{q}_r, \omega) \quad (1.14)$$

*only if* the field  $f$  itself is macroscopic, i. e.,  $f_{\mathbf{G}} = f_{\mathbf{0}} \delta_{\mathbf{0},\mathbf{G}}$ . In this case, the macroscopic response function  $\mathfrak{R}_M$  is simply given by the diagonal element  $\mathfrak{R}_{\mathbf{0}\mathbf{0}}$  of the microscopic response function. Whenever the external potential  $\varphi^e$  is macroscopic, we can therefore introduce the macroscopic dielectric function from eq. (1.9) as

$$\varepsilon_M^{-1}(\mathbf{q}_r, \omega) = \varepsilon_{\mathbf{0}\mathbf{0}}^{-1}(\mathbf{q}_r, \omega), \quad \varepsilon_M(\mathbf{q}_r, \omega) = \frac{1}{\varepsilon_M^{-1}} = \frac{1}{\varepsilon_{\mathbf{0}\mathbf{0}}^{-1}(\mathbf{q}_r, \omega)}. \quad (1.15)$$

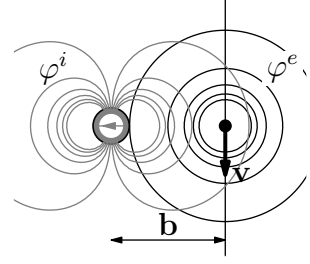
This important connection between microscopic and macroscopic dielectric function has been first given by Adler [49] and Wiser [50]. Note, that the second equation includes a matrix inversion mixing all elements of  $\varepsilon_{\mathbf{G}\mathbf{G}'}$ . If we assume, that also the *total* potential  $\varphi^t$  is macroscopic, we would simply have

$$\varepsilon_M^{\text{NLF}}(\mathbf{q}_r, \omega) = \varepsilon_{\mathbf{0}\mathbf{0}}(\mathbf{q}_r, \omega) \quad (1.16)$$

However, this is generally not the case. Due to the coupling of different  $\mathbf{G}$  modes in inhomogeneous crystals, the induced potential  $\varphi^i$  has microscopic components  $\mathbf{G} \neq 0$  even if the external potential is purely macroscopic. These microscopic induced fields are the so-called *crystal local fields*. Using eq. (1.16) instead of eq. (1.15), we neglect any contributions from these modes, i. e., we neglect the crystal local-field effects (LFE). In chapter 4, we will extensively discuss the role of LFE for the loss spectra of crystals and give a more physical picture of LFE in section 4.2.2.

### 1.3.3 Electron Energy-Loss Probability

The calculation of the electron energy-loss probability consists of three steps (see figure): First, the external electron can be associated with a time-dependent charge density  $\rho^e$  which gives rise to an external potential  $\varphi^e$ . Second, this external potential will perturb the material and induce a response  $\varphi^i$ . Third, the energy loss is then obtained from the work done by the external electron against the total potential  $\varphi^t = \varphi^i + \varphi^e$ .



We assume that the electron moves on a straight line with a velocity  $\mathbf{v}$  and impact parameter  $\mathbf{b}$ . The charge density is given as (in real and reciprocal space, see eq. (A.23))

$$\rho^e(\mathbf{r}t) = -e\delta(\mathbf{r} - \mathbf{v}t - \mathbf{b}) \quad \longleftrightarrow \quad \rho^e(\mathbf{q}\omega) = -2\pi e\delta(\mathbf{q}\mathbf{v} - \omega)e^{-i\mathbf{q}\mathbf{b}}. \quad (1.17)$$

The corresponding external potential can be calculated from the Poisson eq. (1.8):

$$\varphi^e(\mathbf{q}\omega) = \frac{1}{\epsilon^2}v(\mathbf{q})\rho^e(\mathbf{q}\omega) = -\frac{2\pi e}{\epsilon_0 q^2}\delta(\mathbf{q}\mathbf{v} - \omega)e^{-i\mathbf{q}\mathbf{b}}, \quad v(\mathbf{q}) = \frac{e^2}{\epsilon_0 q^2}. \quad (1.18)$$

By the Fourier transform, the external field is decomposed into several plane-wave modes with wave vector  $\mathbf{q}$  and frequency  $\omega$ . They are all purely longitudinal as we have neglected retardation effects and they obey the dispersion relation  $\mathbf{q}\mathbf{v} = \omega$ . The external perturbation will polarise the target and hence induce another potential  $\varphi^i$ . This response is given by the inverse microscopic dielectric function (1.9) which will be determined from a quantum-mechanical calculation later on (see chapter 3). The total energy loss  $P$  then corresponds to the work of the external particle against the total field  $\mathbf{E}^t$  (note that the external field  $\mathbf{E}^e$  will not contribute). With the current density  $\mathbf{j}^e = \mathbf{v}\rho^e$  (which is real) we have in real and reciprocal space [51]

$$P = \int dt \int d\mathbf{r} \mathbf{j}^e(\mathbf{r}t) \cdot \mathbf{E}^t(\mathbf{r}t) \stackrel{(A.23)}{=} \frac{1}{(2\pi)^4} \int d\omega \int d\mathbf{q} [\mathbf{j}^e(\mathbf{q}\omega)]^* \cdot \mathbf{E}^t(\mathbf{q}\omega), \quad (1.19)$$

By means of the continuity equation  $\nabla \cdot \mathbf{j} + \partial_t \rho = 0$  and  $\mathbf{E}^t = -\nabla \varphi^t$  we finally obtain<sup>3</sup>

$$P = \frac{1}{(2\pi)^4} \int_0^\infty d\omega 2\omega \text{Im} \int d\mathbf{q} [\rho^e(\mathbf{q}\omega)]^* \varphi^t(\mathbf{q}\omega) \equiv - \int_0^\infty d\omega \omega P(\mathbf{b}, \omega). \quad (1.20)$$

<sup>3</sup>For a real function  $f(t)$ , we have  $\int_{-\infty}^\infty d\omega \omega f(\omega) = \int_0^\infty d\omega \omega [f(\omega) - f^*(\omega)] = \int_0^\infty d\omega 2i\omega \text{Im} f(\omega)$ .

Collecting all terms, the energy- and position-dependent energy-loss probability reads

$$P(\mathbf{b}, \omega) = -\frac{1}{2\pi^2} \int d\mathbf{q}d\mathbf{q}' v(\mathbf{q}') \operatorname{Im} \left\{ \varepsilon^{-1}(\mathbf{q}, \mathbf{q}'; \omega) e^{i(\mathbf{q}-\mathbf{q}')\mathbf{b}} \right\} \delta(\mathbf{q}\mathbf{v} - \omega) \delta(\mathbf{q}'\mathbf{v} - \omega). \quad (1.21)$$

We have to integrate over the momentum  $\mathbf{q}$  and  $\mathbf{q}'$  as the external potential enters twice in the last equation. Note, that the direction of  $\mathbf{q}$  is actually restricted to a plane perpendicular to the trajectory of the incident electron. The momentum component  $q_v$  along the trajectory is fixed by the dispersion relation  $q_v = \omega/v$ .

In AR-EELS, the external potential is a plane wave with momentum  $\mathbf{q}_0$ . An analogous derivation shows that eq. (1.21) reduces to a single term

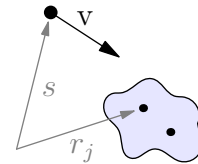
$$P(\mathbf{q}_0, \omega) \propto v(\mathbf{q}_0) \operatorname{Im} \varepsilon^{-1}(\mathbf{q}_0, \mathbf{q}_0, \omega) \quad (1.22)$$

This is the well-known energy-loss function which was already derived by Ritchie [35] and Nozières and Pines [52] for the scattering of electrons by thin foils. Note, however, that we have only used the electrostatic interaction during the derivation above, i. e., retardation effects from the electron or the target are completely neglected. For a detailed discussion of relativistic effects, see e. g. [38, 53, 54].

In the microscopic dielectric formalism, only the transferred momentum  $\mathbf{q} = \mathbf{k}_i - \mathbf{k}_f$  of the external perturbation appears, *not* the initial and final momentum  $\mathbf{k}_i$  and  $\mathbf{k}_f$  of the impinging electron itself. The description of a focussed electron beam with finite objective and collection aperture as needed for the description of a realistic experimental setup is thus not possible. In particular, the assumption of eq. (1.21) that the probe electron prescribes a classical trajectory and is infinitesimally localised, must be questioned at the microscopic level. We can overcome these problems by a full quantum-mechanical treatment of the scattering process which is presented in the following chapter.

## 2 Scattering Theory

In this chapter, we use the quantum-mechanical scattering theory to describe the interaction of a fast electron or photon with a thin target. Two complementing experimental setups are discussed: the broad-beam geometry for angular-resolved measurements (section 2.2), and a focussed-beam geometry for spatially-resolved measurements (section 2.3). As we have seen, the scattering problem is often simplified by treating either the scatterer or the target as a classical particle. In section 2.5, we will therefore discuss in which situations such a treatment is justified.



### 2.1 General Formalism

Consider the collision of a fast particle with a solid. Within the framework of non-relativistic quantum theory, the dynamics of the scattering process is governed by the time-dependent Schrödinger equation

$$i\hbar\partial_t |\Psi(t)\rangle = H_{\text{tot}} |\Psi(t)\rangle, \quad |\Psi(t_0)\rangle = |\Psi_i^0\rangle. \quad (2.1)$$

The wave function  $|\Psi(t)\rangle$  describes the time evolution of both the scattering particle and the target from a given initial state  $|\Psi_i^0\rangle$  at time  $t_0$ . The total Hamiltonian can be split into three parts:

$$H_{\text{tot}} = H_0 + H' = -\frac{\hbar^2}{2m} \nabla_{\mathbf{s}}^2 + H(\{\mathbf{r}_j\}; \{\mathbf{R}_\alpha\}) + H'(\mathbf{s}, \{\mathbf{r}_j\}; \{\mathbf{R}_\alpha\}). \quad (2.2)$$

The first term corresponds to the Hamiltonian of a free scattering particle at position  $\mathbf{s}$ . Inner degrees of freedom, like its spin, shall be ignored. The second term describes the target which is an assembly of electrons at position  $\mathbf{r}_j$  and ions at  $\mathbf{R}_\alpha$ . The last term denotes the interaction between particle and target.

#### 2.1.1 Perturbation Theory

If the interaction  $H'$  is sufficiently weak, the scattering problem (2.1) can be solved using time-dependent perturbation theory (see appendix A.1). Starting point is the time-independent Schrödinger equation  $H_0 |\mathbf{k}, N\rangle = E_{\mathbf{k}N}^0 |\mathbf{k}, N\rangle$  for the non-interacting Hamiltonian. If the scattering particle is distinguishable and not correlated with the

particles of the target,<sup>1</sup> the corresponding eigensolutions can be written as product state

$$|\mathbf{k}, N\rangle = |\mathbf{k}\rangle |N\rangle, \quad \langle \mathbf{s} | \mathbf{k} \rangle = \frac{1}{L^{3/2}} e^{i\mathbf{k}\mathbf{s}}, \quad E_{\mathbf{k}N}^0 = \frac{\hbar^2 k^2}{2m} + \epsilon_N, \quad (2.3)$$

where  $|\mathbf{k}\rangle$  is the box-normalised wave function of the free scattering particle with momentum  $\hbar\mathbf{k}$  and  $|N\rangle$  is an eigenstate of the target  $H|N\rangle = \epsilon_N|N\rangle$ .

Long time before the scattering event takes place, the particle is assumed to be far away from the target. If the interaction is short ranged,  $H'$  vanishes at  $t_0 \rightarrow -\infty$  and the initial state  $|\Psi_i^0\rangle$  must be a solution of the non-interacting problem. In order to avoid a wave-packet description of the scattering particle we can formally include this boundary condition by an adiabatic switching  $H'_\eta = e^{-\eta|t|}H'$  of the time-independent interaction [56]. Within first-order perturbation theory, the transition rate from the non-interacting initial state  $|\mathbf{k}_i, I\rangle$  to a final state  $|\mathbf{k}_f, F\rangle$  is given by Fermi's Golden Rule [see appendix, eq. (A.10)] and reads

$$\Gamma_{i \rightarrow f} = \frac{2\pi}{\hbar} |\langle \mathbf{k}_f, F | H' | \mathbf{k}_i, I \rangle|^2 \delta(E_{\mathbf{k}_f F}^0 - E_{\mathbf{k}_i I}^0), \quad (i \neq f). \quad (2.4)$$

The same result can be derived within time-independent scattering theory using the first Born approximation [56]. Channelling and multi-scattering effects are only included by higher-order terms in the expansion of eq. (A.6) and are therefore neglected in eq. (2.4).

### 2.1.2 Differential Cross Section

In experiment, the final state of the target is generally unknown. One only measures the differential current  $dj$  of particles that are scattered in direction  $\mathbf{k}_f$  within a solid angle  $d\Omega$  and which have a kinetic energy  $T_f = \hbar^2 k_f^2 / 2m$  within an interval  $dT_f$ . Summing over all possible final states  $|F\rangle$  of the target and multiplying with the number of final states  $dn_f$  of the scattering particle, we have [57]

$$dj = \sum_F \Gamma_{i \rightarrow f} dn_f, \quad dn_f = d^3\mathbf{p} / \left(\frac{2\pi\hbar}{L}\right)^3, \quad d^3\mathbf{p} = p^2 d\Omega dp = m\hbar k_f d\Omega dT_f, \quad (2.5)$$

where  $(2\pi\hbar)^3/L^3$  is the phase-space volume of a single momentum state in the normalisation box. We assume that the target is initially in its ground state  $|0\rangle$  and the wave function of the incident particle  $\phi(\mathbf{s})$  is given by a coherent superposition of plane waves  $|\mathbf{k}\rangle$  with same kinetic energy  $T_i = \hbar^2 k_i^2 / 2m$ . The initial state  $|\Psi_i^0\rangle$  is then an eigenstate of the free Hamiltonian  $H_0$ :

$$|\Psi_i^0\rangle = |\phi\rangle |0\rangle, \quad |\phi\rangle = \sum_{|\mathbf{k}|=k_i} \phi(\mathbf{k}) |\mathbf{k}\rangle, \quad H_0 |\Psi_i^0\rangle = (\epsilon_0 + T_i) |\Psi_i^0\rangle. \quad (2.6)$$

The coefficients  $\phi(\mathbf{k})$  depend on the experimental setup. For a broad-beam geometry, the wave function of the incident particle can be approximated by a single plane wave

---

<sup>1</sup>This approximation is only valid if we consider single scattering events. If multiple (elastic and inelastic) scattering takes place, the external electron has to be described using the density matrix [55].

$\phi(\mathbf{s}) = \frac{1}{L^{3/2}} e^{i\mathbf{k}_i \mathbf{s}}$ , i. e.,  $\phi(\mathbf{k}) = \delta_{\mathbf{k}\mathbf{k}_i}$ . In the case of a focussed beam, however, it has to be described by a coherent superposition of infinitely many plane waves.

In the general case, the average current density of the incident particle is given by

$$\mathbf{j}_0 = \frac{1}{L^3} \int d\mathbf{s} \left[ \frac{\hbar}{2mi} (\phi^* \nabla_{\mathbf{s}} \phi - \phi \nabla_{\mathbf{s}} \phi^*) \right] = \frac{\hbar \langle \mathbf{k} \rangle}{mL^3}, \quad \langle \mathbf{k} \rangle = \sum_{|\mathbf{k}|=k_i} \mathbf{k} |\phi(\mathbf{k})|^2, \quad (2.7)$$

where  $\hbar \langle \mathbf{k} \rangle$  is the expectation value of the momentum of the incident particle. Collecting all terms, we finally arrive at the *differential cross section* which is defined as the ratio of outgoing and incoming current  $d\sigma = dj/j_0$ :

$$\frac{\partial^2 \sigma}{\partial \Omega \partial E} = \left[ \frac{mL^3}{2\pi \hbar^2} \right]^2 \frac{k_f}{\langle k \rangle} \sum_F \left| \sum_{|\mathbf{k}|=k_i} \phi(\mathbf{k}) \langle \mathbf{k}_f, F | H' | \mathbf{k}, 0 \rangle \right|^2 \delta(\epsilon_0 - \epsilon_F + E). \quad (2.8)$$

We have introduced the energy loss  $E = T_i - T_f$  of the incident particle and used  $dE = -dT_f$ . Note that the sum over the final target states is a sum of probabilities, while the sum over the incident momentum  $\mathbf{k}$  is a sum of amplitudes (coherent superposition).

In the following, we will refine this general expression for different interaction Hamiltonians  $H'$  describing the scattering of electrons and the scattering of X-ray photons.

## 2.2 Angular-Resolved Electron Energy-Loss Spectroscopy

First, we consider the case of angular-resolved electron scattering (AR-EELS). In a transmission electron microscope, a thin sample is irradiated by a broad beam of fast electrons, which are accelerated to a kinetic energy of about 100 keV. Far away from the target, a detector analyses the energy of the scattered electrons that have been deviated by certain angle  $\vartheta$  (see fig. 2.1). In this thesis, we are mainly interested in the range of low energy transfers between 1 and 30 eV, where (collective) excitations of the *valence* electrons in the target dominate [58].

As the external electron is much faster than the target electrons, we can neglect the corresponding exchange contributions. On the other hand, we assume that the fast electron can be still described within a non-relativistic theory. The interaction Hamiltonian is then given by

$$H' = \sum_{j=1}^{N_e} v(\hat{\mathbf{s}} - \hat{\mathbf{r}}_j) + v_{\text{ion}}(\hat{\mathbf{s}}; \{\mathbf{R}_\alpha\}), \quad v(\mathbf{r} - \mathbf{r}') = \frac{e^2}{4\pi\epsilon_0} \frac{1}{|\mathbf{r} - \mathbf{r}'|}. \quad (2.9)$$

where  $v$  denotes the (longitudinal) Coulomb interaction. Further, we have assumed that the motion of ions and electrons in the target can be separated within the Born-Oppenheimer approximation [59]. In this case, it is sufficient to consider only the electronic problem for fixed ions which are described by a potential  $v_{\text{ion}}(\mathbf{s}; \{\mathbf{R}_\alpha\})$ . Core

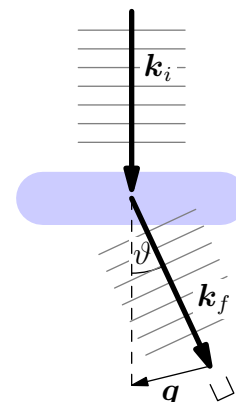


Fig. 2.1: AR-EELS

excitations or phonons are neglected. Note that only if the target has no excess charges, the interaction  $H'$  is short ranged and the scattering theory of section 2.1 can be applied.

We also assume that the scattering events of consecutive electrons are independent from each other. This applies, if the beam intensity is low enough to ensure that the target is not damaged and that it is always relaxed to its ground state. Further, the target shall be very thin in order to avoid multiple-scattering effects, i. e., the consecutive elastic or inelastic scattering of the same electron. With these restrictions in mind, we now return to the calculation of the energy- and momentum-resolved cross section for the scattering of fast electrons.

### 2.2.1 Dynamic Structure Factor

In the case of a broad beam, the incident electron can be approximated by a single plane wave  $|\mathbf{k}_i\rangle$  with momentum  $\hbar\mathbf{k}_i$ . The cross section (2.8) then reads ( $\phi(\mathbf{k}) = \delta_{\mathbf{k}\mathbf{k}_i}$ )

$$\frac{\partial^2 \sigma}{\partial \Omega \partial E} = \left[ \frac{mL^3}{2\pi\hbar^2} \right]^2 \frac{k_f}{k_i} \sum_F |\langle \mathbf{k}_f, F | H' | \mathbf{k}_i, 0 \rangle|^2 \delta(\epsilon_0 - \epsilon_F + E). \quad (2.10)$$

With eq. (2.3) and (2.9), the transition amplitude  $a_{fi}^* = \langle \mathbf{k}_i, 0 | H'^+ | \mathbf{k}_f, F \rangle$  becomes

$$\begin{aligned} a_{fi}^* &= \frac{1}{L^3} \int d\mathbf{s} e^{-i(\mathbf{k}_i - \mathbf{k}_f)\mathbf{s}} \left[ \langle 0 | \sum_j v^*(\mathbf{s} - \hat{\mathbf{r}}_j) | F \rangle + \delta_{0F} v_{\text{ion}}^*(\mathbf{s}) \right] \\ &= \frac{1}{L^3} v^*(\mathbf{q}) \langle 0 | \sum_j e^{-i\mathbf{q}\hat{\mathbf{r}}_j} | F \rangle + \frac{1}{L^3} \delta_{0F} v_{\text{ion}}^*(\mathbf{q}), \\ &= \frac{1}{L^3} v^*(\mathbf{q}) \langle 0 | \hat{n}(\mathbf{q}) | F \rangle (1 - \delta_{0F}) + \frac{1}{L^3} [v^*(\mathbf{q})n_0(\mathbf{q}) + v_{\text{ion}}^*(\mathbf{q})] \delta_{0F}, \end{aligned} \quad (2.11)$$

where we have introduced the momentum transfer  $\mathbf{q} = \mathbf{k}_i - \mathbf{k}_f$ , the Fourier transforms of the potentials  $v$  and  $v_{\text{ion}}$  [see eq. (A.40)], and the density operator of the target electrons:

$$\hat{n}(\mathbf{r}) = \sum_j \delta(\mathbf{r} - \hat{\mathbf{r}}_j) = \hat{n}^+(\mathbf{r}), \quad \hat{n}(\mathbf{q}) = \sum_j e^{-i\mathbf{q}\hat{\mathbf{r}}_j} = \hat{n}^+(-\mathbf{q}). \quad (2.12)$$

In particular, the ground-state density is given by  $n_0(\mathbf{q}) = \langle 0 | \hat{n}(\mathbf{q}) | 0 \rangle$  and the corresponding Hartree potential is  $v_{\text{H}}(\mathbf{q}) = v(\mathbf{q})n_0(\mathbf{q})$ . The transition amplitude (2.11) consists of two terms: the first term describes inelastic scattering ( $|F\rangle \neq |0\rangle$ ), while the last term constitutes the elastic scattering amplitude ( $|F\rangle = |0\rangle$ ). It is given by the potential of the ions and electrons ( $v_{\text{ion}} + v_{\text{H}}$ ) of the unperturbed target. Restricting to inelastic scattering  $E > 0$ , the cross section becomes

$$\frac{\partial^2 \sigma^{\text{inel}}}{\partial \Omega \partial E} = C(\mathbf{q}) S_i(\mathbf{q}, E), \quad C(\mathbf{q}) = \left[ \frac{m}{2\pi\hbar^2} \right]^2 \frac{k_f}{k_i} |v(\mathbf{q})|^2, \quad (2.13)$$

where

$$S_i(\mathbf{q}, E) = \sum_{F \neq 0} |\langle 0 | \hat{n}(\mathbf{q}) | F \rangle|^2 \delta(\epsilon_0 - \epsilon_F + E) = S(\mathbf{q}, E) - |n_0(\mathbf{q})|^2 \delta(E) \quad (2.14)$$

denotes the inelastic part of the *dynamic structure factor* (DSF)<sup>2</sup>

$$S(\mathbf{q}, E) = \sum_F |\langle 0 | \hat{n}(\mathbf{q}) | F \rangle|^2 \delta(\epsilon_0 - \epsilon_F + E). \quad (2.15)$$

The latter describes the properties of the target and is completely independent of the scattering particle or even the interaction potential  $v$ . These properties are only taken into account by the probe factor  $C(\mathbf{q})$ . With the Fourier transform (A.27) of the Coulomb potential  $v$ , we have for the differential cross section in a AR-EELS experiment<sup>3</sup>

$$\frac{\partial^2 \sigma^{\text{inel}}}{\partial \Omega \partial E} = \frac{4}{a_0^2} \frac{1}{q^4} \frac{k_f}{k_i} S(\mathbf{q}, E), \quad a_0 = \frac{4\pi\epsilon_0 \hbar^2}{me^2} \approx 0.529 \text{ \AA}. \quad (2.16)$$

It corresponds to the probability that an incident electron is scattered into direction  $\mathbf{k}_f$  within the solid angle  $d\Omega$  and loses a fractional part  $E \pm dE/2$  of its kinetic energy. For small energy loss, the momentum of the electron  $k_i \approx k_f$  does not change considerably and we have  $q \approx 2k_i \sin(\vartheta/2)$  (see fig. 2.2). The prefactor  $C \approx [4a_0^2 k_i^4 \sin^4(\vartheta/2)]^{-1}$  then takes the form of the Rutherford cross section, corresponding to the classical scattering of an incident electron by a free target electron which is initially at rest. The dynamic structure factor  $S$  can be understood as a quantum-mechanical correction to this classical result which takes into account all many-body interactions between the target electrons.

## 2.2.2 Small-Angle Approximation

The momentum transfer  $\mathbf{q}$  will play a crucial role in the discussion of AR-EELS experiments. Its direction depends both on the scattering angle  $\vartheta$  and the energy transfer  $E$  (see fig. 2.2). This dependence can be simplified in the case of small scattering angles  $\vartheta \ll 1$ . Indeed, in inelastic scattering, most of the electrons are deviated less than a few mrad from the incident direction, which can be inferred from the prefactor  $q^{-4}$  in the cross section. Additionally, the energy loss  $E$  is much smaller than the kinetic energy  $T_i$  of the incident electron, such that  $k_i - k_f \ll k_i$ . Thus

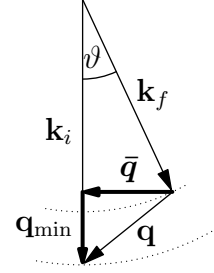


**Fig. 2.2:** Small-angle approximation

$$E = \frac{\hbar^2}{2m} (k_i^2 - k_f^2) \approx \frac{\hbar^2}{2m} 2k_i(k_i - k_f), \quad (2.17)$$

$$q^2 = |\mathbf{k}_i - \mathbf{k}_f|^2 \approx k_i^2 + k_f^2 - 2k_i k_f (1 - \vartheta^2/2) \approx (k_i - k_f)^2 + k_i^2 \vartheta^2,$$

which means that the parameters  $E$  and  $\vartheta$  can be decoupled by splitting  $\mathbf{q}$  in two terms

$$q^2 \approx k_i^2 (\vartheta_E^2 + \vartheta^2), \quad q_{\text{min}} = k_i \vartheta_E, \quad \vartheta_E \equiv \frac{E}{2T_i}. \quad (2.18)$$

The first term corresponds to the component of the momentum transfer along the  $z$ -axis  $\mathbf{q}_{\text{min}} \approx k_i \vartheta_E \mathbf{e}_z$  which takes into account the shortening of the incident momentum  $\mathbf{k}_i$  due to the energy loss. The second term depends on the scattering angle  $\vartheta$  and describes the momentum transfer  $\bar{\mathbf{q}} \approx k_i \vartheta$  in the  $xy$ -plane.

<sup>2</sup>Sometimes, also the term ‘dynamic form factor’ is used in literature.

<sup>3</sup>Instead of  $S(\mathbf{q}, E)$ , one often introduces the loss function  $P$  such that  $\frac{\partial^2 \sigma^{\text{inel}}}{\partial \Omega \partial (\hbar\omega)} = \frac{\hbar}{(\pi a_0)^2} \frac{1}{q^4} P(\mathbf{q}, \omega)$  [60].



**Fig. 2.3:** Probability density  $|\phi(\mathbf{s})|$  of the incident electron in the two-beam case (2.19) for  $k_i - k'_i = 2\pi/a$  and a phase shift (a)  $\varphi = 0$  and (b)  $\varphi = \pi$ . The origin is at the first atom.

The scattering angle  $\vartheta$  is usually much larger than the *characteristic angle*  $\vartheta_E$  for a typical AR-EELS experiment in the low-loss region. For example, considering an energy loss of 10 eV and an incident energy of 100 keV ( $k_i = 170 \text{ \AA}^{-1}$ ), one obtains an angle  $\vartheta_E$  of 0.05 mrad ( $q_{\min} = 0.01 \text{ \AA}^{-1}$ ). In comparison, the experimental resolution limit in a TEM is typically in the order of 0.1 mrad ( $\Delta\bar{q} \approx 0.02 \text{ \AA}^{-1}$  at 100 keV). Thus, in most cases  $\vartheta_E \ll \vartheta$ . The momentum transfer  $\mathbf{q}$  is then nearly perpendicular to the incident beam and independent of the energy loss.

If, in contrast, the scattering angle  $\vartheta$  is much smaller than the characteristic angle  $\vartheta_E$ , the momentum transfer becomes parallel to the beam direction and independent of  $\vartheta$ . In particular, the momentum transfer  $q$  never vanishes, but is always larger than  $q_{\min}$ .

## 2.3 Spatially-Resolved Electron Energy-Loss Spectroscopy

In a plane-wave scattering experiment, we can only measure the modulus of the target electron density  $n(\mathbf{q})$ , but not its phase [see elastic term in eq. (2.14)]. As the Fourier transformation of  $|n(\mathbf{q})|^2$  gives only a spatially averaged quantity, namely the density autocorrelation function, we cannot retrieve direct spatial information about the target system. The physical reason for this so-called *phase problem* is easily understood: in a broad beam geometry, all points of the target are excited with the same intensity and the phase of the outgoing electron is not measured.

We will see in the following that spatial informations can be obtained, if the excitation is spatially modulated. In the simplest case, the excitation is given by a coherent superposition of only two plane waves. In a STEM, the electron beam is focussed by a coherent superposition of infinitely many plane waves.

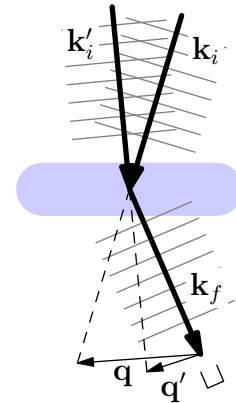


**Fig. 2.4:** Scattering of two coherent waves

### 2.3.1 Two-Beam Scattering

We start with the following gedankenexperiment [61, 62]: Consider a periodic crystal with lattice constant  $a$  and a superposition of two incident plane waves

$$\phi(\mathbf{s}) = \frac{1}{\sqrt{2}}(e^{i\mathbf{k}_i \cdot \mathbf{s}} + e^{-i\varphi} e^{i\mathbf{k}'_i \cdot \mathbf{s}}), \quad |\phi(\mathbf{s})|^2 = 1 + \cos[(\mathbf{k}_i - \mathbf{k}'_i) \cdot \mathbf{s} + \varphi]. \quad (2.19)$$

The probability density  $|\phi(\mathbf{s})|^2$  of the incident electron is no longer constant, but varies periodically in space. If the period is commensurable with the lattice constant, i. e., if

$\mathbf{k}_i - \mathbf{k}'_i = \mathbf{G}$  is a reciprocal lattice vector, the electron will be most likely found at the atoms or in between depending on the choice of the phase  $\varphi$  (see fig. 2.3). Due to this site-specific excitation, it is possible to obtain spatial informations about the system.

But which physical quantity will be actually measured in such an experiment? In order to answer this question, we consider the general case of an electron beam of coherent, mono-energetic electrons (2.6). The differential cross section was given by eq. (2.8):

$$\frac{\partial^2 \sigma}{\partial \Omega \partial E} = \left[ \frac{mL^3}{2\pi\hbar^2} \right]^2 \frac{k_f}{\langle k_i \rangle} \sum_F \sum_{|\mathbf{k}|=|\mathbf{k}'|=k_i} \phi^*(\mathbf{k}) \phi(\mathbf{k}') a_{fi}^* a_{fi'} \delta(\epsilon_0 - \epsilon_F + E). \quad (2.20)$$

With the transition amplitudes  $a_{fi}$  of eq. (2.11), we obtain for inelastic scattering  $E > 0$ :

$$\frac{\partial^2 \sigma^{\text{inel}}}{\partial \Omega \partial E} = \sum_{|\mathbf{k}|=|\mathbf{k}'|=k_i} C(\mathbf{q}, \mathbf{q}') S(\mathbf{q}, \mathbf{q}', E), \quad \mathbf{q}^{(\prime)} = \mathbf{k}^{(\prime)} - \mathbf{k}_f, \quad (2.21)$$

where<sup>4</sup>

$$C(\mathbf{q}, \mathbf{q}') = \left[ \frac{m}{2\pi\hbar^2} \right]^2 \frac{k_f}{\langle k \rangle} \phi^*(\mathbf{k}) \phi(\mathbf{k}') v^*(\mathbf{q}) v(\mathbf{q}'), \quad (2.22)$$

$$S(\mathbf{q}, \mathbf{q}', E) = \sum_F \langle 0 | \hat{n}(\mathbf{q}) | F \rangle \langle F | \hat{n}^\dagger(\mathbf{q}') | 0 \rangle \delta(\epsilon_0 - \epsilon_F + E). \quad (2.23)$$

As above, the cross section can be separated into two parts: first, a probe factor  $C$  which accounts for the geometry of the incident electron and the interaction potential  $v$ . And second, a complicated quantum-mechanical quantity  $S$  which describes the target. The latter is a generalisation of the dynamic structure factor introduced in the previous section and is called *mixed dynamic form factor* (MDFFF) [61]. Note that  $S(\mathbf{q}, \mathbf{q}', E)$  is generally a complex function, which fulfils the relation

$$S(\mathbf{q}, \mathbf{q}', E) = S^*(\mathbf{q}', \mathbf{q}, E), \quad S(\mathbf{q}, E) = S(\mathbf{q}, \mathbf{q}, E). \quad (2.24)$$

Coming back to the two-beam case of eq. (2.19), the cross section simplifies to

$$\frac{\partial^2 \sigma^{\text{inel}}}{\partial \Omega \partial E} \propto \frac{1}{q^4} S(\mathbf{q}, E) + \frac{1}{q'^4} S(\mathbf{q}', E) + \frac{2}{q^2 q'^2} \text{Re} \left\{ e^{-i\varphi} S(\mathbf{q}, \mathbf{q}', E) \right\}. \quad (2.25)$$

As in a double-slit experiment, we obtain two direct terms plus an interference term. The former stem from the incoherent scattering of each of the incoming plane waves. Only the last term accounts for the interference between them and contains spatial information. The importance of these interference terms has been pointed out rather early [63]. Typically, one has a large number of coherent plane waves and therefore many different off-diagonal elements  $S(\mathbf{q}, \mathbf{q}', E)$  are mixed.

---

<sup>4</sup>For  $E > 0$ , we can ignore the difference between  $S_i$  and  $S$ . See eq. (2.14) and (2.15).

## Experiments

The two-beam case can be actually realised in experiment. For example, a charged wire inside the electron beam acts as a biprism that splits an incoming plane wave into two coherent waves [64]. But also the crystal itself can be used as a beam splitter. Indeed, an external plane electron wave will be Bragg scattered inside the crystal leading to a coherent superposition of a discrete set of plane waves. In particular, if one Bragg reflection is dominant, the two-beam case is recovered.

Schattschneider *et al.* [27, 65] have used this method to measure the magnetic circular dichroism in the electron microscope. By properly aligning the crystal to the incident plane electron wave, the phase  $\varphi$  of the Bragg scattered wave is chosen to be  $\pi/2$ . The inelastic signal is then measured for two positions of the detector: first,  $\mathbf{k}_f$  is chosen such that  $\mathbf{q}$  and  $\mathbf{q}'$  are perpendicular to each other and have roughly the same modulus and second,  $\mathbf{k}_f$  is selected such that  $\mathbf{q}$  and  $\mathbf{q}'$  are interchanged. The dichroic signal is then given by the difference of these two measurements, i. e.,

$$\text{EMCD} \propto \text{Im} S(\mathbf{q}, \mathbf{q}', E) - \text{Im} S(\mathbf{q}', \mathbf{q}, E) \quad (2.26)$$

For core-loss spectra, this signal is found to be comparable with the dichroic signal in X-ray absorption [65].

### 2.3.2 Convergent Electron Beam

The image formation in a scanning transmission electron microscope (STEM) can be understood as a more complicated version of the two-beam case which has been considered previously. After the acceleration of the electrons to energies of about 100 keV, the electron beam is focussed by an objective lens in order to prepare a narrow beam. The incident wave packet can be then written as a coherent sum of mono-energetic plane waves [see eq. (2.6)]

$$\phi(\mathbf{s}) = \frac{1}{L^{3/2}} \sum_{|\mathbf{k}|=k_i} \phi(\mathbf{k}) e^{i\bar{\mathbf{k}}\bar{\mathbf{s}}} e^{ik_z s_z}, \quad \mathbf{k} = \bar{\mathbf{k}} + k_z \mathbf{e}_z, \quad (2.27)$$

where we have introduced the on-axis momentum  $k_z$  and the perpendicular momentum  $\bar{\mathbf{k}}$ . The latter is limited by the objective aperture  $\alpha$  which is typically in the order of a few mrad ( $\alpha \ll 1$ ). Thus, the small-angle approximation holds both for the incoming and outgoing electrons (see section 2.2.2). With  $|\bar{\mathbf{k}}| \ll k_z \approx k_i$ , the incident electron wave function can be written as<sup>5</sup>

$$\phi(\mathbf{s}) \approx \bar{\Phi}(\bar{\mathbf{s}} - \bar{\mathbf{b}}) \frac{1}{L^{1/2}} e^{ik_i s_z}, \quad \bar{\Phi}(\bar{\mathbf{s}}) = \frac{1}{L} \sum_{\bar{\mathbf{k}}} \bar{\Phi}(\bar{\mathbf{k}}) e^{i\bar{\mathbf{k}}\bar{\mathbf{s}}}, \quad \phi(\mathbf{k}) = \bar{\Phi}(\bar{\mathbf{k}}) e^{-i\bar{\mathbf{k}}\bar{\mathbf{b}}}. \quad (2.28)$$

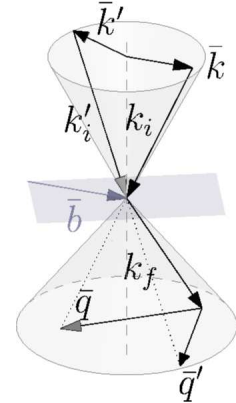


Fig. 2.5: STEM setup

<sup>5</sup>For convenience, the in-plane wave function  $\bar{\Phi}(\bar{\mathbf{s}})$  is normalised to one. To this end, definition (2.28) differs from our convention of the Fourier transform (A.40) and we have  $\bar{\Phi}(\bar{\mathbf{k}}) = \frac{1}{L} \int_{L^2} d\bar{\mathbf{s}} \bar{\Phi}(\bar{\mathbf{s}}) e^{-i\bar{\mathbf{k}}\bar{\mathbf{s}}}$ .

The function  $\bar{\Phi}(\bar{\mathbf{s}} - \bar{\mathbf{b}})$  describes the shape of the incoming electron beam in the object plane at the focus position  $\bar{\mathbf{b}}$  (impact parameter). Assuming a plane wave in front of the objective lens, the coefficients  $\bar{\Phi}(\bar{\mathbf{k}})$  of the wave packet are given by [61]

$$\bar{\Phi}(\bar{\mathbf{k}}) = A_\alpha(\bar{\mathbf{k}}) e^{-i\gamma_0(\bar{\mathbf{k}})}, \quad A_\alpha = \Theta\left(\alpha - \frac{|\bar{\mathbf{k}}|}{k_i}\right), \quad \gamma_0 = k_i \left[ \frac{C_3}{4} \left(\frac{|\bar{\mathbf{k}}|}{k_i}\right)^4 - \frac{\Delta f}{2} \left(\frac{|\bar{\mathbf{k}}|}{k_i}\right)^2 \right], \quad (2.29)$$

where  $A_\alpha$  corresponds to the circular aperture of the objective lens. The phase shift  $\gamma_0$  accounts for the spherical lens aberration  $C_3$  and the defocus  $\Delta f$ , respectively. For simplicity, we neglect this correction in the following. The differential cross section, which has been given for an arbitrary incident wave packet in eq. (2.21), now reads

$$\frac{\partial^2 \sigma^{\text{inel}}}{\partial \Omega \partial E} = \left[ \frac{m}{2\pi \hbar^2} \right]^2 \frac{k_f}{k_i} \sum_{\bar{\mathbf{k}}, \bar{\mathbf{k}'}} A_\alpha^*(\bar{\mathbf{k}}) A_\alpha(\bar{\mathbf{k}'}) e^{i(\bar{\mathbf{k}} - \bar{\mathbf{k}'}) \bar{\mathbf{b}}} v^*(\mathbf{q}) v(\mathbf{q}') S(\mathbf{q}, \mathbf{q}', E) \quad (2.30)$$

where the momentum transfers  $\mathbf{q}$  and  $\mathbf{q}'$  are given by eq. (2.18) as

$$\mathbf{q}^{(\prime)} = \bar{\mathbf{q}}^{(\prime)} + q_z \mathbf{e}_z, \quad \bar{\mathbf{q}}^{(\prime)} = \bar{\mathbf{k}}^{(\prime)} - \bar{\mathbf{k}}_f, \quad q_z = k_i \vartheta_E = Em / (\hbar p_i) = \omega / v \quad (2.31)$$

Note that recoil terms are neglected within the small-angle approximation in the expression for  $E$  [66]. Finally, we have to integrate over all the scattered electrons that enter the detector. With the detector function  $D_\beta(\bar{\mathbf{k}}_f) = \Theta(\beta - \bar{k}_f/k_f)$  which describes a circular on-axis detector with opening angle  $\beta$ , we have for the total cross section

$$\frac{\partial \sigma^{\text{inel}}}{\partial E} = \frac{4}{a_0^2} \sum_{\bar{\mathbf{k}}_f} D_\beta(\bar{\mathbf{k}}_f) \sum_{\bar{\mathbf{q}}, \bar{\mathbf{q}'}} A_\alpha^*(\bar{\mathbf{k}}_f + \bar{\mathbf{q}}) A_\alpha(\bar{\mathbf{k}}_f + \bar{\mathbf{q}'}) \frac{S(\mathbf{q}, \mathbf{q}', E) e^{i(\bar{\mathbf{q}} - \bar{\mathbf{q}'}) \bar{\mathbf{b}}}}{(\bar{q}^2 + q_z^2)(\bar{q}'^2 + q_z^2)}. \quad (2.32)$$

This formula is the main conclusion of this chapter [61]. It describes the energy-loss signal in a scanning transmission electron microscope. We want to add several comments:

- Eq. (2.32) can be considered as a generalisation of the previous AR-EELS result (2.16) and the two-beam scattering (2.25). Indeed, these two cases can be obtained by choosing appropriate delta functions for  $A_\alpha$  and  $D_\beta$ .
- Note that the summation only runs over the perpendicular momentum transfer  $\bar{\mathbf{q}}$ . The on-axis momentum transfer  $q_z = \omega/v$  is determined by the energy loss  $E$  and the velocity  $v$  of the electron by eq. (2.31).
- The contributions from different outgoing electrons are summed *incoherently*, i. e., we sum over probabilities, not the scattering amplitudes as we did for the incident electrons. Indeed, inelastically scattered electrons from different energy-loss bands must be (temporally) incoherent [64, 67–69].
- The position  $\bar{\mathbf{b}}$  of the focus only enters via the exponential  $e^{i(\bar{\mathbf{q}} - \bar{\mathbf{q}'}) \bar{\mathbf{b}}}$ . Therefore, only the off-diagonal terms  $S(\mathbf{q}, \mathbf{q}', E)$  of the mixed dynamic form factor contribute to the spatial information on the target.

- In crystals, the translational symmetry requires that  $\mathbf{q} - \mathbf{q}'$  is a reciprocal lattice vector  $\mathbf{G}$ . Atomic resolution can be only obtained, if the objective aperture is large enough. Indeed, both wave vectors  $\bar{\mathbf{k}}_f + \bar{\mathbf{q}}$  and  $\bar{\mathbf{k}}_f + \bar{\mathbf{q}} + \bar{\mathbf{G}}$  must be included in the incident wave packet for at least one in-plane vector  $\bar{\mathbf{G}}$ . Additionally, the crystal has to be properly aligned with respect to the beam (channelling direction) in order to relate image contrast directly with atomic positions [70].
- The image formation in a STEM and the energy-filtered TEM (EFTEM) are closely related by the reciprocity theorem [61]. In the EFTEM, the object is illuminated by a single plane wave and the scattered electrons are imaged by an objective lens *behind* the object (see section 1.1.2). The camera is placed in the back-focal plane of this lens. Such a setup can be understood as reversed STEM with an infinitely small collection angle. Consequently, one obtains a very similar expression as for the STEM (2.32), where  $\alpha$  becomes the objective aperture of the imaging system and  $\beta \rightarrow 0$ . The vector  $\bar{\mathbf{b}}$  then denotes the position in the image plane or, more precisely, the corresponding point of the object. A detailed discussion has been given by Rose [68] and Findlay *et al.* [71].

## 2.4 Inelastic X-Ray Scattering

So far, we have considered the inelastic scattering of a fast electron for different experimental setups. The properties of the target have been described by the dynamic scattering factor. As we will see in the following, the same information can be obtained by the scattering of a high-energy (X-ray) photon. We briefly review the theory of inelastic X-ray scattering which is discussed in detail by Schülke [72].

Analogous to the previous section, we start from the total Hamiltonian (2.2) that now has to include the external photon field. Using second quantisation, it can be written as

$$H_{\text{tot}} = \sum_{\mathbf{k}\lambda} \hbar\omega_{\mathbf{k}} \left[ \hat{c}_{\mathbf{k}\lambda}^+ \hat{c}_{\mathbf{k}\lambda} + \frac{1}{2} \right] + H + H', \quad \omega_{\mathbf{k}} = c\mathbf{k}, \quad (2.33)$$

where the operator  $c_{\mathbf{k}\lambda}^+$  creates a photon of momentum  $\mathbf{k}$  and polarisation  $\lambda$ . The sum over photon energies  $\hbar\omega_{\mathbf{k}}$  corresponds to the energy of the free radiation field, the second term is the target Hamiltonian  $H$ , and the third term describes the interaction between scattering particle and target electrons. It reads (we neglect spin-dependent terms)

$$H' = \sum_{j=1}^{N_e} \left[ -\frac{e}{m} \mathbf{p}_j \cdot \mathbf{A}(\mathbf{r}_j) + \frac{e^2}{2m} A^2(\hat{\mathbf{r}}_j) \right]. \quad (2.34)$$

The external vector potential  $\mathbf{A}$  can be expressed in terms of the photon operators:

$$\mathbf{A}(\mathbf{r}) = \sum_{\mathbf{k}\lambda} \left( \frac{\hbar}{2\varepsilon_0\omega_{\mathbf{k}}L^3} \right)^{1/2} \left[ \boldsymbol{\varepsilon}_{\mathbf{k}\lambda} \hat{c}_{\mathbf{k}\lambda} e^{i\mathbf{k}\mathbf{r}} + \boldsymbol{\varepsilon}_{\mathbf{k}\lambda}^* \hat{c}_{\mathbf{k}\lambda}^+ e^{-i\mathbf{k}\mathbf{r}} \right], \quad (2.35)$$

where we have introduced the polarisation unit vector  $\boldsymbol{\varepsilon}_{\mathbf{k}\lambda}$  (with  $\mathbf{k} \cdot \boldsymbol{\varepsilon}_{\mathbf{k}\lambda} = 0$ ) and the length  $L$  of the quantisation box.

### 2.4.1 Plane-Wave Scattering

First, we consider the scattering of a single photon on a target which is initially in the ground state  $|0\rangle$ . In second quantisation, this corresponds to a two-photon process including the incident and outgoing photon. First, we want to calculate the transition amplitude for the initial and final states  $|\Psi_i^0\rangle = \hat{c}_{\mathbf{k}_i\lambda_i}^+ |0\rangle$  and  $|\Psi_f^0\rangle = \hat{c}_{\mathbf{k}_f\lambda_f}^+ |F\rangle$ . Within first-order perturbation theory in  $H'$ , we have for inelastic scattering ( $|F\rangle \neq |0\rangle$ )

$$a_{fi}^* = \langle 0 | \hat{c}_{\mathbf{k}_i\lambda_i} H'^+ \hat{c}_{\mathbf{k}_f\lambda_f}^+ | F \rangle = \frac{e^2}{2m} \frac{\hbar}{2\varepsilon_0 \sqrt{\omega_i \omega_f} L^3} (\boldsymbol{\varepsilon}_i^* \cdot \boldsymbol{\varepsilon}_f) \langle 0 | \sum_j 2e^{-i\mathbf{q}\mathbf{r}_j} | F \rangle. \quad (2.36)$$

Only the two terms of  $A^2$  containing  $\hat{c}_i^+ \hat{c}_f$  or  $\hat{c}_f \hat{c}_i^+$  contribute. The  $\mathbf{p} \cdot \mathbf{A}$  term occurs only, if the perturbation theory is applied to second order in  $H'$ :

$$b_{fi}^* = \frac{e^2}{m^2} \sum_{jj',v} \frac{\langle 0 | \hat{c}_i \mathbf{p}_j^+ \cdot \mathbf{A}^+(r_j) | \Psi_v \rangle \langle \Psi_v | \mathbf{p}_{j'}^+ \cdot \mathbf{A}^+(r_{j'}) \hat{c}_i^+ | F \rangle}{(\epsilon_0 + \hbar\omega_i) - E_v} + \mathcal{O}(A^3), \quad (2.37)$$

where  $v$  runs over all *virtual states* of the target and radiation field. Their energy is given by  $E_v = \epsilon_v$  or  $E_v = \epsilon_v + \hbar(\omega_i + \omega_f)$  depending on whether there are zero or two photons in the radiation field of the virtual state.

Both terms  $a_{fi}^*$  and  $b_{fi}^*$  are quadratic in the external field  $A$ , but their relative contribution to the total transition amplitude strongly depends on the denominator in eq. (2.37). If the photon energy  $\hbar\omega_i$  or  $\hbar\omega_f$  is close to a resonance  $\epsilon_0 - \epsilon_v$  of the target (e. g., a core excitation), the denominator vanishes for the corresponding state  $|\Psi_v\rangle$  and  $b_{fi}^*$  dominates the transition amplitude. This is the case of *resonant inelastic X-ray scattering* (RIXS).

If, instead, the photon energy is very different from the typical resonances of the target (e. g., for very high photon energies), the denominator becomes large and  $b_{fi}^*$  vanishes. The transition amplitude is then given by  $a_{fi}^*$  which differs only in the prefactor from the transition amplitude (2.11) for electron scattering. In the following, we will focus to this latter case of *nonresonant inelastic X-ray scattering* (IXS).

Considering the energy dispersion of the outgoing photon  $T_f^2 = \mathbf{p}_f^2 c^2 = (\hbar\mathbf{k}_f c)^2$  in eq. (2.5) and the incident flux  $j_0 = c/L^3$  of the incoming photon, one obtains for the cross section of inelastically scattered, nonresonant photons [see eq. (2.4)]

$$\frac{\partial^2 \sigma^{\text{inel}}}{\partial \Omega \partial E} = \frac{L^6 k_f^2}{(2\pi)^3 \hbar c^2} \frac{2\pi}{\hbar} \sum_F |a_{fi}|^2 \delta(\epsilon_0 - \epsilon_F + E) = C S(\mathbf{q}, E) \quad (2.38)$$

$$C = r_e^2 |\boldsymbol{\varepsilon}_i^* \cdot \boldsymbol{\varepsilon}_f|^2 \frac{k_f}{k_i}, \quad r_e = \frac{1}{4\pi\varepsilon_0} \frac{e^2}{mc^2} \approx 2.82 \cdot 10^{-15} \text{ m},$$

where  $r_e$  denotes the classical electron radius and  $E = \hbar\omega_i - \hbar\omega_f > 0$  the energy loss. The prefactor  $C$  corresponds to the cross section of Thomson scattering, i. e., the elastic scattering of electromagnetic waves by a free electron. The similarity with the cross section of AR-EELS (2.16) is evident. In both cases, the target properties only enter via the dynamic structure factor  $S$ . However, there are important experimental differences:

First, the probe factor  $C$  is orders of magnitudes smaller for photon scattering ( $10^{-10} \text{ \AA}^2$ ) than in the case of electron scattering ( $1 \text{ \AA}^2$  for  $q = 0.5 \text{ \AA}^{-1}$ ). For X-ray scattering, radiation of very high intensity is necessary to obtain reasonable count rates for scattered photons. Therefore, synchrotron radiation sources have become very important for the current advances in IXS. In contrast, the mean-free path of a 100 keV electron is in the order of 100 nm for common materials [9]. To limit multiple-scattering effects, i. e., several consecutive inelastic or elastic scattering events, very thin targets have to be used in transmission electron microscopes.

Second, the probe factor  $C$  does not depend on the transferred momentum  $q$  in IXS. As  $S(\mathbf{q}, \omega) \propto q^2$ , the differential cross section increases with scattering angle  $\vartheta$  in IXS, while it decreases for EELS. The two techniques are therefore rather complementary methods for the determination of the dynamic structure factor  $S(\mathbf{q}, \omega)$ .

## 2.4.2 Two-Beam Scattering

The analog to the two-beam case of electron scattering (section 2.3.1) is known as *coherent inelastic X-ray scattering* (CIXS) [72]. In this type of experiment, the incident photon field is built up from two coherent photons with different momentum  $\mathbf{k}$ . Consequently, the scattering cross section includes an interference term similar to (2.25). Again, the crystal itself can be used as a beam splitter, i. e., the second plane wave is obtained by Bragg reflection of the incident photon inside the crystal. As it is known from dynamical diffraction theory [73], the amplitude and the mutual phase of the Bragg reflected photon can be adjusted by aligning the crystal with respect to the incident photon beam. The off-diagonal elements  $S(\mathbf{q}, \mathbf{q} + \mathbf{G}, E)$  of the mixed dynamic form factor can be then determined as the difference between two measurements with different mutual phase  $\varphi$ . However, the analysis for this experiment is very cumbersome and only few measurements for the off-diagonal elements in silicon have been performed in the valence-loss region [74].

## 2.5 Connection with Dielectric Theory

In all of the previously described scattering experiments, the target entered the cross section only through the (mixed) dynamic form factor. As we will see in the following, this quantity is intimately related to the density response function used in dielectric theory (see chapter 1). Further, we will now answer the following questions: *What can we actually learn from scattering experiments about the target system? Which information is included in the (mixed) dynamic structure factor? And in which cases, the semi-classical derivation reproduces the quantum-mechanical calculation?*

### 2.5.1 Van-Hove Correlation Function

Following the procedure introduced by van Hove [75], we can transform the dynamic structure factor (2.23) into a density-density correlation function. Using the integral

representation of the delta function (A.24), we obtain:

$$\begin{aligned}
S(\mathbf{q}, \mathbf{q}', E) &= \sum_F \langle 0 | \hat{n}(\mathbf{q}) | F \rangle \langle F | \hat{n}^+(\mathbf{q}') | 0 \rangle \frac{1}{2\pi\hbar} \int_{-\infty}^{\infty} d\tau e^{i(\epsilon_0 - \epsilon_F + E)\tau/\hbar} \\
&= \frac{1}{2\pi\hbar} \int d\tau e^{iE\tau/\hbar} \sum_F \langle 0 | e^{iH\tau} \hat{n}(\mathbf{q}) e^{-iH\tau} | F \rangle \langle F | \hat{n}^+(\mathbf{q}') | 0 \rangle \\
&= \frac{1}{2\pi\hbar} \int d\tau e^{iE\tau/\hbar} \langle\langle \hat{n}(\mathbf{q}, \tau) \hat{n}^+(\mathbf{q}', 0) \rangle\rangle_0 = \int d\tau e^{iE\tau/\hbar} S(\mathbf{q}, \mathbf{q}', \tau)
\end{aligned} \tag{2.39}$$

where we have introduced the Heisenberg operator  $\hat{n}(\mathbf{q}, t)$  and the ground-state expectation value  $\langle\langle \cdot \rangle\rangle_0 = \langle 0 | \cdot | 0 \rangle$ . In real space, this equation reads [see eq. (A.31)]

$$S(\mathbf{r}, \mathbf{r}', \tau) = \frac{(2\pi)^2}{\hbar} \langle\langle \hat{n}(\mathbf{r}, \tau) \hat{n}(\mathbf{r}', 0) \rangle\rangle_0 = \frac{(2\pi)^2}{\hbar} g(\mathbf{r}, \mathbf{r}', \tau). \tag{2.40}$$

Thus, the mixed dynamic form factor is the Fourier transform in time and space of the *two-particle density correlation function*  $g(\mathbf{r}, \mathbf{r}')$ . It describes the correlation of the density at one point  $\mathbf{r}'$  with the density at another point  $\mathbf{r}$  after a certain time  $\tau$ . This quantity clearly contains spatial information on the target. But if only the dynamic structure factor  $S(\mathbf{q}, E)$  is known, the Fourier transform of eq. (2.39) gives [see eq. (A.29)]

$$S(\mathbf{r}, \tau) = \frac{1}{2\pi\hbar} \int d\mathbf{r}' \langle\langle \hat{n}(\mathbf{r}' + \mathbf{r}, \tau) \hat{n}(\mathbf{r}', 0) \rangle\rangle_0 = \frac{1}{2\pi\hbar} \int d\mathbf{r}' g(\mathbf{r}' + \mathbf{r}, \mathbf{r}', \tau). \tag{2.41}$$

Thus, the dynamic structure factor  $S(\mathbf{q}, \omega)$  is the Fourier transform in space and time of the *density autocorrelation function* of the target. The latter is also known as the van-Hove space-time correlation function [75]. Note that  $\mathbf{r}$  only corresponds to the distance between two points, not a spatial coordinate itself. Indeed, the integration over  $\mathbf{r}'$  eliminates any information on the inhomogeneity of the system.

### 2.5.2 Fluctuation-Dissipation Theorem

If we consider only inelastic scattering events ( $F \neq 0$ ) we have

$$\langle 0 | \hat{n} | F \rangle = \langle 0 | (\hat{n} - \langle\langle \hat{n} \rangle\rangle_0) | F \rangle = \langle 0 | \tilde{n} | F \rangle \tag{2.42}$$

and the density operator  $\hat{n}$  can be replaced by the *density-fluctuation operator*  $\tilde{n}$  in the previous equations. The inelastic part  $S_i$  of the mixed dynamic form factor is then directly related to the *retarded density response function* [see appendix A.1.2, eq. (A.20)]

$$\begin{aligned}
\chi(\mathbf{q}, \mathbf{q}', \tau) &= \frac{1}{e^2} \frac{\delta\rho^i}{\delta\varphi^e} = \frac{1}{i\hbar} \Theta(\tau) \langle\langle [\tilde{n}(\mathbf{q}, \tau), \tilde{n}^+(\mathbf{q}', 0)]_- \rangle\rangle_0 \\
&= -2\pi i \Theta(\tau) [S_i(\mathbf{q}, \mathbf{q}', \tau) - S_i(-\mathbf{q}', -\mathbf{q}, -\tau)],
\end{aligned} \tag{2.43}$$

which is equivalent to the microscopic susceptibility defined in eq. (1.7). A Fourier transformation (A.23) in time leads to [see convolution theorem (A.28)]

$$\chi(\mathbf{q}, \mathbf{q}', E) = \frac{1}{i\hbar} \int dE' [\Theta(E - E') S_i(\mathbf{q}, \mathbf{q}', E') - \Theta(E + E') S_i(-\mathbf{q}', -\mathbf{q}, E')]. \tag{2.44}$$

The two terms correspond to the resonant and antiresonant part. With the Fourier transformation of the step function  $\frac{1}{\hbar}\Theta(E) = i\mathcal{P}\frac{1}{E} + \pi\delta(E)$ , we finally have

$$\chi(\mathbf{q}, \mathbf{q}', E) = P(\mathbf{q}, \mathbf{q}', E) - i\pi D(\mathbf{q}, \mathbf{q}', E), \quad (2.45)$$

where

$$P(\mathbf{q}, \mathbf{q}', E) = \rlap{-}\int dE' \left[ \frac{S_i(\mathbf{q}, \mathbf{q}', E')}{E - E'} - \frac{S_i(-\mathbf{q}', -\mathbf{q}, E')}{E + E'} \right] \stackrel{(2.24)}{=} P^*(\mathbf{q}', \mathbf{q}, E), \quad (2.46)$$

$$D(\mathbf{q}, \mathbf{q}', E) = S_i(\mathbf{q}, \mathbf{q}', E) - S_i(-\mathbf{q}', -\mathbf{q}, -E) \stackrel{(2.24)}{=} D^*(\mathbf{q}', \mathbf{q}, E). \quad (2.47)$$

The second term in eq. (2.47) vanishes for positive energies  $E$  because  $S_i(E < 0) = 0$  if the system is initially in its ground state [see eq. (2.23)]. Note that  $D(\mathbf{q}, \mathbf{q}')$  and  $P(\mathbf{q}, \mathbf{q}')$  are generally complex valued. Only their diagonal elements  $\mathbf{q} = \mathbf{q}'$  must be real, because  $D$  and  $P$  become complex conjugated by interchanging  $\mathbf{q}$  and  $\mathbf{q}'$ , and we find [76]

$$\text{Im} \chi(\mathbf{q}, \mathbf{q}, E) = -\pi S(\mathbf{q}, E) \quad \text{for } E > 0. \quad (2.48)$$

This is the well-known *fluctuation-dissipation theorem* [52, 77]. It relates the dynamic structure factor  $S$  with the imaginary part of the susceptibility  $\chi$ . As we have seen above, the former describes the density fluctuations in space and time, while the latter is connected to the dissipation in the system. For off-diagonal elements  $\mathbf{q} \neq \mathbf{q}'$ , this connection is less clear. Restricting to  $E > 0$ , we find from the equations above

$$\frac{\text{Im}}{\text{Re}} [\chi(\mathbf{q}, \mathbf{q}') \pm \chi(\mathbf{q}', \mathbf{q})] = \frac{\text{Im}}{\text{Re}} (-i\pi) [D(\mathbf{q}, \mathbf{q}') \pm D^*(\mathbf{q}, \mathbf{q}')] = \mp 2\pi \frac{\text{Re}}{\text{Im}} S(\mathbf{q}, \mathbf{q}'), \quad (2.49)$$

and we have as generalisation of the fluctuation-dissipation theorem [61]:

$$S(\mathbf{q}, \mathbf{q}', E) = \frac{i}{2\pi} [\chi(\mathbf{q}, \mathbf{q}', E) - \chi^*(\mathbf{q}', \mathbf{q}, E)] \quad \text{for } E > 0. \quad (2.50)$$

This equation connects the mixed dynamic form factor  $S$  with the microscopic density response function  $\chi$ . It constitutes a link between the results of the scattering formalism derived in this chapter and the results obtained previously from the microscopic dielectric theory in section 1.3.

### 2.5.3 Dielectric Theory

Using the fluctuation-dissipation theorem, it is now possible to rederive the SR-EELS formula (1.21) that has been obtained in the semi-classical approach. Ritchie and Howie [66] have demonstrated that this is only possible if *all* scattered electrons are collected. To show this, we proceed in three steps: starting from eq. (2.30) we (i) link the MDFF to the microscopic dielectric function  $\varepsilon^{-1}$  defined in eq. (1.10), (ii) express the incident electron wave packet in real space, and (iii) integrate over all outgoing directions  $\mathbf{k}_f$ .

## Microscopic Dielectric Function

With the definition (1.10) of the microscopic dielectric function  $\varepsilon^{-1}(\mathbf{q}, \mathbf{q}', \omega)$ , the fluctuation-dissipation theorem reads (with  $\mathbf{E} = \hbar\omega > 0$  and  $v = v^*$ )

$$S(\mathbf{q}, \mathbf{q}', E) = \frac{i}{2\pi} \left[ \frac{1}{v(\mathbf{q})} \varepsilon^{-1}(\mathbf{q}, \mathbf{q}', E/\hbar) - \frac{1}{v(\mathbf{q}')} \varepsilon^{-1*}(\mathbf{q}', \mathbf{q}, E/\hbar) \right], \quad (2.51)$$

In particular, for AR-EELS we immediately obtain from eq. (2.16)

$$\frac{\partial^2 \sigma^{\text{inel}}}{\partial \Omega \partial \omega} = -\frac{2m^2}{\hbar^3} v(\mathbf{q}) \text{Im} \varepsilon^{-1}(\mathbf{q}, \mathbf{q}, \omega) \quad (2.52)$$

which is exactly the result (1.22) that we have obtained in the semi-classical approach.

## Real-Space Expression

Concerning the SR-EELS expression (2.32), this connection is less obvious. We start from the general expression for the differential cross section (2.21) and switch to a real-space formulation. This can be achieved by expressing the coefficients  $\phi(\mathbf{k})$  in terms of the incident electron wave function  $\bar{\Phi}(\bar{\mathbf{s}} - \bar{\mathbf{b}})$  [see eq. (2.28)] and by introducing the *cross-spectral object transparency* [68] as the inverse Fourier transform (A.42)

$$w(\bar{\mathbf{s}}, \bar{\mathbf{s}}', E) \equiv \frac{1}{L^2} \sum_{\bar{\mathbf{q}}, \bar{\mathbf{q}}'} v^*(\mathbf{q}) v(\mathbf{q}') S(\mathbf{q}, \mathbf{q}', E) e^{i\bar{\mathbf{q}}\bar{\mathbf{s}}} e^{-i\bar{\mathbf{q}}'\bar{\mathbf{s}}'}. \quad (2.53)$$

The differential cross section (2.21) then reads in real-space coordinates [25, 61]

$$\frac{\partial^2 \sigma^{\text{inel}}}{\partial \Omega \partial E} = \left[ \frac{m}{2\pi\hbar^2} \right]^2 \frac{k_f}{k_i} \iint_{L^2} d\bar{\mathbf{s}} d\bar{\mathbf{s}}' \bar{\Phi}^*(\bar{\mathbf{s}} - \bar{\mathbf{b}}) \bar{\Phi}(\bar{\mathbf{s}}' - \bar{\mathbf{b}}) e^{i\bar{\mathbf{k}}_f(\bar{\mathbf{s}} - \bar{\mathbf{s}}')} w(\bar{\mathbf{s}}, \bar{\mathbf{s}}', E), \quad (2.54)$$

i. e., the cross section is given as a convolution of the wave function  $\bar{\Phi}(\bar{\mathbf{s}} - \bar{\mathbf{b}})$  of the focussed electron beam in the object plane and the cross-spectral object transparency. The final momentum  $\bar{\mathbf{k}}_f$  of the scattered electrons appears only in the exponential.

## Infinite Detector

If we sum over all  $\bar{\mathbf{k}}_f$ , i. e., we assume that the detector collects all scattered electrons, this exponential leads to a delta function in  $\mathbf{s} - \mathbf{s}'$  [see eq. (A.41)] and we obtain<sup>6</sup>

$$\frac{\partial \sigma^{\text{inel}}}{\partial E} = \left[ \frac{m}{2\pi\hbar^2} \right]^2 \int_{L^2} d\bar{\mathbf{s}} \left| \bar{\Phi}(\bar{\mathbf{s}} - \bar{\mathbf{b}}) \right|^2 L^2 w(\bar{\mathbf{s}}, \bar{\mathbf{s}}, E) \quad (2.55)$$

<sup>6</sup>As the double-differential cross section rapidly vanishes with increasing  $\bar{\mathbf{q}}$ , only small momentum transfers contribute and the small-angle approximation still holds. In particular, we have  $k_i \approx k_f$ .

In the case of infinite resolution  $|\bar{\Phi}(\bar{\mathbf{s}})|^2 = \delta(\bar{\mathbf{s}})$ , we simply have  $w(\bar{\mathbf{b}}, \bar{\mathbf{b}}, E)$ . Using eq. (2.51), we can directly relate this quantity to the semi-classical result from eq. (1.21):

$$\begin{aligned} L^2 w(\bar{\mathbf{b}}, \bar{\mathbf{b}}, E) &= \frac{i}{2\pi} \sum_{\bar{\mathbf{q}}, \bar{\mathbf{q}}'} \left[ v(\mathbf{q}') \varepsilon^{-1}(\mathbf{q}, \mathbf{q}', \omega) - v(\mathbf{q}) \varepsilon^{-1*}(\mathbf{q}', \mathbf{q}, \omega) \right] e^{i(\bar{\mathbf{q}} - \bar{\mathbf{q}}') \bar{\mathbf{b}}} \\ &= -\frac{1}{\pi} \sum_{\bar{\mathbf{q}}, \bar{\mathbf{q}}'} v(\mathbf{q}') \operatorname{Im} \left[ \varepsilon^{-1}(\mathbf{q}, \mathbf{q}', \omega) e^{i(\bar{\mathbf{q}} - \bar{\mathbf{q}}') \bar{\mathbf{b}}} \right] \propto P(\mathbf{b}, \omega) \end{aligned} \quad (2.56)$$

In the last step, we have interchanged the variables  $\mathbf{q}$  and  $\mathbf{q}'$  for the second term.

Thus, we have shown that the semi-classical loss probability  $P(\mathbf{b}, \omega)$  corresponds exactly to the diagonal part of the cross-spectral object transparency  $w(\bar{\mathbf{b}}, \bar{\mathbf{b}}, E)$ . In particular, if all electrons are collected, eq. (2.55) holds. Then, the quantum-mechanical inelastic-scattering cross section for a focussed electron beam can be understood as an incoherent weighted sum of classical trajectories with an impact parameter  $\bar{\mathbf{s}}$  [66]. The weights are given by the intensity profile  $|\bar{\Phi}(\bar{\mathbf{s}} - \bar{\mathbf{b}})|^2$  of the focussed beam centred at position  $\bar{\mathbf{b}}$  in the object plane.

If, in contrast, the detector collects only a part of the scattered electrons, the full quantum-mechanical formula (2.32) has to be used. The influence of the detector geometry has been investigated, for example, by Kohl and Rose [61] and Cosgriff *et al.* [78] who studied the delocalisation of the EELS signal for a single, isolated atom.

## Conclusions

In this chapter, the scattering of a fast electron has been studied in the framework of quantum-mechanical scattering theory. Only the electrostatic interaction between the scattering particle and the target has been taken into account and relativistic effects have been completely neglected. Additionally, we have restricted our discussion to first-order perturbation theory (first Born approximation).

Within these approximations, we have derived the energy-loss probability for different experimental setups, namely the broad-beam geometry used in angular-resolved EELS, the two-beam geometry which is related to EMCD, and the focussed electron beam used in the STEM. In all cases, the corresponding differential cross section can be split into two contributions: first, a probe factor  $C$  which describes the properties of the incident electron and second, the mixed dynamic form factor  $S(\mathbf{q}, \mathbf{q}', E)$  which describes the target. This separation also holds, when photons instead of electrons are used as scattering particles. The energy-loss probability in inelastic X-ray scattering is found to be very similar to the cross section for electron scattering. Indeed, in both scattering experiments only the probe factor differs.

Further, we have analysed which informations on the target can be obtained from scattering experiments. In AR-EELS, one measures only the diagonal part of the mixed dynamic form factor  $S(\mathbf{q}, \mathbf{q}, E)$  which is the Fourier transform of the density autocorrelation function in space and time. Spatial informations on the target can be accessed only if the off-diagonal elements  $S(\mathbf{q}, \mathbf{q}', E)$  contribute to the scattering cross section.

For instance, this is the case in the STEM, where the incident electron is prepared as a coherent superposition of several plane waves. We have seen that the mixed dynamic form factor  $S(\mathbf{q}, \mathbf{q}', E)$  is related to the microscopic density response function  $\chi(\mathbf{q}, \mathbf{q}', \omega)$  by a generalised fluctuation-dissipation theorem.

Finally, we have discussed the relation between the quantum-mechanical scattering approach from this chapter and the semi-classical dielectric theory used in section 1.3. In the quantum-mechanical approach, both the external electron and the particles of the target have been described by the time-dependent Schrödinger equation. In dielectric theory, instead, the external particle is described in a purely classical framework. One assumes that the electron moves on a definite trajectory and the associated time-dependent potential acts as a perturbation to the target. We have compared the two approaches for the case of angular- and spatially-resolved EELS: For AR-EELS, the dynamic structure factor and the inverse dielectric function are directly related by the fluctuation-dissipation theorem and the two approaches lead to the same results. For SR-EELS, the semi-classical theory gives the same results as the full quantum-mechanical calculation only when all scattered electrons are collected.

The most difficult part of the scattering problem still remains to be solved: The quantum-mechanical description of the target which usually consists of a *very* large number of particles. In the next chapter, we use (time-dependent) density-functional theory to calculate the density response function  $\chi$  numerically. By means of the fluctuation-dissipation theorem, we are then capable of determining the mixed dynamic form factor and the scattering cross section starting from first principles.



## 3 The Many-Body Problem

In the framework of quantum-mechanics, the movement of the particles in the target is governed by the Schrödinger equation. The solution of this many-body problem is a formidable task that has occupied generations of physicists since the early days of quantum mechanics. Nevertheless, an *ab-initio* description of real materials could be envisaged only during the last decades making use of numerical simulations on high-performance computers.

Many approaches exist to find an approximate solution for the many-body problem. Examples are (i) the configuration interaction and the quantum Monte-Carlo approach from quantum chemistry that try to find the full many-body wave function [79, 80], (ii) dynamical mean-field theory, where the many-body problem is replaced by a single-site quantum impurity problem for an effective medium [81], (iii) many-body perturbation theory that is based on the Green's-function formalism [82], and (iv) density-functional theory (DFT) which uses the ground-state density as a basic variable [12].

The method of choice strongly depends on the material, the quantity of interest, and the required accuracy. In this thesis, we use time-dependent density-functional theory (TDDFT) to describe the excitation properties of the target. It has been found that valence-loss EELS and IXS experiments are generally well described within TDDFT using standard approximations both for extended systems and nanostructures [83]. In principle, these calculations are parameter-free and systems with several hundred electrons<sup>1</sup> can be handled.

In the following, we briefly review the basics of static and time-dependent density-functional theory. We explain, how the linear response of the system subject to an external perturbation, namely the density response function  $\chi$ , can be calculated within this formalism. Finally, some numerical details of the used plane-wave pseudopotential code are discussed.

### 3.1 Density-Functional Theory (DFT)

Traditional approaches for the solution of the many-particle Schrödinger equation rely on the many-body wave function. For a system of  $N$  particles, the wave function depends on  $3N$  space variables which are all interconnected. This leads to an exponential increase of the complexity of the problem with the system size. Already small systems that only consist of several tens of atoms become unfeasible.

Density-functional theory, instead, is a formally exact and numerically very efficient method for the determination of geometric and electronic properties of solids and nano-

---

<sup>1</sup>This includes infinite crystals, where the translational symmetry reduces the problem to its unit cell.

structures with hundreds of atoms. Its enormous success is based on two central ideas: First, a much simpler quantity than the multi-particle wave function, namely the electron density distribution  $n(\mathbf{r})$ , is used to describe the quantum system. Second, the many-body problem is mapped to a fictitious single-particle problem of independent Kohn-Sham particles in an effective, local potential  $v_S(\mathbf{r})$ . The one-particle Schrödinger equation can be easily solved with standard techniques. As the potential  $v_S$  implicitly depends on the resulting single-particle wave functions, the solution must be determined in a self-consistent way. In the following, we will briefly present these two concepts. A detailed introduction can be found in [12, 84, 85].

### 3.1.1 Hohenberg-Kohn Theorem

Starting point is the time-independent Schrödinger equation for a system of  $N$  electrons in an external potential  $v_{\text{ext}}$  (compare with section 2.1)<sup>2</sup>

$$H|0\rangle = \epsilon_0|0\rangle, \quad H = T + U + V_{\text{ext}}, \quad V_{\text{ext}} = \int d\mathbf{r} v_{\text{ext}}(\mathbf{r}) n(\mathbf{r}). \quad (3.1)$$

Within the Born-Oppenheimer approximation [59], the motion of electrons and ions can be separated and the Hamiltonian consists of three parts: the kinetic energy  $T$  of the electrons, the electron-electron interaction  $U$ , and the potential  $v_{\text{ext}}$  of the ions which shall be considered as an external single-particle potential.

As  $T$  and  $U$  are the same for all physical systems, the external potential  $v_{\text{ext}}$  uniquely determines the Hamiltonian  $H$  and thus all properties of the many-body system like the ground state  $|0\rangle$  and the density  $n(\mathbf{r})$ . Interestingly, also the inverse statement holds:

**Theorem 3.1** (Hohenberg and Kohn I, 1964, [86]).

*The ground-state density  $n(\mathbf{r})$  of a system of interacting electrons subject to an external potential  $v_{\text{ext}}(\mathbf{r})$  uniquely determines this potential and hence the entire physical system.*

In non-degenerate systems, the ground state  $|0\rangle$ , and thus any observable, becomes a functional of the density. In particular, the energy  $E_{v_0}[n] = \langle 0, [n] | H_{v_0} | 0, [n] \rangle$  is a functional of the density, where  $H_{v_0} = T + U + V_0$  denotes the Hamiltonian for a fixed external potential  $v_0$ . The Ritz principle immediately leads us to the second important

**Theorem 3.2** (Hohenberg und Kohn II, 1964, [86]).

*The energy functional  $E_{v_0}[n]$  is minimised by the ground-state density  $n_0$  that corresponds to the external potential  $v_0$ :  $E_{v_0}[n] \geq E_{v_0}[n_0]$ .*

If the energy functional were explicitly known, the ground-state density  $n_0$  could have been determined by a seemingly trivial minimisation of  $E_{v_0}[n]$  with respect to the three-dimensional trial function  $n(\mathbf{r})$ . The main problem is to find reasonable approximations for the energy functional.

---

<sup>2</sup>In the following,  $V$  denotes the energy of a charge density  $n$  inside the single-particle potential  $v$ .

Already in 1927, Thomas and Fermi proposed to approximate the electron-electron interaction  $U$  by the classical Hartree term  $V_H$  and the kinetic energy  $T$  within a local-density approximation using the kinetic energy of a homogeneous electron gas:

$$U_{\text{TF}} = V_H = \frac{e^2}{8\pi\epsilon_0} \int d\mathbf{r} d\mathbf{r}' \frac{n(\mathbf{r})n(\mathbf{r}')}{|\mathbf{r} - \mathbf{r}'|}, \quad T_{\text{TF}} = \frac{3}{5}(3\pi^2)^{2/3} \frac{\hbar^2}{2m} \int d\mathbf{r} n^{5/3}(\mathbf{r}). \quad (3.2)$$

But this approximation failed to describe, for instance, the shell structure of atoms or chemical bonding.

### 3.1.2 Kohn-Sham Equations

Kohn and Sham (KS), instead, expressed  $T[n]$  in terms of the kinetic energy of an auxiliary system of independent particles. This system is introduced by the following

**Definition 3.3** (Kohn-Sham system, 1965, [87]).

*Each system of interacting particles in the external potential  $v_0$  can be mapped to a system of fictitious, non-interacting Kohn-Sham particles in the effective, local potential  $v_S$  such that both have the same ground-state density  $n_0$ :  $H = T + U + V_0 \xleftrightarrow{n_0} H_S = T_S + V_S$ .*

If the KS-potential  $v_S$  is known, we can easily solve the single-particle SEQ for the KS-system and calculate the corresponding wave functions  $|\varphi_\lambda^{\text{KS}}\rangle$  and energies  $\epsilon_\lambda^{\text{KS}}$ . The ground-state density  $n_0$  and the kinetic energy  $T_S$  of the KS-particles are then given by

$$n_0(\mathbf{r}) = \sum_{\lambda=1}^N |\varphi_\lambda^{\text{KS}}(\mathbf{r})|^2, \quad T_S[n] = \sum_{\lambda=1}^N \langle \varphi_\lambda^{\text{KS}} | \left( -\frac{\hbar^2 \nabla^2}{2m} \right) | \varphi_\lambda^{\text{KS}} \rangle. \quad (3.3)$$

In contrast to the Thomas-Fermi approximation, we rewrite the energy functional as

$$E_{v_0}[n] = T_S[n] + V_H[n] + V_0[n] + V_{\text{XC}}[n], \quad (3.4)$$

where  $V_{\text{XC}}$  is the *exchange-correlation* energy. It corresponds to that part of the exact energy functional, that we essentially do not know and which has been therefore called *stupidity energy* by Feynman [88]. But as long as  $T_S + V_H$  is rather close to  $T + U$  of the real system, the remainder  $V_{\text{XC}}$  is small and can be approximated in a rough way.

As the energy functional of the interacting system  $E_{v_0}[n]$  and that of the KS-system  $E^{\text{KS}}[n] = T_S[n] + V_S[n]$  have to take their minimum at the *same* density  $n_0$ , we have

$$v_S(\mathbf{r}, [n_0]) = v_0(\mathbf{r}) + v_H(\mathbf{r}, [n_0]) + v_{\text{XC}}(\mathbf{r}, [n_0]), \quad v_{\text{XC}}(\mathbf{r}, [n_0]) = \left. \frac{\delta V_{\text{XC}}}{\delta n(\mathbf{r})} \right|_{n_0} \quad (3.5)$$

The ground-state density can be now determined in a self-consistent iteration: Starting with a test density  $\tilde{n}$ , we solve the single-particle Schrödinger equation for the Kohn-Sham potential  $v_S(\mathbf{r}, [\tilde{n}])$ . If the density calculated by eq. (3.3) differs from  $\tilde{n}$ , the process is iterated until they become equal.

## Exchange and Correlation Potential

All equations have been formally exact so far. But we still have to find an explicit functional for  $V_{XC}$ . If this term is completely neglected, one obtains the Hartree approximation. Many of the standard DFT calculations today use the *local-density approximation* (LDA) that was introduced by Kohn and Sham in 1965 [87]. Similar to the Thomas-Fermi approximation, the system is locally considered as interacting homogeneous electron gas:

$$V_{XC} = \int d\mathbf{r} n(\mathbf{r})v_{XC}(\mathbf{r}, [n]) \quad \longrightarrow \quad V_{XC}^{LDA} = \int d\mathbf{r} n(\mathbf{r})\epsilon_{XC}(n(\mathbf{r})), \quad (3.6)$$

where  $\epsilon_{XC}(n)$  is a function (not a functional) of the density  $n(\mathbf{r})$  at point  $\mathbf{r}$ . For the homogeneous interacting electron gas, reliable parametrisations of  $\epsilon_{XC}(n)$  are available from quantum Monte-Carlo simulations [89, 90]. The LDA has been successfully applied for the calculation of ground-state properties in a large variety of systems like solids, nanostructures, and even molecules. Typically, the lattice parameters, ground-state energies, and the bulk modulus are in agreement with experimental results within few percent.

## Kohn-Sham Bandstructure

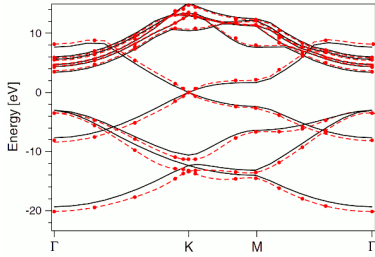


**Fig. 3.1:** LDA-KS (solid) and GW bandstructure (red dashed) of graphene (Reproduced from [91], © 2008 by The American Physical Society).

The Kohn-Sham energies  $\epsilon_{\lambda}^{KS}$  should not be confused with the quasiparticle bandstructure of the system which is measured, e. g., in photo-emission experiments. Indeed, static density-functional theory is not meant to describe the excited states of the system. The eigenfunctions and -energies of the fictitious Kohn-Sham system have no direct physical meaning. Only the energy of the highest occupied Kohn-Sham state corresponds to the exact ionisation energy of the system [92].

Instead, one can use Green's function techniques to calculate the correct quasiparticle energies and lifetimes [82]. In practice, one often uses the so-called GW-approximation for the self-energy [93] and the quasiparticle bandstructure is calculated in a perturbative treatment starting from the LDA Kohn-Sham orbitals. In strongly correlated systems, the quasiparticle corrections can lead to important qualitative changes.

Nevertheless, there are also many systems where the corrections are quite small and the Kohn-Sham energies can be understood as a first approximation to the quasiparticle bandstructure. For example, fig. 3.1 shows the difference for the bandstructure of graphene. The LDA-KS bandstructure (solid) is corrected by less than 1 eV within the GW-approximation (red dashed) [91]. In this thesis, we will only consider Kohn-Sham energies for a qualitative discussion of the bandstructure of carbon materials.

## 3.2 Time-Dependent Density-Functional Theory (TDDFT)

In order to describe the interaction of the target with an external scattering particle, we are interested in the neutral excitations of the system and not only the ground-state properties described in DFT. In 1984/85, the basic ideas of static density-functional theory have been formally extended to the more general situation of systems subject to a *time-dependent* external perturbation by Runge, Gross, and Kohn [13, 94]. Indeed, first calculations have been already performed by Zangwill and Soven [95] in 1980. A recent overview of the current developments in TDDFT can be found in [83, 96].

### 3.2.1 Runge-Gross Theorem

Starting point is now the *time-dependent* Schrödinger equation [compare with eq. (3.1)]

$$i\hbar\partial_t |\Psi(t)\rangle = H_t |\Psi(t)\rangle, \quad |\Psi(t_0)\rangle = |\Psi_0\rangle, \quad H_t = T + U + V_{\text{ext}}(t). \quad (3.7)$$

The external potential  $v_{\text{ext}}(t)$  is given by the potential of the ions plus a time-dependent scalar field  $\varphi^e(t)$  that acts as a perturbation to the system. Analogous to the static DFT, the time-dependent density  $n(t)$  can be introduced as basic variable by means of a one-to-one correspondence between the density  $n(t)$  and the external potential  $V_{\text{ext}}(t)$ :

**Theorem 3.4** (Runge and Gross I, 1984, [13]).

*The densities  $n(\mathbf{r}, t)$  and  $n'(\mathbf{r}, t)$  evolving from a common initial state  $|\Psi_0\rangle$  at  $t_0$  under the influence of the two Taylor expandable potentials  $v_{\text{ext}}(\mathbf{r}, t)$  and  $v'_{\text{ext}}(\mathbf{r}, t)$  differ, if and only if the potentials differ by more than a time-dependent constant  $v_{\text{ext}} - v'_{\text{ext}} \neq c(t)$ .*

The constant  $c(t)$  only results in a time-dependent phase factor in the corresponding wave function  $|\Psi(t)\rangle$ . Because this phase is irrelevant for the calculation of expectation values  $O[n](t) = \langle \Psi(t), [n] | O | \Psi(t), [n] \rangle$ , any physical observable is a functional of the time-dependent density. Of course, the total energy is no longer a conserved quantity and there is hence no minimisation principle for  $E$ . Alternatively, we can use the quantum-mechanical action,<sup>3</sup> which becomes stationary for the solution  $|\Psi(t)\rangle$  of the SEQ (3.7)

$$\mathcal{A}[n] = \int_{t_0}^{t_1} dt \langle \Psi(t) | i\hbar\partial_t - H_t | \Psi(t) \rangle. \quad (3.8)$$

Due to theorem 3.4, the action must be a functional of the density which leads us to the

**Theorem 3.5** (Runge and Gross II, 1984, [13]).

*For a given initial state  $|\Psi_0\rangle$  at  $t_0$ , the action  $\mathcal{A}_{v_0}[n]$  becomes stationary at the density  $n_0(\mathbf{r}, t)$  that corresponds to the external potential  $v_0(\mathbf{r}, t)$ :  $[\delta\mathcal{A}_{v_0}[n]/\delta n(\mathbf{r}, t)]_{n_0} = 0$ .*

---

<sup>3</sup>Actually, this definition has several problems. For example, the exchange-correlation potential deduced from the action is not causal, and the endpoints at  $t_0$  and  $t_1$  are not independent. These problems could be solved as proposed by van Leeuwen [97] by using the time-contour formalism of Keldysh.

### 3.2.2 Kohn-Sham Equations

In order to approximate the unknown action functional  $\mathcal{A}[n]$ , Gross and Kohn [94] have introduced a fictitious system of non-interacting Kohn-Sham particles that satisfy the *time-dependent Kohn-Sham equations* for the effective single-particle potential  $v_S(\mathbf{r}, t)$

$$i\hbar\partial_t \left| \phi_\lambda^{\text{KS}}(t) \right\rangle = \left( -\frac{\hbar^2 \nabla^2}{2m} + v_S \right) \left| \phi_\lambda^{\text{KS}}(t) \right\rangle, \quad n(\mathbf{r}, t) = \sum_{\lambda=1}^N \left| \phi_\lambda^{\text{KS}}(\mathbf{r}, t) \right|^2, \quad (3.9)$$

and whose density  $n(\mathbf{r}, t)$  is identical to the one of the interacting system. The existence of the potential  $v_S$  for any density  $n(\mathbf{r}, t)$  can be inferred from the Runge-Gross theorem 3.4 and has been rigorously proven in [98]. By decomposing the action functional (3.8) analogously to eq. (3.4) of static DFT as  $\mathcal{A}[n] = \mathcal{T}_S[n] + \mathcal{A}_H[n] + \mathcal{A}_0[n] + \mathcal{A}_{\text{XC}}[n]$ , we finally obtain from the variational principle stated in theorem 3.5

$$v_S(\mathbf{r}, t, [n_0]) = v_0(\mathbf{r}, t) + v_H(\mathbf{r}, t, [n_0]) + v_{\text{XC}}(\mathbf{r}, t, [n_0]), \quad v_{\text{XC}} \equiv \left. \frac{\delta \mathcal{A}_{\text{XC}}}{\delta n(\mathbf{r}, t)} \right|_{n_0} \quad (3.10)$$

where  $v_{\text{XC}}(\mathbf{r}, t, [n])$  is the *time-dependent exchange-correlation potential*. The two equations (3.9) and (3.10) form a system of self-consistent equations. For a given approximation of the exchange-correlation potential  $v_{\text{XC}}$ , it can be solved by iteration.

### Adiabatic Local-Density Approximation (ALDA)

Most calculations simply use one of the established functionals of static density-functional theory. The most popular choice is the adiabatic local-density approximation which is local both in time and space:

$$v_{\text{XC}}^{\text{ALDA}}(\mathbf{r}, t, [n]) = v_{\text{XC}}^{\text{LDA}}(n(\mathbf{r}, t)) \stackrel{(3.6)}{=} \frac{d}{dn} \left[ n \epsilon_{\text{XC}}(n) \right]_{n=n(\mathbf{r}, t)} \quad (3.11)$$

The function  $\epsilon_{\text{XC}}(n)$  denotes again the exchange-correlation energy of the homogeneous electron gas with a density given by  $n(\mathbf{r}, t)$  at point  $\mathbf{r}$  and time  $t$ . For a discussion of its deficiencies and recent approaches towards better kernels see reference [96].

### 3.2.3 Linear Density-Response Theory

Consider a system that is initially in its ground state  $|0\rangle$  for  $t < t_0$ . The corresponding density  $n_0$  and the KS wave functions  $|\varphi_\lambda^{\text{KS}}\rangle$  can be uniquely determined by a DFT calculation. Switching on an external perturbation  $v_{\text{ext}}(t) = -e\hat{\varphi}^e(t)$  at time  $t_0$ , the density  $n$  will deviate from the initial state  $n_0$ . The evolution of the KS orbitals  $|\phi_\lambda^{\text{KS}}(t)\rangle$  and the corresponding density  $n(t)$  is described by the time-dependent Kohn-Sham eq. (3.9) with the initial states  $|\phi_\lambda^{\text{KS}}(t_0)\rangle = |\varphi_\lambda^{\text{KS}}\rangle$ . As far as we are only interested in the *linear response* of the system, it is even not necessary to solve the full Kohn-Sham equations.

For instance, the density-response function  $\chi$  can be directly calculated from the *ground-state* wave function  $|0\rangle$  using time-dependent perturbation theory. Indeed, we have seen in section 2.5.2 that the susceptibility

$$\chi(\mathbf{r}, \mathbf{r}', t - t') = \frac{\delta n(\mathbf{r}t)}{\delta v_{\text{ext}}(\mathbf{r}', t')} \Big|_{v_{\text{ext}}=v_{\text{ext}}(t_0)} = \frac{1}{e^2} \frac{\delta \rho}{\delta \varphi^e} \Big|_{\varphi^e=0}, \quad (3.12)$$

is directly related to the ground-state expectation value of the density-density commutator (2.43) by means of the fluctuation-dissipation theorem. For the system of independent Kohn-Sham particles this commutator can be easily evaluated leading to an efficient formulation of linear response in the framework of TDDFT.

### Independent-Particle Polarisability $\chi^0$

Due to the time-dependence of the external potential  $v_{\text{ext}}$ , also the effective Kohn-Sham potential  $v_S$  will change and thus the density  $n$ . The corresponding response function  $\chi^0$  of the Kohn-Sham particles with respect to the potential  $v_S$  is defined as [see eq. (3.12)]

$$\chi^0 = \frac{\delta n}{\delta v_S} = \frac{1}{i\hbar} \theta(t - t') \langle \varphi_1^{\text{KS}} \dots \varphi_N^{\text{KS}} | [\hat{n}(\mathbf{r}, t), \hat{n}(\mathbf{r}', t')]_- | \varphi_1^{\text{KS}} \dots \varphi_N^{\text{KS}} \rangle \quad (3.13)$$

where  $|\dots\rangle$  denotes the Slater determinant of the single-particle orbitals  $|\varphi_\lambda^{\text{KS}}\rangle$ . In crystals, they are given by Bloch functions  $|\varphi_{n,\mathbf{k}}^{\text{KS}}\rangle$ , where  $n$  denotes the band index and  $\mathbf{k}$  the wave vector. In Fourier space, the polarisability then reads [83] (see appendix A.2.2)

$$\chi_{\mathbf{G}\mathbf{G}'}^0(\mathbf{q}_r, \omega) = \frac{1}{V} \sum_{knn'} \frac{(f_{n'\mathbf{k}-\mathbf{q}_r} - f_{n\mathbf{k}}) \tilde{\rho}_{\mathbf{k}}^{nn'}(\mathbf{q}_r + \mathbf{G}) [\tilde{\rho}_{\mathbf{k}}^{nn'}(\mathbf{q}_r + \mathbf{G}')]^*}{\hbar\omega + (\epsilon_{n'\mathbf{k}-\mathbf{q}_r}^{\text{KS}} - \epsilon_{n\mathbf{k}}^{\text{KS}}) + i\eta}, \quad (3.14)$$

with the transition-matrix elements

$$\tilde{\rho}_{\mathbf{k}}^{nn'}(\mathbf{q}_r + \mathbf{G}) = \langle \varphi_{n',\mathbf{k}-\mathbf{q}_r}^{\text{KS}} | e^{-i(\mathbf{q}_r+\mathbf{G})\cdot\mathbf{r}} | \varphi_{n,\mathbf{k}}^{\text{KS}} \rangle. \quad (3.15)$$

The wave vectors  $\mathbf{k}$  and  $\mathbf{q}_r$  are restricted to the first Brillouin zone, while  $\mathbf{G}^{(l)}$  corresponds to a reciprocal lattice vector of the crystal. Further,  $\epsilon^{\text{KS}}$  and  $f$  denote the energy and the occupation number of the corresponding Kohn-Sham orbital. Neglecting spin-polarisation effects, we assume that each state is occupied by the same number of spin-up and spin-down electrons ( $f \in [0, 2]$ ). The sum is normalised by the volume  $V$  of the crystal (see appendix A.3.1) and the broadening  $\eta$  should be infinitesimal small. For diagonal elements  $\mathbf{G} = \mathbf{G}'$ , eq. (3.14) reduces to the *Ehrenreich-Cohen formula* [99].

### TDDFT Dyson-Equation

Making use of the fact that the densities of the real system and the non-interacting Kohn-Sham system are identical, one can now establish a direct link between the corresponding correlation functions  $\chi$  and  $\chi^0$ . With eq. (3.10), we find

$$\chi = \frac{\delta n}{\delta v_{\text{ext}}} = \frac{\delta n}{\delta v_S} \frac{\delta v_S}{\delta v_{\text{ext}}} = \chi^0 \frac{\delta(v_{\text{ext}} + v_{\text{H}} + v_{\text{XC}})}{\delta v_{\text{ext}}} = \chi^0 \left[ \hat{1} + \left( \frac{\delta v_{\text{H}}}{\delta n} + \frac{\delta v_{\text{XC}}}{\delta n} \right) \frac{\delta n}{\delta v_{\text{ext}}} \right]$$

and thus we obtain a *Dyson-like screening equation*<sup>4</sup> that connects  $\chi$  and  $\chi^0$ :

$$\chi = \chi^0 + \chi^0(v + f_{\text{XC}})\chi, \quad v = \frac{e^2}{4\pi\epsilon_0|r - r'|}, \quad f_{\text{XC}}(\mathbf{r}, t; \mathbf{r}', t') \equiv \frac{\delta v_{\text{XC}}(\mathbf{r}, t)}{\delta n(\mathbf{r}', t')}. \quad (3.16)$$

The functional derivative of the Hartree potential  $v_{\text{H}}$  corresponds to the Coulomb potential  $v$  and the one of  $v_{\text{XC}}$  is the so-called *exchange-correlation kernel*  $f_{\text{XC}}$ . Additionally, we can derive a direct relation between the polarisability  $\pi$  and the independent-particle polarisability  $\chi^0$  from the Dyson equation (1.11) of section 1.3

$$\pi = \chi^0 + \chi^0 f_{\text{XC}} \pi. \quad (3.17)$$

In order to understand the physical meaning of eq. (3.16), consider the system of independent Kohn-Sham particles. If the external potential  $v_{\text{ext}}$  is changed, also the induced Hartree potential  $v_{\text{H}}$  and the exchange-correlation potential  $v_{\text{XC}}$  will change. This corresponds to the screening of the external potential due to the Coulomb interaction of the classical electrons and the quantum nature of the interacting particles, respectively. The total response of the non-interacting particles is therefore a sum of three contributions  $\delta n = \chi^0 [\delta v_{\text{ext}} + \delta v_{\text{H}} + \delta v_{\text{XC}}]$ . By means of the Dyson equation (3.16), this self consistent screening is incorporated into the susceptibility  $\chi$ , such that  $\delta n = \chi \delta v_{\text{ext}}$  holds. Therefore, the susceptibility  $\chi$  is a much more complicated quantity than  $\chi^0$ . For example,  $\chi$  can be strongly dependent on the shape of the crystal due to the long-range Coulomb interaction, while  $\chi^0$  is generally not. We will come back to this important difference in section 5.4.1.

### Exchange-Correlation Kernel

As we have discussed earlier, we have to find useful approximations for the exchange-correlation potential  $v_{\text{XC}}$  and hence also for  $f_{\text{XC}}$ . In this thesis, we have mainly used the *Random Phase Approximation* (RPA)<sup>5</sup>

$$\text{RPA:} \quad f_{\text{XC}} = 0 \quad \longrightarrow \quad \pi = \chi^0, \quad \epsilon \stackrel{(1.10)}{=} \hat{1} - v\chi^0. \quad (3.18)$$

Exchange and correlation effects are completely neglected in the response of the system. Using instead the *adiabatic local-density approximation* (ALDA) for  $v_{\text{XC}}$ , we have

$$\text{ALDA:} \quad f_{\text{XC}}(\mathbf{r}, t; \mathbf{r}', t') = \delta(\mathbf{r} - \mathbf{r}')\delta(t - t') \frac{d^2}{dn^2} [n \epsilon_{\text{XC}}(n)]_{n=n(\mathbf{r}, t)}. \quad (3.19)$$

By construction, the ALDA kernel is local both in time and space. Memory effects or the influence of the charge distribution at a distant point (e.g., for the Van-der-Waals interaction) are not included. Nevertheless, ALDA and even RPA calculations are generally in good agreement with electron energy-loss experiments for solids and nanostructures (except for strongly correlated materials). For absorption spectra in extended systems, like bulk silicon, both RPA and ALDA fail and improved kernels have to be used [83].

<sup>4</sup>It can be also understood as a Bethe-Salpeter equation for two-point functions [83].

<sup>5</sup>The change of the Hartree potential, and in particular crystal local-field effects, are still included. We will refer to the *Independent-Particle Approximation* (IPA), if we also neglect the local-field effects.

### 3.2.4 Summary

For a crystal, the microscopic density-response function  $\chi_{\mathbf{G}\mathbf{G}'}(\mathbf{q}_r, \omega)$  and thus the mixed dynamic form factor  $S(\mathbf{q}_r + \mathbf{G}, \mathbf{q}_r + \mathbf{G}'; \omega)$  can be calculated in the following four steps:

1. **Ground-state calculation** in the framework of static DFT. For a given exchange-correlation potential  $v_{\text{XC}}$ , the Kohn-Sham eigenstates  $|\varphi_{n,\mathbf{k}}^{\text{KS}}\rangle$  and -energies  $\epsilon_{n,\mathbf{k}}^{\text{KS}}$  are calculated for sufficiently many bands  $n$  and wave vectors  $\mathbf{k}$  (see section 3.1.2).
2. **The independent-particle polarisability**  $\chi^0$  can be determined by eq. (3.14) for a sufficient number of matrix elements  $\chi_{\mathbf{G}\mathbf{G}'}^0$ .
3. **The susceptibility**  $\chi$  of the interacting system is calculated by a solution of the Dyson eq. (3.16):  $\chi = [\hat{1} - \chi^0(v + f_{\text{XC}})]^{-1} \chi^0$  for a reasonable approximation of the exchange-correlation kernel  $f_{\text{XC}}$ . As all quantities are matrices in the reciprocal lattice vectors  $\mathbf{G}$ , the matrix elements  $\chi_{\mathbf{G}\mathbf{G}'}$  will be mixed during the inversion.
4. **The electron energy-loss spectrum** can be obtained from the equations of the previous chapter. In particular, for AR-EELS we have  $\frac{\partial^2 \sigma}{\partial \Omega \partial E} \propto \frac{1}{|\mathbf{q} + \mathbf{G}|^4} \chi_{\mathbf{G}\mathbf{G}}(\mathbf{q}_r, \omega)$ , where  $\mathbf{q}_r + \mathbf{G}$  corresponds to the momentum transfer [see eq. (2.16)].

Of course, also the microscopic dielectric functions  $\epsilon$  and  $\epsilon^{-1}$  as well as the macroscopic equivalent  $\epsilon_M$  can be directly calculated from  $\chi$  using eq. (1.10) and eq. (1.15).

## 3.3 Numerical Details

The numerical calculations have been performed using a plane-wave basis set and norm-conserving pseudopotentials for the description of the ions. We have used the ABINIT-code [100, 101] in order to determine the ground-state within DFT-LDA and further the DP-code [102, 103] to calculate the response of the material. In the following, we will shortly discuss some of the numerical details and the necessary convergence tests. A general introduction to the practical implementation of the DFT formalism is given, e. g., by Payne *et al.* [104].

### 3.3.1 Pseudopotentials

The chemical properties and the low-energy-loss spectra of a material mainly depend on the *valence electrons* which must be described very accurately. In contrast, the tightly-bound *core electrons* will be hardly influenced by the environment and they can be considered to form, together with the nucleus, an immutable ion. The pseudopotential method [105] is based on this observation. It can be divided into two steps:

#### Separation of Valence and Core Electrons

Within the *frozen-core approximation*, one assumes that the core electrons and the corresponding density  $n_c$  are independent of the external perturbation and the chemical

environment of the atom. They can be determined from an all-electron calculation for a single atom. In the full (TD)DFT calculation, only the valence electrons have then to be taken into account explicitly, while the core states are included in the ion potential. Any linear functional of the density, like the Hartree potential, can be easily separated into a contribution from the cores  $n_c$  and a functional that depends only on the valence electron density  $n_v$ . For nonlinear functionals, like the exchange-correlation energy, this is only possible when the densities are spatially separated. This is roughly fulfilled when the core states form a closed shell like in the materials studied in this thesis. In general, this is of course an approximation and may lead to errors in the total energy [106].

### Introduction of a Pseudo-Ion

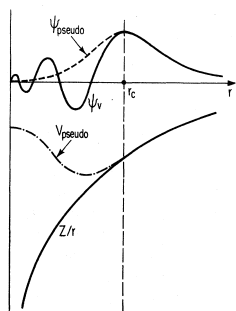


**Fig. 3.2:** From [104], © 1992 by The American Physical Society.

Although the core electrons partially screen the nuclear charges, the ion potential still has a Coulomb singularity at the nucleus. Due to this steep potential and their orthogonality to the core wave functions, the single-particle valence wave functions strongly oscillate in the core region. Consequently, it becomes very difficult to describe them numerically in this region. However, the binding properties are largely independent on the exact form of the wave functions close to the nucleus. The main idea is to introduce a ‘pseudo’ ion which has the same chemical properties as the real one, but whose ‘pseudo’ wave functions are smooth inside a small sphere with radius  $r_c$  around the ion. Therefore, one starts from an all-electron calculation of a single atom and replaces the real ion potential by a *pseudopotential* such that the following quantities remain unchanged

1. the Kohn-Sham energies,
2. the Kohn-Sham wave functions outside of the cutoff radius  $r_c$ ,
3. the total charge density inside the sphere, and
4. the scattering properties or phase shifts

The third criterion actually corresponds to the norm conservation of the wave function.<sup>6</sup> With the remaining degrees of freedom one can optimise the pseudopotential such that the resulting pseudo wave functions become smooth inside the small sphere. The resulting pseudopotential is generally nonlocal as the phase shift produced by the ion core is different for each angular momentum component of the valence wave function [104].

Several methods have been proposed to construct transferable pseudopotentials from an all-electron calculation of the isolated atom. In this thesis, we use norm-conserving potentials of Troullier-Martins [108] and Hamann type [109].

<sup>6</sup>Following Vanderbilt [107], one can drop the norm conservation to construct ultrasoft pseudopotentials.

### 3.3.2 Plane-Wave Basis Set

Although DFT in principle uses the density as a ground-state variable, one still has to solve a single-particle Schrödinger equation for the Kohn-Sham particles. The corresponding smooth pseudo wave functions  $|\varphi_\lambda^{\text{KS}}\rangle$  can be represented quite efficiently by a plane-wave basis set. This basis has several advantages: First, it is very simple to use. Because the plane waves form a complete set of orthogonalised functions, the quality of the sampling can be systematically improved. No special knowledge about the contributing atomic orbitals is necessary. Second, the evaluation of the kinetic energy and the Hartree potential becomes particularly simple in Fourier space. Switching between real-space and plane-wave representation is numerically very efficient by means of the Fast Fourier Transform. Third, plane waves are very efficient for periodic systems.

Of course, for a numerical treatment, one has to restrict the basis to a finite set of plane waves. This is achieved by a discrete  $k$ -point grid and a certain cutoff energy  $E_{\text{cut}}$ .

#### **$k$ -point Grid:**

In periodic systems, the Bloch theorem holds, i. e., any wave function can be written as a sum of plane waves with the same reduced momentum  $\mathbf{k}$

$$\varphi_\lambda = \varphi_{n,\mathbf{k}}(\mathbf{r}) = \sum_{\mathbf{G}} C_{n,\mathbf{k}}(\mathbf{G}) e^{i(\mathbf{k}+\mathbf{G})\cdot\mathbf{r}}. \quad (3.20)$$

The summation runs over all reciprocal lattice vectors  $\mathbf{G}$ . Each wave function  $|\varphi_\lambda\rangle$  can be uniquely identified by the band index  $n$  and the wave vector  $\mathbf{k}$  which is a continuous parameter restricted to the first Brillouin zone.<sup>7</sup>

Moreover, the wave functions are almost identical for two  $k$  points which are close together. It is therefore sufficient to sample the Brillouin zone by a discrete set of  $k$  points. Any integration over the Brillouin zone, like in the calculation of the density (3.3), is then approximated by a finite sum. The resulting error can be always reduced by increasing the density of the  $k$ -point mesh. It has been shown [110] that Monkhorst-Pack grids are particularly efficient. It corresponds to a grid of equidistant  $k$  points which is invariant under the point symmetries of the system. The calculation can be restricted to symmetrically inequivalent  $k$  points in the irreducible Brillouin zone and the number of  $k$  points is considerably decreased.

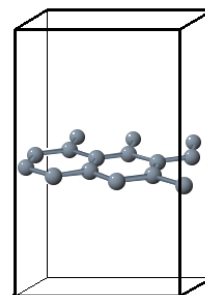


**Fig. 3.3:** Supercell

In order to deal with non-periodic systems in a plane-wave basis, one has to use a *supercell* which is periodically repeated in each direction. This cell has to be sufficiently large in order to avoid interactions between the artificial replicas. This point will be of particular interest in chapter 5, where the loss function for an isolated graphene sheet and the influence of the supercell size will be studied in detail.

<sup>7</sup>The spin quantum number  $\sigma$  shall be included in the band index.

### Cutoff Energy:

Additionally, one has to restrict the number of  $\mathbf{G}$  vectors used for the expansion of the wave function at a given  $\mathbf{k}$  point. As the coefficients  $C_{n,\mathbf{k}}(\mathbf{G})$  with small kinetic energy  $(\hbar^2/2m)|\mathbf{k} + \mathbf{G}|^2$  are typically more important, one truncates the summation at a certain cutoff energy  $E_{\text{cut}}$  and neglects contributions with high spatial frequency. Again, the error can be systematically decreased by increasing  $E_{\text{cut}}$ .

Of course, the value of  $E_{\text{cut}}$  that is necessary for a converged result strongly depends on the quantity of interest. For example, the ground-state energy converges very slowly, as every improvement in the description of the ground state lowers the total energy. Nevertheless, the optimal lattice parameters converge rather quickly with  $E_{\text{cut}}$  because the systematic error in the total energy due to the restricted basis set has only little influence if we compare two different geometries.

### 3.3.3 Response Functions

Accordingly, also the convergence properties of the independent-particle polarisability  $\chi^0$  have to be considered separately. The matrix elements (3.15) are found to converge typically with a cutoff well below  $E_{\text{cut}}$ . The corresponding number of plane waves is specified by `npwfn`. The dimension of the matrix  $\chi_{\mathbf{G}\mathbf{G}'}$  is given by `npwmat`. If only one  $\mathbf{G}$  vector is taken into account in this matrix, one neglects crystal LFE (see section 1.3.2).

Additionally, also the empty states are now needed in the evaluation of the sum (3.14) and a large number of bands `nbands` is necessary. Also the  $k$ -point sampling of the Brillouin zone needs to be much denser than in the case of a ground-state calculation. This can be understood by the fact that the spectrum contains much more information than an integrated quantity like the total energy.

### Shifted $k$ -point Grids

For finite momentum transfer  $\mathbf{q} = \mathbf{q}_r + \mathbf{G}$ , both the wave function at  $\mathbf{k}$  and  $\mathbf{k} + \mathbf{q}_r$  have to be known in order to calculate the matrix elements (3.15). This has two consequences: First, the choice of  $\mathbf{q}_r$  is restricted to a discrete set of vectors that can be represented as a difference of two  $k$  points in the chosen grid. Second, the summation in eq. (3.14) can be only simplified using symmetry operations that leave  $\mathbf{q}$  unchanged. Therefore, one generally has to perform a sum over the *full* Brillouin zone, not just the irreducible one.

This summation converges much faster, if we use a set of symmetrically inequivalent  $k$  points instead of the original Monkhorst-Pack grid. Indeed, we then have more inequivalent transitions for a given number of  $k$  points. The asymmetry can be easily introduced by a small shift  $\mathbf{s}$  of the equidistant Monkhorst-Pack grid along an arbitrary direction. The optimal length of the shift  $\mathbf{s}$  can be estimated by the following consideration:

If we apply all point-group symmetries to the shifted grid, one obtains a non-regular set of points which are distributed on small spheres of radius  $s$  around the  $k$  points of the unshifted grid. In fig. 3.4a, a section of a shifted  $k$ -point grid for a hexagonal system is shown (dots) together with all these symmetrically equivalent points (crosses). For an optimal shift  $\mathbf{s}$ , the latter should be homogeneously distributed. Requiring, that the

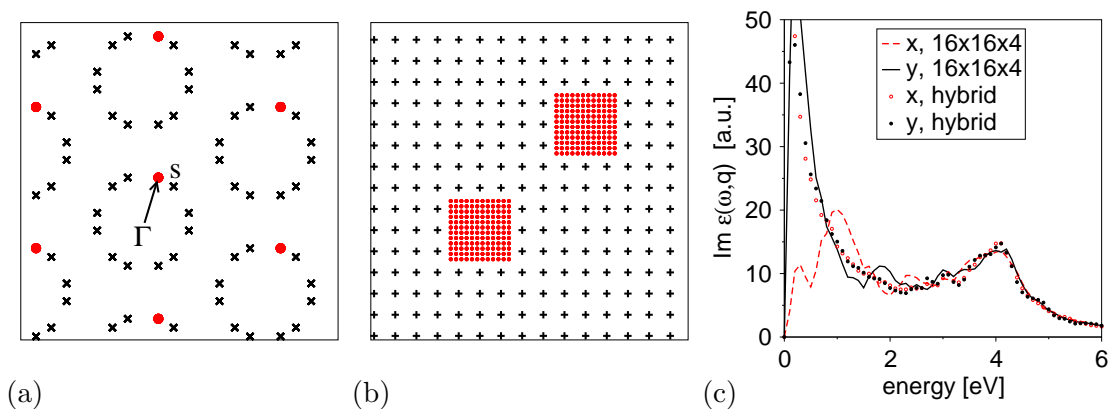


**Fig. 3.4:** (a) Section of a shifted  $k$ -point grid in Cartesian coordinates (red dots) and the symmetrically equivalent points (crosses). (b) Hybrid mesh in reciprocal Coordinates. The regions around the  $K$  and  $K'$  point in the Brillouin zone of Graphite are sampled with a dense grid. (c) Comparison of  $\text{Im } \varepsilon$  in Graphite (NLF) for a small momentum transfer  $q \rightarrow 0$  along the Cartesian  $x$  and  $y$  direction. At small energies, the shifted grid is not sufficiently dense (lines). The hybrid-grid calculation, instead, correctly reproduces the isotropic in-plane behaviour (dots)

distance between two circles is about three times the radius, we obtain as a possible shift

$$\mathbf{s}_{\text{hex}} \approx (1/8, 2/8, 1/4), \quad \mathbf{s}_{\text{fcc}} \approx (1/8, 2/8, 3/8). \quad (3.21)$$

The coordinates are given with respect to the primitive vectors of the  $k$ -point lattice, i. e., any vector  $(n, m, l)$  with integer coordinates corresponds to a  $k$  point of the unshifted grid. The second shift was determined analogously for a fcc structure like bulk silicon.

Although the results using shifted grids normally converge very rapidly, in certain situations the shift  $\mathbf{s}$  may introduce an artifact which only vanishes for very high sampling densities. Figure 3.4c shows such an example for Graphite. The in-plane directions of this hexagonal system are equivalent in the limit of small momentum transfers  $q \rightarrow 0$ . However, the calculation using an equidistant  $16 \times 16 \times 4$  mesh which is shifted by  $\mathbf{s} = (0.1, 0.3, 0.3)$  shows an artificial anisotropy at low energies for the dielectric constant  $\varepsilon$  (lines). It is due to the asymmetry of the shifted  $k$ -point grid and the artefact will vanish only for very dense grids.

### Other $k$ -point Grids

One can avoid this problem by several approaches: First, one can use a symmetric  $k$ -point grid. The resulting spectra do not show this artifact, but converge very slowly.

Second, one can use *random k-point sets*. As a further advantage, the convergence tests become very simple—one can iteratively refine the summation in eq. (3.14) by restarting the calculation with a new set of random  $k$  points adding them to the previous results.

Third, one can use an inhomogeneous *hybrid mesh* [111]. In graphite, the low-energy contributions originate only from transitions at the  $KH$  and  $K'H'$  lines in the Brillouin zone (compare with graphene, section 5.3.3). Accordingly, a dense sampling is only

necessary for a small part of the Brillouin zone and few bands. Figure 3.4b shows such a sampling with 2000  $k$  points that corresponds to a homogeneous grid of  $60 \times 60 \times 4$  points (14000 points).

I have extended the DP-code in order to use such non-equidistant  $k$  point meshes. To this end, one has to take into account the  $k$ -space volume associated with each  $k$  point in the evaluation of the integrals. Indeed, the artificial anisotropy shown in fig. 3.4c for the shifted grid is much less pronounced if we add a dense sampling along the  $KH$  and  $K'H'$  lines (see dots).

### Doubled $k$ -point Grid

All these methods can not be directly used for finite momentum transfers because both  $\mathbf{k}$  and  $\mathbf{k} + \mathbf{q}_r$  must be present in the  $k$ -point grid. This limitation can be easily overcome by using two different  $k$ -points sets which are shifted against each other by the vector  $\mathbf{q}_r$ . Of course, one has to re-calculate the  $k$ -point set for each different momentum transfer.

I have implemented this method in the DP-code in order to (i) use inhomogeneous  $k$ -point grids also at finite momentum transfer, (ii) calculate the loss spectra of silicon exactly at the experimental momentum transfer  $\mathbf{q}$ , and (iii) to study the influence of quadrupole effects in the optical limit  $q \rightarrow 0$ . In this case, the second  $k$  point is obtained within first-order  $\mathbf{k} \cdot \mathbf{p}$  perturbation theory and higher order terms, like the quadrupole contributions, are neglected in the standard implementation.

### 3.3.4 Example: Graphite

As example, we briefly consider the calculation of the AR-EELS loss function for bulk Graphite. The unit cell of the hexagonal lattice is spanned by the primitive vectors

$$\mathbf{a}_1 = a \mathbf{e}_x, \quad \mathbf{a}_2 = a \left( -\frac{1}{2} \mathbf{e}_x + \frac{\sqrt{3}}{2} \mathbf{e}_y \right), \quad \mathbf{a}_3 = c \mathbf{e}_z, \quad (3.22)$$

with the lattice constants  $a$  and  $c$ . It contains 4 carbon atoms at the positions

$$\boldsymbol{\tau}_1 = \mathbf{0}, \quad \boldsymbol{\tau}_2 = \frac{1}{3} \mathbf{a}_1 + \frac{2}{3} \mathbf{a}_2, \quad \boldsymbol{\tau}_3 = \frac{1}{2} \mathbf{a}_3, \quad \boldsymbol{\tau}_4 = \frac{2}{3} \mathbf{a}_1 + \frac{1}{3} \mathbf{a}_2 + \frac{1}{2} \mathbf{a}_3. \quad (3.23)$$

We use norm-conserving pseudopotentials of Troullier-Martins type [108] and include only the four valence electrons of the  $2s^2$  and the  $2p^2$  orbitals explicitly in our calculation. Thus, the unit cell contains 16 electrons in total.

### DFT

First, the ground state is calculated self-consistently in DFT-LDA using the ABINIT-code. The total energy of the system is converged with respect to the cutoff energy and the  $k$ -point grid. Then, we determine the optimal lattice constants  $a$  and  $c$  such that the calculated total energy is minimal and the stress on the cell vanishes (see fig. 3.5a for the parameters). The Kohn-Sham eigenfunctions and -energies for the following TDDFT calculation (kss) are evaluated in a non-self-consistent calculation.

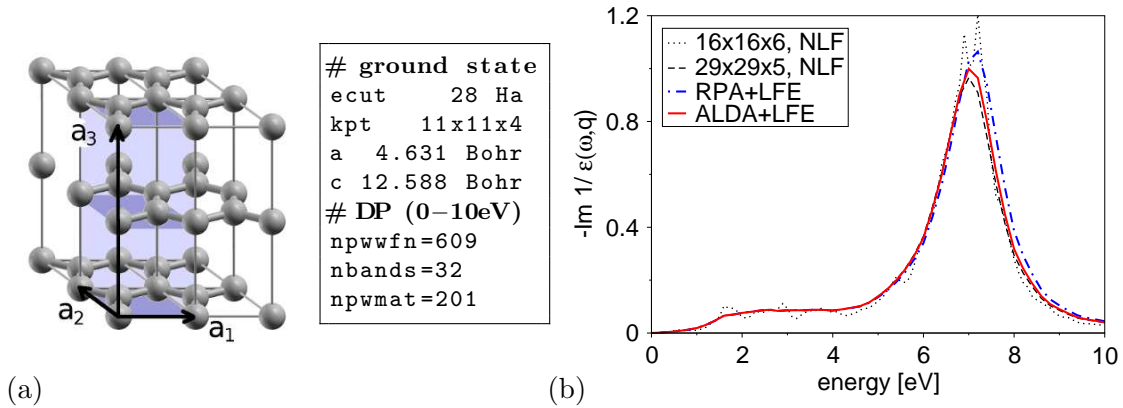


**Fig. 3.5:** (a) Unit cell (blue) and converged parameters for graphite (Bernal stacking). (b) Calculated loss function for graphite at small in-plane momentum  $q = 0.2 \text{ \AA}^{-1}$ . Two  $k$ -point samplings, calculations with and without LFE, and different TDDFT kernels  $f_{XC}$  are compared.

## TDDFT

Starting from this Kohn-Sham structure, the loss function is calculated with the DP-code (see section 3.2.4). We converge first the number of plane waves `npwfn`, then the number of bands `nbands`, and finally the dimension of the response matrix `npwmat` (see fig. 3.5a). Additionally, the  $k$ -point grid has to be tested by increasing the sampling density. In fig. 3.5b, we show the loss function of graphite for in-plane momentum transfer  $q = 0.2 \text{ \AA}^{-1}$ . It clearly shows the  $\pi$  plasmon peak which is observed at low energy losses. If the  $k$ -point grid is not dense enough, small additional oscillations appear (dotted line). LFE are found to shift the plasmon to higher energies (dash-dotted line) and the inclusion of exchange-correlation effects within the ALDA have the opposite effect. For increasing in-plane momentum transfer  $q$  up to  $1 \text{ \AA}^{-1}$ , we find that LFE become more and more important, while exchange-correlation effects are generally small and shift the plasmon energy by less than 0.2 eV towards lower energies within ALDA [112]. In this thesis, we will therefore mainly restrict to the random phase approximation including crystal local-field effects. In principle, this protocol has to be repeated for each material, quantity of interest, and parameter range (energy  $\omega$ , momentum transfer  $q$ ).

## Conclusions

In this chapter, the many-body problem has been addressed in the framework of (time-dependent) density-functional theory. Instead of solving the many-body Schrödinger equation, the ground-state properties can be obtained from a minimisation of a density functional for the total energy. Using the density as basic variable results in an enormous computational simplification compared to approaches working directly with the high-dimensional many-body wave function. The unknown density functional is constructed by mapping the interacting system to a fictitious system of independent particles, the so-called Kohn-Sham system. The latter constitutes an effective single-particle problem

which is much easier to solve than the many-body problem of interdependent particles. This mapping is exact and results in a set of self-consistent equations—the Kohn-Sham equations—which can be solved numerically by iteration.

Excitation properties, like the linear response to an external perturbation, can be accessed in the framework of time-dependent density-functional theory. It is based on the same ideas as static density-functional theory, but the time evolution of the density is formally given by the stationary solution of a quantum-mechanical action functional and can be calculated from the time-dependent Kohn-Sham equations. Within this formalism, the microscopic density-response function  $\chi(\mathbf{q}, \mathbf{q}', \omega)$ , and thus the mixed-dynamic form factor  $S(\mathbf{q}, \mathbf{q}', \omega)$ , can be obtained in a very efficient way: First, the independent-particle polarisability  $\chi^0$  of the Kohn-Sham particles is calculated and second, one solves the Dyson equation for the response  $\chi$  of the interacting system.

In principle, no parameters are involved in the theory. In practice, however, one has to select an approximation for the exchange-correlation potential and often pseudopotentials are used to reduce the size of the problem. In this thesis, the plane-wave codes ABINIT and DP are used for the determination of the ground-state and the excited-state properties, respectively. We have briefly discussed the basic workflow of the numerical calculations including the necessary convergence tests.

Experience shows that the loss function of solids and molecules is usually very accurately described within the TDLDA or even the RPA approximation. Especially in graphite and other carbon systems, exchange-correlation effects are often negligible for the loss spectrum because quasiparticle corrections and electron-hole effects tend to cancel each other. We will see in the following chapters that crystal local-field effects are very important, though. They play an important role in low-dimensional systems, where the electrons are confined in one or more directions (see chapter 5 and 6). And even in solids, they can give rise to important changes of the loss function with varying momentum transfer (see chapter 4).

Together with the results from the previous chapter 2, we are now able to calculate the energy-loss probability for inelastic electron scattering on solids, molecules, and nanostructures starting from first principles. This allows us to make a direct comparison with experimental results and even the prediction of new effects. We will see in the following chapters that *ab-initio* calculations are of great use for the detailed analysis and the explanation of experimental results.

**Part II**

**Developments and Applications**



## 4 Anisotropy of the Mixed Dynamic Form Factor

As we have seen in chapter 2, the momentum-resolved and frequency-dependent mixed dynamic form factor  $S(\mathbf{q}, \mathbf{q}', \omega)$  (MDFF) is a fundamental quantity in the description of scattering experiments. The diagonal part  $S(\mathbf{q}, \mathbf{q}, \omega)$  is proportional to the loss function  $-\text{Im} \varepsilon^{-1}(\mathbf{q}, \mathbf{q}, \omega)$  of the material and can be directly accessed by AR-EELS measurements. These are particularly efficient for moderate momentum transfer, i.e., when  $\mathbf{q}$  is shorter than a reciprocal-lattice vector, and as long as multiple scattering effects remain secondary. Off-diagonal elements are only included in the case of a focussed electron beam and correspond to interference terms between two incoming plane-waves. Even in the simplest case of a two-beam scattering experiment (see section 2.3.1), it is difficult to extract them from the measurements. Therefore, only little is known about the behaviour of the MDFF at large momentum transfers and its off-diagonal part.

Only recently, modern synchrotron radiation sources have opened the way to study electronic excitations at large momentum transfer using inelastic X-ray scattering (IXS). New phenomena can be observed in this range, such as a periodic plasmon dispersion in magnesium diboride  $\text{MgB}_2$  [113], plasmon-band effects in silicon [114], or zone-boundary collective states in aluminium [115, 116] and sodium [115–119]. Off-diagonal elements of the MDFF have been measured using coherent IXS [74].

In this chapter, we will perform *ab-initio* calculations to study the MDFF of crystals for large momentum transfers. We predict an angular anomaly in the momentum dependence of the dynamic structure factor  $S(\mathbf{q}, \mathbf{q}, \omega)$  which should also be important for the theory of spatially resolved EELS. In section 4.2 the effect is explained by a discussion of the crystal local-field effects (LFE) which become increasingly important for large  $\mathbf{q}$  and are closely connected to the off-diagonal elements of the mixed dynamic form factor. Finally, we consider both anisotropic (graphite) and isotropic systems (silicon) and verify our findings by means of IXS experiments.

### 4.1 Discontinuity in the MDFF: an Overview of our Results

*What do we mean by ‘angular anomaly’ or ‘discontinuity’ of the dynamic form factor?* For a momentum transfer close to certain reciprocal-lattice vectors  $\mathbf{Q}$  of the crystal, we observe drastic changes in the loss spectrum  $S(\mathbf{q}, \omega)$  upon small variations in  $\mathbf{q} = \mathbf{Q} + \boldsymbol{\eta}$  (see fig. 4.1). For small  $\eta \rightarrow 0$ , the loss function is found to depend exclusively on the direction of the deviation  $\boldsymbol{\eta}$ , not its modulus. This is similar to the well-known behaviour of  $S(\mathbf{q}, \omega)$  in the optical limit  $q \rightarrow 0$  for anisotropic systems, but occurs at

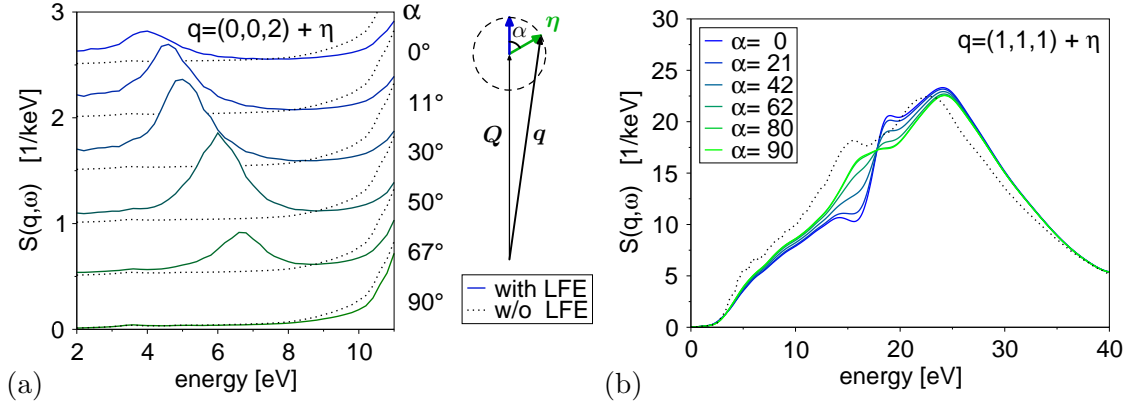


**Fig. 4.1:** Prediction of anisotropic behaviour of the dynamic structure factor  $S(\mathbf{q}, \omega)$  in the vicinity of a Bragg reflection (a)  $\mathbf{Q} = (0, 0, 2)$  for graphite and (b)  $\mathbf{Q} = (1, 1, 1)$  for silicon (see text). Spectra in (a) are shifted along the ordinate for better visibility.

large momentum transfers. Additionally, the effect has been predicted by our TDDFT calculations both in graphite which is anisotropic, but also in silicon which is an isotropic material.

### Graphite

In Figure 4.1a, the loss function of graphite is shown for different momentum transfers  $\mathbf{q} = \mathbf{Q} + \boldsymbol{\eta}$  close to the  $\mathbf{Q} = (0, 0, 2)$  Bragg reflection. The direction of the deviation  $\boldsymbol{\eta}$  is changed, but not its modulus  $\eta = 0.001 \text{ \AA}^{-1}$ . In experimental practice one usually assumes that such a tiny variation in the momentum transfer  $\mathbf{q}$  does not influence the corresponding loss spectrum at all.<sup>1</sup> Contrarily, our calculations show a strong effect (solid lines). Depending on the angle  $\alpha$  between the Bragg momentum  $\mathbf{Q}$  and the deviation  $\boldsymbol{\eta}$ , the loss function changes considerably. The actual modulus of the deviation  $\boldsymbol{\eta}$  is not very important as long as  $\eta < 0.1 \text{ \AA}^{-1}$ . Neglecting crystal local-field effects in our calculations, this discontinuous behaviour disappears (dotted lines, same for all  $\alpha$ ).

### Silicon

The question arises if the angular anomaly can also appear in isotropic materials like bulk silicon. Interestingly, our *ab-initio* calculations predict a similar effect also for this system (see fig 4.1b). In the vicinity of the  $\mathbf{Q} = (1, 1, 1)$  reflection, the loss function depends strongly on the direction of the tiny deviation  $\boldsymbol{\eta}$ : it shows a Fano resonance [114] at  $\alpha = 0^\circ$ , but not at  $\alpha = 90^\circ$  (solid lines). Neglecting crystal local-field effects in our calculations, both the Fano resonance and the anomaly disappears (dotted line, same for all  $\alpha$ ).

<sup>1</sup>To measure a loss spectrum close to a Bragg reflection one often adds a small deviation in  $\mathbf{q}$  in order to avoid the high intensity contributions from elastic scattering.

## Spatially-Resolved EELS

We can find a similar behaviour for the off-diagonal elements  $S_{\mathbf{G}\mathbf{G}'}(\mathbf{q}_r, \omega)$  of the mixed dynamic form factor. This is of particular importance for the calculation of SR-EEL spectra using eq. (2.32). Under channelling conditions, one has to integrate over a plane in reciprocal space that is close to several Bragg-reflections. An understanding of the angular dependence of the MDF is then relevant for the theory of SR-EELS in crystals.

By our predictions, several questions arise which shall be answered during the course of this chapter: *What is the origin of the angular anomaly? Why does it also appear in isotropic materials? Can we find a simple model for the angular dependence? Which Bragg reflections show this behaviour? Which excitation can be attributed to the strong peak in graphite? Can we understand the origin of the Fano resonance? What is the difference to multiple scattering? Can the effect be observed in experiment?* In order to answer these questions a detailed theoretical discussion of the dielectric properties of crystals is necessary and will be given in the following section.

## 4.2 Dielectric Properties of Crystals

In this section, the predicted anomaly will be explained in terms of an interplay between anisotropy and crystal local-field effects (LFE). The latter originate from the periodic modulation of the electron density in the crystal. The influence of this density modulation on the electronic excitation spectrum is best understood in a nearly-free-electron picture by comparing excitations in a homogeneous electron gas (HEG) and in a crystal.

### 4.2.1 Excitations in Crystals

Figure 4.2a (left panel) shows the well known electron-hole excitations in the homogeneous electron gas (shaded region) and the corresponding plasmon excitation (red line). In a homogeneous system, a plasmon is a longitudinal charge oscillation in the form of a plane wave with momentum  $\mathbf{q}$  and energy  $\omega(q)$  that depends quadratically on  $q$ . It has an infinite lifetime at small momentum transfers below the critical momentum  $q_c$ . For large momenta  $q > q_c$ , the plasmon decays rapidly by exciting electron-hole pairs.

In a crystal, this image is complicated by Umklapp processes and the crystal local-field effects: Adding a weak periodic crystal potential will couple excitations of momentum  $\mathbf{q}$  and  $\mathbf{q} + \mathbf{G}$  via Umklapp processes and Bragg scattering ( $\mathbf{G}$  denotes a reciprocal lattice vector of the crystal). Both electrons and plasmons become Bloch waves and, in a first approximation, the excitation spectrum of the crystal can be obtained by folding the free-electron excitations back into the first Brillouin zone (fig. 4.2a, right panel). This has three important consequences: First, interband transitions to bands from higher Brillouin zones become possible via Umklapp effects and contribute to the damping of the plasmon at low momentum  $q < q_c$  (1). They are responsible for the finite lifetime of the plasmon in solids even at small momentum  $q$ . Second, crystal local-field effects

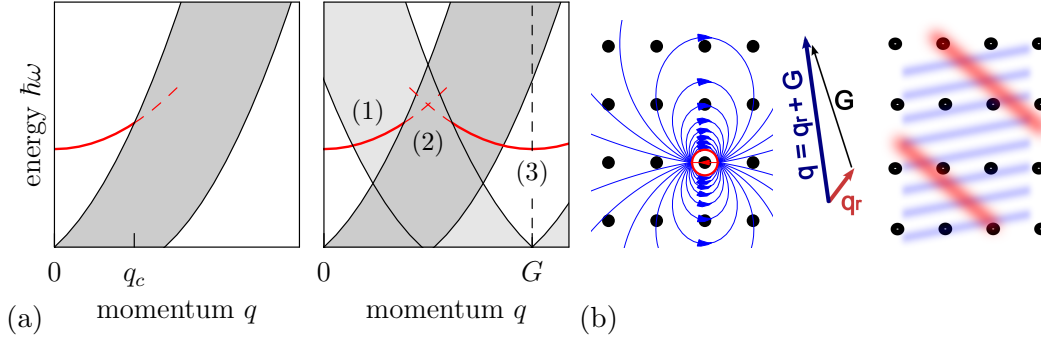


**Fig. 4.2:** (a) Excitation spectrum of free electrons (left) and electrons in a weak periodic crystal potential (right). Shaded regions indicate electron-hole excitations, thick, red lines the plasmon dispersion (adapted from [120]). (b) Visualisation of crystal local-field effects as induced dipoles (left) or Bragg reflected waves (right). See text.

become more and more important with increasing strength of the crystal potential. They couple excitations with momentum  $\mathbf{q}$  and  $\mathbf{q} + \mathbf{G}$  from different Brillouin zones. When this coupling is strong, the plasmon dispersion can develop several plasmon bands [120]. In analogy to the electron bandstructure, an energy splitting at the Brillouin zone boundary at  $\mathbf{q} = \mathbf{G}/2$  can occur (2). Finally, the plasmon with small momentum  $q < q_c$  may reappear in higher Brillouin zones (3) at momentum  $\mathbf{q} + \mathbf{G}$  [113, 114]. This will be the key for understanding the discontinuity of the loss spectra presented in Fig. 4.1.

#### 4.2.2 Crystal Local-Field Effects

For a better understanding of the plasmon bands in crystals, we recall two physical pictures for LFE [121] and discuss the relation with the dielectric matrix  $\epsilon_{\mathbf{G}\mathbf{G}'}$ :

**LFE in real space:** Using a purely classical picture, a crystal may be approximated as a periodic system of dipoles [43]. A given external perturbation will polarise each dipole (see fig. 4.2b) and therefore induce additional Hartree potentials—these are the crystal local fields. They itself act as a perturbation to the other dipoles and hence contribute to the total response of the solid in a self-consistent manner. Formally, this process is described by the Dyson equation (1.11) which can be expanded as

$$\chi(\mathbf{r}, \mathbf{r}') = \pi(\mathbf{r}, \mathbf{r}') + \int d\mathbf{r}_1 d\mathbf{r}_2 \pi(\mathbf{r}, \mathbf{r}_1) v(\mathbf{r}_1, \mathbf{r}_2) \pi(\mathbf{r}_2, \mathbf{r}') + \dots \quad (4.1)$$

The polarisability  $\pi(\mathbf{r}_2, \mathbf{r}')$  specifies the induced charge at the point  $\mathbf{r}_2$  due to the perturbing field at point  $\mathbf{r}'$ . This charge will induce an additional field that propagates in free space and is given by the Coulomb potential  $v(\mathbf{r}_1, \mathbf{r}_2)$ . This local field, in turn, will contribute to the polarisation of the medium and so on. The total response of the system to an external field is given by the susceptibility  $\chi$  which contains the infinite sum of all possible sequences of polarisation and propagation up to infinite order.

**LFE in reciprocal space:** Alternatively, one can understand LFE in a plane-wave picture [122]. In reciprocal space, eq. (4.1) reads (we omit the dependence on the reduced momentum  $\mathbf{q}_r$  and the energy  $\hbar\omega$ )

$$\chi_{\mathbf{G}\mathbf{G}'} = \pi_{\mathbf{G}\mathbf{G}'} + \sum_{\mathbf{G}_1} \pi_{\mathbf{G}\mathbf{G}_1} v_{\mathbf{G}_1} \pi_{\mathbf{G}_1\mathbf{G}'} + \dots, \quad v_{\mathbf{G}} = \frac{e^2}{\varepsilon_0} \frac{1}{(\mathbf{q}_r + \mathbf{G})^2}. \quad (4.2)$$

Note that the Coulomb potential becomes diagonal and the response function is a matrix in the reciprocal lattice vectors  $\mathbf{G}$  and  $\mathbf{G}'$  due to the translational symmetry of the crystal (see appendix A.2.2). Physically, LFE can now be understood as internal Bragg scattering which couples all modes with the same reduced momentum transfer  $\mathbf{q}_r$  (see fig. 4.2b): As  $\pi$  is a matrix, an external potential with momentum  $\mathbf{q}_r + \mathbf{G}'$  can induce spatial charge fluctuations, whose momentum  $\mathbf{q}_r + \mathbf{G}_1$  differs by any reciprocal-lattice vector, and to which the system will also respond. The corresponding induced fields  $v_{\mathbf{G}_1} \pi_{\mathbf{G}_1\mathbf{G}'}$  can be understood as Bragg-reflected modes that constitute the LFE. Usually they have a very short wavelength and can not leave the crystal as long as the dispersion relation in vacuum  $\omega = cq$  is not fulfilled. Nevertheless, they can be again Bragg scattered and thus contribute to the total response of the crystal with momentum  $\mathbf{q}_r + \mathbf{G}$ .

## Dielectric Matrix

In a homogeneous medium, Bragg scattering does not take place and all response functions are diagonal, i. e.,  $\pi_{\mathbf{G}\mathbf{G}'} = \pi(\mathbf{q}_r + \mathbf{G})\delta_{\mathbf{G}\mathbf{G}'}$ . The Dyson eq. (4.2) reduces to a simple scalar equation which can be solved analytically. In particular, the plasmon will be given by the zeros of the dielectric function  $\varepsilon(\mathbf{q}, \omega) = 1 - v(\mathbf{q})\pi(\mathbf{q}, \omega)$ . Off-diagonal elements  $\pi_{\mathbf{G}\mathbf{G}'}$  are only present in crystals and are responsible for the LFE. Plasmon modes are then defined by  $\det \varepsilon_{\mathbf{G}\mathbf{G}'}(\mathbf{q}_r, \omega) = 0$  leading to several plasmon bands for the same reduced momentum transfer  $\mathbf{q}_r$ . As a consequence, a plasmon is no longer a single plane-wave oscillation inside a crystal, but should be considered as a Bloch wave.

### 4.2.3 Effective Dielectric Function

As we have seen in section 2.5.2, the mixed dynamic form factor  $S(\mathbf{q}, \mathbf{q}'; \omega)$  is directly related to the inverse dielectric matrix  $\varepsilon_{\mathbf{G}\mathbf{G}'}^{-1}(\mathbf{q}_r, \omega)$ . In particular, the loss function for plane-wave scattering is given by the diagonal element  $\mathbf{G} = \mathbf{G}'$  [see eq. (2.16)]. One usually introduces an effective scalar dielectric function  $\varepsilon_M$  corresponding to an effective homogeneous material with the same loss function  $-\text{Im} 1/\varepsilon_M$  by<sup>2</sup> [49, 50]

$$\varepsilon_M(\mathbf{q}_r + \mathbf{G}, \omega) \equiv \frac{1}{\varepsilon_{\mathbf{G}\mathbf{G}}^{-1}(\mathbf{q}_r, \omega)} = \varepsilon_{\mathbf{G}\mathbf{G}} - \sum_{\mathbf{K}, \mathbf{K}' \neq \mathbf{G}} \varepsilon_{\mathbf{G}\mathbf{K}} M_{\mathbf{K}\mathbf{K}'}^{-1} \varepsilon_{\mathbf{K}'\mathbf{G}}. \quad (4.3)$$

It is given by the diagonal element  $\varepsilon_{\mathbf{G}\mathbf{G}}$  of the dielectric matrix plus a correction term that constitutes the LFE. It depends on the off-diagonal elements  $\varepsilon_{\mathbf{G}\mathbf{K}}$  and the submatrix  $M_{\mathbf{K}\mathbf{K}'}$  of the dielectric matrix  $\varepsilon_{\mathbf{G}\mathbf{G}'}$  which does not contain the  $\mathbf{G}$ th row and column.

<sup>2</sup>For  $\mathbf{G} = \mathbf{0}$ , we obtain the definition of the spatially averaged macroscopic dielectric constant  $\varepsilon_M$ .

## Nearly-Free-Electron Model

For weak crystal potential  $U$ , one can expand the elements of dielectric matrix  $\varepsilon_{\mathbf{G}\mathbf{G}'}$  in terms of the Fourier coefficients  $U_{\mathbf{G}}$  using second-order perturbation theory [50, 123]. To lowest order, all diagonal elements are independent of  $U_{\mathbf{G}}$ , and all off-diagonal elements are linear in  $U_{\mathbf{G}}$ . If we keep only terms to second order in  $U_{\mathbf{G}}$ , eq. (4.3) becomes:<sup>3</sup>

$$\varepsilon_M(\mathbf{q}_r + \mathbf{G}, \omega) \approx \varepsilon_{\mathbf{G}\mathbf{G}} - \sum_{\mathbf{K} \neq \mathbf{G}} \frac{\varepsilon_{\mathbf{G}\mathbf{K}} \varepsilon_{\mathbf{K}\mathbf{G}}}{\varepsilon_{\mathbf{K}\mathbf{K}}}. \quad (4.4)$$

It should be noted that this expansion is only applicable for energies  $\hbar\omega$  that are large compared to the gap in semiconductors [123]. If one of the coupling elements  $\varepsilon_{\mathbf{G}\mathbf{K}}$  is dominant, the summation in eq. (4.4) reduces to a single term. If the same coupling element is also dominant for  $\varepsilon_M(\mathbf{q}_r + \mathbf{K})$ , the loss function can be rewritten as

$$\frac{1}{\varepsilon_M(\mathbf{q}_r + \mathbf{G})} \approx \frac{1}{\varepsilon_{\mathbf{G}\mathbf{G}}} + f \frac{1}{\varepsilon_M(\mathbf{q}_r + \mathbf{K})}, \quad f = \frac{\varepsilon_{\mathbf{G}\mathbf{K}} \varepsilon_{\mathbf{K}\mathbf{G}}}{\varepsilon_{\mathbf{G}\mathbf{G}}^2} \quad (4.5)$$

This equation is fundamental for the explanation of the angular anomaly. The first term corresponds to the zero-order approximation in the crystal potential  $U$  where LFE are completely ignored and we have  $\varepsilon_M^{\text{NLF}} = \varepsilon_{\mathbf{G}\mathbf{G}}$  [see eq. (1.16)]. The last term is a second-order correction and leads to the reappearance of the loss function  $1/\varepsilon_M(\mathbf{q}_r + \mathbf{K})$  from a *different* Brillouin zone. The weighting factor  $f$  is determined by the off-diagonal elements  $\varepsilon_{\mathbf{G}\mathbf{K}}$ . For example, the periodic plasmon dispersion in magnesium diboride  $\text{MgB}_2$  has been explained by the reappearance of the spectrum from the first Brillouin zone  $\mathbf{K} = \mathbf{0}$  for momentum transfers  $\mathbf{q}_r + \mathbf{G}$  at higher Brillouin zones [113].

## Two-Plasmon-Band Model

A very similar equation can be obtained within the two-plasmon-band model [120, 124, 125]. But in contrast to eq. (4.5), the resulting expression is in principle exact. Starting point is the bandstructure picture of the electronic excitations in crystals (see section 4.2.1). In principle, the evaluation of  $\det \varepsilon_{\mathbf{G}\mathbf{G}'}(\mathbf{q}_r, \omega) = 0$  leads to infinitely many plasmon bands. However, as in any other bandstructure calculation, one is usually interested in a limited number of interacting modes. For instance, one only needs two bands in order to describe band-splitting effects at the boundary of the Brillouin zone. As in the derivation of eq. (4.5), we assume that the excitation spectrum at a given momentum  $\mathbf{q} = \mathbf{q}_r + \mathbf{G}$  is mainly coupled to excitations at  $\mathbf{q}_r + \mathbf{K}$ , where  $\mathbf{K} \neq \mathbf{G}$ . These two modes can be described by an effective  $2 \times 2$  matrix  $\tilde{\varepsilon}$  which corresponds to a fictitious material with two plasmon bands. Formally,  $\tilde{\varepsilon}$  is obtained by a *downfolding* of the dielectric matrix  $\varepsilon_{\mathbf{G}\mathbf{G}'}$ . For a given  $\mathbf{G}$  and  $\mathbf{K}$ , we divide  $\varepsilon$  and  $\varepsilon^{-1}$  into block

<sup>3</sup>In zeroth order,  $\varepsilon$  becomes diagonal. Thus, the two off-diagonal elements must be evaluated to first order and the submatrix  $M$  has to be evaluated to zeroth order which gives  $M_{\mathbf{K}\mathbf{K}'}^{-1} \approx 1/\varepsilon_{\mathbf{K}\mathbf{K}} \delta_{\mathbf{K}\mathbf{K}'}$ .

matrices such that

$$\varepsilon = \begin{pmatrix} P & Q \\ R & S \end{pmatrix}, \quad \varepsilon^{-1} = \begin{pmatrix} A & B \\ C & D \end{pmatrix}, \quad P = \begin{pmatrix} \varepsilon_{GG} & \varepsilon_{GK} \\ \varepsilon_{KG} & \varepsilon_{KK} \end{pmatrix}, \quad A = \begin{pmatrix} \varepsilon_{GG}^{-1} & \varepsilon_{GK}^{-1} \\ \varepsilon_{KG}^{-1} & \varepsilon_{KK}^{-1} \end{pmatrix}. \quad (4.6)$$

The remaining blocks are defined accordingly. The effective dielectric matrix

$$\tilde{\varepsilon} = \begin{pmatrix} \tilde{\varepsilon}_{GG} & \tilde{\varepsilon}_{GK} \\ \tilde{\varepsilon}_{KG} & \tilde{\varepsilon}_{KK} \end{pmatrix} \equiv A^{-1} \stackrel{(A.81)}{=} P - QS^{-1}R, \quad (4.7)$$

can be understood as a generalisation of the scalar effective dielectric function  $\varepsilon_M$  defined by eq. (4.3). The first term on the right-hand side is simply the corresponding  $2 \times 2$  block of the dielectric matrix  $\varepsilon$ . The second term corresponds to the local-field corrections due to modes different from  $\mathbf{K}$  and  $\mathbf{G}$ . We can hence think of a separation of LFE in modes taken into account explicitly and implicitly. This is particular useful when the corrections due to the second term are small and can be thus approximated using perturbation theory. Such a model dielectric function has been successfully applied to study, e. g., the zone-boundary collective states [116] and the plasmon-band splitting [126].

By construction, the loss function  $-\text{Im} \varepsilon_{GG}^{-1}$  is now given by the corresponding diagonal element of  $\tilde{\varepsilon}^{-1}$ . Inverting the effective  $2 \times 2$  matrix  $\tilde{\varepsilon}$ , we finally obtain the *exact* result:

$$\tilde{\varepsilon}_{GG}^{-1}(\mathbf{q}_r, \omega) = \frac{1}{\tilde{\varepsilon}_{GG}} + \tilde{f} \tilde{\varepsilon}_{KK}^{-1}, \quad \tilde{f} = \frac{\tilde{\varepsilon}_{GK} \tilde{\varepsilon}_{KG}}{\tilde{\varepsilon}_{GG}^2}. \quad (4.8)$$

In particular, we formally recover our previous result from eq. (4.5) if we neglect the second term in eq. (4.7), i. e., by replacing  $\tilde{\varepsilon}$  with  $\tilde{\varepsilon}^{\text{NLF}} = P$ . The formalism can be easily extended for an arbitrary number of plasmon bands. In particular, the macroscopic dielectric function (4.3) is recovered if we consider a single plasmon band, i. e., a  $1 \times 1$  matrix.

#### 4.2.4 Model for the Anisotropy

Let us now come back to the discontinuous behaviour of the loss function for momentum transfers close to certain Bragg reflections. In fig. 4.1 we have noticed that the effect only appears, when LFE are taken into account. In principle, all  $\mathbf{G}$  modes are then coupled by internal Bragg reflection and contribute to the total response of the system.

*But which of these modes are the most important ones for the anisotropy?* In RPA, the dielectric matrix  $\varepsilon = \hat{1} - v\chi^0$  is directly related to the independent-particle polarisability  $\chi^0$  that is given by eq. (3.14). For vanishing reduced momentum transfers  $\mathbf{q}_r = \boldsymbol{\eta} \rightarrow \mathbf{0}$ , the matrix element  $\chi_{GG'}^0$  for non-zero reciprocal lattice vectors is clearly independent of  $\boldsymbol{\eta}$  because the exponential  $e^{i(\boldsymbol{\eta}+\mathbf{G})r} \approx e^{i\mathbf{G}r}$  is unchanged. Only the head  $\chi_{00}^0$  and the wing elements  $\chi_{0\mathbf{G}}^0$  or  $\chi_{\mathbf{G}0}^0$  vary with  $\boldsymbol{\eta}$ . The anisotropic behaviour of the loss function at large momentum transfers must be due to the long-wavelength mode.

It is therefore reasonable to separate the LFE into contributions from the anisotropic  $\mathbf{K} = \mathbf{0}$  mode and contributions from the remaining microscopic modes. Within the two-plasmon-band model, the former are explicitly taken into account by the effective  $2 \times 2$

matrix  $\tilde{\varepsilon}$  which contains both the  $\mathbf{0}$  and the  $\mathbf{Q}$  mode if we are interested in momentum transfers close to the Bragg reflection  $\mathbf{Q}$ . The loss function is then given by eq. (4.8) as

$$-\text{Im} \tilde{\varepsilon}_{\mathbf{Q}\mathbf{Q}}^{-1}(\boldsymbol{\eta}, \omega) = -\text{Im} \frac{1}{\tilde{\varepsilon}_{\mathbf{Q}\mathbf{Q}}} - \text{Im} \tilde{f} \tilde{\varepsilon}_{\mathbf{0}\mathbf{0}}^{-1}, \quad \tilde{f} = \frac{\tilde{\varepsilon}_{\mathbf{Q}\mathbf{0}} \tilde{\varepsilon}_{\mathbf{0}\mathbf{Q}}}{\tilde{\varepsilon}_{\mathbf{Q}\mathbf{Q}}^2}. \quad (4.9)$$

The different terms can be interpreted as follows (see also fig. 4.3):

$\tilde{\varepsilon}_{\mathbf{Q}\mathbf{Q}}^{-1}$ : Its imaginary part gives the loss function at  $\mathbf{q} = \boldsymbol{\eta} + \mathbf{Q}$  including all LFE.

$\frac{1}{\tilde{\varepsilon}_{\mathbf{Q}\mathbf{Q}}}$ : Its imaginary part corresponds to the loss function at the same  $\mathbf{q}$  taking into account all LFE *except* the  $\mathbf{0}$  mode. This can be seen from eq. (4.7), which reads

$$\tilde{\varepsilon}_{\mathbf{Q}\mathbf{Q}} = \varepsilon_{\mathbf{Q}\mathbf{Q}} - \sum_{L, L' \notin \{\mathbf{0}, \mathbf{Q}\}} \varepsilon_{\mathbf{Q}L} S_{LL'}^{-1} \varepsilon_{L'\mathbf{Q}}$$

and shows that  $\tilde{\varepsilon}_{\mathbf{Q}\mathbf{Q}}$  does not include any of the wing elements  $\varepsilon_{\mathbf{0}\mathbf{G}}$ . Consequently, it must be also independent of the direction of  $\boldsymbol{\eta}$ .

$\tilde{\varepsilon}_{\mathbf{0}\mathbf{0}}^{-1}$ : Its imaginary part gives the loss function for  $\mathbf{q} = \boldsymbol{\eta}$  inside the *first* Brillouin zone including all LFE. It is anisotropic in non-cubic systems and generally depends on the direction of  $\boldsymbol{\eta}$ . Note that also its real part may contribute when  $\tilde{f}$  is complex.

$\tilde{\varepsilon}_{\mathbf{Q}\mathbf{0}}$ : The two off-diagonal terms strongly depend on  $\boldsymbol{\eta}$  and will therefore determine the anisotropy of the coupling factor  $\tilde{f}$  in eq. (4.9).

In conclusion, we have shown that the origin of the anisotropy in the loss function at large momentum transfers is twofold: First, the spectrum from the first Brillouin zone may reappear. It depends on the direction of  $\boldsymbol{\eta}$  if the material is anisotropic. Second, the coupling factor  $\tilde{f}$  determines the intensity of this reappearing spectrum. It depends on the off-diagonal elements  $\tilde{\varepsilon}_{\mathbf{Q}\mathbf{0}}$  which are themselves anisotropic. Although eq. (4.9) seems to be very simple, it gives rise to a rather complicated behaviour of the loss function at large momentum transfers. In the following, we will discuss several examples in graphite and silicon focussing on two effects that were, to our knowledge, never predicted before.

### 4.3 Graphite

In order to confirm our explanation of the anisotropy, we have performed RPA calculations of the full microscopic dielectric function  $\varepsilon_{\mathbf{G}\mathbf{G}'}(\boldsymbol{\eta}, \omega)$  for graphite. The numerical details have been described earlier in section 3.3.4. We considered 6 different directions for the reduced momentum transfer  $\boldsymbol{\eta}$ : starting from the  $z$ -direction (along the  $c$ -axis), the vector  $\boldsymbol{\eta}$  is turned by an angle<sup>4</sup>  $\beta = 0, 20, 40, 60, 80,$  and  $90^\circ$  towards  $\mathbf{b}_1$  ( $\Gamma M$  direction). Its modulus is kept constant at  $\eta = 0.001 \text{ \AA}^{-1}$ . For a given  $\mathbf{Q}$ , we construct the block matrices of eq. (4.6) and calculate the effective dielectric function  $\tilde{\varepsilon}$  and  $\tilde{\varepsilon}^{\text{NLF}}$ . The latter is simply given by the  $2 \times 2$  submatrix of  $\varepsilon$ , i. e.,  $\tilde{\varepsilon}^{\text{NLF}} = P = \begin{pmatrix} \varepsilon_{\mathbf{Q}\mathbf{Q}} & \varepsilon_{\mathbf{Q}\mathbf{0}} \\ \varepsilon_{\mathbf{0}\mathbf{Q}} & \varepsilon_{\mathbf{0}\mathbf{0}} \end{pmatrix}$ , thus neglecting local-field contributions from any mode different from  $\mathbf{Q}$  and  $\mathbf{0}$ . We will see in the following that it often behaves very similarly to the exact response  $\tilde{\varepsilon}$ .

<sup>4</sup> Instead of  $\beta$ , we usually use the angle  $\alpha$  between  $\boldsymbol{\eta}$  and  $\mathbf{Q}$  to indicate the direction of  $\boldsymbol{\eta}$  (see fig. 4.1).

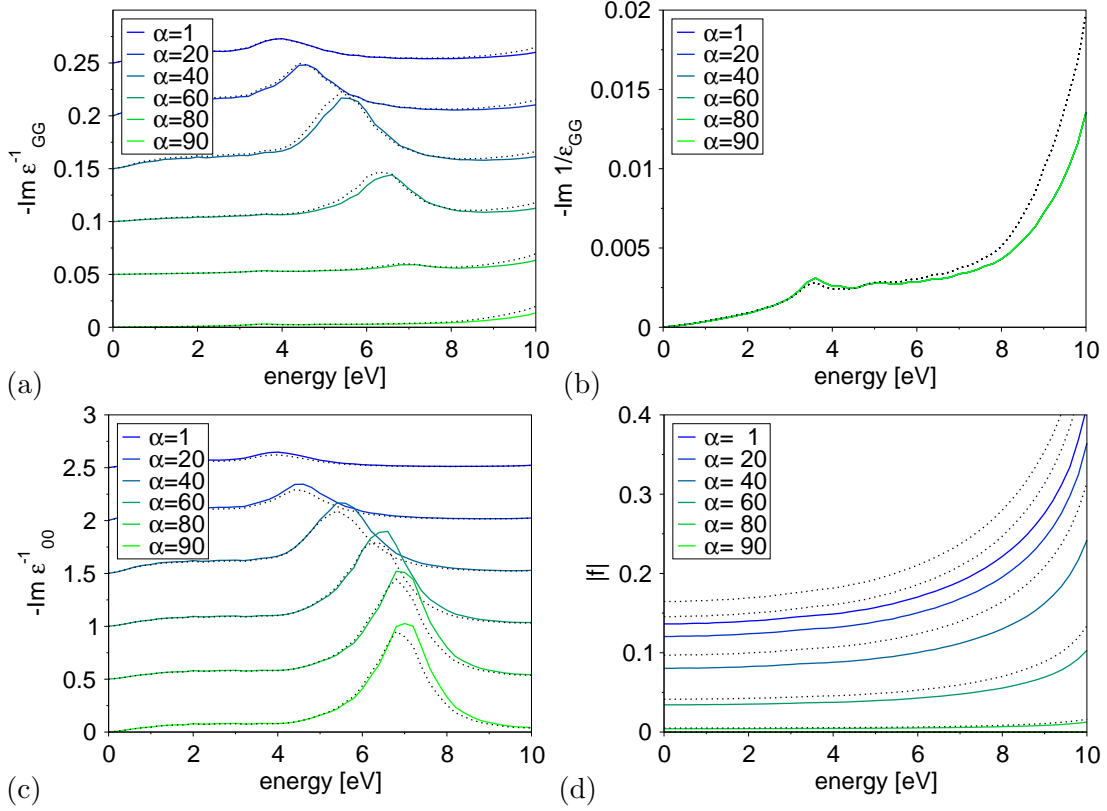


**Fig. 4.3:** Analysis of the discontinuity in graphite close to the Bragg reflection  $\mathbf{Q} = (0, 0, 2)$ . We have calculated (a) the loss function  $-\text{Im} \varepsilon_{\mathbf{Q}\mathbf{Q}}^{-1}$  as in fig. 4.1a and (b-d) the different terms in eq. (4.9) in dependence of the direction  $\alpha$  of the small deviation  $\boldsymbol{\eta}$ . Both the results including only the  $\mathbf{0}$  and  $\mathbf{Q}$  mode (dots,  $\tilde{\varepsilon}^{\text{NLF}}$ ) and those including all LFE are shown (solid lines,  $\tilde{\varepsilon}$ ). The spectra in (a) and (c) are shifted along the ordinate.

### 4.3.1 (002)-Reflection

We start with the  $\mathbf{Q} = (0, 0, 2)$  reflection that was already considered in the introduction and which will now be analysed using the two-plasmon-band model. In fig. 4.3, we show all terms of eq. (4.9) for the different directions of  $\boldsymbol{\eta}$  separately. We use both, the exact effective dielectric matrix  $\tilde{\varepsilon}$  (solid lines), and the approximation  $\tilde{\varepsilon}^{\text{NLF}}$  (dots).

The loss function  $-\text{Im} \tilde{\varepsilon}_{\mathbf{Q}\mathbf{Q}}^{-1}$  at large momentum  $\mathbf{q} = \mathbf{Q} + \boldsymbol{\eta}$  is shown in fig. 4.3a. It shows a strong dependence on  $\boldsymbol{\eta}$ . The plasmon peak shifts in energy and vanishes for  $\alpha = 90^\circ$ , i.e., when  $\boldsymbol{\eta}$  is perpendicular to the  $\mathbf{Q}$  vector. In this case, the spectrum becomes identical to the isotropic term  $-\text{Im} 1/\tilde{\varepsilon}_{\mathbf{Q}\mathbf{Q}}$  which is shown in fig. 4.3b. It is essentially flat and indeed does not depend on  $\boldsymbol{\eta}$ . The full loss function is therefore governed by the second term in eq. (4.9). As we have discussed in section 4.2.4, the anisotropy enters in two ways:

(i) The loss function  $-\text{Im} \tilde{\varepsilon}_{\mathbf{00}}^{-1}$  at small momentum transfers  $\boldsymbol{\eta}$  is anisotropic in graphite (see fig. 4.3c). For  $\alpha = 90^\circ$ , we find the in-plane  $\pi$  plasmon of graphite at 7 eV. The peak shifts to lower energies as the momentum transfer is turned towards the  $c$  axis [127]. A comparison between panel (a) and (c) clearly shows that the loss spectrum from the first Brillouin zone reappears in the loss spectrum at large momentum transfers.

(ii) Additionally, the reappearing spectrum is weighted by the coupling factor  $\tilde{f}$  which also depends on  $\boldsymbol{\eta}$ . In the present case, it is real valued and nearly constant below 8 eV (see fig. 4.3d). The coupling  $|\tilde{f}|$  decreases with increasing  $\alpha$ . In particular, it vanishes exactly when  $\boldsymbol{\eta}$  is perpendicular to  $\mathbf{Q}$ . This explains the absence of the plasmon peak in the loss function at large momentum transfers for  $\alpha = 90^\circ$ .

### Coupling Factor $\tilde{f}$

Still, it remains to be understood why the coupling factor  $\tilde{f}$  disappears for in-plane directions of  $\boldsymbol{\eta}$ . To this end, we can make use of the general properties of the dielectric function in semiconductors. In the limit of very high frequencies and assuming a local effective crystal potential, the independent-particle polarisability becomes [124, 128, 129]

$$\chi_{\mathbf{G}\mathbf{G}'}^0(\boldsymbol{\eta}, \omega) \approx \frac{1}{em\omega^2} (\boldsymbol{\eta} + \mathbf{G}) \cdot (\boldsymbol{\eta} + \mathbf{G}') \rho(\mathbf{G} - \mathbf{G}'), \quad (4.10)$$

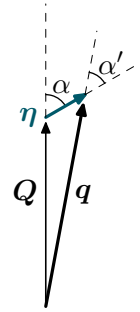
where  $\rho(\mathbf{G} - \mathbf{G}')$  denotes the Fourier coefficient of the ground-state electron density. A very similar expression can be derived in the framework of a quasifree electron gas by expanding the single-particle Bloch functions and energies to second order in the crystal potential  $U_G$  [123]. We can, therefore, assume that the following conclusions are still valid even at lower frequencies  $\omega$ :

First, we see that the coupling between density fluctuations with momentum  $\boldsymbol{\eta} + \mathbf{G}$  and  $\boldsymbol{\eta} + \mathbf{G}'$  is proportional to the cosine of the enclosed angle  $\alpha'$ . Hence, the prefactor for the dielectric function  $\tilde{\varepsilon}^{\text{NLF}}$  becomes

$$\tilde{f} \approx \tilde{f}^{\text{NLF}} = \frac{\varepsilon_{\mathbf{Q0}} \varepsilon_{\mathbf{0Q}}}{\varepsilon_{\mathbf{Q}\mathbf{Q}}^2} \propto \cos^2 \alpha'. \quad (4.11)$$

In particular, it vanishes for in-plane directions of  $\boldsymbol{\eta}$  as  $\alpha = 90^\circ \approx \alpha'$ .

Second, the coupling element vanishes when the Fourier coefficient  $|\rho(\mathbf{G} - \mathbf{G}')|^2$  is zero. In this case, also the Bragg reflection itself disappears. Note that  $\rho(\mathbf{G})$  is closely related to the crystal structure factor. For graphite in Bernal stacking, one finds that any Bragg reflection  $(0, 0, 2m + 1)$  where  $m$  is an integer is forbidden, i. e., the crystal structure factor is zero. Thus, also the off-diagonal element  $\varepsilon_{\mathbf{Q0}}$  vanishes and no anisotropy is found for the  $(0, 0, 1)$  reflection [130, 131]. Following eq. (4.10), we expect a strong anisotropy effect close to a strong Bragg reflection.



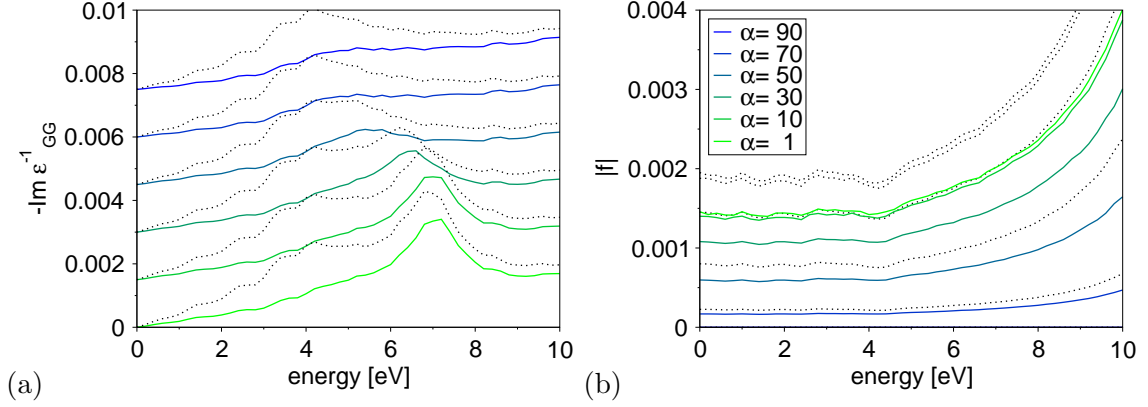


**Fig. 4.4:** Angular anomaly in graphite at the  $(0, 2, 0)$  reflection. Same as fig. 4.3a and d.

### Which LFE Contribute?

The results using  $\tilde{\varepsilon}^{\text{NLF}}$  (dotted lines) are very close to the full calculations. This might be rather astonishing, because the calculations neglecting *all* LFE have not been able to describe the anisotropy (see fig. 4.1a). The inclusion of a *single* mode, namely the long-wavelength mode  $\mathbf{K} = \mathbf{0}$ , is now sufficient to reproduce the discontinuity.

*Why are the other local-field corrections mainly small and isotropic?* We have seen in eq. (4.9) that the anisotropy can be only due to  $\tilde{\varepsilon}_{\mathbf{0}\mathbf{0}}^{-1}$  and  $\tilde{\varepsilon}_{\mathbf{Q}\mathbf{0}}$ . For the first term, it is already known that LFE are of minor importance for the loss function at small momentum transfers. The second term is given by eq. (4.7) and explicitly reads (the prime indicates that the  $\mathbf{0}$  and  $\mathbf{Q}$  modes are excluded from the summation)

$$\tilde{\varepsilon}_{\mathbf{Q}\mathbf{0}} = \varepsilon_{\mathbf{Q}\mathbf{0}} + \sum'_{\mathbf{L}, \mathbf{L}'} \varepsilon_{\mathbf{Q}\mathbf{L}} S_{\mathbf{L}\mathbf{L}'}^{-1} \varepsilon_{\mathbf{L}'\mathbf{0}} \approx \varepsilon_{\mathbf{Q}\mathbf{0}} + \sum'_{\mathbf{L}'} \frac{\varepsilon_{\mathbf{Q}\mathbf{L}'} \varepsilon_{\mathbf{L}'\mathbf{0}}}{\varepsilon_{\mathbf{L}'\mathbf{L}'}}. \quad (4.12)$$

In the last step, we have used the same approximation  $S_{\mathbf{L}\mathbf{L}'}^{-1} \approx 1/\varepsilon_{\mathbf{L}\mathbf{L}} \delta_{\mathbf{L}\mathbf{L}'}$  as in eq. (4.4). As discussed before, only  $\varepsilon_{\mathbf{Q}\mathbf{0}}$  and  $\varepsilon_{\mathbf{L}'\mathbf{0}}$  depend on  $\boldsymbol{\eta}$ . The former is explicitly taken into account in the  $2 \times 2$  matrix  $\tilde{\varepsilon}^{\text{NLF}}$  of the two-plasmon-band model. The latter is weighted by further matrix elements. In particular, it contributes only to second order in the crystal potential  $U$  and is generally small. Off-diagonal elements different from  $\varepsilon_{\mathbf{Q}\mathbf{0}}$  and  $\varepsilon_{\mathbf{0}\mathbf{Q}}$  can therefore often be neglected and despite its simplicity, the  $2 \times 2$  matrix model  $\tilde{\varepsilon}^{\text{NLF}}$  is sufficient to describe the anisotropy effect.

### 4.3.2 Other Bragg Reflections

We will repeat our analysis for two other Bragg reflections by choosing always the same small momentum deviations  $\boldsymbol{\eta}$  as above, but changing the vector  $\mathbf{Q}$ . Note that we only have to repeat the downfolding procedure for the new  $\mathbf{Q}$  vector, not the *ab-initio* calculation of the microscopic dielectric function  $\varepsilon_{\mathbf{G}\mathbf{G}'}(\boldsymbol{\eta}, \omega)$ .

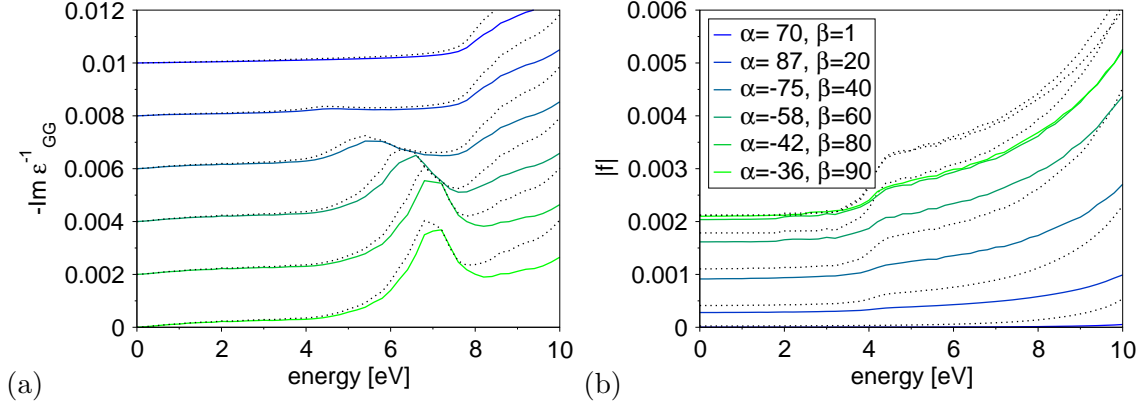


**Fig. 4.5:** Angular anomaly in Graphite at the  $(\bar{1}, \bar{1}, 2)$  reflection. Same as fig. 4.3a and d.

### (020)-Reflection

In fig. 4.4a, the loss function is shown for momentum transfers close to the  $\mathbf{Q} = (0, 2, 0)$  Bragg reflection. Again, the spectra strongly depend on the deviation  $\boldsymbol{\eta}$ . But in contrast to fig. 4.3a, the in-plane  $\pi$  plasmon at 7 eV reappears, not the peak for small on-axis momentum transfer. This is simply due to the different direction of  $\mathbf{Q}$ : If the deviation  $\boldsymbol{\eta}$  is chosen along the  $c$ -axis (blue line at the top) it is now perpendicular to  $\mathbf{Q}$  ( $\alpha = 90^\circ$ ) and the coupling vanishes. The spectrum is then identical to the isotropic contribution  $-\text{Im } 1/\tilde{\epsilon}_{\mathbf{Q}\mathbf{Q}}$ . Indeed, the coupling factor  $f$  shown in fig. 4.4b is again real and scales as  $\cos^2 \alpha$ . Note that the contribution of the LFE neglected in  $\tilde{\epsilon}^{\text{NLF}}$  are now more important than for the  $(0, 0, 2)$  reflection. However, they do not contribute to the anisotropy.

### (1-bar 1-bar 2)-Reflection

In fig. 4.5a, we consider a Bragg reflection for a diagonal direction  $\mathbf{Q} = (\bar{1}, \bar{1}, 2)$ . The corresponding loss function shows again a strong dependence on the direction of  $\boldsymbol{\eta}$  which is very similar to the behaviour at the in-plane  $(0, 2, 0)$  reflection. However, we find that the approximation (4.10) for the off-diagonal element  $\epsilon_{\mathbf{Q}\mathbf{0}}$  seems to fail in this case. Indeed, the coupling factor  $f$  (and the wing element) does not show a scaling with  $\cos^2 \alpha$  (see fig. 4.5b): while  $f$  vanishes for the on-axis deviation  $\boldsymbol{\eta}$  ( $\alpha = 70^\circ$ ), it is much larger for a comparable angle  $\alpha = -75^\circ$  (for comparison, also the angle  $\beta$  towards the  $c$ -axis is given). The same behaviour is found for the simplified model using  $\tilde{\epsilon}^{\text{NLF}}$ , i. e., the coupling to other local-field modes different from  $\mathbf{0}$  cannot be the origin of this behaviour. It is only due to the angular dependence of the wing element  $\epsilon_{\mathbf{Q}\mathbf{0}}$ .

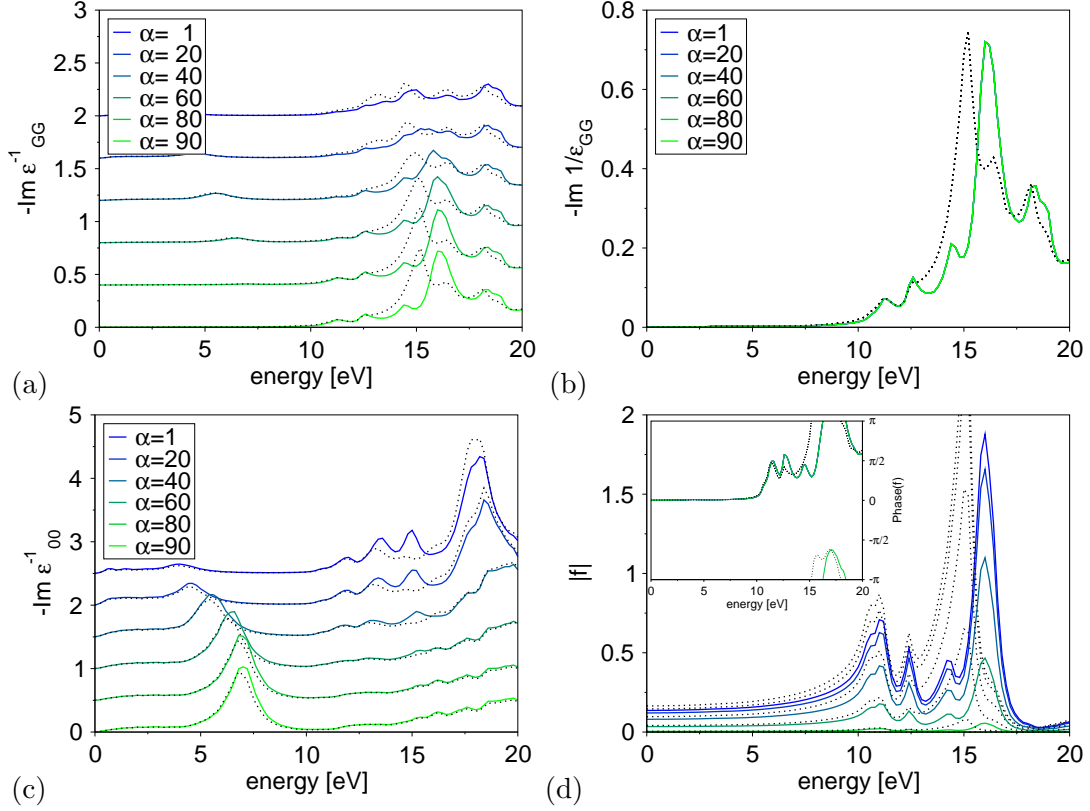


**Fig. 4.6:** Angular anomaly in graphite at the (0,0,2) reflection. Same as fig. 4.3 for higher energies up to 20 eV. The inset in (d) shows the phase of the coupling factor  $f$  in radians.

### 4.3.3 Higher Energies

Finally, we extend our studies to the range of higher energies up to 20 eV, where also  $\sigma$  electrons contribute to the excitation. The loss function becomes much more complicated, but the general explanation for the anisotropy remains valid.

We will only consider the  $\mathbf{Q} = (0, 0, 2)$  reflection. The loss function for  $\mathbf{q} = \boldsymbol{\eta} + \mathbf{Q}$  is shown in fig. 4.6a. The energy-loss probability strongly increases at high energies such that the low-energy excitations shown in fig. 4.3 are hardly visible. For increasing angle  $\alpha$ , a strong peak appears at about 16 eV. At first glance, this appears very puzzling because (i) the loss function in the first Brillouin zone does not show any peak at this energy (see fig 4.6c) and (ii) the coupling factor should vanish for  $\alpha = 90^\circ$ .

Nonetheless, the behaviour of the loss function can be again understood using the two-plasmon-band model. First, we see from fig. 4.6b that the peak at 16 eV is actually due to the isotropic contribution  $-\text{Im } 1/\epsilon_{\mathbf{Q}\mathbf{Q}}$ . Second, the coupling indeed vanishes for  $\alpha = 90^\circ$  as we expect from eq. (4.10) (see fig. 4.6d). But at energies beyond 10 eV, the coupling factor  $f$  becomes *complex*. Its phase does not depend on the direction of  $\boldsymbol{\eta}$  (see

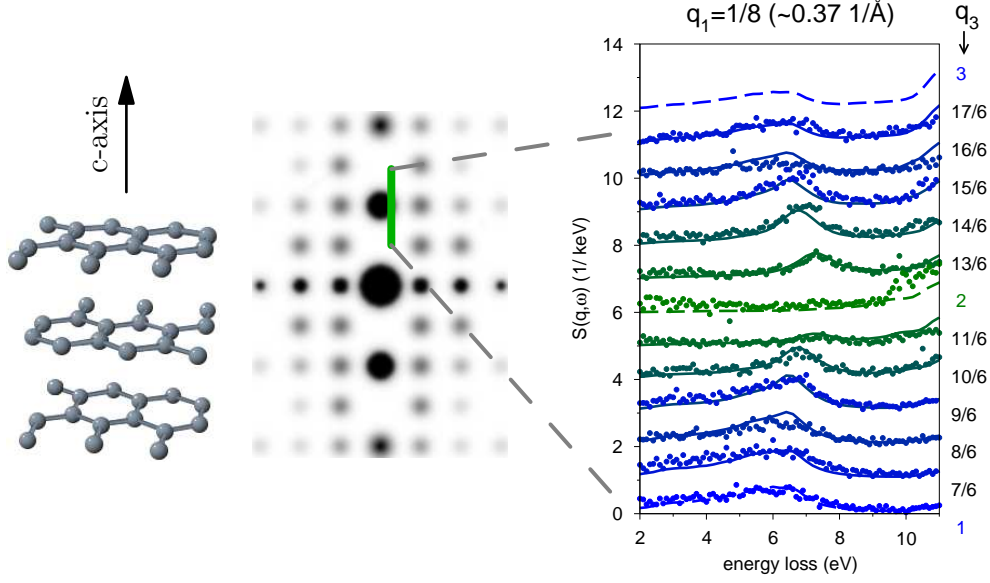


**Fig. 4.7:** Comparison of the structure factor  $S(\mathbf{q}, \omega)$  measured by IXS-experiments (dots) and calculated in RPA (lines; dashed for integer  $q_3$ ) for  $\mathbf{q} = (\frac{1}{8}, 0, q_3)$ . The position of the momentum transfer in reciprocal space is indicated on the left. The elastic tail has been removed from the raw experimental data and a uniform scaling has been applied.

inset). At 16 eV,  $\arg f$  is close to  $\pm\pi$ , i. e.,  $f$  is *negative* and the peak in the isotropic contribution is actually cancelled by the anisotropic second term.

As a consequence, the interpretation of the angular anomaly becomes slightly different compared to the previous cases: For a deviation  $\boldsymbol{\eta}$  perpendicular to  $\mathbf{Q}$ , the loss function at  $\mathbf{q} = \boldsymbol{\eta} + \mathbf{Q}$  is equivalent to the isotropic contribution which has a strong peak at 16 eV. For small  $\alpha$ , the anisotropic second factor in eq. (4.9) contributes and suppresses the peak at 16 eV. As the off-diagonal element  $\tilde{\epsilon}_{\mathbf{Q}0}$  strongly varies with  $\omega$ , the spectrum from the first Brillouin zone is not recognised in the loss function. For instance, the perpendicular plasmon peak at 18 eV does not reappear (compare upper blue lines in fig. 4.6a and c).

#### 4.3.4 Experimental Verification

In order to validate our predictions we have proposed inelastic X-ray scattering experiments [130]. The measurements were carried out at the Taiwan inelastic-scattering beam line in SPring-8 using a graphite single crystal. The results of our joint theoretical and experimental study have been recently published [131].

To verify the angular anisotropy, we did not consider momentum transfers exactly along the  $c$ -axis of graphite, but added a small in-plane component  $q_1 = 0.37 \text{ \AA}^{-1}$  that was kept constant, while the momentum along the  $c$ -axis  $q_3$  was varied from  $0.94 \text{ \AA}^{-1}$  to  $2.84 \text{ \AA}^{-1}$ . By this choice of  $\mathbf{q}$  vectors, the elastic contributions at the Bragg reflections

are avoided. Approaching the Bragg reflection at  $\mathbf{Q} = (002)$ , the peak in the spectra is strongly shifted in energy and, most importantly, it abruptly disappears next to  $\mathbf{Q}$  ( $q_3 = 2 \cdot 2\pi/c = 1.88 \text{ \AA}^{-1}$ ). Both effects are a clear signature of the anisotropy.

Figure 4.7 shows the measured spectra (dots) together with the corresponding *ab-initio* calculations (lines). The agreement is very good; in particular, the predicted peak shift is clearly seen in the measurements, as well as the abrupt change from a peaked spectrum for  $\mathbf{q} = (\frac{1}{8}, 0, \frac{13}{6})$  to a completely flat one at  $\mathbf{q} = (\frac{1}{8}, 0, 2)$ , when  $\alpha \approx 90^\circ$ . The IXS measurements give unambiguous support to the presented theoretical predictions.

### Measuring Off-Diagonal Elements

It is interesting to note that our experiments, in principle, give access to the off-diagonal element  $\tilde{\varepsilon}_{\mathbf{Q}\mathbf{0}}$ . Within the limits of the two-plasmon-band model (4.8), the coupling factor  $f$  and thus  $\tilde{\varepsilon}_{\mathbf{Q}\mathbf{0}}$  can be determined from the difference of the spectra at  $\alpha = 0^\circ$  and  $90^\circ$ , whenever the anisotropy effect is strong.

Indeed, such an experiment is very similar to the coherent inelastic X-ray measurements proposed by Schülke and Kaprolat [74] or the EMCD experiments in the electron microscope proposed by Schattschneider *et al.* [65]. In both cases, the system is perturbed by a superposition of two plane waves with wave vectors that differ by a reciprocal lattice vector  $\mathbf{Q}$ . As we have seen in section 2.3.1, the off-diagonal element of the mixed-dynamic form factor  $S(\mathbf{q}, \mathbf{q}', \omega)$  then enters as an interference term. It can be extracted from the difference of two measured loss functions.

Nevertheless, the connection between the angular anomaly and these two-beam experiments is still an open question. First, the form factor  $S$  is related to the *inverse* dielectric function  $\varepsilon^{-1}$  via the fluctuation-dissipation theorem (2.50), while the anisotropy is determined by the off-diagonal elements of the dielectric function  $\varepsilon$  itself. Second, the two external plane waves in the experiments of Schülke and Kaprolat [74] and Schattschneider *et al.* [65] are directly generated inside the crystal by internal Bragg reflection of an external broad beam. This can be interpreted as a coherent elastic and inelastic scattering event [27]. Our calculations, however, only include a single inelastic scattering event for a single external plane wave.

## 4.4 Silicon

Finally, we consider the angular anomaly in silicon which becomes interesting for two reasons: First, silicon has cubic symmetry and is an isotropic material for long-wavelength excitations. At first glance, the presence of the angular anomaly shown in fig 4.1b might, therefore, be astonishing. Indeed, the loss function for small momentum transfers  $-\text{Im} \varepsilon_{\mathbf{0}\mathbf{0}}^{-1}(\boldsymbol{\eta}, \omega)$  does not depend on the direction of  $\boldsymbol{\eta}$ . But at large momentum transfers, also the microscopic structure of the system is probed and we will find anisotropic contributions from the coupling factor  $f$ . Second, the loss function in silicon shows a prominent Fano resonance close to the  $\mathbf{Q} = (1, 1, 1)$  reflection [114]. We investigate this structure by means of TDDFT calculations. Previous *ab-initio* studies [132] on silicon

have shown that exchange and correlation effects have to be taken into account for an accurate description of experimental measurements. We closely follow their approach using the adiabatic local-density approximation plus lifetime corrections (see below).

## Numerical Details

```
# ground state
a : 10.263 Bohr
ecut: 30 Ha
# kss
kptrlatt 8 -8 8
          -8 8 8
          -8 -8 8
shiftk
0.62 0.74 0.86
```

```
# tddft ALDA+LT
npwfn 181
nbands 100
npwmat 89
```

The electronic ground state is calculated in DFT-LDA (local-density approximation) with ABINIT [100]. Nonlocal, norm-conserving pseudopotentials of Hamann-type [109] and a plane-wave basis set (with an energy cutoff radius of 30 Ha and a regular grid of 2048 shifted  $k$ -points) are used. The microscopic dielectric matrix  $\varepsilon_{\mathbf{G}\mathbf{G}'}$  is calculated in the framework of TDDFT using the DP code [102]. For a better convergence, we have used shifted  $k$ -point grids (see section 3.3.3) and it was carefully checked that the shift does not introduce any artificial anisotropy. Exchange and correlation effects are taken into account within the adiabatic local-density approximation (see chapter 3). Additionally, lifetime effects are included in the calculation of the independent-particle polarisability (3.14) by an energy-dependent broadening  $i\eta = i|\Sigma''(E_v)| + i|\Sigma''(E_c)|$ . Fleszar and Hanke [133] have calculated the self-energy matrix elements  $|\text{Im}\Sigma(E)|$  for silicon in dependence of the LDA Kohn-Sham energies. We use the following rough parametrisation of their results [132]:

$$\Sigma''(E) = \begin{cases} 0.01(E + 1.5)^2 & E < -1.5 \\ 0 & -1.5 < E < 1.5 \\ 0.004333(E - 1.5)^2 & 1.5 < E < 28 \\ 0.02857(E - 28) + 3.0428 & 28 < E, \end{cases} \quad (4.13)$$

where all energies are given in eV. The inclusion of the lifetime effects has been shown to be important for the momentum-dependent loss function of silicon at high energies [132].

As in the case of graphite, we will analyse the resulting loss function in terms of the two-plasmon-band model. Therefore, the microscopic dielectric matrix  $\varepsilon_{\mathbf{G}\mathbf{G}'}(\boldsymbol{\eta}, \omega)$  is calculated for six different deviations  $\boldsymbol{\eta}$ . The modulus is again constant  $\eta = 10^{-3} \text{ \AA}^{-1}$ , while the direction is changed by turning  $\boldsymbol{\eta}$  from the  $[111]_{\text{cc}}$  direction<sup>5</sup> towards the  $[11\bar{2}]_{\text{cc}}$  direction by an angle of  $\beta = 0, 20, 40, 60, 80$ , and  $90^\circ$ . Finally, the dielectric matrix is separated into the different blocks (4.6) and we calculate  $\tilde{\varepsilon}$  and  $\tilde{\varepsilon}^{\text{NLF}}$ .

In our calculations, the momentum transfer is usually restricted by the set of  $\mathbf{k}$ -points, because  $\mathbf{k}$  and  $\mathbf{k}' = \mathbf{k} + \mathbf{q}$  have to be included in the mesh of equidistant  $\mathbf{k}$ -points. To circumvent this restriction, we have used *two*  $\mathbf{k}$ -point grids which are shifted against each other by the momentum transfer  $\mathbf{q}$ . Using this `doublegrid` method, we can calculate the loss function for arbitrary momentum transfers that correspond exactly to the experimental conditions.

<sup>5</sup>We use the conventional unit cell. Directions are then given in Cartesian coordinates in units of  $2\pi/a$ .

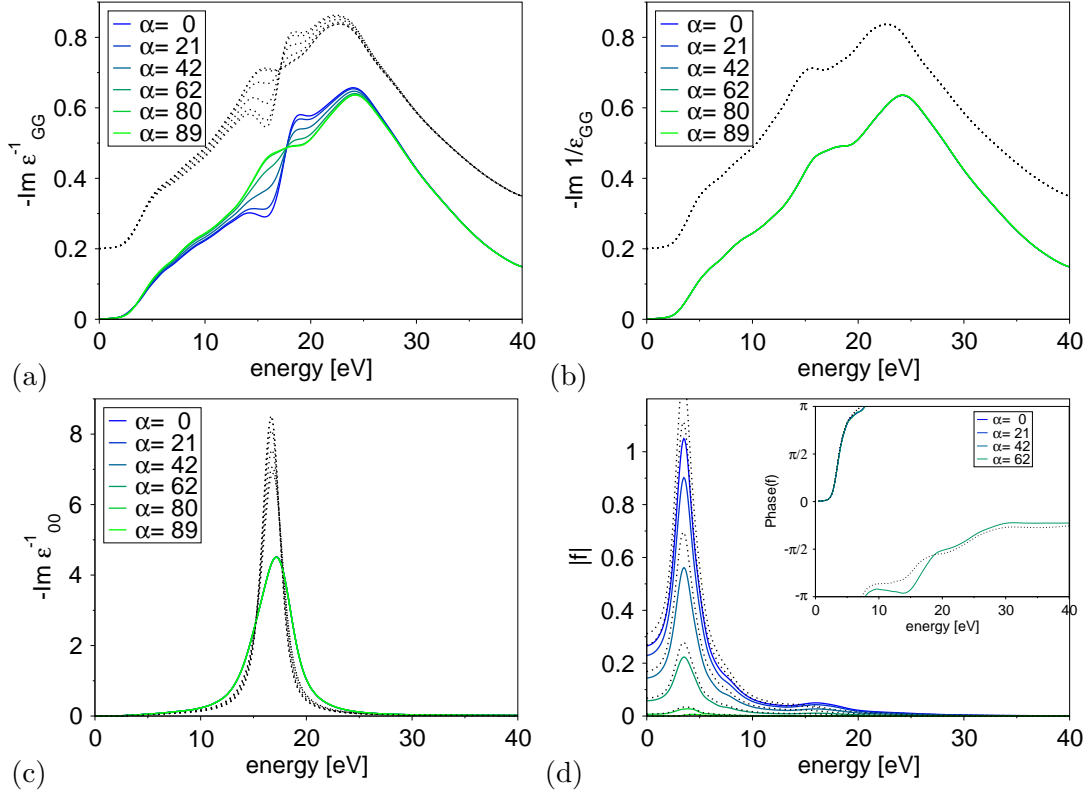


**Fig. 4.8:** (a) Anisotropic behaviour of the loss function  $-\text{Im} \varepsilon_{\mathbf{Q}\mathbf{Q}}^{-1}$  close to the Bragg reflection  $\mathbf{Q} = (1, 1, 1)$  in silicon. (b-d) Analysis of the contributions to the loss function following eq. (4.8). Both, results including only the  $\mathbf{0}$  and  $\mathbf{Q}$  mode (dotted lines,  $\varepsilon^{\text{NLF}}$ ) and those including all LFE are shown (solid lines,  $\varepsilon$ ). The NLF spectra in (a) and (b) are shifted along the ordinate.

#### 4.4.1 (111)-Reflection

Let us now reconsider the Fano resonance for momentum transfers close to the  $\mathbf{Q} = (1, 1, 1)$  reflection. In fig. 4.8a, the calculated loss functions for the different deviations  $\boldsymbol{\eta}$  are shown. We clearly find a strong dependence of the Fano resonance at about 17 eV on the angle  $\alpha$  between the deviation  $\boldsymbol{\eta}$  and the reciprocal lattice vector  $\mathbf{Q}$ . Using the two-plasmon-band model, we again find that the loss function for  $\alpha = 90^\circ$  is given by the isotropic first term of eq. (4.9) (see fig. 4.8b). The Fano resonance, instead, is a consequence of the second term. As we can see in fig. 4.8c, the loss function from the first Brillouin zone is now isotropic. It shows a strong plasmon peak at 17 eV which does not depend on  $\alpha$ . Nevertheless, the coupling factor  $f$  shows the  $\cos^2 \alpha$  scaling as predicted by eq. (4.10) (see fig. 4.8d). Its modulus is nearly constant for the energies of interest but its phase rapidly changes between  $-\pi$  at 15 eV and  $-\pi/2$  at 20 eV (see inset). This is the reason for the negative contribution of the anisotropic term in the first case and the positive contributions in the latter.

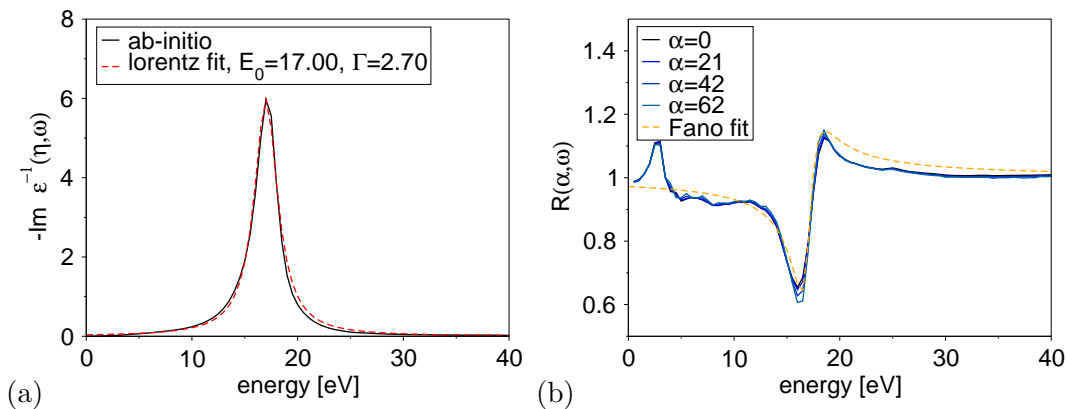


**Fig. 4.9:** Analysis of the Fano line shape. (a) Lorentz fit for the plasmon resonance at low momentum transfer. (b) Fano fit for the loss function at large momentum transfer close to the  $(1, 1, 1)$  reflection (see text). We used the  $2 \times 2$  model dielectric function  $\tilde{\epsilon}^{\text{NLF}}$  calculated in RPA.

The structure at 17 eV has been already investigated by Sturm *et al.* [114]: It was interpreted as a *plasmon-Fano resonance*, because it is due to the coupling between the discrete plasmon excitation at small momentum  $\boldsymbol{\eta}$  and the electron-hole continuum at large momentum transfers  $\boldsymbol{\eta} + \boldsymbol{Q}$ . The effect was studied by comparison of the loss spectra at large momentum transfers  $|\boldsymbol{q}| = 2.36 \text{ \AA}^{-1}$  for two different directions: the  $[111]_{\text{cc}}$  direction, where the Fano resonance is present, and the  $[100]_{\text{cc}}$  direction, where it is completely absent. This difference could be explained in terms of the two-plasmon-band model. As the coupling factor  $f$  depends on the Fourier coefficient  $U_{\boldsymbol{Q}}$  of the effective crystal potential,<sup>6</sup> it strongly differs for the two directions of  $\boldsymbol{q}$ . Indeed, the coefficient  $U_{(100)}$  and thus the coupling to the  $\mathbf{0}$  mode vanishes in silicon, while  $U_{(111)}$  is rather large. We extend these investigations by several aspects:

1. We studied momentum transfers very close to Bragg reflections. The anisotropy effect is not directly visible at momentum transfers studied by Sturm *et al.* [114].
2. Instead of changing the direction of the momentum transfer  $\boldsymbol{q}$ , we only change the direction of the reduced momentum  $\boldsymbol{\eta}$ . Indeed,  $\boldsymbol{q}$  is nearly constant in our case.
3. The coupling factor  $f$  therefore changes strongly with the angle  $\alpha$ , while the Fourier coefficient  $U_{\boldsymbol{Q}}$  is always the same.

As in the case of graphite, the contribution of the long-wavelength charge oscillation  $\boldsymbol{K} = \mathbf{0}$  is by far the most important one. Neglecting all the other local fields (dotted lines in fig. 4.8) does not considerably change the behaviour of the loss function. Only the plasmon excitation in the first Brillouin zone is broadened if we include all LFE.

<sup>6</sup>Or, equivalently, on the Fourier coefficient  $\rho_{\boldsymbol{Q}}$  of the electron charge density; see eq. (4.10).

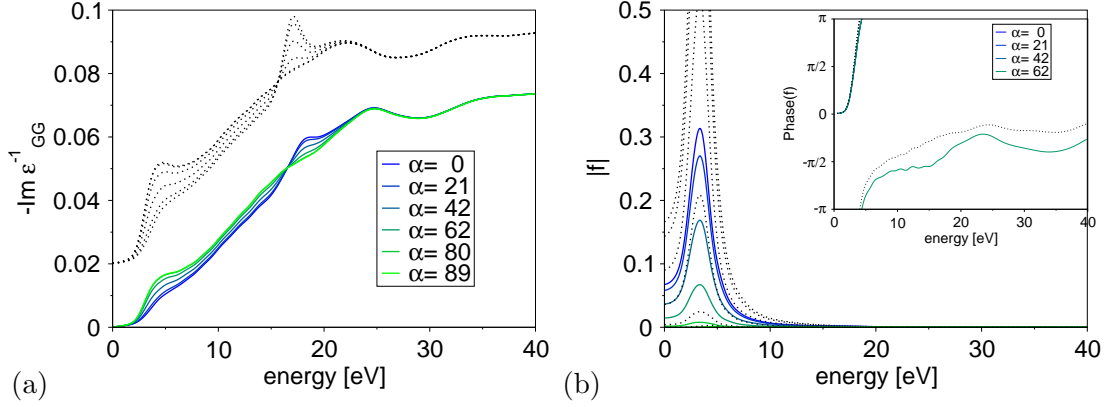


**Fig. 4.10:** Angular anomaly in silicon at the (2, 2, 2) reflection. Same as fig. 4.8a and d.

### Fano Line Shape

We might wonder if the line shape can be really described by the Fano model. Assuming that a discrete state is coupled to an overlapping continuum, Fano obtained a characteristic line shape for the cross section of scattering experiments [134]:

$$F(\omega) = A^2 \frac{(\tilde{q} + \epsilon)^2}{(1 + \epsilon)^2} + (1 - A), \quad \epsilon = \frac{\hbar\omega - E_0}{\Gamma/2}, \quad (4.14)$$

where  $\tilde{q}$  denotes the Fano parameter,  $\epsilon$  the reduced energy,  $E_0$  and  $\Gamma$  correspond to the energy and the broadening of the isolated resonance, and  $A$  is the coupling strength.

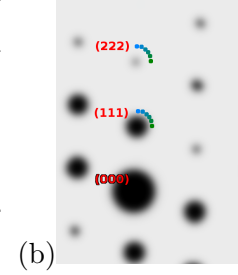
For simplicity, we will only consider the  $2 \times 2$  model function  $\tilde{\epsilon}^{\text{NLF}}$  and neglect exchange and correlation effects in the following. In this case, the discrete resonance corresponds to the plasmon at low momentum transfers neglecting all LFE. By fitting a Lorentzian function to the NLF spectrum at vanishing momentum transfer  $\boldsymbol{\eta}$ , we determine the parameters  $E_0 = 17$  eV and  $\Gamma = 2.7$  eV (see fig. 4.9a). For  $\alpha = 90^\circ$  the coupling vanishes and the loss function at large momentum transfers does not contain any contributions from the discrete resonance. For any other angle  $\alpha$ , the change in the spectrum due to the coupling to this resonance is described by the ratio (we omit the index NLF)

$$R(\alpha, \omega) = \frac{1}{\cos^2 \alpha} \frac{\text{Im } \tilde{\epsilon}_{\mathbf{Q}\mathbf{Q}}^{-1}(\alpha)}{\text{Im } \tilde{\epsilon}_{\mathbf{Q}\mathbf{Q}}^{-1}(\alpha = 90^\circ)} \quad (4.15)$$

between the loss functions at  $\alpha$  and  $\alpha = 90^\circ$  (see fig. 4.9b, solid lines). The factor  $\cos^2 \alpha$  accounts for the scaling of the coupling factor  $f$  and we find a universal line shape for all angles  $\alpha$ . The Fano fit of eq. (4.14) for the parameters  $\tilde{q} = 0.64$  and  $A = 0.6$  is in rather good agreement with the RPA results which validates the interpretation of the structure at 17 eV as a plasmon-Fano resonance.

$\mathbf{q}_{cc} [2\pi/a]$	$\mathbf{q}_{rc}$	$ \mathbf{q}  \text{ \AA}$	$\alpha$	
$\mathbf{Q} + (111)_{cc}/16$	$\mathbf{Q} + (111)_{rc}/16$	0.12	0	doublegrid
$\mathbf{Q} + (011)_{cc}/8$	$\mathbf{Q} + (211)_{rc}/16$	0.20	35	
$\mathbf{Q} + (100)_{cc}/8$	$\mathbf{Q} + (011)_{rc}/16$	0.14	54	
$\mathbf{Q} + (2\bar{1}1)_{cc}/16$	$\mathbf{Q} + (031)_{rc}/32$	0.18	doublegrid	

(a)



(b)

**Tab. 4.1:** Momentum transfers  $\mathbf{q}$  for the loss functions in fig. 4.11 at the  $\mathbf{Q} = (111)$  and  $(222)$  reflection: (a) given in Cartesian and reciprocal coordinates and (b) shown in reciprocal space.

#### 4.4.2 (222)-Reflection

Another interesting case is found at the  $(222)$  reflection in silicon. Neglecting the form factor of the atoms, the crystal structure factor  $S(\mathbf{Q}) = \sum_n e^{-i\mathbf{Q}\tau_n}$  vanishes for this reflection. However, it is well known that the charge distribution in the covalently bonded crystal actually leads to a very small but nonzero structure factor (factor 100 compared to the  $(111)$  reflection, see [135]). Following eq. (4.10), we would expect a very weak angular anomaly. Figure 4.10a shows that the change of the loss function with the deviation  $\eta$  is nevertheless visible for the  $(2, 2, 2)$  reflection. We find again a Fano-like line shape at 17 eV which originates from the coupling to the plasmon excitation at low momentum transfers. Additionally, the anisotropic correction becomes important at lower energies. This is mainly due to the much lower intensity of the isotropic contribution at larger momentum transfers (compare scales of fig. 4.10a and fig. 4.8a). As the phase of the coupling factor is approximately  $\pm\pi$ , the intensity is reduced at 5 eV for  $\alpha = 0^\circ$ .

#### 4.4.3 Experimental Verification

To verify our theoretical prediction of an angular anomaly in the loss function of silicon, high-quality measurements of dynamic structure factor  $S(\mathbf{q}, \omega)$  have been performed for large momentum transfers close to the  $(1, 1, 1)$  and  $(2, 2, 2)$  reflection. The IXS experiments on a single crystal of silicon have been carried out at the beamline ID16 of the ESRF synchrotron radiation source in Grenoble. I have participated in the measurements in collaboration with Simo Huotari and Giulio Monaco.

##### Details of the Measurements

The  $(111)$  surface of a single crystal of silicon has been chosen as sample. In Bragg geometry (reflection), we could use a massive sample that is stable against vibrations. The incident photon beam was monochromatised with a double-crystal Si(111) monochromator and a Si(440) channel-cut to an energy bandwidth of 220 meV. The spectra have been analysed using a backscattering crystal spectrometer equipped with a Si(660) analyser crystal. A total energy resolution of  $\Delta E < 0.5$  eV has been estimated from the width of the elastic line.

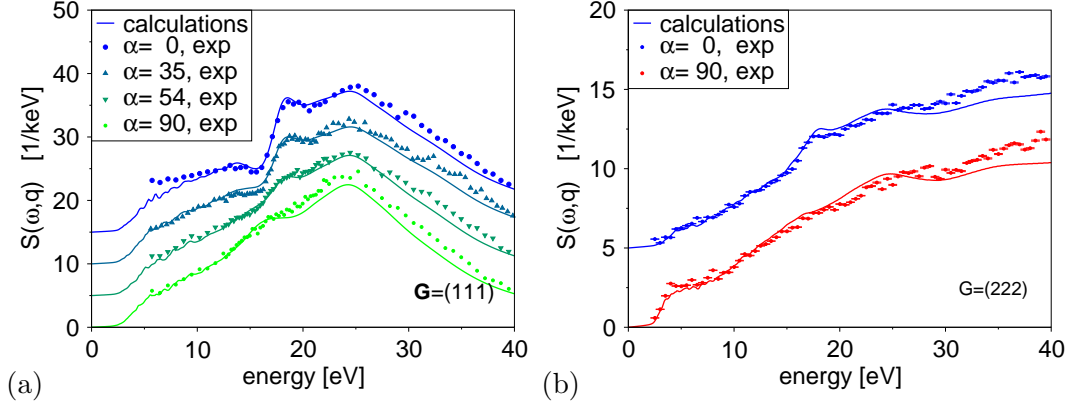


**Fig. 4.11:** Experimental verification of the angular anomaly in silicon. We compare IXS measurement (dots) and ALDA+LT calculations (solid lines) for loss functions close to the (a) (111) and (b) (222) reflections. The exact momentum transfers are given in fig. 4.1. The experimental curves have been scaled by a factor of 5 and 7 in (a) and (b), respectively. All curves are shifted for better visibility.

The count rate of the collected photons and the resulting signal-to-noise ratio is determined by several experimental parameters: the polarisation angle, the size of the beam spot on the illuminated sample (footprint), the energy resolution  $\Delta E$ , and the resolution in the angular momentum  $\mathbf{q}$ . In order to measure the loss spectra close to a Bragg reflection, a very high momentum resolution is necessary: First, contributions from the elastic scattering at the Bragg reflection should be avoided. Second, the deviation in the angle  $\alpha$  should be small. As a compromise, an analyser slit of 10 mm width and height at a distance of 1 m has been chosen. For an incident beam energy of 7.91 keV, i. e., a photon momentum of  $4 \text{ \AA}^{-1}$ , we have a momentum resolution of  $\Delta q_{\parallel} = \pm 0.005 \text{ \AA}^{-1}$  inside and  $\Delta q_z = \pm 0.02 \text{ \AA}^{-1}$  perpendicular to the scattering plane.

Additionally, we have used rather large deviations  $|\boldsymbol{\eta}| \approx \pm 0.15 \text{ \AA}^{-1}$  from the Bragg reflection, as the angular anomaly mainly depends on the direction and not the size of the deviation. The momentum transfers used in the experiment are shown in table 4.1a. The average uncertainty of the direction of  $\boldsymbol{\eta}$  is about  $\Delta\alpha \approx \pm 10^\circ$ .

## Results

The results are shown in fig. 4.11 (dots) together with our ALDA+LT calculations (solid lines). The experiments clearly confirm the validity of our calculations and the presence of a strong angular anomaly in silicon.

Note that there are two slight deviations: First, the calculated spectrum for  $\alpha = 0^\circ$  in fig. 4.11a is slightly different from the measured loss function at low energies. Second, the agreement becomes worse for high energies  $E > 30 \text{ eV}$ . This might be due to the bad description of the lifetime effects by the rough parametrisation (4.13) at high energies and should be corrected by including the quasi-particle corrections for each single-particle state as it was already proposed in reference [132].

## 4.5 Conclusions

In this chapter, we have investigated the response of a crystal to an external plane-wave perturbation both theoretically and experimentally. We have predicted that the dynamic structure factor  $S(\mathbf{q}, \omega)$ —or equivalently the inverse dielectric function  $\text{Im} \varepsilon_M^{-1}(\mathbf{q}, \omega)$ —can show an angular discontinuity at large momentum transfers  $\mathbf{q}_r + \mathbf{Q}$  close to Bragg allowed reciprocal-lattice vectors  $\mathbf{Q}$ : infinitesimal changes in the momentum transfer then induce strong changes in the resulting energy-loss spectra. This general effect has been explained in terms of crystal local-field effects which cause a strong coupling between excitations at small and large momentum transfers via internal Bragg scattering. It has been verified by *ab-initio* calculations and inelastic X-ray scattering experiments for two materials, namely graphite and silicon.

In graphite, we found that the discontinuity at large momentum transfers  $\mathbf{q} = \mathbf{q}_r + \mathbf{Q}$  is due to the reappearance of the spectrum from the first Brillouin zone. This has been explained in terms of a two-plasmon-band model which describes the coupling between the microscopic perturbing plane wave  $e^{i(\mathbf{q}_r + \mathbf{Q}) \cdot \mathbf{r}}$  and the induced macroscopic mode  $e^{i\mathbf{q}_r \cdot \mathbf{r}}$  via crystal local-field effects. We find that the discontinuity of the loss spectrum at large momentum transfers is the result of three superposing effects: (i) The reappearing spectrum from the first Brillouin zone strongly depends on the direction of the reduced momentum transfer  $\mathbf{q}_r$  due to the anisotropy of graphite. (ii) The coupling between excitations from different Brillouin zones depends on the angle between  $\mathbf{q}$  and  $\mathbf{q}_r$  which enforces the angular anisotropy. (iii) The coupling strength also depends on the Fourier coefficient  $\rho_{\mathbf{Q}}$  of the ground-state charge density and no discontinuity is observed when the crystal structure factor vanishes. It is hence a consequence of the Bernal stacking of the graphene layers that no changes occur at  $\mathbf{Q} = (0, 0, 1)$ .

We have also investigated the response of silicon which is a macroscopically *isotropic* system. In this material, the angular anomaly has different consequences than in graphite: Our *ab-initio* calculations show that the coupling factor is complex valued which leads to a Fano-resonance in the energy-loss function at the  $(1, 1, 1)$  reflection. Again, the coupling strongly depends on the direction of the reduced momentum transfer  $\mathbf{q}_r$  and the Fano-coupling between the plasmon and electron-hole excitations can be ‘switched-off’ by a very small change in  $\mathbf{q}$ .

Our predictions in graphite and silicon have been clearly confirmed by inelastic X-ray scattering (IXS) measurements of the dynamic structure factor. We expect similar observations in all crystals that show strong crystal local-field effects, especially for layered or quasi one-dimensional structures. As a consequence, (i) anisotropic excitations from the first Brillouin zone might reappear at large momentum transfers leading to an anomalous angular dependence of the spectra, (ii) these recurring excitations belong to a direction  $\mathbf{q}_r$  that is different from  $\mathbf{q}$ , and (iii) measurements of the loss function close to an allowed Bragg reflection may be extremely sensitive on the chosen momentum transfer. Additionally, the angular anisotropy might be important for the understanding of spatially-resolved EELS.

We will see in the following chapters that crystal local-field effects become also very important for isolated nanostructures like graphene and single-wall carbon nanotubes.

## 5 Polarisability of Two-Dimensional Systems

A system is generally called *dynamically two-dimensional*, if the electrons and holes are free to move in two dimensions, but have their motion constrained along the third direction [136]. The wave vector is then a good quantum number for the two dimensions, but not for the third. A typical example are carriers which are trapped at interfaces between an insulator and a semiconductor. But also surfaces, heterostructures, intercalated systems, and thin films can be understood as dynamically two-dimensional systems.

Only recently, real two-dimensional crystals have been realised experimentally. Although being studied extensively as a theoretical model, such systems have been considered to be thermodynamically unstable. In 2004, however, Novoselov and Geim were able to produce flat monolayers of carbon atoms, the so called *graphene*, by exfoliation of the weakly bound layers of graphite [137]. Single layers of boron nitride, several dichalcogenides, and complex oxides have been produced similarly [138].

Due to their outstanding mechanical and electronic properties, graphene layers have attracted much attention in the last few years [5]. It is a *building block* for graphitic materials of all other dimensionalities: it can be wrapped up into 0D fullerenes, rolled into 1D nanotubes, or stacked into 3D graphite. In the following, we focus on the properties of single graphene layers and especially the description of collective excitations in this system.

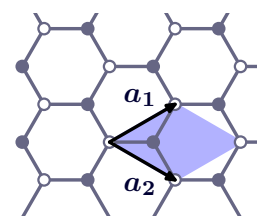


Fig. 5.1: graphene

### 5.1 Graphene

The graphene sheet is a flat monolayer of carbon atoms forming a two-dimensional honeycomb lattice (see fig. 5.1). The primitive unit cell of the hexagonal lattice is spanned by the two basis vectors  $\mathbf{a}_1$  and  $\mathbf{a}_2$  and contains two carbon atoms at positions  $\boldsymbol{\tau}_\alpha$ ,

$$\mathbf{a}_{1,2} = \frac{\sqrt{3}a}{2} \mathbf{e}_x \pm \frac{a}{2} \mathbf{e}_y, \quad \boldsymbol{\tau}_A = \mathbf{0}, \quad \boldsymbol{\tau}_B = \frac{1}{3}(\mathbf{a}_1 + \mathbf{a}_2). \quad (5.1)$$

The experimental lattice constant of  $a \approx 2.4 \text{ \AA}$  corresponds to a nearest-neighbour distance of about  $1.4 \text{ \AA}$  [139]. It has been found that the graphene sheet is stabilised by a weak buckling at finite temperatures [140] which solves the contradiction with the predicted instability of real 2D crystals. The amplitude of the ripples of about  $1 \text{ \AA}$  is very small compared to their wavelength of  $80 \text{ \AA}$ . Therefore, we can neglect these deviations from the perfectly flat graphene for our purposes. The flat graphene crystal has a six-fold rotational axis, six perpendicular mirror planes and one mirror plane which coincides with the sheet. The resulting 24 symmetry operations form the point group  $D_{6h}$ .

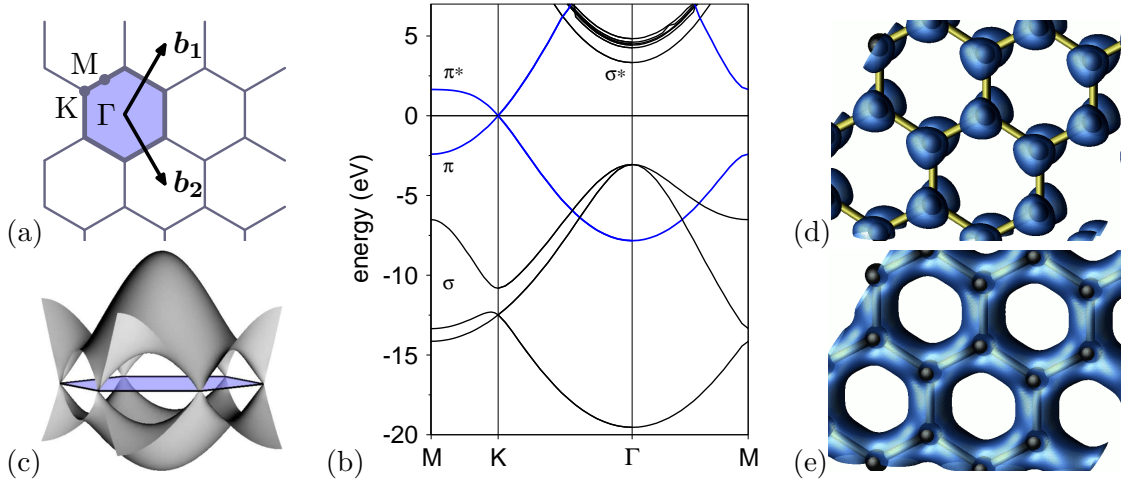


**Fig. 5.2:** (a) Brillouin zone of graphene in reciprocal space. (b) Electronic band structure of graphene. The  $\pi$  bands (blue) are also shown for the full Brillouin zone in (c). Partial-charge densities of a state at the  $\Gamma$  point for the  $\pi$  band (d), and the  $\sigma$  band (e).

The reciprocal lattice is again hexagonal (see fig. 5.2a) but rotated by 90 degrees with respect to the real space lattice. The reciprocal unit vectors are given by

$$\mathbf{b}_{1,2} = \frac{b}{2} \mathbf{e}_x \pm \frac{\sqrt{3}b}{2} \mathbf{e}_y, \quad b = \frac{4\pi}{\sqrt{3}} \frac{1}{a} \quad (5.2)$$

and the shaded hexagon corresponds to the Brillouin zone. We define the high symmetry points  $\Gamma$ ,  $K$ , and  $M$  as the centre, the corner, and the centre of the edge, respectively.

### Single-Particle Bandstructure

The electronic band structure<sup>1</sup> along the high symmetry line  $M$ – $K$ – $\Gamma$ – $M$  is shown in fig. 5.2b. Below the Fermi energy at 0 eV, we distinguish four valence bands. At zero temperature, each of them is occupied with two of the eight valence electrons in the primitive unit cell. The 1s core states of carbon are at much lower energies ( $\approx -300$  eV) and will be considered to be chemically inert in the following discussion.

In a tight-binding description, the three lowest bands are formed by the three  $sp^2$  hybridised atomic orbitals which point in direction of the three neighbouring atoms. These so-called  $\sigma$  states are mainly localised inside the plane, close to the atoms and have thus a rather low energy (see fig. 5.2e). The corresponding anti-binding  $\sigma^*$  states are found more than 5 eV above the Fermi level. The remaining  $p_z$  orbitals which are perpendicular to the plane, form the bonding  $\pi$  band (highest occupied valence state) and anti-binding  $\pi^*$  band (lowest unoccupied conduction state). These states are delocalised, have a node at the graphene plane, and therefore small binding energies (see fig. 5.2d).

<sup>1</sup>Here, only the Kohn-Sham eigenvalues are shown. Compare with discussion in section 3.1.2.

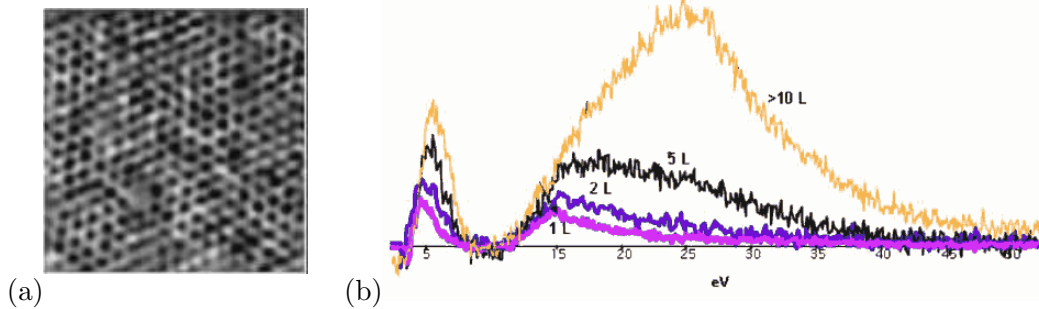


**Fig. 5.3:** (a) Annular dark field STEM image of a free-standing graphene sheet. (b) Experimental electron energy-loss spectra of one, two, five and many layers of graphene. Main features are the  $\pi$ - and  $\pi+\sigma$ -plasmon excitations at about 6 eV and 15–25 eV, respectively. Both figures are reproduced from [141], © 2008 by The American Physical Society.

The  $\pi$  and  $\pi^*$  bands are degenerate at the K point where they cross the Fermi level. As a consequence, undoped graphene is a zero-gap semiconductor, with a Fermi surface that only consists of six points at the edges of the Brillouin zone (see fig. 5.2c). At these points, the bands are *linear* in a good approximation. Thus, the electrons at the Fermi level have a constant group velocity  $v_F \approx 10^6$  m/s and a vanishing effective mass like photons! This peculiar behaviour gives rise to new phenomena, such as a fractional quantum hall effect or phenomena known from quantum electrodynamics [5]. These effects are restricted to very small excitation energies of the order of few 100 meV. Beyond this limit, bandstructure effects and the dispersion of the bands become dominant.

### Collective Excitations

The collective excitations of graphene have been recently studied by Eberlein *et al.* [141], Gass *et al.* [142]. Using a scanning transmission electron microscope, they were able to measure the electron energy-loss spectrum of single- and few-layer graphene in vacuum (fig. 5.3). The two main features are due to a charge oscillation of the  $\pi$  electrons at low energies and of both  $\pi$  and  $\sigma$  electrons at high energies [see fig. 5.2(d) and (e), respectively]. For isolated graphene, the  $\pi$  and  $\pi + \sigma$  surface-plasmon excitations are found at 4.7 eV and 14.6 eV, respectively. In systems with more and more layers, their energy increases until it reaches the value of bulk graphite (>10 layers). Thus, the inelastic-scattering signal can be used to determine the number of layers in a graphene sample and to distinguish single-layer and few-layer graphene.

*But, how can we describe the excitations in a single layer of graphene theoretically?* The effective-medium approach, i. e., to model the system by a thin slab of homogeneous bulk material, is of course questionable in the case of a monoatomic layer. In the following, we will therefore use *ab-initio* calculations to derive the momentum- and energy-dependent EEL spectra of single- and few-layer graphene. However, for the physical understanding it is useful to review the simplest approaches first.

## 5.2 Models for the Dielectric Properties

We consider two models for the dielectric properties of an isolated two-dimensional system: First, one can apply effective-medium theory considering a thin slab of homogeneous material in the limit of vanishing thickness. Second, the tight-binding (TB) approach can be used to calculate the dielectric response of a graphene layer in random phase approximation.

### 5.2.1 Dielectric Theory

Using classical electromagnetic theory, Ritchie [35] has calculated the energy loss of fast electrons traversing a thin foil of thickness  $d$ .<sup>2</sup> In the limit of a thick slab, the two planar interfaces do not interact with each other and the energy-loss probability becomes very similar to eq. (1.1).

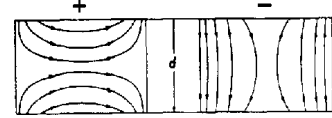


**Fig. 5.4:** Surface modes [30].

It only differs in the prefactor  $K_0$  for the contributions from the two surfaces. Using the Lorentz model (1.4) for the dielectric function of the slab, one finds a volume plasmon at  $(\omega_p^2 + \omega_0^2)^{1/2}$  and two degenerate surface-plasmon excitations at  $(\omega_p^2/2 + \omega_0^2)^{1/2}$ . For thin slabs, the bulk contribution vanishes with  $d$  and the surface modes start to interact with each other (see fig. 5.4). One obtains two different surface-plasmon frequencies depending on whether the electrons on the two sides oscillate in phase (+) or out-of phase (-) [30]

$$\omega_{\pm}^2(q) = \frac{1}{2}(1 \pm e^{-qd})\omega_p^2 + \omega_0^2, \quad q = 2\pi/\lambda. \quad (5.3)$$

The frequency of these modes now depends on the momentum transfer  $q$  parallel to the slab, i. e., the wavelength  $\lambda$  of the charge oscillation. For large  $qd \gg 1$ , one recovers the limit of the thick film. For small  $qd \ll 1$ , instead, tangential oscillations at frequency

$$\omega_- = (\omega_p^2 qd/2 + \omega_0^2)^{1/2} \quad (5.4)$$

become dominant and normal oscillations at frequency  $\omega_+^2 = \omega_p^2 + \omega_0^2$  can be associated with the depolarisation effect. Clearly, it depends on the in-plane momentum transfer  $q$  if the slab can be considered to be thin or not. Concerning the plasmon dispersion in graphene, we might expect to find the square-root behaviour of the tangential mode (5.4) for momentum transfers  $q < 1 \text{ \AA}^{-1}$ . However, the application of effective-medium theory for the description of atomically thin sheets is very questionable.

### 5.2.2 Tight-Binding

During this thesis, I have implemented a minimal tight-binding approach for graphene in order to complement our *ab-initio* results and to facilitate their interpretation. For simplicity, we consider only  $\pi$  orbitals and limit ourselves to nearest-neighbour interactions. Despite this crude approximation, the results are sufficient for a qualitative description of the excitation properties of graphene. Indeed, we should consider even third-nearest-neighbour interactions for an accurate description of the  $\pi$  bands [144], as well as contributions from  $\sigma$  orbitals at higher energies [145]. We follow [4, 146].

<sup>2</sup>The plasmon dispersion of multi-layer systems has been discussed by Fetter [143].

## Schrödinger Equation

For the ground-state problem, we have to calculate the energies and the wave functions of the  $\pi$  bands, i. e., we have to solve the effective single-particle Schrödinger equation

$$H\psi_{n\mathbf{k}}(\mathbf{r}) = E_{n\mathbf{k}}\psi_{n\mathbf{k}}(\mathbf{r}), \quad \psi_{n\mathbf{k}}(\mathbf{r} + \mathbf{R}) = e^{i\mathbf{k}\mathbf{R}}\psi_{n\mathbf{k}}(\mathbf{r}). \quad (5.5)$$

Due to crystal symmetry, a translation of the wave function  $\psi$  by an arbitrary lattice vector  $\mathbf{R}$  introduces only a phase shift. Thus, the wave function can be written as a Bloch function  $\psi_{n\mathbf{k}}$  with band index  $n$  and the (two-dimensional) wave vector  $\mathbf{k}$ . With Born-van-Kármán boundary conditions  $\psi(\mathbf{r} + N_i\mathbf{a}_i) = \psi(\mathbf{r})$  along the two directions  $\mathbf{a}_1$  and  $\mathbf{a}_2$ , the wave vector becomes discrete (see appendix A.3.1).

Starting point for the tight-binding approach is the construction of two families of Bloch functions  $\phi_{\mathbf{k}}^A$  and  $\phi_{\mathbf{k}}^B$  which form a complete set of orthonormal wave functions,

$$\phi_{\mathbf{k}}^\alpha(\mathbf{r}) = \frac{1}{\sqrt{N}} \sum_{\mathbf{R}} e^{i\mathbf{k}(\mathbf{R}+\boldsymbol{\tau}_\alpha)} \varphi^\alpha(\mathbf{r} - \mathbf{R}), \quad \varphi^\alpha(\mathbf{r}) = \varphi_z(\mathbf{r} - \boldsymbol{\tau}_\alpha), \quad \alpha \in \{A, B\}. \quad (5.6)$$

They are given as linear combination of the normalised atomic orbitals  $\varphi_z$  of the sublattice of  $A$  or  $B$  atoms at positions  $\boldsymbol{\tau}_A + \mathbf{R}$  and  $\boldsymbol{\tau}_B + \mathbf{R}$  (white or black dots in fig. 5.1, respectively). The sum runs over the totality of  $N = N_1N_2$  unit cells in the normalisation box with the corresponding lattice vectors  $\mathbf{R}$ . Expanding  $\psi_{n\mathbf{k}}$  in the basis (5.6),

$$\psi_{n\mathbf{k}}(\mathbf{r}) = C_{n\mathbf{k}}^A \phi_{\mathbf{k}}^A(\mathbf{r}) + C_{n\mathbf{k}}^B \phi_{\mathbf{k}}^B(\mathbf{r}), \quad \mathcal{C}_{n\mathbf{k}} \equiv (C_{n\mathbf{k}}^A, C_{n\mathbf{k}}^B)^T, \quad (5.7)$$

we can rewrite the Schrödinger equation (5.5) in matrix notation ( $\alpha, \beta \in \{A, B\}$ ) [4]

$$\mathcal{H}_{\mathbf{k}} \mathcal{C}_{n\mathbf{k}} = E_{n\mathbf{k}} \mathcal{S}_{\mathbf{k}} \mathcal{C}_{n\mathbf{k}}, \quad \mathcal{H}_{\mathbf{k}}^{\alpha\beta} = \langle \phi_{\mathbf{k}}^\alpha | H | \phi_{\mathbf{k}}^\beta \rangle, \quad \mathcal{S}_{\mathbf{k}}^{\alpha\beta} = \langle \phi_{\mathbf{k}}^\alpha | \phi_{\mathbf{k}}^\beta \rangle. \quad (5.8)$$

For each wave vector  $\mathbf{k}$ , this equation corresponds to a generalised eigenvalue problem. Assuming, that we know the  $2 \times 2$  *transfer-integral matrix*  $\mathcal{H}_{\mathbf{k}}$  and the *overlap-integral matrix*  $\mathcal{S}_{\mathbf{k}}$ , we can easily calculate the eigenvalues  $E_{n\mathbf{k}}$  and eigenvector coefficients  $\mathcal{C}_{n\mathbf{k}}$ .

## Transfer and Integral Matrix Elements

Of course, we do not know neither  $\mathcal{H}$  nor  $\mathcal{S}$ . But we can simplify the problem within the tight-binding approximation using the localisation of the atomic orbitals  $\varphi_z(\mathbf{r})$  and the geometry of the crystal. Unknown quantities are considered as *fitting parameters* that can be determined by a comparison with experiments or *ab-initio* calculations.

First, we consider the on-site matrix element  $\mathcal{H}^{AA}$ . With eq. (5.6) we find

$$\mathcal{H}_{\mathbf{k}}^{AA} = \frac{1}{N} \sum_{\mathbf{R}, \mathbf{R}'} e^{-i\mathbf{k}(\mathbf{R}-\mathbf{R}')} \langle \varphi^A(\mathbf{r}-\mathbf{R}) | H | \varphi^A(\mathbf{r}-\mathbf{R}') \rangle \stackrel{\text{NN}}{\approx} \langle \varphi_z | H | \varphi_z \rangle \equiv E_0. \quad (5.9)$$

In nearest-neighbour (NN) approximation, we keep only the on-site term  $\mathbf{R} = \mathbf{R}'$ , assuming that the matrix elements vanish for  $\mathbf{R} \neq \mathbf{R}'$  due to the small overlap between atomic

orbitals localised at A atoms of different unit cells (they are at least second-nearest neighbours). Due to the equivalence of the two carbon atoms, we have  $\mathcal{H}^{AA} = \mathcal{H}^{BB} \equiv E_0$ .

The evaluation of the hopping term  $\mathcal{H}^{AB}$  follows the same idea:

$$\begin{aligned} \mathcal{H}_k^{AB} &= \frac{1}{N} \sum_{\mathbf{R}, \mathbf{R}'} e^{-i\mathbf{k}(\mathbf{R} + \boldsymbol{\tau}_A - \mathbf{R}' - \boldsymbol{\tau}_B)} \langle \varphi^A(\mathbf{r} - \mathbf{R}) | H | \varphi^B(\mathbf{r} - \mathbf{R}') \rangle \\ &\stackrel{\text{NN}}{\approx} \sum_{j=1}^3 e^{i\mathbf{k}\mathbf{t}_j} \langle \varphi_z(\mathbf{r}) | H | \varphi_z(\mathbf{r} - \mathbf{t}_j) \rangle \equiv g(\mathbf{k})\gamma_0. \end{aligned} \quad (5.10)$$

We have kept only contributions from the three nearest neighbours at position  $\mathbf{t}_j$  (see fig. 5.5c). Due to the 3-fold symmetry, the *interaction energy*  $\gamma_0 = \langle \varphi_z(\mathbf{r}) | H | \varphi_z(\mathbf{r} - \mathbf{t}_j) \rangle$  is identical for all three neighbours  $j$ . The geometry factor  $g(\mathbf{k})$  can be evaluated as<sup>3</sup>

$$g(\mathbf{k}) = \sum_{j=1}^3 e^{i\mathbf{k}\mathbf{t}_j} = e^{i\mathbf{k}(\mathbf{a}_1 + \mathbf{a}_2)/3} \left( 1 + e^{-i\mathbf{k}\mathbf{a}_1} + e^{-i\mathbf{k}\mathbf{a}_2} \right). \quad (5.11)$$

Analogously, the overlap-integral matrix elements are given by

$$\mathcal{S}^{AA} = \mathcal{S}^{BB} = 1, \quad \mathcal{S}^{AB} = (\mathcal{S}^{BA})^* = s_0 g(\mathbf{k}), \quad (5.12)$$

where we have introduced the *overlap integral*  $s_0 = \langle \varphi_z(\mathbf{r}) | \varphi_z(\mathbf{r} - \mathbf{t}_j) \rangle$  with  $0 \leq s_0 \leq 1$ .

## Bandstructure and Wave Functions

With these nearest-neighbour matrix elements, the Schrödinger equation (5.8) now reads

$$\begin{pmatrix} E_0 & \gamma_0 g(\mathbf{k}) \\ \gamma_0 g^*(\mathbf{k}) & E_0 \end{pmatrix} \begin{pmatrix} C^A \\ C^B \end{pmatrix} = E_{n\mathbf{k}} \begin{pmatrix} 1 & s_0 g(\mathbf{k}) \\ s_0 g^*(\mathbf{k}) & 1 \end{pmatrix} \begin{pmatrix} C^A \\ C^B \end{pmatrix}. \quad (5.13)$$

where  $E_0$ ,  $\gamma_0$ , and  $s_0$  are empirical fitting parameters. The two solutions of this equation correspond to a bonding ( $\epsilon_v = +1$ ) and anti-bonding state ( $\epsilon_c = -1$ ) which are given by

$$\begin{aligned} E_{n\mathbf{k}} &= \frac{E_0 + \epsilon_n \gamma_0 |g(\mathbf{k})|}{1 + \epsilon_n s_0 |g(\mathbf{k})|}, & \psi_{n\mathbf{k}} &= A_n (\phi_{\mathbf{k}}^A + B_n \phi_{\mathbf{k}}^B), \\ A_n(\mathbf{k}) &= \left( 1 + |B_n|^2 + 2s_0 \text{Re}\{g(\mathbf{k})B_n\} \right)^{-\frac{1}{2}}, & B_n(\mathbf{k}) &= \frac{E_{n\mathbf{k}} - E_0}{g(\mathbf{k})(\gamma_0 - s_0 E_{n\mathbf{k}})}. \end{aligned} \quad (5.14)$$

The three unknown parameters have to be determined by comparison with experiments or *ab-initio* calculations. Considering the expression for the bandstructure in eq. (5.14), we can already restrict the parameter range. At the K point  $(2\mathbf{b}_1 + \mathbf{b}_2)/3$ , the geometry factor  $g(\mathbf{k})$  vanishes and the valence and conduction bands become degenerate with an energy  $E_0$ . In undoped graphene, this energy corresponds to the Fermi level and thus  $E_0 = 0$  eV. Additionally,  $\gamma_0$  has to be negative in order to have  $E_{v\mathbf{k}} \leq E_{c\mathbf{k}}$ .<sup>4</sup> Typically, values of  $\gamma_0$  between  $-2.5$  eV and  $-3$  eV and overlap integrals  $s_0 < 0.1$  are used.

<sup>3</sup>Our notation differs from Reich *et al.* [146] as they use  $-\mathbf{t}_j$  for the nearest-neighbour positions instead.

<sup>4</sup>In some references [e.g. 147, 148],  $\gamma_0$  is defined to be positive, i. e.,  $-\gamma_0$  has to be used in all equations.

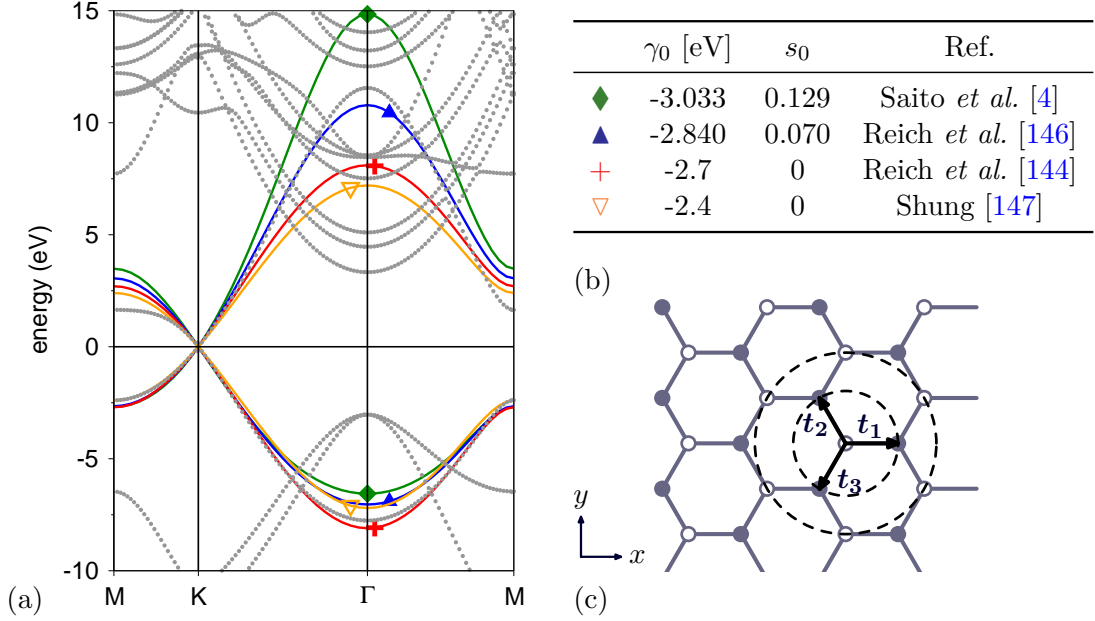


**Fig. 5.5:** Tight-binding bandstructure of graphene in nearest-neighbour approximation. (a) The  $\pi$  bands (lines) are calculated from eq. (5.14) for different parameters  $\gamma_0$  and  $s_0$  taken from literature (b). For comparison, an *ab-initio* bandstructure (dots) of LDA Kohn-Sham energies is shown. (c) Nearest and second-nearest neighbours of the A atom.

In figure 5.5, we compare the *ab-initio* bandstructure of graphene with the  $\pi$  bands calculated using the tight-binding approximation for different parameters  $\gamma_0$  and  $s_0$ . The overall shape of the  $\pi$  bands is quite satisfactory, if the overlap  $s_0$  is taken into account. Without overlap, the valence and conduction band are symmetric with respect to the Fermi level.

Most importantly, the simple tight-binding model describes the linear dispersion of the  $\pi$  bands in the vicinity of the K point [149], the so-called *Dirac cone*. An expansion of eq. (5.14) in  $\mathbf{k}$  around the K point gives a Fermi-velocity of  $v_F = -\gamma_0 a \sqrt{3}/2$ . However, for an accurate description of the full  $\pi$ -band dispersion, a tight-binding model including interactions even with the third-nearest neighbours has to be used [144].

### Independent-Particle Polarisability $\bar{\chi}^0$

So far, we have only considered ground-state properties. Now, we will turn to the collective excitations of graphene by calculating the dielectric response in RPA [147, 148]. Following section 3.2.3, we start with the independent-particle polarisability  $\bar{\chi}_{\mathbf{G}\mathbf{G}'}^0(\mathbf{q}, \omega)$  which is given by eq. (3.14). We neglect crystal local-field effects and calculate only the macroscopic component  $\bar{\chi}_{\mathbf{0}\mathbf{0}}^0$ . Having already an analytic expression for the tight-binding energies, the remaining problem is the calculation of the  $\mathbf{q}$ -dependent matrix elements  $\tilde{\rho}_{\mathbf{k}}^{nn'}(\mathbf{q}) = \langle \psi_{n'\mathbf{k}-\mathbf{q}} | e^{-i\mathbf{q}\mathbf{r}} | \psi_{n\mathbf{k}} \rangle$  or, equivalently,  $\tilde{\rho}_{\mathbf{k}}^{\alpha\beta}(\mathbf{q}) = \langle \phi_{\mathbf{k}-\mathbf{q}}^\alpha | e^{-i\mathbf{q}\mathbf{r}} | \phi_{\mathbf{k}}^\beta \rangle$ . Similar to the

evaluation of  $\mathcal{H}^{\alpha\beta}$  in eq. (5.9) and (5.10), one finds in nearest-neighbour approximation

$$\tilde{\rho}_{\mathbf{k}}^{AA}(\mathbf{q}) = \langle \varphi_z | e^{-i\mathbf{q}\mathbf{r}} | \varphi_z \rangle, \quad \tilde{\rho}_{\mathbf{k}}^{AB}(\mathbf{q}) = \sum_{j=1}^3 e^{i\mathbf{k}\mathbf{t}_j} \langle \varphi_z(\mathbf{r}) | e^{-i\mathbf{q}\mathbf{r}} | \varphi_z(\mathbf{r} - \mathbf{t}_j) \rangle. \quad (5.15)$$

Due to the  $\mathbf{q}$  dependence, we cannot proceed as before and simply introduce two new fitting parameters. Instead, we will use a model function for the atomic orbital  $\varphi_z(\mathbf{r})$  in order to calculate the remaining matrix elements. For the sake of simplicity, we will ignore the overlap between neighbouring atoms in the following, i. e., we let  $s_0 = 0$  and neglect the matrix elements  $\tilde{\rho}_{\mathbf{k}}^{AB}(\mathbf{q})$  which actually correspond to the Fourier transform of the overlap. The tight-binding energies and wave functions (5.14) then read

$$E_{n\mathbf{k}} = E_0 + \epsilon_n \gamma_0 |g(\mathbf{k})|, \quad \psi_{n\mathbf{k}} = \frac{1}{\sqrt{2}} \left( \phi_{\mathbf{k}}^A + \epsilon_n \frac{g^*(\mathbf{k})}{|g(\mathbf{k})|} \phi_{\mathbf{k}}^B \right) \quad (5.16)$$

and one finally obtains with  $\tilde{\rho}_{\mathbf{k}}^{AB} = \tilde{\rho}_{\mathbf{k}}^{BA} = 0$  and  $\tilde{\rho}_{\mathbf{k}}^{AA} = \tilde{\rho}_{\mathbf{k}}^{BB}$

$$\tilde{\rho}_{\mathbf{k}}^{nn'}(\mathbf{q}) = \frac{I(\mathbf{q})}{2} \left[ 1 + \epsilon_n \epsilon_{n'} \frac{g(\mathbf{k} - \mathbf{q}) g^*(\mathbf{k})}{|g(\mathbf{k} - \mathbf{q})| |g(\mathbf{k})|} \right], \quad I(\mathbf{q}) = \langle \varphi_z | e^{-i\mathbf{q}\mathbf{r}} | \varphi_z \rangle. \quad (5.17)$$

The matrix elements for intraband ( $c \rightarrow c$  and  $v \rightarrow v$ ) and interband ( $c \rightarrow v$  and  $v \rightarrow c$ ) transitions differ only in the sign  $\epsilon_n \epsilon_{n'}$ . Note, that  $\mathbf{k}$  is a two-dimensional wave vector and  $\mathbf{q}$  is understood to be parallel to the plane, i. e.,  $q_z = 0$ .

### Momentum Distribution of $\varphi_z$

Following Zener [150], the  $2p_z$  orbital of the Carbon atom has the same functional form as the Hydrogen  $1p_z$  orbital and is approximately given by

$$\varphi_z(\mathbf{r}) = A r \cos \vartheta \exp\left[-\frac{Zr}{2a_0}\right], \quad z = r \cos \vartheta, \quad (5.18)$$

where  $Z = 3.18$  is a fitting parameter corresponding to an effective core charge. The normalisation constant  $A$  is determined by  $\langle \varphi_z | \varphi_z \rangle = 1$  and  $a_0$  denotes the Bohr radius. For an in-plane momentum  $\mathbf{q} = (\bar{\mathbf{q}}, q_z = 0)$ , we obtain for the momentum distribution [147]

$$I(\bar{\mathbf{q}}, q_z = 0) = \int d\mathbf{r} |\varphi_z(\mathbf{r})|^2 e^{-i\bar{\mathbf{q}}\mathbf{r}} = \left[ 1 + \left( \frac{a_0 \bar{q}}{Z} \right)^2 \right]^{-3}. \quad (5.19)$$

Collecting all terms, we have now an analytic approximation for the contribution of the  $\pi$  bands to the polarisability of graphene.

### Dielectric Function in RPA

In RPA, the dielectric function of a two-dimensional layer is given by [147]

$$\bar{\epsilon}(\bar{\mathbf{q}}, \omega) = \epsilon_\sigma - v_{2D} \bar{\chi}^0, \quad v_{2D} = \frac{e^2}{2\epsilon_0} \frac{1}{\bar{q}}, \quad (5.20)$$

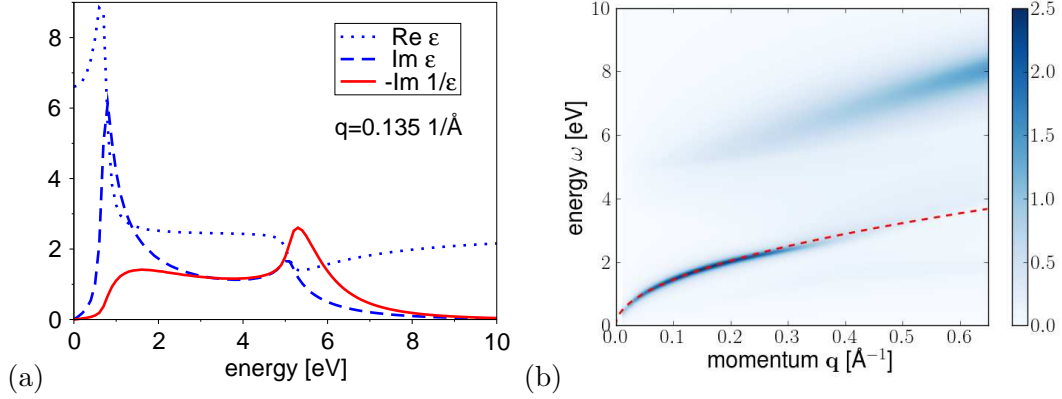


**Fig. 5.6:** (a) Dielectric function  $\bar{\epsilon}$  and EEL spectrum  $-\text{Im} 1/\bar{\epsilon}$  for undoped graphene calculated within the tight-binding approximation. The momentum transfer  $|\mathbf{q}| = 0.135 \text{ \AA}^{-1}$  is chosen along the  $\Gamma\text{M}$  direction. (b) Plasmon dispersion for doped graphene ( $E_F = 1.9 \text{ eV}$ ) with increasing momentum transfer  $|\mathbf{q}|$  along the  $\Gamma\text{K}$  direction. Additionally to the  $\pi$  plasmon at 7 eV, an intraband plasmon with square-root dispersion (dashed line) appears at small energies.

The two-dimensional Coulomb potential  $v_{2\text{D}}$  accounts for the modified screening properties of the charges localised on a two-dimensional sheet as compared to the three-dimensional case. This important point will be discussed in detail in section 5.4. The background dielectric constant  $\epsilon_\sigma = 2.4$  accounts for the contributions of the  $\sigma$  electrons to the screening of the system [151]. This is necessary because only the  $\pi$  bands were explicitly taken into account in our tight-binding approach. Finally, the electron energy-loss spectrum is given by  $-\text{Im} 1/\bar{\epsilon}$  as we have seen before.

## Discussion

First, we consider the case of undoped graphene where only *interband* transitions contribute. Figure 5.6a shows the calculated dielectric function and the EEL spectrum (solid line) for a small in-plane momentum transfer  $q = 0.135 \text{ \AA}^{-1}$  using the tight-binding parameters  $\gamma_0 = -2.5 \text{ eV}$ ,  $s_0 = 0$ , and  $\epsilon_0 = 2.4$  of reference [148, 152]. We find a  $\pi$ -plasmon excitation at about 5.2 eV, but also a strong shoulder at low energies (compare with fig. 5.3b). Similar calculations have been performed recently by Stauber *et al.* [153].

Second, we calculate the plasmon dispersion for n-doped graphene. The additional electrons form a 2D electron gas that can support a new plasma oscillation at low energies. The properties of this collective excitation can be tuned by changing the doping level and hence the 2D carrier density  $n$ . In our calculation we model n-doped graphene by simply increasing the Fermi level  $E_F$ . The conduction band then becomes partially occupied and *intraband* transitions contribute to the spectra. Figure 5.6b shows the calculated plasmon dispersion for a Fermi level  $E_F$  of 1.9 eV, i. e., a density of  $n \approx 2 \cdot 10^{14} \text{ cm}^{-2}$ . In agreement with previous tight-binding calculations [154, fig. 2a], we find a square-root behaviour for small momentum transfer  $q \rightarrow 0$ . Hwang and

Das Sarma [155] derived an analytical expression for the dispersion (see dashed line)

$$\omega \approx \bar{\omega}_p \sqrt{\bar{q}}, \quad \bar{\omega}_p^2 = 2e^2/E_F, \quad E_F = \gamma \sqrt{\pi n}, \quad \gamma = \frac{\sqrt{3}}{2} a \gamma_0, \quad (5.21)$$

where  $\gamma = 5.34 \text{ eV}\text{\AA}$  corresponds to the slope of the  $\pi$  bands near the K point. Note that the plasma frequency  $\bar{\omega}_p$  is proportional to  $n^{1/4}$  in contrast to the normal two-dimensional electron gas, where  $\omega_p \propto n^{1/2}$  [see eq. (1.2)].

Clearly, the tight-binding calculations can give important physical insight. Most of the quantities are given analytically and numerical simulations become very fast (the presented results have been calculated in a few seconds). However, their use for a detailed analysis of experiments is often limited: First, the results strongly depend on the fitting parameters. Their number increases rapidly, especially when more refined tight-binding models beyond the nearest-neighbour approximation are used. Second, the range of application is rather limited. Due to our approximations, we are restricted (*i*) to small energies ( $\hbar\omega < 10 \text{ eV}$ ), where only transitions between the  $\pi$  bands contribute and (*ii*) to small momentum transfers ( $\bar{q} < 1/a \approx 0.5 \text{ \AA}^{-1}$ ), so that the exact form of the orbitals is not very important and crystal local-field effects can be neglected.

## 5.3 Ab-Initio Calculations

To overcome the limitations of the models described above, we have performed *ab-initio* calculations for isolated graphene. In particular, all contributing valence and conduction states ( $\pi$ ,  $\sigma$  and empty states) are included, as well as crystal local-field effects (LFE).

### 5.3.1 Calculation Parameters

We will concentrate on the  $\pi$ -plasmon excitation in single graphene layers and stacked systems. Electron energy-loss spectra in the range of low energies (0–15eV) and for in-plane momentum transfers  $\mathbf{q}$  ( $0.1\text{--}1\text{\AA}^{-1}$ ) have been calculated using (time-dependent) density-functional theory. As described in section 3.3, first the electronic ground state of the system was calculated in DFT-LDA (local density approximation) with ABINIT [100]. A plane-wave basis set and norm-conserving pseudopotentials [108] have been used. Second, the Kohn-Sham band-structure and wave functions are taken as input for the DP-code [102] to compute the independent-particle polarisability  $\chi^0$  and the microscopic dielectric function  $\varepsilon_{\mathbf{G}\mathbf{G}'}(\mathbf{q}, \omega)$  of the system.

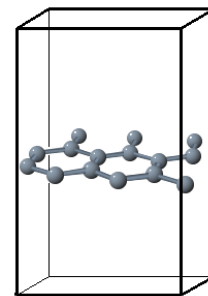


Fig. 5.7: Supercell

### Supercell Approach

Due to the plane-wave basis set, the finite system has to be included in a supercell which is periodically continued in every direction. One actually calculates the response of an infinite stack of identical graphene layers (AA stacking<sup>5</sup>) with an interlayer distance  $d$

<sup>5</sup>In bulk graphite, the stacking was found to have no influence on the loss function for in-plane momentum transfer  $\mathbf{q}$ . In the following, we will not distinguish between graphite in AA and AB stacking.

$d/d_0$	$d$ [Å]	$k$ -point grid	npwfn	nbands	npwmat	# Geometry
1	3.33	$44 \times 44 \times 4$	317	40	41	a : 4.631 Bohr
2	6.66	$44 \times 44 \times 2$	409	60	65	d0: 6.294 Bohr
4	13.3	$44 \times 44 \times 1$	817	80	83	# ground state
8	26.6	$44 \times 44 \times 1$	1555	80	199	ecut: 30 Ha
16	53.3	$44 \times 44 \times 1$	1999	150	299	toldfe: 1.0d-10
32	107	$44 \times 44 \times 1$	4983	200	609	# kss
						tolwfr: 1.0d-16
						shiftk: 0 0 0
						symmorphi: 0

**Tab. 5.1:** Calculation parameters of DP (left) and ABINIT (right) for graphene stacks with different interlayer distances  $d$ . The convergence of  $\varepsilon_M$  and EELS has been tested for in-plane momentum transfers  $\bar{q} < 2 \text{ \AA}^{-1}$  and excitation energies up to 15 eV using a broadening of 0.2 eV.

that is given by the height of the cell. In order to check that the interaction between the artificial replicas can be neglected, we consider increasing interlayer distances ranging from the graphite value  $d_0 = 3.33 \text{ \AA}$  up to huge distances of  $32d_0 = 11 \text{ nm}$ . In the limit of non-interacting sheets, the polarisability  $\pi(\mathbf{r}, \mathbf{r}')$  and the susceptibility  $\chi(\mathbf{r}, \mathbf{r}')$  have to be independent of the supercell size. The Fourier transformed quantities (A.42) are then inversely proportional to the volume  $\Omega$  of the supercell

$$\chi(\mathbf{q}, \mathbf{q}') \propto \Omega^{-1}, \quad \pi(\mathbf{q}, \mathbf{q}') \propto \Omega^{-1}, \quad \Omega \propto d/d_0 \quad (5.22)$$

and we have to scale the EEL spectra accordingly. For comparability, also the convergence parameters have to be adapted for each distance (see table 5.1). Increasing the supercell, the reciprocal lattice vector  $\mathbf{b}_3$  becomes smaller and we have to enhance npwfn and npwmat. Additionally, free-electron states enter the energy-range of interest so that the number of bands nbands has to be increased (see also fig. 5.19).

### 5.3.2 From Graphite to Graphene

Extending our previous work [130], we investigated the influence of the interlayer distance  $d$  on the macroscopic dielectric function  $\varepsilon_M$  and the loss spectrum  $-\text{Im} 1/\varepsilon_M$ .

#### Loss Function and $\text{Im} \varepsilon_M$

First, we consider the dielectric response of the graphene stack for large in-plane momentum transfer  $q = 0.27 \text{ \AA}^{-1}$  along the  $\Gamma M$  direction (see top of fig. 5.8). The loss spectrum (left panel) shows a  $\pi$ -plasmon peak which shifts to lower energies going from graphite to graphene. This is consistent with the experimental observations for few-layer graphene (see fig. 5.3b) and with the prediction of dielectric theory that surface excitations are lower in energy compared to the bulk excitations (see sec. 5.2.1).

In contrast, the imaginary part of the dielectric function  $\text{Im} \varepsilon_M$  (centre panel) shows the opposite behaviour. In the limit of isolated graphene,  $\text{Im} \varepsilon_M$  becomes equivalent to

(a)  $\left(\frac{d}{d_0}\right) - \text{Im } 1/\varepsilon_M$       (b)  $\left(\frac{d}{d_0}\right) \text{Im } \varepsilon_M$       (c)  $\left(\frac{d}{d_0}\right) \text{Im } v\chi_{00}^0$

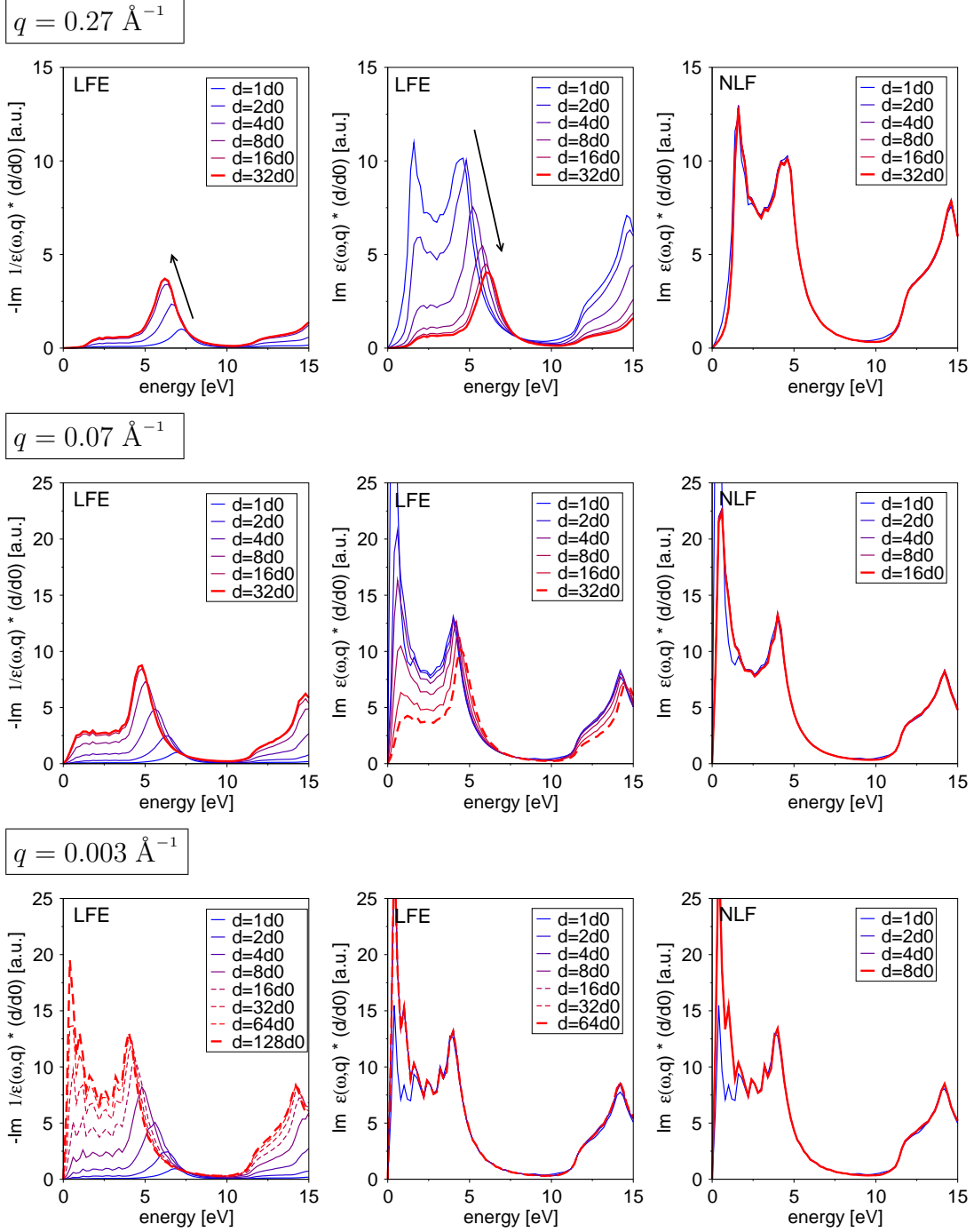


**Fig. 5.8:** Influence of the interlayer distance  $d$  on the dielectric properties of stacked graphene layers. We show (a) the EEL spectrum and (b) the macroscopic dielectric function  $\text{Im } \varepsilon_M$  for three different in-plane momentum transfers  $q$  along the  $\Gamma M$  direction. (c) Neglecting LFE, the dielectric function  $\text{Im } \varepsilon_M^{\text{NLF}} \propto \text{Im } \chi^0$  does not vary with  $d$ . All spectra are scaled by the factor  $d/d_0$ , where  $d_0 = 3.33 \text{ \AA}$  corresponds to the interlayer distance of graphite.

the EELS signal as the screening  $\varepsilon_M - 1 \propto \Omega^{-1}$  vanishes in finite systems [see eq. (5.22)]:

$$-\text{Im} \varepsilon_M^{-1} = \frac{\text{Im} \varepsilon_M}{(\text{Re} \varepsilon_M)^2 + (\text{Im} \varepsilon_M)^2} \xrightarrow{\Omega \rightarrow \infty} \text{Im} \varepsilon_M, \quad (5.23)$$

Note, that the loss spectra converge faster towards the graphene limit than  $\text{Im} \varepsilon_M$ .

### Crystal Local-Field Effects

The strong change of the spectra with the distance  $d$  is actually due to crystal local-field effects (LFE). It is well known, that they have only little influence on the in-plane excitations in bulk graphite [112]. Indeed,  $\text{Im} \varepsilon_M$  (centre panel) and  $\text{Im} \varepsilon_M^{\text{NLF}}$  (right panel) do not differ for  $d = d_0$ . Increasing the interlayer distance  $d$ , the results without LFE do not change at all, while  $\text{Im} \varepsilon_M$  converges towards the graphene loss function. Clearly, crystal local-field effects are of major importance for isolated sheets.

This is mainly due to the inhomogeneity of the system along the  $z$ -direction, while in-plane contributions are generally small. Indeed, for increasing interlayer distance  $d$ , the reciprocal lattice vector  $\mathbf{b}_3$  shortens and more and more perpendicular  $\mathbf{G}$ -vectors have to be included in the calculation in order to describe the localisation in real space with the same accuracy. The importance of crystal local-field effects in a supercell calculation is directly related to the depolarisation effects in the isolated system.

### Influence of the Momentum Transfer

In the second row of figure 5.8 we repeat our analysis for a small in-plane momentum transfer  $q = 0.07 \text{ \AA}^{-1}$ . In principle, the conclusions above change only quantitatively: First, LFE become less important for graphene (compare fig. 5.8b and c), as we would generally expect for smaller momentum transfers  $q$  [83]. Second, we need larger distances  $d$  in order to avoid interlayer interactions and to reach the limit of an isolated sheet. The latter can be explained with a simple dielectric analogue (see also [156]): Assuming a homogeneous 2D electron gas for each layer, the perturbation with in-plane momentum transfer  $q$  will induce charge oscillations of wavelength  $2\pi/q$  in each plane. The electrostatic interaction between the sheets does not change if both the wavelength and the distance are scaled by the same factor. Its strength is determined by the parameter<sup>6</sup>  $qd$  and vanishes if  $qd \gg 1$ . Thus, larger distances  $d$  become necessary when  $q$  decreases.

This trend continues when  $q \rightarrow 0$  reaches the optical range (see bottom of figure 5.8). In this limit, LFE become even unimportant for the graphene spectra, but very large distances  $d > 50 \text{ nm}$  are necessary to converge the loss function.

### Convergence to the Loss Function of Graphene

In the optical limit,  $\text{Im} \varepsilon_M$  converges already for very small  $d$ , i. e., much faster than the loss spectrum. The opposite has been found for large momentum transfers. This behaviour can be understood by the fact that the difference between  $\text{Im} \varepsilon_M$  and the loss

<sup>6</sup>Note that the same factor  $qd$  already appeared in the discussion of a thin slab (see section 5.2.1).

$q$ [ $1/\text{\AA}$ ]	(a) with LFE		(b) without LFE	
	EELS	$\text{Im } \varepsilon$	EELS	$\text{Im } \varepsilon$
0.001	$d > 500 \text{ \AA}$	$d > 7 \text{ \AA}$	–	$d > 7 \text{ \AA}$
0.07	$d > 30 \text{ \AA}$	$d > 150 \text{ \AA}$	–	$d > 7 \text{ \AA}$
0.3	$d > 10 \text{ \AA}$	$d > 50 \text{ \AA}$	$d > 200 \text{ \AA}$	$d > 4 \text{ \AA}$
1.3	$d > 7 \text{ \AA}$	$d > 30 \text{ \AA}$	$d > 60 \text{ \AA}$	$d > 4 \text{ \AA}$

**Tab. 5.2:** Minimal interlayer distance  $d$  for isolated graphene sheets.

spectrum is given by the *macroscopic* component  $v_0 \propto 1/q^2$  of the Coulomb potential, which only contributes to the loss spectrum [83]. As the two spectra have to coincide for graphene, it is  $v_0$  which determines the convergence: For small  $q$ , this component diverges and large distances are necessary to converge the loss spectrum (bottom). For large  $q$ , instead, *microscopic* components  $v_{G \neq 0}$  (i. e., LFE) become more important and screen  $v_0$ . In this case, the loss spectrum converges faster than  $\text{Im } \varepsilon_M$  (top). We use this behaviour in our calculations for the loss function of graphene and use either  $\text{Im } \varepsilon_M$  or  $-\text{Im } 1/\varepsilon_M$ —whatever converges faster with the distance  $d$  (see table 5.2).

It is remarkable that in the optical limit  $q \rightarrow 0$  the loss function of graphene becomes identical to  $\text{Im } \varepsilon_M^{\text{NLF}}$ , i. e., the absorption spectrum of graphite neglecting LFE. This statement still holds when exchange-correlation effects are taken into account in the calculation of the polarisability  $\pi$ . A rigorous justification will be given in section 5.4.2.

### 5.3.3 Linear Plasmon Dispersion in Graphene

Having studied the convergence of the loss function with the interlayer distance  $d$ , we are now able to investigate the plasmon dispersion for isolated graphene. To this end, the loss function  $-\text{Im } \varepsilon^{-1}(\mathbf{q}, \omega)$  of graphene was calculated for different in-plane momentum transfers  $\mathbf{q}$  along the  $\Gamma\text{M}$  and  $\Gamma\text{K}$  directions with increasing modulus up to  $0.8 \text{ \AA}^{-1}$ . The results of our RPA calculation are shown in fig. 5.9b (thick line). In the range of 0.1 to 0.8 eV, we find an almost linear plasmon dispersion which is in very good agreement with EELS measurements on isolated single-wall carbon nanotubes with large radius (see [157] for details of the comparison). A very similar result can be found using the tight-binding calculations described in section 5.2.2 (see [152]). Also the dielectric model (5.4) might be fitted to our results obtaining  $\hbar\omega_0 \approx 4.4 \text{ eV}$  and  $\hbar^2\omega_p^2 d \approx 140 \text{ eV}^2 \text{ \AA}$ . For a detailed analysis, it is useful to investigate the loss spectra at different levels of approximation, namely (i) the independent-particle approximation (IPA) where exchange-correlation and local-field effects are completely neglected ( $\varepsilon_M^{\text{NLF}} = 1 - v\chi^0$ ) and (ii) the random phase approximation (RPA) which takes into account LFE via eq. (1.15).

#### Neglecting Local-Field Effects

Starting with the IPA, the loss function of isolated systems  $-\text{Im } 1/\varepsilon_M^{\text{NLF}} \propto \text{Im } \chi^0$  is directly given by the independent-particle response [see eq. (5.22)]. Thus, it can be

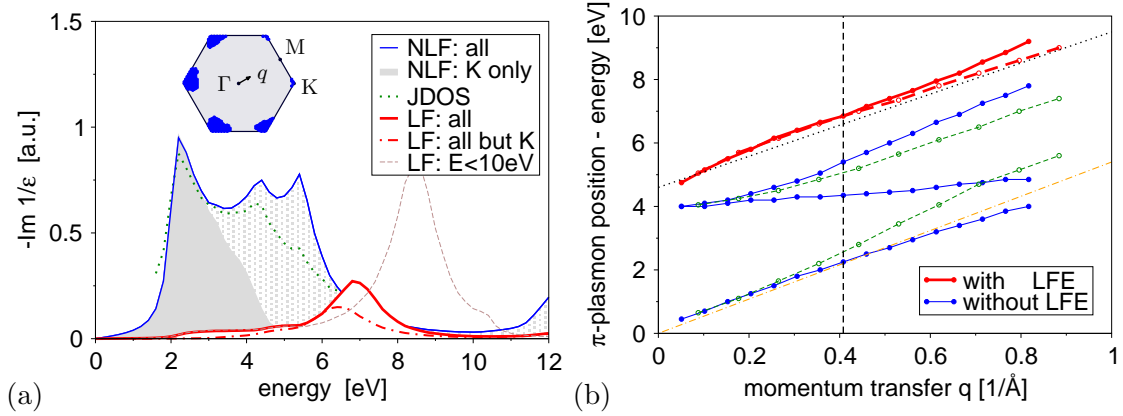


**Fig. 5.9:** (a) Loss function of graphene at  $q = 0.41 \text{ \AA}^{-1}$  along  $\Gamma M$  calculated from the JDOS (dots), within the bare RPA (blue) and in RPA including LFE (red, thick). The latter changes significantly, when transitions next to the K point (shaded area, see inset) are excluded (red, dot-dashed). (b) Dispersion of the peaks in the loss function for different momenta along  $\Gamma M$  (solid lines) and  $\Gamma K$  (dashed lines).

interpreted as a sum of independent transitions (3.14) which are directly related to the bandstructure. Figure 5.9a shows a typical spectrum for  $q = 0.41 \text{ \AA}^{-1}$ . In the low energy region ( $\hbar\omega < 10 \text{ eV}$ ), only transitions between the  $\pi$  and  $\pi^*$  bands contribute to the spectrum which consists of three peaks in  $\Gamma M$  direction (blue solid line) but only two peaks for  $\Gamma K$  (not shown). In fig. 5.9b the corresponding dispersion curves are depicted (blue solid & green dashed lines). The first peak arises from transitions that are localised around the K point in reciprocal space (see inset<sup>7</sup>). According to the linear  $\pi$  bands in this region, the peak disperses *linearly* from 0.5 eV to 4.0 eV with a slope of  $\gamma = 5.4 \text{ eV \AA}$ . This is in good agreement with the slope of the  $\pi$  bands used in the tight-binding calculations before [see eq. (5.21)]. The second peak, only visible for  $\Gamma M$ , is a weaker structure around 4 eV and shows almost no dispersion. The last peak starting at 4.0 eV shows a quadratic dispersion at small  $q$ . It is attributed to transitions near the edge of the Brillouin zone close to M. This peak is almost undetectable when matrix elements are ignored (dotted line in fig. 5.9a) like in the joint density-of-states (JDOS).

### Including Local-Field Effects

We have seen before, that crystal local-field effects have a strong influence on the loss-functions of graphene for  $q > 0$ . They almost completely suppress the linearly dispersing low-energy structure as well as the very weakly dispersing second peak. Instead, the peak starting at 4 eV is blue shifted by about 0.8 eV and becomes the dominant structure in the spectrum. Its dispersion is strongly modified: LFE transform the formerly quadratic

<sup>7</sup>The inset shows all  $k$  points in the Brillouin zone which contribute to  $\text{Im} \chi^0$  at 2.4 eV ( $\eta = 0.2 \text{ eV}$ , final  $k$  points). The 6-fold symmetry is broken due to the finite momentum transfer  $q$ . Calculating  $\text{Im} \chi^0$  including only these few  $k$  points, we obtain the dark shaded peak shown in fig. 5.9a.

dispersion into an almost linear one (red line in fig. 5.9b). One can understand the LFE as a mixing of transitions by the Dyson eq. (3.16).<sup>8</sup> The resulting spectra should therefore consist of a mixture of the formally distinct peaks. This can involve a significant energy range and it is interesting to see, whether the linearly dispersing low-energy peak has a considerable influence on the spectra including LFE.

### Which Transitions Contribute?

By excluding selected transitions from the summation in  $\chi^0$ , we can estimate their influence on the linear plasmon dispersion including LFE. First, we consider low energy contributions from the linear region of the  $\pi$  bands around the K point. Despite the very different energy ranges, the final loss is indeed significantly affected by the inclusion (red solid line) or exclusion (red dot-dashed line) of these transitions: in the latter case the dominant structure is reduced (the integrated intensity decreases by more than 30%) and red shifted by about 0.4 eV. There are, hence, considerable contributions from low energy transitions in the LFE corrected plasmon response.

Second, the same analysis can be repeated for high-energy transitions. We find that energies beyond 15 eV contribute to the plasmon, i. e., transitions between the  $\sigma$  bands are important, too. They basically screen the charge oscillation of the  $\pi$  electrons and shift the plasmon to lower energies. Indeed, the plasmon peak is found at much larger energies, if we exclude all transitions with energies larger than 10 eV (fig. 5.9a, dashed line). In the tight-binding calculations, these high-energy contributions have been taken into account empirically by the background dielectric constant  $\varepsilon_\sigma$  in eq. (5.20). Generally, if the transitions are clearly separated in energy, one can split the macroscopic dielectric function  $\varepsilon_M = 1 + v\chi_\pi + v\chi_\sigma$  according to the contributing electrons and use, e. g., a simple plasmon-pole model for the high-energy contributions  $\varepsilon_\sigma = 1 + v\chi_\sigma \approx \text{const}$  [151].

We conclude that the mixing of transitions of different energies also mixes the different dispersion relations. The resulting almost linear dispersion is indeed a superposition of the dispersion of the main structures in the IPA loss functions, including the low-energy peak originating from the ‘Dirac cone’ as well as the screening from the  $\sigma$  electrons.

### Excitonic Effects in the Optical Limit

In the optical limit  $q \rightarrow 0$ , our RPA calculations predict a plasmon peak at 3.95 eV and thus a square-root dispersion for very small  $q \ll 0.1$  eV (see bottom of fig. 5.8 and dispersion in fig. 5.9b). The tight-binding results of Huang *et al.* [152] show a parabolic dispersion, instead. In both calculations, exchange and correlation effects are neglected.

It is well-known that excitonic effects can become important in the limit  $q \rightarrow 0$  [158]. Their effect on the optical response of graphene is currently under debate [159, 160]. Yang *et al.* [159] have performed Bethe-Salpeter calculations on graphite and graphene and predict a main absorption peak at 4.5 eV and 4.55 eV, respectively. Unfortunately, only few experiments on graphene exist in this range, but the predictions are in good

<sup>8</sup>As the Dyson equation is nonlinear in  $\chi^0$ , its real and imaginary part will be mixed. The former contains contributions from all energies via the Kramers-Kronig transform  $\text{Re } \chi^0 = \frac{\mathcal{P}}{\pi} \int d\omega' \frac{\text{Im } \chi^0(\omega')}{\omega' - \omega}$ .

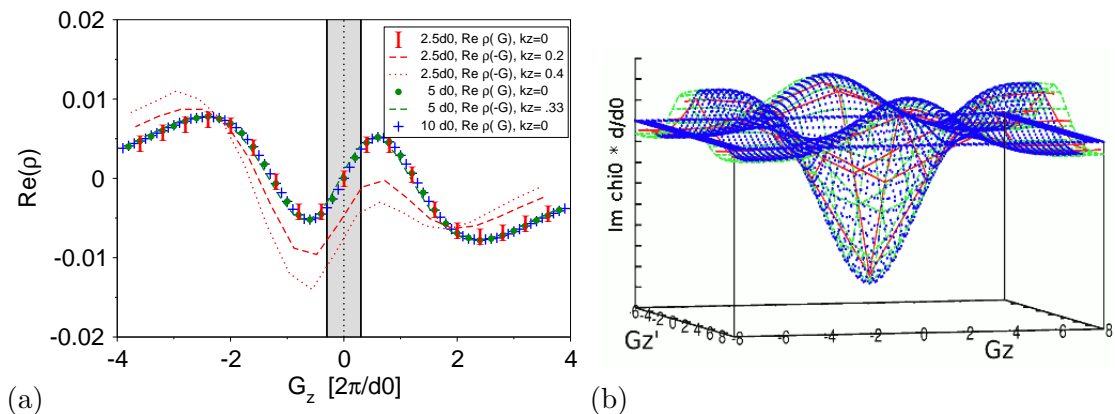


**Fig. 5.10:** Independent-particle quantities  $\tilde{\rho}$  and  $\chi^0$  for graphene stacks with different interlayer distances  $d = 2.5d_0$  (red),  $d = 5d_0$  (green), and  $d = 10d_0$  (blue) for a momentum transfer  $q = 0.27 \text{ \AA}^{-1}$  along  $\Gamma M$  and an energy  $\omega$  of 4 eV: (a) Matrix elements  $\tilde{\rho}_{\mathbf{k}\pi\pi^*}^{\pi\pi^*}(\mathbf{q} + \mathbf{G})$  in dependence of the z-component  $G_z$  for fixed in-plane components  $\bar{\mathbf{G}} = (G_x, G_y) = (0, 1)$ . We consider a transition between the  $\pi$  and  $\pi^*$  band at the  $k$  point  $\mathbf{k} = (4/11, 0, 0)$  (symbols) or  $k$  points with non-zero  $k_z$  component (lines). The region of interest is shaded in gray. (b) Independent-particle polarisability  $\chi_{\mathbf{G}\mathbf{G}'}^0$  (scaled by  $d/d_0$ ) depending on both  $G_z$  and  $G'_z$  for fixed  $\bar{\mathbf{G}} = \bar{\mathbf{G}}' = (0, 0)$ .

agreement with X-ray absorption measurements on isolated single-wall carbon nanotubes with large diameters (see fig. 6.15a, [161]). As the loss spectrum at  $q \rightarrow 0$  and the absorption spectrum become identical in finite systems [see eq. (5.22)], we can also expect a peak at 4.55 eV in the loss function of graphene. The energy shift with respect to the RPA results is due to a quasiparticle correction of +1.1 eV that is partially compensated by  $-0.6$  eV when electron-hole interactions are taken into account [159]. It is remarkable that we obtain the same energy of 4.5 eV if we extrapolate the linear plasmon dispersion that was calculated in RPA to  $q = 0$  (see fig. 5.9b). Also note, that *ab-initio* calculations of Trevisanutto *et al.* [160] have predicted a strong excitonic resonance at about 8.3 eV in graphene. High-resolution EELS measurements could help to verify their findings.

At finite momentum transfer  $q > 0$ , instead, we expect small corrections of the plasmon energy of the order of few 100 meV compared to the RPA results. However, the question of the importance of exchange-correlation effects for finite momentum transfers  $q$  is still an open problem and only few calculations are available in literature, e. g., [162, 163].

### 5.3.4 Numerical Extrapolation for Isolated Systems

In section 5.3.2 we found that the independent-particle polarisability  $\chi^0$  converges much faster with the interlayer distance  $d$  than the full susceptibility  $\chi$ . This is due to the long-range part  $v_0$  of the Coulomb interaction which couples neighbouring layers. It is tempting to separate the calculation of  $\chi^0$  and the solution of the Dyson equation (3.16)  $\chi = \chi^0 + \chi^0 v \chi$ . The independent-particle polarisability  $\chi^0$ , which is computationally the most demanding part, can be then calculated for a much smaller system.

## Microscopic Polarisability Matrix

So far we have only considered the convergence of the head element  $\chi_{00}^0$  of the microscopic polarisability matrix  $\chi_{\mathbf{G}\mathbf{G}'}$  (see fig. 5.8c). We might wonder, if even the full matrix is independent of the interlayer distance  $d$ . Therefore, we first consider the transition-matrix elements  $\tilde{\rho}$  which are the main ingredients of  $\chi_{\mathbf{G}\mathbf{G}'}$  [see eq. 3.14]. Figure 5.10a shows the typical example for the dependence of  $\tilde{\rho}_{\mathbf{k}}^{vc}(\mathbf{q}_r + \mathbf{G})$  on the z-component  $G_z$  for the AA stacked graphene layers. With increasing supercell size  $d$ , the lattice vector  $\mathbf{b}_3$  shrinks and the reciprocal lattice vectors  $\mathbf{G}$  become denser along the z-direction. For in-plane  $k$  points (symbols), we generally find that the matrix elements  $\tilde{\rho}$  of systems with large distances  $d$  (blue +) can be easily obtained from the ones of the bulk system (red I) by means of a simple *interpolation*. For non-zero  $k_z$  (lines), the corresponding wave function describes an electron that is moving in  $z$ -direction which is clearly irrelevant for the isolated case. Note, that  $\tilde{\rho}$  is approximately linear for the  $\mathbf{G}$  vectors that contribute significantly<sup>9</sup> to the LFE in graphene (indicated by the gray region).

Exactly the same behaviour is found for the independent-particle polarisability  $\chi^0$  itself. Figure 5.10b shows the dependence of  $\chi_{\mathbf{G}\mathbf{G}'}$  on  $G_z$  and  $G'_z$  which is found to be a smooth function. As in the case of  $\tilde{\rho}$ , we can obtain  $\chi^0$  for large interlayer separations from a calculation of  $\chi^0$  of a bulk-like system using a simple interpolation.

## Extrapolation to Isolated Systems

It is numerically more efficient to interpolate directly the summed quantity  $\chi^0$  instead of first interpolating all the transition-matrix elements  $\tilde{\rho}$  and summing afterwards. The interpolation method consists of the following three steps:

### Procedure I: Interpolation Method

1. Starting point is an *ab-initio* calculation of the microscopic bulk polarisability  $\chi_d^0$  for a stack of graphene layers with doubled interlayer distance  $d = 2d_0 \approx 7 \text{ \AA}$ . This assures that the Kohn-Sham orbitals of neighbouring layers do not overlap.<sup>10</sup> We restrict the  $k$ -point grid to the  $xy$ -plane ( $k_z = 0$  for all points).
2. The bulk polarisability  $\chi_d^0$  is read by a post-processing program and extrapolated to large distances  $D = N \cdot 2d_0$ . I have implemented two interpolation methods: a cubic-spline interpolation for the real and imaginary part of  $\chi_d^0(G_z, G'_z)$ , and a Fourier-interpolation method. As a result, we obtain a new polarisability  $\tilde{\chi}_D^0$  with more  $G$  vectors (factor of  $\approx N^2$ ).
3. Finally, we continue with the usual procedure of solving the Dyson eq. (3.16) and calculating the macroscopic dielectric response (see section 3.2.4).

<sup>9</sup>Increasing the dimension `npwmat` of the polarisability matrix  $\chi^0$  in the calculation for  $d = 10d_0$ , we find that already the first 6  $\mathbf{G}$  vectors give roughly converged loss spectra. In particular, these vectors are all pointing along the  $z$ -direction, i. e., in-plane LFE are not very important in graphene.

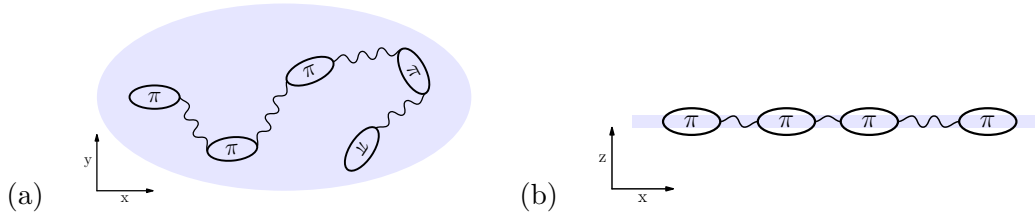


**Fig. 5.11:** Localisation of the susceptibility  $\chi = \pi + \pi v \pi + \dots$  in a two-dimensional system. (a) Inside the plane the response can be very delocalised, (b) but not in perpendicular direction.

This method reproduces exactly the corresponding *ab-initio* calculations for the isolated system, while we gain a factor of 100 in computation time (see fig. C.4a). Indeed, all dashed lines in fig. 5.8 have been calculated using the Fourier-interpolation method. Otherwise, *ab-initio* calculations with a supercell size of 50 nm would not have been feasible. A more detailed description of our implementation can be found in appendix C.4.

## 5.4 Local-Response Approximation

The discussion so far might have raised several questions, like: *What do we actually mean by strong local-field effects in graphene? Why do they vanish in the optical limit  $q \rightarrow 0$ ? At which point, these local-field effects enter in the tight-binding calculation? What can we learn from a comparison between the tight-binding and the full *ab-initio* results? Why do we use a different Coulomb potential  $v_{2D}$  in tight-binding, but not in our *ab-initio* calculations? And what is the connection between a 2D and a 3D response function?* We will answer these questions by reconsidering the response of a two-dimensional system from a theoretical point of view. The formalism is close to the dielectric theory of surfaces [33, 164] or the models developed for thin slabs including spatial dispersion [36].

### 5.4.1 Polarisability vs. Susceptibility

The polarisability  $\pi = \delta\rho^i / \delta\varphi^t$  is known to have a very small non-locality radius  $r_c$  of the order of a few Ångström [e.g. 121]. In RPA ( $\pi = \chi^0$ ), this can be understood if we rewrite the expression (3.14) for the independent-particle polarisability  $\chi^0$  in terms of Wannier functions [50] and assume that they have a finite spatial extent  $\mu$ . Indeed, Wannier functions are exponentially localised in insulators if time-reversal symmetry is satisfied [165, 166]. Similar to the tight-binding approximation, we can then neglect interactions between distant orbitals and we have

$$\pi(\bar{\mathbf{r}}, \bar{\mathbf{r}}') \approx 0, \quad \text{for } |\bar{\mathbf{r}} - \bar{\mathbf{r}}'| \gg \mu. \quad (\text{in-plane}) \quad (5.24)$$

<sup>10</sup>Note that even for  $d = d_0$ , the hybridisation of the wave functions from neighbouring layers are barely visible in the polarisability (see fig. 5.8c). Therefore we will not strictly distinguish between bulk systems with graphite interlayer distance  $d_0$  and artificial graphene stacks with  $d = 2d_0$  in the text.

In a slab, the orbitals are all localised at the  $z = 0$  plane. We can expect, that they vanish exponentially with a decay length  $\lambda$  of a few Ångstrom. Thus we have

$$\pi(z, z') \approx 0, \quad \text{for } |z| \gg \lambda, \text{ or } |z'| \gg \lambda. \quad (\text{out-of-plane}) \quad (5.25)$$

In contrast, the susceptibility  $\chi = \delta\rho^i/\delta\varphi^e$  can have a macroscopic nonlocality radius. Expanding the Dyson equation  $\chi = \pi + \pi v \pi + \dots$ , we can interpret each term as a series of local polarisations  $\pi(\mathbf{r}, \mathbf{r}' \approx \mathbf{r})$  and nonlocal propagations of the induced secondary fields described by the long-range Coulomb interaction  $v(\mathbf{r}, \mathbf{r}')$  (see fig. 5.11a). Therefore,  $\chi(\bar{\mathbf{r}}, \bar{\mathbf{r}}')$  may be nonzero even for large distances  $|\bar{\mathbf{r}} - \bar{\mathbf{r}}'|$ .

The situation is completely different in finite systems (see fig. 5.11b). As polarisable charges are bound to the sheet,  $\chi$  becomes localised in perpendicular direction

$$\chi(z, z') \approx 0, \quad \text{for } |z| \gg \lambda, \text{ or } |z'| \gg \lambda. \quad (\text{out-of-plane}) \quad (5.26)$$

This important difference between extended and finite systems will allow us to introduce two-dimensional response functions and to solve the Dyson eq. (1.11) analytically.

## 5.4.2 Dyson Equation for Two-Dimensional Systems

Note that our system is not two-dimensional in a strict sense: first, because its wave functions have a finite spatial extent in  $z$ -direction and second, because electromagnetic fields are not confined to a plane but spill out into the third dimension [136]. To switch from three- to two-dimensional quantities, we use a 2D Fourier transform according to the in-plane periodicity of the system [164, 167]. The Dyson eq. (1.11) then becomes (for a compact notation, we will sometimes omit the comma between arguments)

$$\chi(\bar{\mathbf{q}}\bar{\mathbf{q}}'; z z') = \pi(\bar{\mathbf{q}}\bar{\mathbf{q}}'; z z') + \sum_{\bar{\mathbf{q}}''} \int dz_1 dz_2 \pi(\bar{\mathbf{q}}\bar{\mathbf{q}}''; z z_1) v(\bar{\mathbf{q}}''; z_1 z_2) \chi(\bar{\mathbf{q}}''\bar{\mathbf{q}}'; z_2 z'), \quad (5.27)$$

where  $\bar{\mathbf{q}}$  denotes the in-plane momentum transfer. The Coulomb potential then reads

$$v(\bar{\mathbf{q}}''; z_1 z_2) = v_{2D}(\bar{\mathbf{q}}'') e^{-|\bar{\mathbf{q}}''||z_1 - z_2|}, \quad v_{2D}(\bar{\mathbf{q}}'') = \frac{e^2}{2\varepsilon_0} \frac{1}{\bar{\mathbf{q}}''}. \quad (5.28)$$

Physically, it corresponds to the potential of a charged plane which is located at position  $z_2$  and whose charge oscillates with a wavelength  $2\pi/\bar{\mathbf{q}}''$  inside the plane. For finite wavelength, the potential decays exponentially with increasing distance  $|z_1 - z_2|$ .

### Local-Response Approximation

Using the locality of both  $\chi$  and  $\pi$  (see section 5.4.1), we can now restrict the  $z$ -integration in eq. (5.27) to a very small range around zero, namely  $|z_1|, |z_2| \lesssim \lambda$ . The exponential in the Coulomb interaction is then nearly a constant for small momentum  $\bar{\mathbf{q}}''$

$$e^{-|\bar{\mathbf{q}}''||z_1 - z_2|} \approx 1, \quad \text{for } |\bar{\mathbf{q}}''| \ll 2\pi/\lambda, \quad |z_1|, |z_2| \lesssim \lambda. \quad (5.29)$$

For a decay length of  $\lambda = 1 \text{ \AA}$ , we obtain an upper limit  $\bar{q}'' \ll 5 \text{ \AA}^{-1}$  which is fairly large. Let us assume for the following that we are interested in sufficiently small momentum transfers  $\bar{\mathbf{q}}$  and that *in-plane* local-field effects are negligible. In this case, both  $\chi$  and  $\pi$  become diagonal  $\chi(\bar{\mathbf{q}}\bar{\mathbf{q}}') \approx \chi(\bar{\mathbf{q}})\delta(\bar{\mathbf{q}} - \bar{\mathbf{q}}')$  and we finally find for eq. (5.27)

$$\chi(\bar{\mathbf{q}}; zz') \approx \pi(\bar{\mathbf{q}}; zz') + \int dz_1 dz_2 \pi(\bar{\mathbf{q}}; zz_1) v_{2D}(\bar{\mathbf{q}}) \chi(\bar{\mathbf{q}}; z_2 z'). \quad (5.30)$$

The Coulomb interaction becomes independent of  $z$  and the Dyson equation decouples. We will call this approximation *local-response approximation* (LRA) in the following.

## Two-Dimensional Response Functions

It is useful to introduce the *slab polarisation function*

$$\bar{\pi}(\bar{\mathbf{q}}) \equiv \int dz dz' \pi(\bar{\mathbf{q}}; zz') = L_z \pi(\bar{\mathbf{q}}\bar{\mathbf{q}}, q_z=0=q'_z), \quad (5.31)$$

and analogously the *slab susceptibility*  $\bar{\chi}(\bar{\mathbf{q}})$ . It is simply the in-plane component of the three-dimensional Fourier transform (A.42), scaled by the size  $L_z$  of the normalisation box along the  $z$ -direction.<sup>11</sup> The Dyson eq. (5.30) then reads (we integrate over  $z$  and  $z'$ )

$$\bar{\chi}(\bar{\mathbf{q}}) \stackrel{\text{LRA}}{\approx} \bar{\pi}(\bar{\mathbf{q}}) + \bar{\pi}(\bar{\mathbf{q}}) v_{2D}(\bar{\mathbf{q}}) \bar{\chi}(\bar{\mathbf{q}}), \quad \bar{\chi}(\bar{\mathbf{q}}) \stackrel{\text{LRA}}{\approx} \frac{\bar{\pi}(\bar{\mathbf{q}})}{1 - v_{2D}(\bar{\mathbf{q}})\bar{\pi}(\bar{\mathbf{q}})}, \quad (5.32)$$

which formally resembles the Dyson eq. (1.10) of a three-dimensional system except for the modified Coulomb potential and the important difference that the Dyson equation is now scalar. For convenience, we define the (*inverse*) *two-dimensional dielectric function*

$$\bar{\varepsilon}(\bar{\mathbf{q}}) \equiv 1 - v_{2D}(\bar{\mathbf{q}})\bar{\pi}(\bar{\mathbf{q}}), \quad \bar{\varepsilon}^{-1}(\bar{\mathbf{q}}) \equiv 1 + v_{2D}(\bar{\mathbf{q}})\bar{\chi}(\bar{\mathbf{q}}), \quad (5.33)$$

which are inverse to each other by virtue of eq. (5.32).

Physically, the slab response functions  $\bar{\pi}$  and  $\bar{\chi}$  relate the induced surface charge  $\sigma^i$  with the total or external potential  $\varphi^e$ , respectively. To see this connection, we start from the general definition of the susceptibility  $\rho^i(\mathbf{r}) = \int d\mathbf{r}' \chi(\mathbf{r}, \mathbf{r}') \varphi^e(\mathbf{r}')$ . In the limit of an ideal localisation perpendicular to the sheet, the induced charge can be written as  $\rho^i(\mathbf{r}) = \sigma^i(\bar{\mathbf{r}})\delta(z)$  and the susceptibility becomes  $\chi(\mathbf{r}, \mathbf{r}') = \bar{\chi}(\bar{\mathbf{r}}, \bar{\mathbf{r}}')\delta(z)\delta(z')$ . We obtain

$$\sigma^i(\bar{\mathbf{r}}) \equiv \int dz \rho^i(\mathbf{r}) = \int d\bar{\mathbf{r}}' \bar{\chi}(\bar{\mathbf{r}}, \bar{\mathbf{r}}') \varphi^e(\bar{\mathbf{r}}, z=0) \quad \Rightarrow \quad \bar{\chi} = \left. \frac{\delta\sigma^i}{\delta\varphi^e} \right|_{z=0} \quad (5.34)$$

Note that the slab response function  $\bar{\chi}$  defined here differs from the response function that connects the (longitudinal) field  $\mathbf{E}^e = -\nabla\varphi^e$  with the induced surface charge. The limit of ideal localisation can be extended, whenever the delocalisation length  $\lambda$  is small and the potential  $\varphi^e$  is approximately constant in the range  $\pm\lambda$ . The two-dimensional

<sup>11</sup>The spatial average of a function is given by the zero-frequency component of its Fourier transform.

dielectric functions  $\bar{\varepsilon}$  and  $\bar{\varepsilon}^{-1}$  then connect the external and the total potential at the surface, i. e.,  $\varphi^e(z=0)$  and  $\varphi^t(z=0)$ . Indeed, the definition (5.33) implies

$$\bar{\varepsilon}(\bar{\mathbf{q}}) = \int dz' \varepsilon(\bar{\mathbf{q}}; z=0, z') = \sum_{q_z} \varepsilon(\bar{\mathbf{q}}; q_z, q'_z=0) \quad (5.35)$$

and *not* simply  $\varepsilon(\bar{\mathbf{q}}; q_z=0=q'_z)$  as one might guess from eq. (5.31). The same holds for the inverse dielectric function  $\bar{\varepsilon}^{-1}$ .

### From Bulk to Isolated Sheets

Within the local-response approximation, we can now understand the importance of crystal local-field effects for graphene. To this end, we compare two limits in the supercell calculations of section 5.3.2: First, we consider the bulk system of interacting sheets at distance  $d_0$  (corresponding to graphite in AA stacking). As crystal local-field effects are very small in this case, the loss function for the bulk material is given by [see eq. (1.16)]

$$-\text{Im} \varepsilon_{\text{b}}^{-1}(\mathbf{q}\mathbf{q}) \stackrel{\text{NLF}}{\approx} -\text{Im} \{1/\varepsilon_{\text{b}}\} = -v_{3\text{D}} \text{Im} \{\pi_{\text{b}}(\mathbf{q}\mathbf{q})/\varepsilon_{\text{b}}(\mathbf{q}\mathbf{q})\}. \quad (5.36)$$

Second, we consider a stack of graphene sheets with an interlayer distance  $d$  that is sufficiently large to prohibit any interaction between neighbouring sheets. It corresponds to an isolated slab with three-dimensional periodic boundary conditions (three-dimensional  $\varepsilon$  quantity). Its energy-loss function  $-\text{Im} \varepsilon_{\text{s}}^{-1}$  can be expressed in terms of the two-dimensional response function  $\bar{\varepsilon}^{-1}$  of a single sheet using eq. (5.31) for  $\chi$  ( $v_{3\text{D}} = \frac{e^2}{\varepsilon_0 \bar{q}^2}$ )

$$-\text{Im} \varepsilon_{\text{s}}^{-1}(\bar{\mathbf{q}}\bar{\mathbf{q}}; q_z=0=q'_z) = -\frac{v_{3\text{D}}}{d} \text{Im} \bar{\chi}(\bar{\mathbf{q}}) = -\frac{2}{|\bar{\mathbf{q}}|d} \text{Im} \bar{\varepsilon}^{-1}(\bar{\mathbf{q}}). \quad (5.37)$$

Within the local-response approximation, we have with eq. (5.32)

$$-\text{Im} \varepsilon_{\text{s}}^{-1}(\bar{\mathbf{q}}\bar{\mathbf{q}}) \stackrel{\text{LRA}}{\approx} -\frac{v_{3\text{D}}}{d} \text{Im} \{\bar{\pi}(\bar{\mathbf{q}})/\bar{\varepsilon}(\bar{\mathbf{q}})\}, \quad \bar{\pi}(\bar{\mathbf{q}}) = d \pi_{\text{s}}(\bar{\mathbf{q}}\bar{\mathbf{q}}), \quad (5.38)$$

where  $\pi_{\text{s}}$  is the polarisability of the graphene stack. As we have discussed in section 5.4.1, the polarisability is a transferable quantity. Besides a scaling with the interlayer distance, it is essentially the same for the bulk material and the isolated sheet ( $\pi_{\text{b}} d_0 \approx \pi_{\text{s}} d$ ) when hybridisation effects between neighbouring layers can be neglected (see fig. 5.8c).

In contrast, the electron energy-loss function of the bulk system and isolated sheets is very different (see fig. 5.8a). Comparing eq. (5.36) and (5.38), this can be understood from the different screening functions  $\varepsilon_{\text{b}}$  and  $\bar{\varepsilon}$  in the bulk and the sheet. Actually, it can be traced back to the different Coulomb interaction  $v_{2\text{D}}$  or  $v_{3\text{D}}$  in the two- or three-dimensional system, respectively. Switching back to reciprocal space, this very intuitive explanation can be finally related to our previous finding that crystal local-field effects are very important in graphene (see section 5.3.2). Indeed, a strong localisation of  $\pi(z, z')$  in real space corresponds to a nearly constant function  $\pi_{G_z G'_z}$  in Fourier space. Thus, in the Dyson eq. (1.13), contributions for  $|G_z| > 0$  will become most important, i. e., the strong difference of the loss spectra of graphite and graphene must be associated to the perpendicular local-field modes in graphene which arise from the strong inhomogeneity of the system in  $z$ -direction.

## Optical Limit

Equation (5.38) is particularly interesting for the discussion of the optical limit  $\bar{q} \rightarrow 0$  where LFE become negligible (see section 5.3.2). In RPA we have  $\pi_s = \chi_s^0 \propto \bar{q}^2$  [see eq. (3.14)], while  $v_{2D} \propto \bar{q}^{-1}$ . The screening  $\bar{\epsilon} \rightarrow 1$  then vanishes for small  $\bar{q}$  as we can see from eq. (5.33). Thus, the loss-function of the sheet becomes identical to  $-\text{Im} \frac{v_{3D}}{d} \chi_s^0(\bar{q}\bar{q})$  and differs from the NLF absorption spectrum  $\text{Im} v_{3D} \chi_b^0(\bar{q}\bar{q})$  of the bulk system only by a scaling factor  $d_0$ . This is finally the explanation for the convergence behaviour shown in the lower panel of fig. 5.8.

Note that we can arrive at the same conclusion if we start from the effective Dyson eq. (5.32) which can be expanded as  $\bar{\chi} = \bar{\pi} + \bar{\pi} v_{2D} \bar{\pi} + \dots = \bar{\pi} + \mathcal{O}(\bar{q}^3)$ . Thus, we find again  $\bar{\chi} \approx \bar{\pi}$  for  $\bar{q} \rightarrow 0$ , i. e., the influence of the Coulomb potential vanishes for isolated systems in the optical limit.

## Conclusions

The equations derived so far allow us to answer several of the questions stated above:

- We have seen that the local-field components perpendicular to the sheet are the most important ones for the difference between graphite and graphene spectra. They arise from the confinement of the electrons on the sheet and account for the different screening in three- and two-dimensional systems.
- The behaviour at the optical limit  $q \rightarrow 0$  has been explained. The Coulomb potential has no effect, i. e., the loss function of graphene becomes equivalent to the absorption spectrum in the corresponding bulk material (if in-plane local-field effects and the hybridisation of the wavefunctions of neighbouring layers can be neglected in the bulk material).
- A connection between the three- and two-dimensional response functions is given.
- Within the local-response approximation (LRA), i. e., assuming a perfect localisation perpendicular to the sheet, the two-dimensional response functions obey an effective scalar Dyson eq. (5.32) which includes the modified Coulomb potential  $v_{2D}$ .
- This Dyson equation can be solved analytically obtaining a simple expression for the influence of the Coulomb interaction in finite systems within the limits of the LRA. This has been already used in our tight-binding calculations [see eq. (5.20)].

### 5.4.3 LRA for Ab-initio Calculations

Within the local-response approximation, the calculation of the loss function of graphene becomes very simple. Instead of solving the Dyson eq. (1.13) for large matrices  $\pi_{GG'}$  in order to include LFE that arise from the localisation of the electrons on the sheet, one just has to solve an *effective* Dyson eq. (5.32) for scalar quantities. The two-dimensional geometry of the system is taken into account by the modified Coulomb potential  $v_{2D}$ .

This effective Dyson equation has been already used in our tight-binding calculations in section 5.2.2, but the evaluation of the polarisability  $\pi$  involves a number of restrictive approximations and we had to use several fitting parameters. To overcome these problems, we will now use *ab-initio* calculations to determine the polarisability  $\pi$ , and compute the loss function within the local-response approximation:

### Procedure II: LRA method

1. Starting point is an RPA *ab-initio* calculation of the polarisability  $\pi_d = \chi_d^0$  for a graphene stack with doubled interlayer distance  $d = 2d_0$  in order to avoid interlayer hybridisation. In contrast to the interpolation method I, we just need to calculate the macroscopic component  $\chi_d^0(\bar{q}, \bar{q}, q_z = 0 = q'_z)$  which is found in the DP output file `outnlf.mdf`.
2. The slab polarisability  $\bar{\pi}(\bar{q}) = d \cdot \chi_d^0(\bar{q}, \bar{q}, q_z = 0 = q'_z)$  is a transferable quantity. It is the same for any distance  $D > d$ , and the isolated system (see fig. 5.8c).
3. Using the scalar Dyson eq. (5.32), we calculate the slab susceptibility  $\bar{\chi}$  and the corresponding inverse dielectric function  $\bar{\epsilon}^{-1}$ . Its imaginary part is proportional to the energy-loss function of the slab [see eq. (5.37)].

In figure 5.12a, we compare the results of the LRA method (dashed lines) to our full *ab-initio* calculations of graphene (solid lines). For small momentum transfer  $q$ , the agreement is perfect. Note, that in this region rather large interlayer distances were necessary to converge the spectra of the isolated sheet (see table 5.2). Using the LRA method, we avoid this long calculation by taking into account the modified Coulomb potential  $v_{2D}$  in our equations. As all quantities are scalar functions, the computation time reduces to the calculation of the polarisability in the first step which takes only a few minutes. For larger momentum transfers  $q > 0.2 \text{ \AA}^{-1}$ , the LRA method fails.

### Comparison with Tight-Binding

In principle, the LRA method should be better than the tight-binding results for the following reasons: First, both approaches rely on the local-response and random phase approximation. But the LRA method improves the calculation of the polarisability  $\bar{\pi}$ . Second, the  $\sigma$  electrons are correctly taken into account instead of using a background dielectric constant  $\epsilon_\sigma$ . Third, the matrix elements are calculated from first-principles instead of using the nearest-neighbour approximation and parametrised model orbitals.

The failure in the polarisability due to the nearest-neighbour approximation is shown in fig. 5.12b. We compare a tight-binding calculation with an *ab-initio* calculation that includes only the  $\pi \rightarrow \pi^*$  transitions. Although the overall agreement—even in the intensities—is very astonishing, the peak at 5 eV is not correctly described in the nearest-neighbour tight-binding approximation.

Comparing with the full *ab-initio* calculations for the loss function of graphene (see fig. 5.12a), the overall shape and the intensity of the  $\pi$  plasmon is clearly much better

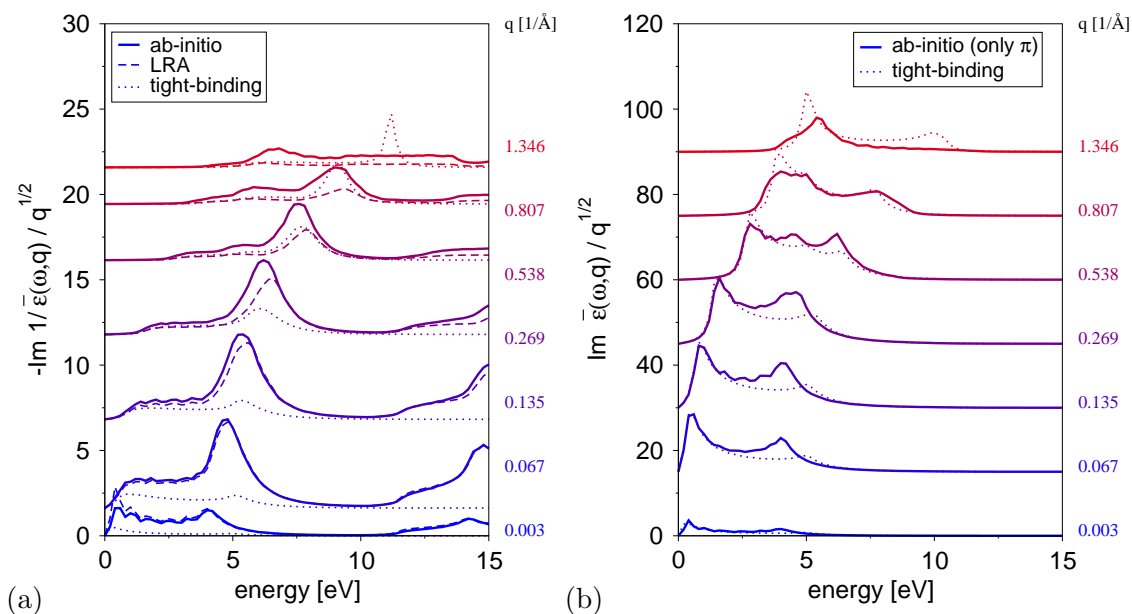


**Fig. 5.12:** (a) The loss function of isolated graphene for different in-plane momentum transfers. We compare the results of a tight-binding calculation (dotted), *ab-initio* calculations using the local-response approximation (dashed), and full *ab-initio* calculations (solid). (b) The two-dimensional dielectric function  $\bar{\epsilon}$  of graphene calculated from a tight-binding calculation (dotted) and an *ab-initio* calculation including only  $\pi \rightarrow \pi^*$  transitions is compared. The spectra are scaled by  $q^{1/2}$  and shifted along the  $y$ -axis for better visibility.

for the LRA method than in the TB calculation (dotted lines). In particular, the tight-binding fails in the optical limit  $q \rightarrow 0$ . Indeed,  $\bar{\pi}_{\text{TB}} \neq \bar{\chi}_{\text{TB}}$  in contrast to our general findings above. The reason is the use of the empirical screening constant  $\epsilon_\sigma$  which does not vanish in the limit  $q \rightarrow 0$ . This problem can be circumvented by including also the  $\sigma$  electrons in the TB calculation. It is rather surprising that the  $\pi$ -plasmon position seems to be correct in TB even at momentum transfers up to  $1 \text{ \AA}^{-1}$ . We will see in the next section that the empirical screening constant  $\epsilon_\sigma$  does not only take into account the screening from the  $\sigma$  electrons, but implicitly also corrects the local-response approximation at large  $q$ .

## 5.5 Beyond the Local-Response Approximation

The LRA fails for large momentum transfer  $q$ , i. e., when the exponential in eq. (5.29) is no longer constant. If we include the  $z$ -dependence of the Coulomb potential, we can no longer introduce the integrated quantities  $\bar{\pi}$  and  $\bar{\chi}$  and we have to solve the full Dyson eq. (5.27) instead. In the first part of this section, we will try to avoid this complication by introducing an empirical correction to the LRA. It can be justified by assuming an exponential decay of the atomic wave functions with increasing distance from the sheet. In a second part, we will numerically solve the full Dyson equation and discuss the relation with the interpolation method described earlier.

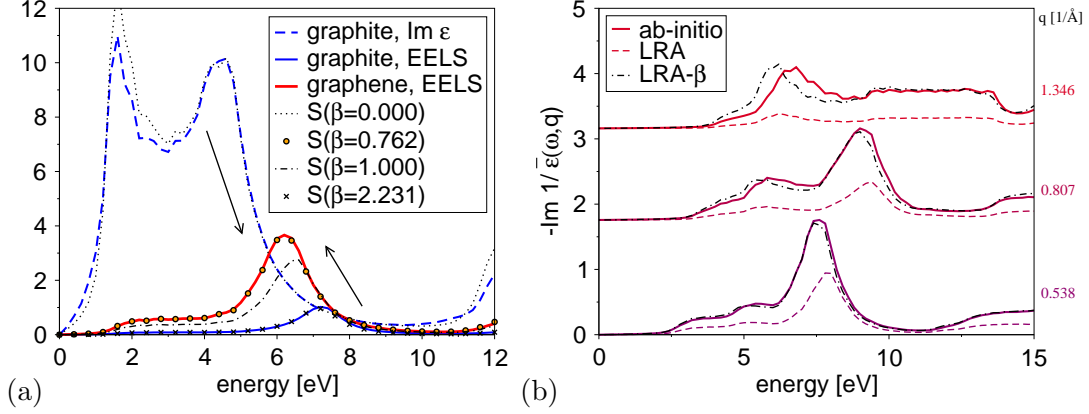


**Fig. 5.13:** (a) Comparison of graphite and graphene spectra for  $q=0.269 \text{ \AA}^{-1}$  with the generalised spectra  $\mathcal{S}_\beta$  for different parameters  $\beta$  (see text). (b) Best fit of the generalised spectrum  $\mathcal{S}_\beta$  (dash-dotted line) to the *ab-initio* graphene loss function (solid lines) for large momentum transfers. The LRA result, i. e.,  $\mathcal{S}_1$  is shown for comparison (dashed lines).

### 5.5.1 Scaling of the Coulomb Potential

Discussing the local-response approximation, we have seen that the loss function of the graphene sheet is closely related to the spectrum of graphite. Comparing eq. (5.38) and (5.36), the difference between the two is essentially due to the different screening in the sheet  $\bar{\epsilon}(\bar{q}) = 1 - v_{2D}\bar{\pi}(\bar{q})$  and the bulk system  $\epsilon(\bar{q}) = 1 - v_{3D}\pi_b(\bar{q}\bar{q})$ . The loss function of both systems can be then described by the following unified expression ( $\bar{\pi} = \pi_s d = \pi_b d_0$ )

$$\mathcal{S}_\beta \cdot d_0 \equiv -v_{3D} \text{Im} \{ \bar{\pi}(\bar{q}) / \bar{\epsilon}_\beta(\bar{q}) \}, \quad \bar{\epsilon}_\beta(\bar{q}) = 1 - \beta v_{2D} \bar{\pi}(\bar{q}), \quad (5.39)$$

if we choose the parameter  $\beta$  appropriately. In order to illustrate this point, we consider the loss function of graphene and graphite for  $\bar{q} = 0.27 \text{ \AA}^{-1}$  (see fig. 5.13a):

- For  $\beta = 0$ , the screening vanishes and  $\mathcal{S}_\beta = \text{Im} \epsilon_b$  corresponds to the dielectric function of graphite neglecting LFE (dotted line). The full LFE spectra of graphite is very similar (blue dashed line) and starts to differ only for very large  $q$  [112].
- For  $\beta = 2/(\bar{q}d_0) \approx 2.2$ , the screening function  $\bar{\epsilon}_\beta$  is identical to the bulk screening  $\epsilon_b$  and the generalised spectrum  $\mathcal{S}_\beta = -\text{Im} 1/\epsilon_b$  corresponds to the loss function of graphite neglecting LFE (cross symbols). Again, it is very close to the loss function of graphite including LFE (blue solid line).
- For  $\beta = 1$ , we reproduce the LRA result. By construction,  $\mathcal{S}_\beta = -(d/d_0) \text{Im} \epsilon_s^{-1}$  becomes the (scaled) loss function of the graphene sheet calculated within the local-response approximation (dash-dotted line). Compared to the *ab-initio* result for graphene (red solid line), it slightly deviates due to the problems discussed above.

By tuning the parameter  $\beta$ , the generalised spectrum  $\mathcal{S}_\beta$  continuously changes between the dielectric function of graphite and its loss function. The graphene loss function can be found somewhere in between these two limits. Most interestingly, it can be exactly reproduced by  $\mathcal{S}_\beta$  if we choose  $\beta = 0.76$  (see dots in fig. 5.13a). Of course, this empirical parameter  $\beta$  depends on the size of the momentum transfer: (i) In the optical limit, the graphene loss function is perfectly described within the LRA as we have seen before ( $\beta = 1$ ). (ii) For large momentum transfers  $\bar{q} \gg 1/d_0 \approx 0.3 \text{ \AA}^{-1}$ , the loss function of graphene and graphite become identical [ $\beta = 2/(\bar{q}d_0)$ ] because the Coulomb potential is then sufficiently localised and neighbouring sheets do no longer interact.

### LRA- $\beta$ Method

We fit the generalised spectrum  $\mathcal{S}_\beta$  to our *ab-initio* results for graphene shown in fig. 5.12a and determine the empirical parameter  $\beta$  for each  $\bar{q}$ . We find that  $\mathcal{S}_\beta$  indeed reproduces exactly the *ab-initio* results for a suitable choice of  $\beta$  even for rather large  $\bar{q}$  (see fig. 5.13b, dash-dotted lines). Only for  $\bar{q} > 1 \text{ \AA}^{-1}$  the shape differs due to the increasing importance of in-plane crystal LFE which are neglected in the LRA.

The dependence of the inverse fit parameter  $1/\beta$  on the momentum transfer  $\bar{q}$  is shown in figure 5.14 (dots). It starts at  $\beta = 1$  (LRA spectrum) and increases linearly compensating the failure of the LRA at large momentum  $\bar{q}$ . The range of validity of the LRA can be therefore easily extended by introducing a screened Coulomb potential  $v_{2D} \rightarrow \beta v_{2D}$  in eq. (5.33) with a  $\bar{q}$ -dependent parameter  $\beta$  (LRA- $\beta$  method).

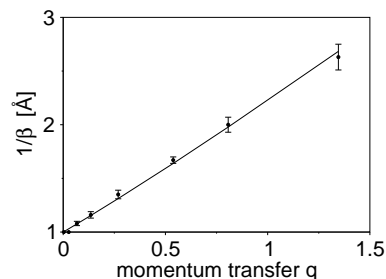


**Fig. 5.14:** Parameters from fitting  $\mathcal{S}_\beta$  to the loss function of graphene.

### Model for the $z$ -Dependence

*What is the origin of this additional screening of the Coulomb potential? And can we find a simple model for the linear dependence of  $\beta$  on the momentum transfer  $\bar{q}$ ?* To answer these questions, we have to consider the  $z$ -dependence of the Coulomb potential and the polarisability in eq. (5.27). For simplicity, we neglect in-plane local-field effects and consider an effective homogeneous electron gas of quasi two-dimensional electrons. The single-particle wave functions then become plane waves  $\psi_{n\bar{k}}(\mathbf{r}) = \sqrt{C} \psi_{n\bar{k}}(z) e^{i\bar{k}\bar{\mathbf{r}}}$  that decay along the  $z$ -direction. Assuming an exponential decay  $e^{-|z|/\lambda}$  with an averaged decay length  $\lambda$  independent on  $\bar{k}$  or  $n$ , the independent-particle polarisability reads<sup>12</sup>

$$\chi^0(\bar{\mathbf{q}}; zz') = C^2 e^{-2(|z|+|z'|)/\lambda} \chi^0(\bar{\mathbf{q}}), \quad (5.40)$$

where  $C$  is the normalisation constant of the wave function  $\psi_{n\bar{k}}(\mathbf{r})$ . Rewriting eq. (5.27) as a series expansion  $\chi = \hat{1} + \chi^0 v \chi^0 + \dots$ , we can perform the  $z$  integration analytically

<sup>12</sup>A more realistic, but also more complicated model has been introduced by Dahl and Sham [167].

and introduce an effective Dyson equation as in the case of the LRA. We find

$$\int dz_1 dz_2 \chi^0(\bar{\mathbf{q}}; zz_1) v(\bar{\mathbf{q}}; z_1 z_2) \chi^0(\bar{\mathbf{q}}; z_2 z') = \chi^0(\bar{\mathbf{q}}) \tilde{\beta}(\bar{\mathbf{q}}) v_{2D}(\bar{\mathbf{q}}) \chi^0(\bar{\mathbf{q}}),$$

$$\tilde{\beta}(\bar{\mathbf{q}}) = C^2 \int dz_1 dz_2 e^{-|z_1 - z_2| |\bar{\mathbf{q}}|} e^{-2(|z_1| + |z_2|)/\lambda} = \frac{4 + \bar{q}\lambda}{(2 + \bar{q}\lambda)^2}, \quad (5.41)$$

where  $\tilde{\beta}$  is the additional screening of the Coulomb potential  $v_{2D}$  due to the exponential  $z$ -dependence of the polarisability. Expanding  $1/\tilde{\beta} \approx 1 + \frac{3}{4}\bar{q}\lambda + \frac{1}{16}(\bar{q}\lambda)^2 + \dots$  we find a nearly linear behaviour similar to the case of graphene. Indeed, for an average decay length of  $\lambda_\pi = 1.5 \text{ \AA}$ , eq. (5.39) reproduces the empirical dependence of the fitting parameter  $\beta$  in the previous section (solid line in fig. 5.14).

Thus, the set of fitting parameters  $\beta(\bar{\mathbf{q}})$  is reduced to a single parameter  $\lambda$  which can be interpreted as the average decay length of the contributing states along the  $z$ -direction. The screening of the effective Coulomb potential  $v_{2D}$  in the LRA- $\beta$  method is due to the exponential decay of the full Coulomb interaction given in eq. (5.28). In the tight-binding approach it is implicitly included in the screening parameter  $\varepsilon_\sigma$  when we fit the plasmon positions at large momentum transfers to the experimental values.

### 5.5.2 Solution of the Full Dyson Equation

We finally consider the numerical solution of the full  $z$ -dependent Dyson eq. (5.27) in real space. This approach is actually closely related to the use of a Coulomb cutoff.<sup>13</sup>

#### Procedure III: Coulomb-cutoff method

1. Similar to the interpolation method I, we start from an *ab-initio* calculation of the microscopic bulk polarisability  $\pi_d = \chi_d^0$  of a graphene stack with small interlayer distance  $d = 2d_0$  for a given in-plane momentum transfer  $\bar{\mathbf{q}}$  (RPA)
2. Using a 2D Fourier transformation, we calculate  $\pi_d(\bar{\mathbf{q}} + \bar{\mathbf{G}}, \bar{\mathbf{q}} + \bar{\mathbf{G}}'; zz')$  (see fig. 5.15a). The real-space grid extends from  $z = -d_0$  to  $z = d_0$  and is sampled by  $N_z$  points which is exactly the number of  $\bar{\mathbf{G}}$  vectors along the  $z$ -direction.
3. The Dyson equation is solved by inverting the dielectric matrix (see fig. 5.15b)

$$\varepsilon(\bar{\mathbf{q}} + \bar{\mathbf{G}}, \bar{\mathbf{q}} + \bar{\mathbf{G}}'; zz') = \delta_{\bar{\mathbf{G}}, \bar{\mathbf{G}}'} - \int dz_1 v(\bar{\mathbf{q}} + \bar{\mathbf{G}}; zz_1) \pi_d(\bar{\mathbf{q}} + \bar{\mathbf{G}}, \bar{\mathbf{q}} + \bar{\mathbf{G}}'; z_1 z'). \quad (5.42)$$

By the inversion,  $\varepsilon(zz')$  is intrinsically set to zero for all  $z$ -points outside the real-space grid, i. e., the Coulomb potential is cut-off at the borders of the grid.

4. We calculate the susceptibility  $\chi_d(\bar{\mathbf{q}} + \bar{\mathbf{G}}, \bar{\mathbf{q}} + \bar{\mathbf{G}}', zz')$  which is very localised (vanishes at the border of the grid) and can be transformed back to reciprocal space. The loss function of an isolated graphene sheet in a 3D normalisation box of height  $d$  is then given by  $-\text{Im} \varepsilon^{-1}(\mathbf{q}\mathbf{q}) = -v(\mathbf{q}) \text{Im} \chi_d(\mathbf{q}\mathbf{q})$ .

<sup>13</sup>The use of a Coulomb cutoff for finite systems has been studied before, see e. g. [168–170].

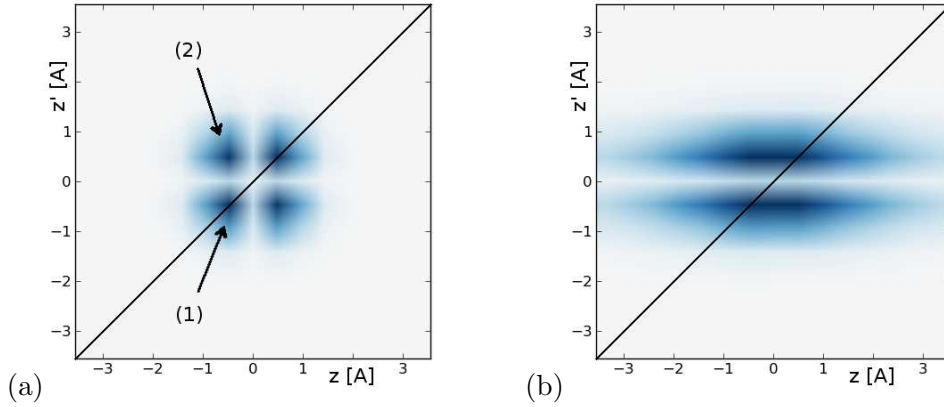


**Fig. 5.15:** (a) Polarisability  $\pi_d(\bar{\mathbf{q}}\bar{\mathbf{q}}', zz')$  for a graphene sheet in real-space. The response is clearly localised on the sheet at  $z = 0$  within less than 1 Å. (b) The dielectric function  $\varepsilon(\bar{\mathbf{q}}\bar{\mathbf{q}}', zz')$  is delocalised in  $z$  due to the folding with the Coulomb potential. In both cases, the imaginary part is shown for RPA calculations with wave vector  $\bar{\mathbf{q}} = \bar{\mathbf{q}}' = 0.54 \text{ \AA}^{-1}$  and energy  $\hbar\omega = 4 \text{ eV}$ .

The results are found to be identical to the full *ab-initio* calculations of graphene as we should certainly expect (see appendix, fig. C.4) while the computational cost is as low as for the interpolation method I. Beyond this simple test for the validity of our equations, the Coulomb-cutoff method is interesting for three reasons which will be discussed in the following: First, looking at the polarisability  $\pi_d(\bar{\mathbf{q}} + \bar{\mathbf{G}}, \bar{\mathbf{q}} + \bar{\mathbf{G}}'; zz')$ , we can directly verify our assumptions in section 5.4.2. Second, the Coulomb-cutoff method is closely related to the interpolation method I and we can finally understand why the latter has been so successful. Third, a very similar approach will be used for the calculation of loss spectra in isolated carbon nanotubes in the following chapter.

### Localisation of the Polarisability

In fig. 5.15a, the polarisability  $\pi_d(zz')$  for fixed in-plane wave vector  $\bar{\mathbf{q}} = 0.54 \text{ \AA}^{-1}$  and energy  $\hbar\omega = 4 \text{ eV}$  is shown. The colour indicates the amplitude of the charge oscillation at distance  $z'$  from the graphene sheet that is induced by a plane-wave perturbation  $e^{i\bar{\mathbf{q}}\bar{\mathbf{r}}} \delta(\mathbf{r} \cdot \mathbf{e}_z - z)$  at distance  $z$ . The response is clearly localised within  $\pm 1 \text{ \AA}$  around the graphene sheet in agreement with our assumptions in section 5.4.2.

*What is the origin of the four maxima?* To answer this question, we first consider the two spots on the main diagonal  $z = z'$  (1). In this case, the response and the perturbation are located at the same point we probe the *local response*. It is zero at  $z = 0 = z'$  and has a maximum at  $z = \pm 0.5 \text{ \AA}^{-1}$ . This is clearly a signature of the  $\pi$  orbitals which are excited at  $\hbar\omega = 4 \text{ eV}$  (compare with fig. 5.2d). The two spots on the second diagonal  $z = -z'$  (2) are related to the *nonlocal response* of the system. Perturbing the lower lobe of a  $\pi$  orbital will also induce a response in the upper lobe, and vice versa.

The discussion can be repeated for the susceptibility  $\chi_d$  which indeed looks very similar (not shown). Note that  $\text{Im} \chi_d(zz')$  is directly related to the mixed dynamic form factor  $S(zz')$  in real space by means of eq. (2.50). The latter has been extensively discussed by Schattschneider *et al.* [55].

## Comparison with the Interpolation Method

The dielectric function  $\varepsilon(zz')$  is much less localised along the  $z$  coordinate (see fig. 5.15b). Indeed, the Coulomb potential ‘smears out’ most of the microscopic details. Note that the images only show one unit cell which is periodically repeated along  $z$  and  $z'$ . For small  $q$ , the Coulomb potential (5.28) shows a long-range behaviour. The sheet at  $z = 0$  then starts to interact with the replicas at  $z = \pm d$  and is no longer isolated. In the method described above, the replicas are not taken into account in the inversion on the real-space grid. This corresponds to an artificial cutoff in the Coulomb potential.

Alternatively, we could simply enlarge the unit cell for the polarisability in order to avoid spurious interlayer interactions. If the polarisability vanishes at the border, we just have to add zeros at larger  $z$  and  $z'$  coordinates. This is exactly the interpolation method (see p. 92) when we use the Fourier interpolation (see appendix C.4). *Implicitly, the interpolation method increases the interlayer distance under the assumption that the polarisability  $\pi(zz')$  does not change and is zero at the border of the unit cell.*

## 5.6 Building-Block Approach

In the following, we will extend our discussion to multilayer systems, i. e., stackings of several identical graphene layers with an interlayer distance of graphite  $d_0$ . One possibility to calculate the loss spectrum of such a system would be to increase the number of graphene layers in the supercell and eventually apply the interpolation method I in order to avoid interactions between the artificial replicas.

Alternatively, we can construct the response of the multilayer system from the response of its building block—the single layer graphene. Due to the strong localisation of the sheet polarisability  $\pi_s$ , the multilayer polarisability is given by [e.g. 147]

$$\pi_{\text{stack}}(z, z') \approx \sum_l \pi_s(z - ld_0, z' - ld_0), \quad (5.43)$$

where  $l$  runs over the number of layers and  $d_0$  denotes the interlayer distance. Any change of the wave functions due to the presence of the other sheets is neglected in this model. The different layers will only interact via the Coulomb potential (see fig. 5.16a).

### 5.6.1 Bilayer Graphene

First, we consider full *ab-initio* calculations for the bilayer graphene system inside a large unit cell ( $d = 10d_0$ ). Fig. 5.16b clearly shows a difference between the loss function of the single- (dashed) and the double-layer system (solid lines) at moderate momentum transfers (see [130] for details). On the other hand, we have used the building-block approach (BBA) from eq. (5.43) to calculate the loss function for bilayer graphene. The translation of  $\pi_s$  by the vector  $\boldsymbol{\tau} = d_0 \mathbf{e}_z$  in real space becomes a phase shift in reciprocal space and we have [see eq. (A.39)]

$$\pi_{\text{stack}}(q_z, q'_z) = \pi_s(q_z, q'_z) \left( 1 + e^{-i(q_z - q'_z)d_0} \right). \quad (5.44)$$

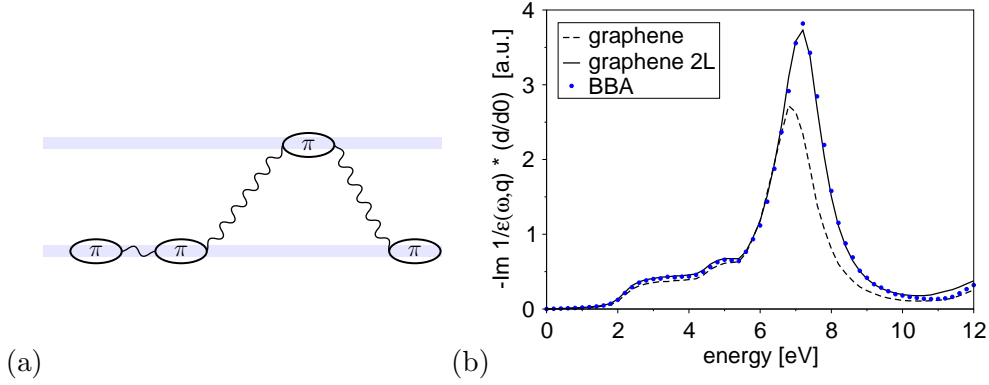


**Fig. 5.16:** (a) Coulomb interaction between sheets. (b) Loss spectrum of single- (dashed line) and double-layer graphene (solid line) for in-plane momentum transfer  $q = 0.41 \text{ \AA}^{-1}$ . The dots correspond to the result from the building-block approach (see text).

Starting from the interpolation method for graphene (see page 92, step 1+2), we only have to take this phase factor into account before we solve the Dyson equation in step 3. This approach exactly reproduces the *ab-initio* results for the bilayer graphene system (see blue dots in fig. 5.16b). Thus, the change of the loss function for multi-layer systems is only due to the Coulomb interaction, while the difference in the wave functions or energies is too small to have a major influence [171].

This allows us, in principle, to build arbitrary stacks of shifted and eventually also rotated layers from a single calculation of the polarisability of graphene. In particular, the loss function of complex systems like mixed graphene and h-BN stacks for different stacking sequences can be easily understood in terms of the corresponding phase factors.

## 5.6.2 Back to Graphite

As an example, we consider graphite in Bernal stacking, i. e., an infinite stack of graphene layers of A and B type. The polarisability  $\pi_{AB}$  shows an interesting behaviour in reciprocal space: The dots in fig. 5.17a show  $\pi_{AB}$  in dependence of  $G_z$  and  $G'_z$  from a full *ab-initio* calculation in RPA. The polarisability seems to consist of two distinct parts which are distributed on a checkerboard pattern in reciprocal space: ‘white fields’ are zero, while ‘black fields’ are non-zero. One might wonder, if the interpolation method I would still work for such a system (compare with AA stacked graphite which does not this behaviour, see fig. 5.10b).

We can explain this behaviour within the building-block approach by describing the graphite system as a sum of shifted graphene sheets. Indeed, the B layer can be obtained by translation  $\boldsymbol{\tau} = \frac{2}{3}\mathbf{a}_1 + \frac{1}{3}\mathbf{a}_2 + \frac{c}{2}\mathbf{e}_z$  of the A layer. The infinite stack of A and B layers is then given by [see eq. (5.43) and (A.39)]

$$\pi_{AB}(\mathbf{q}, \mathbf{q}') = \sum_{l \in \mathbb{Z}} \pi_s(\mathbf{q}, \mathbf{q}') e^{-i(q_z - q'_z)ld} \left(1 + e^{-i(\mathbf{q} - \mathbf{q}')\boldsymbol{\tau}}\right), \quad (5.45)$$

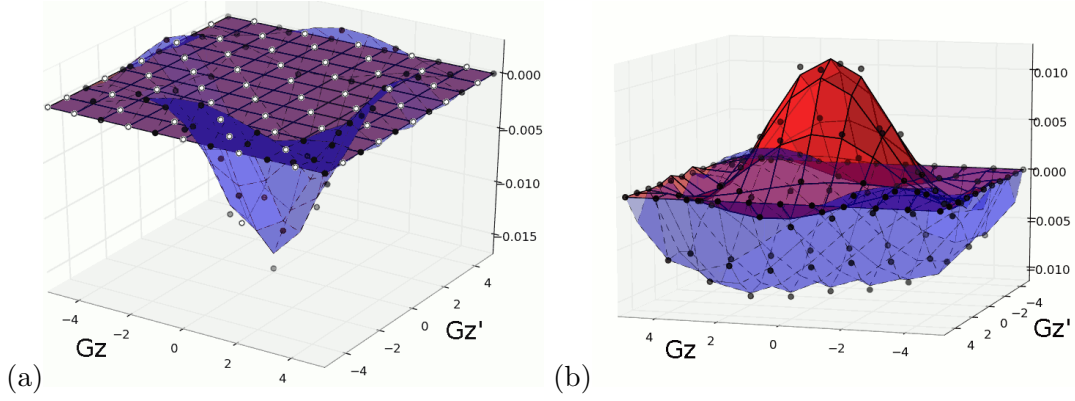


**Fig. 5.17:** The polarisability  $\pi_{AB}$  of graphite AB consists of two parts. The dots in panel (a) show  $\text{Im } \pi_{AB}$  in dependence of  $G_z$  and  $G'_z$ , while the in-plane momenta  $\bar{\mathbf{G}} = (1, 0)$  and  $\bar{\mathbf{G}}' = (\bar{1}, 1)$  are fixed. The two surfaces correspond to  $\pi_s(\mathbf{q}, \mathbf{q}')$  and  $\pi_s(\mathbf{q}, \mathbf{q}')e^{-i(\mathbf{q}-\mathbf{q}')\tau}$ , respectively. (b) Same for  $\text{Re } \pi_{AB}$  with  $\bar{\mathbf{G}} = (1, 0)$  and  $\bar{\mathbf{G}}' = (0, 1)$ . From a RPA calculation for  $q = 0.4 \text{ \AA}^{-1}$ ,  $\omega = 8 \text{ eV}$ .

where  $d = 2d_0$  denotes the size of the unit cell along  $z$ . The sum is only non-zero, if  $q_z - q'_z = \Delta G_z 2\pi/d$  is an integer multiple of  $2\pi/d$ . In contrast to AA stacked graphene, the sum of the phase factors

$$F = 1 + e^{-i(\mathbf{q}-\mathbf{q}')\tau} = 1 + (-1)^{\Delta G_z} \Phi, \quad \Phi_{\bar{\mathbf{G}}\bar{\mathbf{G}}'} = e^{-2\pi i \left[ \frac{2}{3}(G_1 - G'_1) + \frac{1}{3}(G_2 - G'_2) \right]} \quad (5.46)$$

now depends on  $\Delta G_z$  and the in-plane reciprocal lattice vectors  $\bar{\mathbf{G}} = (G_1, G_2)$ . This is the reason for the appearance of the two different contributions in  $\pi_{AB}$ . Indeed, we have  $\Phi_{\bar{\mathbf{G}}\bar{\mathbf{G}}'} = 1$  for the case shown in fig. 5.17a and the factor  $F$  becomes 2 or 0 when  $\Delta G_z$  is even (blue surface) or odd (red plane). In the case shown in fig. 5.17b,  $\Phi_{\bar{\mathbf{G}}\bar{\mathbf{G}}'} = -\frac{1}{2} + \frac{\sqrt{3}}{2}i$  is complex and we obtain two non-zero contributions to  $\pi_{AB}$ . This clearly explains the origin of the checkerboard structure of the polarisability of graphite AB.

Note that the difference between the full *ab-initio* calculations (dots) and the results from the BBA (surface) is very small in fig. 5.17. This validates the use of the building-block approach even in bulk systems like graphite. We will make use of this fact in the next chapter by calculating the response of a carbon nanotube from the polarisability of its building block—which is also a single graphene layer.

## 5.7 Further Studies

Additionally to the studies for the in-plane excitations at low energies, we have also considered the range of  $\pi + \sigma$  excitations at energies up to 40 eV both for in-plane and out-of-plane momentum transfers.

### 5.7.1 Higher Energies

The extension of our *ab-initio* calculations to higher energies is, in principle, straightforward. Repeating the convergence tests described in section 3.3.4, we find that the dimension of the dielectric matrix  $\varepsilon_{\mathbf{G}\mathbf{G}'}$  has to be considerably increased at high energies (see table). Indeed, in-plane LFE become more important for the localised  $\sigma$  electrons than for the rather homogeneously distributed  $\pi$  electrons [112]. As the numerical effort increases quadratically with `npwmat`, the calculations for isolated graphene become only feasible by means of the interpolation method I. Starting from a calculation with a small supercell of  $d = 4d_0$ ,<sup>14</sup> we extrapolate the spectra for distances up to  $d = 32d_0$ . The convergence with the interlayer distance  $d$  is found to be comparable to our low-energy results given in section 5.3.2. The loss spectra for isolated graphene at different in-plane momentum transfers along the  $\Gamma\text{M}$  direction are shown in fig. 5.18a (solid lines). We find a strong  $\pi + \sigma$ -plasmon peak which disperses to higher energies for increasing  $\bar{q}$ .

<code># ground state</code>
<code>d=4d0, 22x22x1</code>
<code>npwfn 817</code>
<code>nbands 80</code>
<code>npwmat 359</code>
<code>broad 0.5</code>

#### Comparison with Experiment

The spectra at low momentum transfers are in very good agreement with the EELS measurements on single-layer graphene shown in fig. 5.3b [141]. The  $\pi$  and  $\pi + \sigma$  plasmons are found at 4.2 eV and 14.5 eV, respectively and also the characteristic shape of the  $\pi + \sigma$ -plasmon peak is reproduced. Note that a direct comparison is eventually hampered by (i) the zero-loss peak which masks contributions at low energies below 5 eV and (ii) the fact that the experimental spectrum is actually a weighted sum of loss spectra for different in-plane momentum transfers  $\bar{q}$ .

#### Local-Response Approximation

As in the case of low energies, the local-response approximation reproduces exactly our *ab-initio* results when the momentum transfer  $\bar{q}$  is sufficiently small (see dashed lines in fig. 5.18a). At larger momentum transfers  $\bar{q} > 0.2 \text{ \AA}^{-1}$ , we can partially correct the failure of the LRA by adding an empirical screening of the Coulomb potential as described in section 5.5.1. The results of this LRA- $\beta$  method are shown as dash-dotted lines. The  $\bar{q}$  dependent screening factor  $\beta$  has been calculated from eq. (5.41) using the empirical parameter  $\lambda_\sigma = 0.8 \text{ \AA}$  for the average decay length of the  $\sigma$  orbitals perpendicular to the sheet (compare with  $\lambda_\pi = 1.5 \text{ \AA}$  used at low energies for the  $\pi$  orbitals). Although the position of the plasmon peak can be corrected quite satisfactorily, its shape is still different. This should be attributed to the in-plane LFE which become more important for the localised  $\sigma$  states and which are completely neglected in the LRA- $\beta$  method.

<sup>14</sup>We increased the starting distance to be sure that also for the high-energy states the orbitals from different layers are not hybridised.

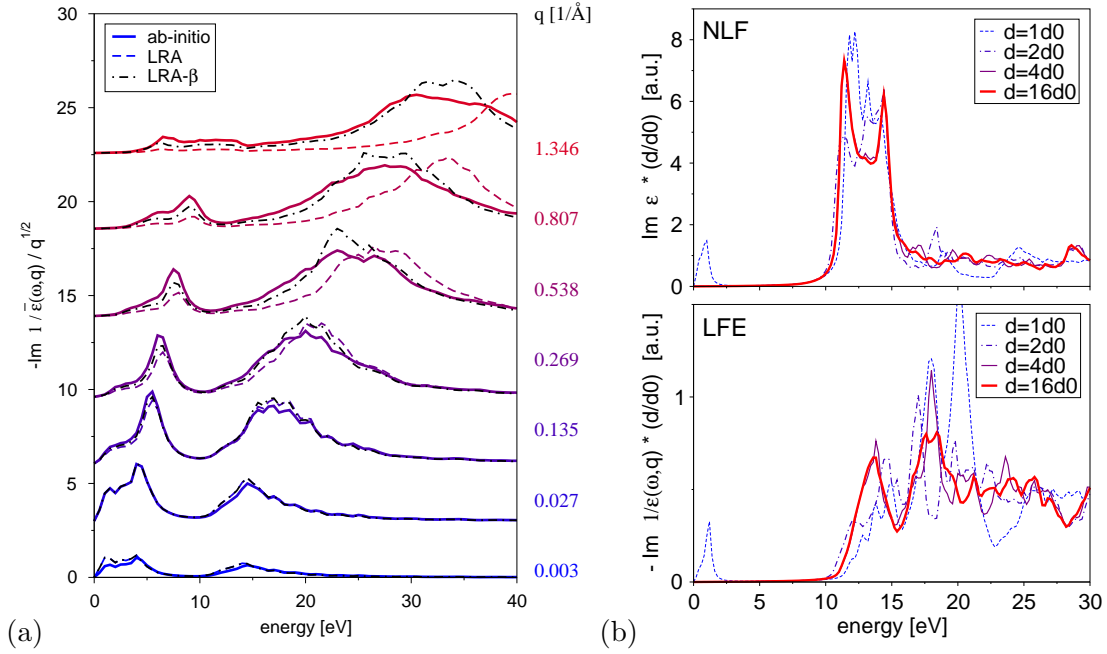


**Fig. 5.18:** Calculated excitation spectrum of graphene for energies including the  $\pi + \sigma$  plasmon. (a) Loss function of graphene for different in-plane momentum transfers  $\bar{q}$ . We compare full *ab-initio* calculations (solid lines) with the LRA (dashed) and LRA- $\beta$  results (dash-dotted,  $\lambda = 0.8 \text{ \AA}$ ). (b) *Ab-initio* calculations of the polarisability (top) and susceptibility (bottom) in graphene stacks with different interlayer distances  $d$  for perpendicular momentum transfer  $|q| = 0.47 \text{ \AA}^{-1}$ . Analogous to fig. 5.8a and c.

## 5.7.2 Perpendicular Momentum Transfer

Finally, we have also considered momentum transfers which are perpendicular to the sheet. Several problems have been encountered in this case.

### Convergence with Interlayer Distance

First, we have tried to converge the independent-particle polarisability  $\chi^0$  and the loss function  $-\text{Im} 1/\varepsilon_M$  with respect to the interlayer distance  $d$  (see fig. 5.18b top and bottom, respectively). Both spectra are completely flat up to 10 eV as the  $\pi - \pi^*$  transitions are dipole-forbidden. The small peak at very low energies is only due to the overlap of the wave functions of different layers in AA stacked graphite [112]. At energies beyond 10 eV, we find a strong peak in  $\chi^0$  at about 15 eV. Its intensity is strongly reduced, when LFE are included (see scale in top and bottom panel). This is the well known *depolarisation effect* which is of particular importance in finite systems.

However, neither the loss spectrum  $-\text{Im} 1/\varepsilon_M$  nor the polarisability  $\chi^0$  converge with the interlayer distance  $d$ . Especially for  $\chi^0$  this behaviour is in stark contrast to our in-plane results (see fig. 5.8c). Additionally, one has to include  $k$ -points in  $z$ -direction to converge the spectra and the interpolation method I seems to fail.

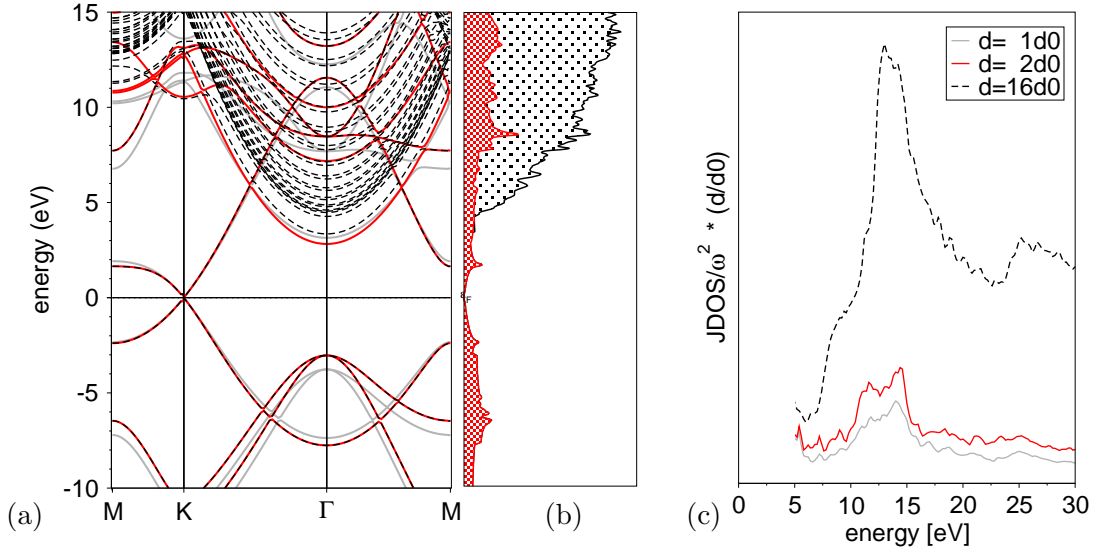


**Fig. 5.19:** (a) The Kohn-Sham bandstructure at  $k_z = 0$ , (b) the corresponding DOS and (c) JDOS for perpendicular polarisation  $q_z$  are compared for graphene stacks with different interlayer distances  $d$ . The contribution of free-electron states clearly vanishes for small supercell size  $d$ .

### Free-Electron States

One possible explanation for these problems is the bad description of free-electron states within the supercell approach. Indeed, in a (quasi) two-dimensional system only the in-plane momentum  $\bar{k}$  is a good quantum number. The eigenspectrum of the 2D Hamiltonian contains both (i) electron states which are localised at the sheet and therefore have a low energy and (ii) free-electron states which have a non-zero average momentum component  $\langle k_z \rangle$  perpendicular to the sheet. The latter can be associated to electrons that move in perpendicular direction and are weakly scattered when they cross the graphene layer. These scattering states form a continuum and have a parabolic dispersion with energies well beyond the Fermi level.

If we consider in-plane momentum transfers, transitions between a bound electron with  $\langle k_z \rangle = 0$  and these scattering states are generally forbidden. For perpendicular momentum transfers, instead, this is no longer the case. Transitions to free-electron states will contribute to the polarisability of the system. Although the corresponding excitation energies are rather high, LFE mix transitions of very different energies and the free-electron states can easily contribute to the screening of the system (see section 5.3.3).

In the supercell approach, however, the system is artificially repeated along the perpendicular direction and the momentum component  $k_z$  becomes a good quantum number. For a given momentum transfer  $q_z$ , the bound state at wave vector  $k_z$  can be only excited to a free-electron state with  $k'_z = k_z + q_z + G_z$ , where  $G_z$  is an integer multiple of  $2\pi/d$ . Thus, the continuum of free-electron states is replaced by a set of discrete bands

with parabolic dispersion and the number of possible transitions decreases with smaller interlayer distance  $d$ .

This general argument can be easily verified by considering the Kohn-Sham band-structure of graphene stacks for decreasing interlayer distance  $d$  (see fig. 5.19a). The valence states of the system, which are located at the layer, hardly depend on the interlayer distance  $d$ . Only in graphite ( $d = d_0$ ), the orbitals of neighbouring graphene layers start to overlap and we observe a small band splitting (gray lines). In contrast, the number of free-electron states above 5 eV clearly decreases with decreasing supercell size  $d$  (only states with  $k_z = G_z$  are shown) [112]. The same behaviour can be observed in the density-of-states and joint density-of-states (see fig. 5.19b and c).

As a consequence, the contribution of the free-electron states to the polarisability slowly converges with the interlayer distance  $d$ . One might try to add these transitions to the scattering states analytically, e. g., using a nearly-free electron model. In particular the matrix elements have to be evaluated properly. *Nevertheless, we find that only in-plane excitations contribute to the dielectric response of graphene at low energies  $E < 10$  eV (see fig. 5.18b)*

## Conclusions

In this chapter, I studied the dielectric response of a two-dimensional system. In particular, I performed *ab-initio* and tight-binding calculations for the loss function of an isolated graphene sheet within the random phase approximation. In these calculations, a plane-wave basis set is used and large supercells are required in order to avoid spurious Coulomb interactions between the artificial replicas, i. e., the calculations become numerically very demanding. Based on the observation that the induced charge is strongly localised in direction perpendicular to the sheet, I developed and implemented several methods to overcome this problem:

- First, I have considered the limit of a perfectly localised response. Starting from a microscopic formalism, one can introduce scalar, two-dimensional response functions and derive an effective Dyson equation (5.32) which is known from local dielectric theory. In particular, one obtains an analytic relation between the in-plane dielectric function of graphite and the two-dimensional response function of graphene [see eq. (5.38)]. For momentum transfers up to  $0.1 \text{ \AA}^{-1}$ , this analytic expression reproduces exactly our full *ab-initio* results for the dielectric response of graphene.
- Second, I have included nonlocal effects by introducing an empirical parameter  $\lambda$  that is related to the average decay length of the orbitals perpendicular to the sheet. Fitting this parameter, the full *ab-initio* results for graphene can be reproduced for momentum transfers up to  $1 \text{ \AA}^{-1}$ .
- Third, I have substantially reduced the computational effort that is needed to solve the microscopic Dyson equation in our *ab-initio* calculations (speed-up of  $\approx 100$ ). To this end, I developed and implemented an interpolation method in reciprocal space (p. 92) and alternatively a cutoff method for the Coulomb potential in real space (p. 102). With this method, it is possible to compute the nonlocal, microscopic dielectric response of a two-dimensional system starting from a calculation of the independent-particle polarisability using a relatively small supercell.

These methods have been applied to study collective excitations in single and multi-layer graphene. The following main results have been obtained in this chapter:

- The in-plane dispersion of the  $\pi$  plasmon in isolated graphene has been studied. Crystal local-field effects are found to strongly mix electronic transitions over a large range of energies which results in a nearly linear plasmon dispersion.
- These local-field effects are mainly due to the inhomogeneity of the system perpendicular to the sheet. In-plane local-field effects become only noticeable for large momentum transfers  $q \gtrsim 1 \text{ \AA}^{-1}$ .
- In the limit of vanishing momentum transfers  $q \rightarrow 0$ , the loss function of graphene is found to be nearly identical to the absorption spectrum of graphite. This can be

understood by the following two facts: first, hybridisation effects between wave functions from different sheets and crystal local-field effects are very small in graphite. And second, the influence of the long-range component of the Coulomb interaction vanishes in two-dimensional systems for  $q \rightarrow 0$ .

- The accuracy of the nearest-neighbour tight-binding approach and the local-response approximation have been discussed by comparison with our full *ab-initio* results for graphene.
- Finally, a building-block approach for the microscopic dielectric response of assembled systems (like multi-layer graphene) has been presented. We will make use of this concept in the next chapter, where the response of a single-wall carbon nanotube will be described starting from the response of its building block, namely graphene.

## 6 Polarisability of Carbon Nanotubes

Single-wall carbon nanotubes are prototypes of (quasi) one-dimensional systems. They correspond to atomically thin hollow cylinders of rolled graphene. Within the *zone-folding model*, one can directly derive the ground-state properties of a tube from the graphene band structure. In this chapter, we extend this idea and apply the zone-folding model to the microscopic dielectric function  $\varepsilon(\mathbf{q}, \mathbf{q}', \omega)$  which describes the excitation properties of the tube. This allows us to describe collective excitations in single-wall carbon nanotubes starting from the polarisability of graphene. We will use this method to analyse the anisotropic behaviour of the plasmon dispersion in SWCNTs and to explain corresponding AR-EELS experiments.

To this end, we proceed in close analogy to the previous chapter: First, we review the basic theory of SWCNTs (see also [4, 14, 146]). The geometry and the ground-state properties are discussed within the zone-folding model. Second, we establish a connection between the microscopic polarisability  $\pi(\mathbf{q}, \mathbf{q}', \omega)$  of graphene and the isolated nanotube. Within the local-response approximation, we can introduce cylinder response functions and derive an effective Dyson equation as in the case of two-dimensional systems. Third, we relate the cylinder response functions with the energy-loss probability measured in AR-EELS experiments. The anisotropic plasmon dispersion in isolated tubes is studied and explained. Finally, the full Dyson equation will be solved by extending the Coulomb-cutoff method III (see p. 102) for cylindrical geometries.

### 6.1 Single-Wall Carbon Nanotubes

A single-wall carbon nanotube (SWCNT) is basically a sheet of graphene that is rolled up into a hollow cylinder (see fig. 6.1). Each tube can be identified by the *chiral vector*  $\mathbf{C} = n\mathbf{a}_1 + m\mathbf{a}_2$  which corresponds to a graphene lattice vector and indicates which atoms are identified by rolling up the sheet. Its modulus and direction correspond to the circumference of the tube and the curling direction, respectively. The pair of integer numbers  $n \geq m \geq 0$  uniquely characterises the nanotube geometry. Tubes of the type  $(n, 0)$  and  $(n, n)$  are called *zig-zag* and *armchair* tubes according to the characteristic atom pattern along their circumference. Any other  $(n, m)$  tube is called *chiral* SWCNT.

The chiral vector  $\mathbf{C}$  can be identified with a pure rotation of the tube by  $2\pi$ . The *translational vector*  $\mathbf{T}$ , instead, corresponds to the primitive translation along the tube axis. It is defined as the shortest lattice vector of the unrolled graphene sheet that is perpendicular to  $\mathbf{C}$  (see fig. 6.1a). One has [4]:

$$\mathbf{T} = \frac{2m+n}{d_R}\mathbf{a}_1 - \frac{m+2n}{d_R}\mathbf{a}_2, \quad d_R = \text{gcd}(2m+n, m+2n). \quad (6.1)$$

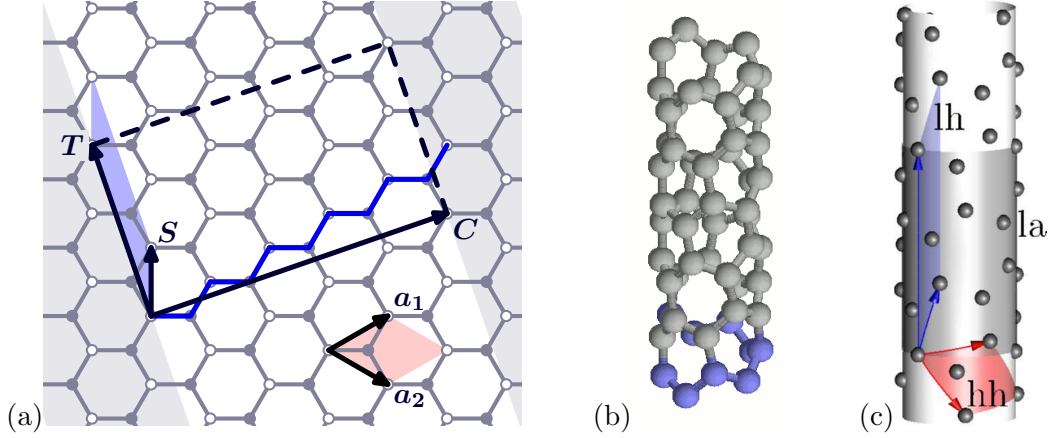


**Fig. 6.1:** Geometry of the chiral (4,1) nanotube. (a) Unit cell of the corresponding graphene-ribbon which is (b) rolled up into the nanotube. (c) Alternative choices for the unit cell of the tube: (la) linear-angular, (lh) linear-helical, and (hh) helical-helical unit cell.

The rectangle spanned by  $\mathbf{T}$  and  $\mathbf{C}$  corresponds to the primitive unit cell of the tube. It contains  $N = 2(n^2 + m^2 + nm)/d_R$  graphene unit cells and thus  $2N$  carbon atoms. The positions of these atoms can be easily expressed in terms of the *symmetry vector*  $\mathbf{S}$ .<sup>1</sup> It is defined as the graphene lattice vector inside the rectangular unit cell with minimal projection along  $\mathbf{C}$ , or equivalently, by the unique solution of the equations [4]

$$\mathbf{S} = \tilde{p}\mathbf{a}_1 + \tilde{q}\mathbf{a}_2, \quad \mathbf{S} \cdot \mathbf{C} = C^2/N, \quad 0 \leq \mathbf{S} \cdot \mathbf{T} < T^2, \quad (6.2)$$

for integer numbers  $\tilde{p}$  and  $\tilde{q}$ . Each of the  $2N$  atomic sites inside the rectangle can be successively reached by the vector  $i\mathbf{S} + \boldsymbol{\tau}_\alpha$ , going first to the graphene unit cell with index  $i = 1, \dots, N$  and then to one of the two atoms given by the basis vector  $\boldsymbol{\tau}_A$  or  $\boldsymbol{\tau}_B$  in eq. (5.1). Whenever  $i\mathbf{S}$  crosses the border of the rectangular unit cell, it is wrapped back by a translation with  $\mathbf{T}$ . Thus, the geometry of the tube is entirely defined.

It should be noted that this ideal geometry is slightly distorted for the smallest tubes with diameters  $d < 1$  nm: First, the diameter is found to be larger than  $C/\pi$  in order to compensate the shortening of the nearest-neighbour distance on the curved surface. Second, the strong curvature leads to a rehybridisation, mixing the formerly orthogonal  $\pi$  and  $\sigma$  orbitals. For larger tubes, however, these corrections can be safely ignored.

### Symmetry and the Reduced Unit Cell

The symmetry group of the SWCNT is extensively discussed by Barros *et al.* [172] or in [4, 146]. Most of the symmetry operations of the nanotube can be derived from the unrolled graphene sheet (see table 6.1): First, each lattice vector  $\mathbf{R}$  in graphene corresponds to a screw operation in the tube with a rotation of  $2\pi \frac{\mathbf{R} \cdot \mathbf{C}}{C^2}$  and a translation by  $\mathbf{R} \cdot \mathbf{T}/T$  along the axis. Second, some of these operations are actually pure rotations if

<sup>1</sup>It corresponds to the vector  $\mathbf{R}$  in [4].

	CNT	Graphene
$\{C_N, t\}$	screw axis operation with a rotation by $\frac{2\pi}{N}$ and a shift $t = \frac{(m\tilde{p}-n\tilde{q})T}{N}$	translation by $\mathbf{R}$
$\{\hat{1}, T\}$	translation along axis	translation by $\mathbf{T}$
$C_d$	rotation around axis by $2\pi/d$	translation by $\mathbf{C}/d$
$C_2$	rotation perpendicular to axis by $\pi$	rotation of the sheet by $\pi$
$\sigma_h$	horizontal mirror plane (achiral tube)	mirror plane perp. to $\mathbf{T}$
$\sigma_v$	vertical mirror plane (achiral tube)	—

**Tab. 6.1:** Symmetry operations of a SWCNT and their correspondence in the unrolled graphene sheet. The last two mirror planes are only present in achiral tubes.

the chiral vector  $\mathbf{C}$  is a multiple of a graphene lattice vector. The tube then has a  $d$ -fold rotation axis  $C_d$ , where  $d = \text{gcd}(n, m)$ . Third, the translation vector  $\mathbf{T}$  corresponds to a primitive translation of the tube along its axis. And finally, a two-fold rotation axis perpendicular to the tube can be derived from the six-fold rotation symmetry of the hexagons. It interchanges the  $A$  and  $B$  atoms. Achiral tubes (zig-zag and armchair) have additional horizontal and vertical mirror planes. The latter has no correspondence in graphene.

Taking into account all screw symmetries, the nanotube structure can be obtained from a *reduced unit cell* using two non-collinear screw vectors (arrows in fig. 6.1c). In the unrolled graphene sheet, they become two lattice vectors spanning a unit cell which can be smaller than the rectangular cell of the tube. Two choices are of particular interest:

1. *helical-helical construction:* The unit cell is spanned by the screw vectors that correspond to the primitive translations  $\mathbf{a}_1$  and  $\mathbf{a}_2$  in graphene (denoted by hh, fig. 6.1c). This choice makes a direct mapping between graphene and tube coordinates possible.
2. *linear-helical construction:* The unit cell is spanned by the translation vector  $\mathbf{T}$  and the screw operation that corresponds to the symmetry vector  $\mathbf{S}$  (denoted by lh).

We will see in the following that this alternative description of the tube geometry has many advantages over the 1D description which uses only the primitive translation  $T$  along the tube axis. For example, the reduced unit cell contains only two carbon atoms and implicitly accounts for all screw symmetries of the system.

## Reciprocal Space

The symmetries of a system are closely related to conservation laws. One example is the Bloch theorem in crystals which uses the fact that any eigenstate of the Hamiltonian must be also an eigenstate of the translation operator  $e^{\nabla \cdot \mathbf{R}}$ . The corresponding eigenvalue  $e^{i\mathbf{k} \cdot \mathbf{R}}$  is then conserved during time-evolution and the wave vector  $\mathbf{k}$  can only change by a reciprocal lattice vector  $\mathbf{G}$ . The reduced momentum  $\hbar \mathbf{k}_r$  is a good quantum number.

In a SWCNT, the translational period  $T$  leads to the conservation of the *on-axis momentum*  $k$ , while the screw symmetries are connected with the *helical momentum*  $\tilde{h}$ . Again, these quantum numbers can be understood by unfolding the tube. The screw symmetries then become translations in graphene leading to a direct mapping between the quantum numbers of the tube and the in-plane momentum  $\mathbf{k}$  in graphene:

$$k = \mathbf{k} \cdot \mathbf{T} / T, \quad \tilde{h} = \mathbf{k} \cdot \mathbf{S} / S, \quad \mathbf{k} = \frac{kT}{2\pi} \mathbf{b}_T + \frac{\tilde{h}S}{2\pi} \mathbf{b}_S. \quad (6.3)$$

Here we have introduced the reciprocal lattice vectors  $\mathbf{b}_T$  and  $\mathbf{b}_S$ . They are defined by  $\mathbf{T} \cdot \mathbf{b}_T = \mathbf{S} \cdot \mathbf{b}_S = 2\pi$  and  $\mathbf{S} \cdot \mathbf{b}_T = \mathbf{T} \cdot \mathbf{b}_S = 0$ , and span the reciprocal unit cell for the linear-helical construction of the tube [172]. As the reduced unit cell only contains two atoms, there exists a unique mapping from the eigenstates of the nanotube to the eigenstates of the graphene layer. Equivalently, the reciprocal-space structure of the tube can be superimposed on that of the graphene layer (see fig. 6.2a).

Additionally to the symmetry properties, the periodicity of the wave function along the circumference has to be taken into account. Any state of the tube must be invariant under a rotation of  $2\pi$ , i. e., the corresponding phase shift  $\mathbf{C} \cdot \mathbf{k} = 2\pi j$  must be an integer multiple of  $2\pi$ .<sup>2</sup> Thus, the momentum  $\mathbf{k}$  is restricted to a set of parallel lines with equal distance  $2\pi/C$  and the Brillouin zone of the nanotube can be understood as the sum of  $N$  line segments<sup>3</sup> of length  $2\pi/T$  (see fig. 6.2a). The line index  $j = \mathbf{C} \cdot \mathbf{k} / (2\pi)$  corresponds to the projection of  $\mathbf{k}$  along the direction of the pure rotations and can be interpreted as quasi-angular momentum (see [172] for details).

For the sake of simplicity, one often uses  $j = 0, \dots, N-1$  and the on-axis momentum  $k \in [0, 2\pi/T)$  to label the eigenstates of the tube instead of working with the helical coordinates  $\tilde{h} \in [0, 2\pi/S)$  and  $k$ . However, it is important to note that  $j$  is *not* conserved when  $k$  crosses the Brillouin zone boundary. In this case, one has to use the vectors  $\mathbf{b}_T$  and  $\mathbf{b}_S$  to translate it back into the first Brillouin zone. This does not affect the helical quantum number  $\tilde{h}$ , but changes the projection  $j$  (e. g., see dashed lines in fig. 6.2a for a crossing at the  $\Gamma$  point). This fact complicates the evaluation of selection rules involving *Umklapp processes*, i. e., transitions between different Brillouin zones [146]. In these cases, one has to use helical coordinates or, equivalently, the associated quasi-two-dimensional wave vector  $\mathbf{k}$  given in eq. (6.3).

## Ground State and Single-Particle Bandstructure

We have seen that the electronic states of the SWCNT and the graphene sheet can be mapped onto each other. This is a consequence of the equivalent symmetry properties. No assumption on the actual form of the wave function has been made so far.

It has been found that many properties of the nanotube can be directly derived from graphene within the following *zone-folding model*: Neglecting any curvature effects, one assumes that the eigenstates and -energies do not change when the sheet is rolled up

<sup>2</sup>We consider only the spin-independent part of the wave function.

<sup>3</sup>It is convenient to use lines of the same length. The rectangle between two line segments corresponds to the Brillouin zone of the rectangular unit cell of the tube which contains  $N$  graphene unit cells.

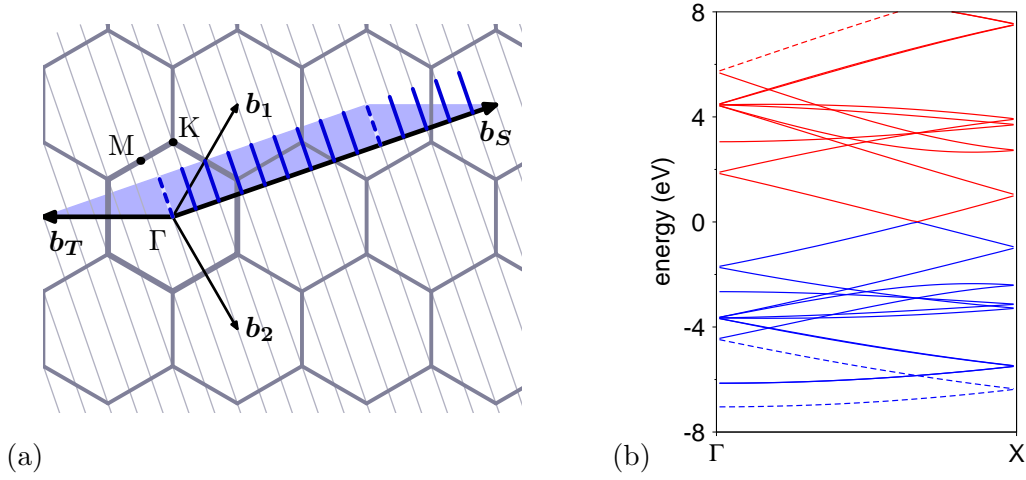


**Fig. 6.2:** Zone-folding for the chiral (4,1) nanotube. (a) Superposition of the reciprocal space of graphene (plane) and the nanotube (cutting lines). The Brillouin zone of the tube is spanned by  $\mathbf{b}_T$  and  $\mathbf{b}_S$  and contains  $N$  parallel line segments (blue) of length  $2\pi/T$ . (b) Tight-binding bandstructure of the (4,1) tube within the zone-folding model ( $\gamma_0 = -2.84$  eV,  $s_0 = 0.07$ ).

into a cylinder. Thus, the electronic structure of the SWCNT can be directly obtained from that of graphene using the mapping (6.3) in reciprocal space.

For example, figure 6.2b shows the bandstructure of a chiral (4,1) nanotube that has been derived from the tight-binding bandstructure of graphene (see section 5.2.2). The cutting lines in the nanotube Brillouin zone give rise to  $N$  valence  $\pi$  bands (blue) and  $N$  conduction  $\pi^*$  bands (red). Due to the perpendicular rotation axis  $C_2$  of the tube, the bandstructure is symmetric  $E_{n,j,k} = E_{n,j,-k}$ . One can restrict to quantum numbers  $k$  along the  $\Gamma X$  line, where X denotes the zone boundary at  $\pi/T$ .

Within the zone-folding model, the (4,1) tube is metallic due to the degeneracy of the  $\pi$  bands at the  $K$  point. In general, any  $(n,m)$  tube whose Brillouin-zone line segments intersect the  $K$  point of graphene, is predicted to be metallic. This is the case, if

$$2\pi j \stackrel{\perp}{=} \mathbf{C} \cdot \mathbf{K} = (n\mathbf{a}_1 + m\mathbf{a}_2) \cdot \left(\frac{1}{3}\mathbf{b}_1 - \frac{1}{3}\mathbf{b}_2\right) = \frac{2\pi}{3}(n - m), \quad (6.4)$$

for any line index  $j$ . The tube is metallic if and only if  $(n - m)/3$  is an integer number.

The predictions of the zone-folding model are found to be reliable for tubes with diameters larger than 1 nm. Only for the smallest tubes, the strong curvature leads to a rehybridisation of the  $\pi$  and  $\sigma$  states which modifies the band structure [e. g. 130, 146]. For example, the (5,0) nanotube is actually metallic contrary to the rule of thumb (6.4).

### Excitations in SWCNTs

Experimentally, it is very complicated to investigate the characteristic excitation spectrum of a *single* nanotube. It has been possible to measure the energy-loss spectrum for an isolated tube using a scanning transmission electron microscope (see fig. 7.4b,

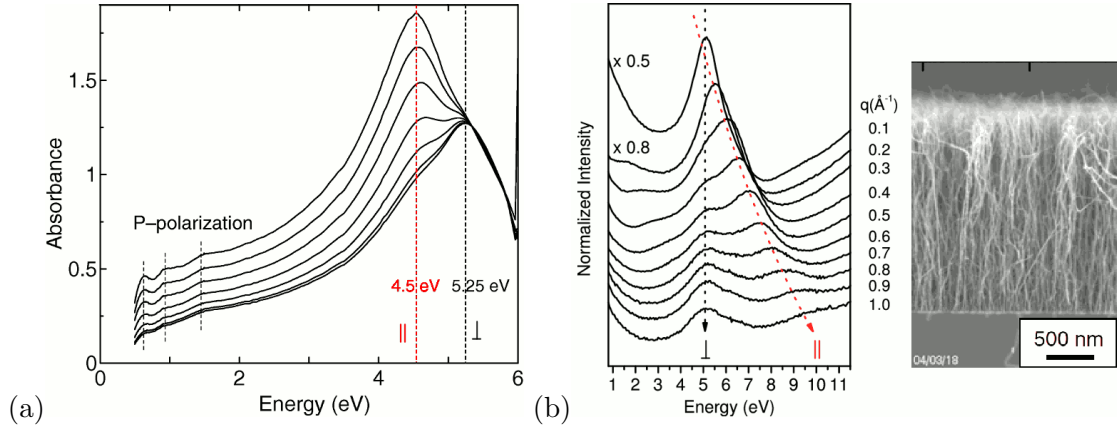


**Fig. 6.3:** Measurements of the anisotropic excitations in isolated SWCNTs (diameter of 2 nm). (a) Absorption spectra for different polarisation directions. The orientation is varied from  $\vartheta = 45^\circ$  (top) to  $\vartheta = 90^\circ$  (bottom), where the polarisation becomes perpendicular to axis (Reproduced from [161], © 2005 by The American Physical Society). (b) AR-EELS measurements for increasing momentum transfer  $q$  (Reproduced from [157], © 2008 by The American Physical Society).

[173, 174]). But absorption experiments can be only performed on bulk samples. Much effort has been dedicated to the synthesis of samples with nanotubes of similar size and thickness. Recently, Murakami *et al.* [175] were able to grow forests of single-wall carbon nanotubes on top of a substrate (see fig. 6.3). These tubes have an average diameter of 2 nm, are sufficiently isolated from each other, and are aligned within  $30^\circ$ . This allows us to study the anisotropic behaviour of excitations in SWCNT.

Figure 6.3a shows absorption measurements on these samples for different directions of the linear polarisation [161]. Two excitation peaks at 4.5 eV and 5.25 eV can be identified which become visible for a polarisation parallel and perpendicular to the tube axis, respectively. They have been compared with the excitations of graphite, namely the in-plane excitation peak  $\text{Im } \varepsilon_\perp \approx 4.5$  eV and the out-of-plane plasmon  $\text{Im } \varepsilon_\parallel^{-1} \approx 5.2$  eV.<sup>4</sup>

The same samples have been also investigated using AR-EELS measurements [157]. Figure 6.3b shows the energy-loss spectra for increasing momentum transfer  $q$ . Again, two excitations are distinguished: (i) a peak at 5.2 eV which does not disperse and is therefore attributed to a perpendicular excitation, and (ii) a dispersing peak which is identified with an on-axis plasmon in the nanotube. In the limit of large tubes, the latter should be similar to an in-plane excitation in graphene. Comparing the plasmon dispersion between the nanotube samples and graphene (fig. 6.3b vs. fig. 5.9b), we found indeed a very good agreement (see [157] for details). The origin of the perpendicular peak is still under debate. Recent inelastic X-ray scattering experiments on similar samples did not show this peak at all [176].

<sup>4</sup>The notation  $\varepsilon_\parallel$  and  $\varepsilon_\perp$  used in literature refers to the normal axis of the sheet, not the layer itself.

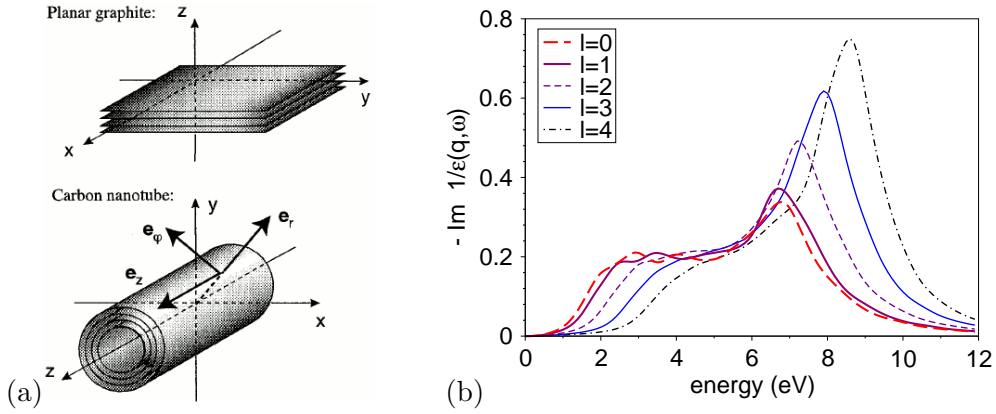


**Fig. 6.4:** (a) Model dielectric function of a multi-wall CNT. The dielectric tensor of graphite has been projected onto a cylinder. From [37]. (b) Tight-binding calculation for the loss function  $-\text{Im} \bar{\epsilon}_{\text{CNT}}^{-1}$  of a (23, 0) SWCNT for  $p = 0.2 \text{ \AA}^{-1}$  and different angular momenta  $l$ .

These results lead us to several questions that have motivated our following discussion: *Can we decompose the spectra into a perpendicular and parallel contribution? Should we also decompose the momentum transfer  $\mathbf{q}$  into the corresponding components? Why do we observe excitation energies at the same energies as in graphite? How can we calculate the loss function of a tube for perpendicular momentum transfer? Can we derive a formal relation between excitations in carbon nanotubes and excitations in graphene?*

## 6.2 Model Calculations

In this section, we briefly review the effective-medium approach and the tight-binding method for the calculation of the electronic response of a nanotube.

### 6.2.1 Dielectric Theory

Dielectric response theory (see section 1.2.1) has been successfully applied for a large variety of systems, such as slabs, spheres, composite systems, and cylindrical interfaces [30, 33, 177]. In order to describe excitations in multi-wall CNTs, the formalism has been extended to account for the local anisotropy [37]. The basic idea is sketched in fig. 6.4a: The dielectric response of the system is locally approximated by the dielectric tensor of graphite. Due to the anisotropy of graphite, the in-plane component  $\epsilon_{\perp}$  and out-of-plane component  $\epsilon_{\parallel}$  differ. Using cylindrical coordinates, one has for the tube

$$\hat{\epsilon}_{\text{CNT}}(\omega) = \epsilon_{\parallel}(\omega) \hat{e}_{\theta\theta} + \epsilon_{\perp}(\omega) \hat{e}_{\varphi\varphi} + \epsilon_{\perp}(\omega) \hat{e}_{33}, \quad (6.5)$$

where  $\hat{e}_{\alpha\beta}$  corresponds to the local tensor basis. The dielectric function of graphite can be obtained from absorption experiments or *ab-initio* calculations of the bulk material. Taking into account the appropriate boundary conditions at the inner and outer radius  $r$  and  $R$  of the cylinder, the Maxwell equations can now be solved analytically [178].

One obtains an expression for the response function  $\varepsilon_{\text{CNT}}^{-1}(lp; \omega)$  of the nanotube which depends on the on-axis momentum  $p$  and the angular momentum  $l$  of the external perturbation. The energy loss of a fast electron can be written in the form (for a compact notation we sometimes omit the comma between the arguments)

$$\frac{dP}{dE}(\omega) = - \sum_l \int dp C_{lp}^2(\omega) \text{Im} \varepsilon_{\text{CNT}}^{-1}(lp; \omega), \quad (6.6)$$

where  $C_{lp}$  is a kinematical factor that depends only on the experimental conditions for the probing electron. The resulting energy-loss spectrum can be understood as a weighted sum of nanotube loss functions  $-\text{Im} \varepsilon_{\text{CNT}}^{-1}(lp; \omega)$ . Thus, the main excitation peaks can be related to the normal modes (plasmons) of the nanotube (zeros of  $\text{Re} \varepsilon_{\text{CNT}}$ ).

The dielectric model was found to be in good agreement with EELS experiments for different  $r/R$  ratios and, surprisingly, even for ideally thin tubes  $r/R \rightarrow 1$  [174]. In this limit, the dielectric model predicts two excitation peaks which are given by the maxima of  $\text{Im} \varepsilon_{\perp}(\omega)$  and  $-\text{Im} \varepsilon_{\parallel}^{-1}(\omega)$  and correspond to a symmetric (tangential) and antisymmetric (radial) mode, respectively [179, 180]. The latter is found to vanish with decreasing wall thickness [174]. Interestingly, the two modes in the absorption measurements on SWCNTs are found at the same energies (see fig. 6.3a) [161].

## 6.2.2 Tight Binding

The response function  $\varepsilon_{\text{CNT}}^{-1}(lp; \omega)$  of a SWCNT can be also calculated within a tight-binding approach [181–185]. This becomes particularly simple in the zone-folding approximation, because all eigenstates and -energies are readily obtained from graphene

$$E_{n,j,k} = E_{nk}, \quad |n, j, k\rangle = \psi_{nk}, \quad \mathbf{k} \stackrel{(6.3)}{=} 2\pi j \mathbf{C}/C^2 + k \mathbf{T}/T, \quad (6.7)$$

where  $E_{nk}$  and  $\psi_{nk}$  are given by eq. (5.14) and  $j$  and  $k$  denote the quasi-angular and on-axis momentum of the corresponding eigenstate in the tube, respectively.

### Polarisability $\bar{\chi}_{\text{CNT}}^0$

Analogous to section 5.2.2, I have calculated the independent-particle polarisability  $\bar{\chi}_{\text{CNT}}^0$  of the nanotube from eq. (3.14). The Brillouin-zone integration is now restricted to the  $N$  discrete lines that constitute the Brillouin zone of the nanotube. If the tube is large, the cutting lines become sufficiently dense and the expression converges towards the polarisability of the graphene sheet.

The momentum transfer  $\mathbf{q} = 2\pi l \mathbf{C}/C^2 + p \mathbf{T}/T$  is given in terms of an angular and on-axis part  $l$  and  $p$ , respectively. The angular momentum transfer  $l$  is restricted to integer values as the quasi-angular momentum  $j$ . By construction, the matrix elements  $\tilde{\rho}^{nn'}(lp)$  of the nanotube are equivalent to  $\tilde{\rho}_{\mathbf{k}}^{nn'}(\mathbf{q})$  of graphene which are given by eq. (5.17):

$$\tilde{\rho}_{jk}^{nn'}(lp) = \langle n', j-l, k-p | e^{-il\varphi} e^{-ip\delta} | n, j, k \rangle = \langle \psi_{n'\mathbf{k}-\mathbf{q}} | e^{-i\mathbf{q}\mathbf{r}} | \psi_{n\mathbf{k}} \rangle = \tilde{\rho}_{\mathbf{k}}^{nn'}(\mathbf{q}). \quad (6.8)$$

In particular, Umklapp effects are correctly taken into account because the mapping of eq. (6.7) implicitly employs helical coordinates, namely the reduced coordinates of  $\mathbf{k}$ .

## Dielectric Function in RPA

In RPA, the dielectric function of the nanotube is now given by [181]

$$\bar{\epsilon}_{\text{CNT}}(lp; \omega) = \epsilon_\sigma - v_{\text{CNT}} \bar{\chi}_{\text{CNT}}^0, \quad v_{\text{CNT}} = \frac{e^2}{\epsilon_0} I_l(|p|\mathcal{R}) K_l(|p|\mathcal{R}) \quad (6.9)$$

where  $\epsilon_\sigma = 2.4$  is the background dielectric constant [151] and  $v_{\text{CNT}}$  denotes the Coulomb potential of a charged cylinder with radius  $\mathcal{R} = \frac{1}{2\pi}C$ . The functions  $I_l$  and  $K_l$  are the modified Bessel functions (see appendix A.4.3).

Figure 6.4b shows the resulting loss function  $-\text{Im} \bar{\epsilon}_{\text{CNT}}^{-1}$  of a (23, 0) nanotube for different angular momentum transfers  $l$  (compare with [181, fig. 2(a)]). The dispersion of the  $\pi$ -plasmon peak with increasing  $l$  can be easily understood from the in-plane plasmon dispersion in graphene. The details of the implementation of the tight-binding method are described in appendix C.1.

## 6.3 Zone-folding for Excitations

Tight-binding calculations are of great use for a qualitative description of the dielectric properties of nanotubes (see section 6.4). But they cannot provide qualitative predictions. The failures have been discussed in the previous chapter (see section 5.4.3). On the other hand, *ab-initio* calculations for the excitation spectra of the full nanotube are restricted to very small tubes with diameters below 1 nm. *In this section, we overcome these problems by combining the effective-medium approach with ab-initio calculations for graphene:*

First, we apply the zone-folding approach to the microscopic dielectric function  $\epsilon(\mathbf{q}\mathbf{q}'; \omega)$ . The dielectric properties of an arbitrary single-wall carbon nanotube are then derived from the excitations in a stripe of graphene. The latter can be efficiently calculated from first principles using the methods developed in chapter 5 and the tight-binding results presented above can be considerably improved.

Second, we derive an effective Dyson equation for the response function of a cylinder within the local-response approximation. As in the two-dimensional case, we can give a rigorous definition of the cylinder response function that was already used in eq. (6.9).

And finally, we calculate the probe factor  $C$  of eq. (6.6) for a broad-beam geometry. Thus, the loss-function measured in AR-EELS experiments can be expressed in terms of the cylinder response functions.

### 6.3.1 Zone-folding for the Polarisability

In chapter 5 we have seen that the polarisability  $\pi$  of graphene and graphite are closely related. In general, the polarisation of the system at point  $\mathbf{r}$  is only influenced by its neighbourhood  $|\mathbf{r}' - \mathbf{r}| < r_c$ , where the non-locality radius  $r_c$  is in the order of a few Ångstrom. Thus, the polarisability  $\pi$  can be transferred to systems of very different geometry as long as the nearest neighbourhood of each point is unchanged. This fact is used in dielectric theory, where the material of a nanoparticle is described by the

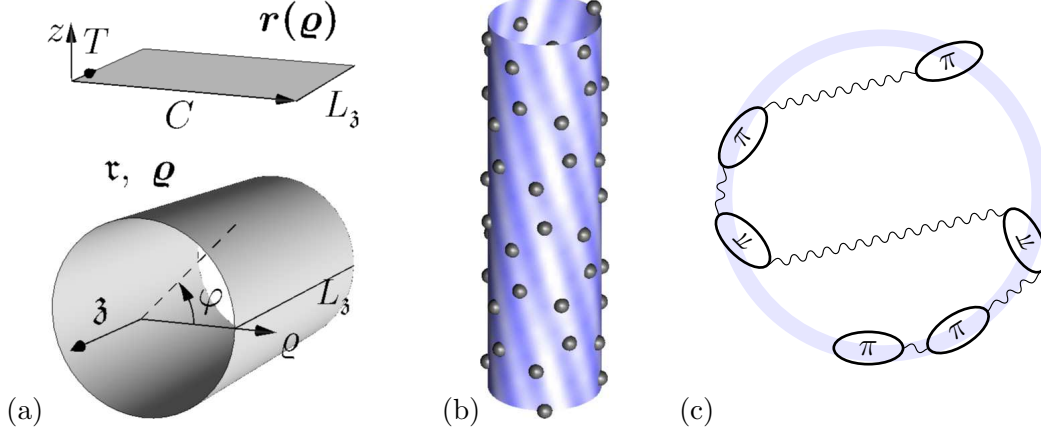


**Fig. 6.5:** Zone-folding for the microscopic polarisability. (a) Geometry of the cylinder and the unrolled graphene sheet. (b) Surface mode in a (4, 1) nanotube for a helical momentum  $\xi = (l, p)$  with angular projection  $l=10$  and on-axis part  $p=10 \text{ \AA}^{-1}$ . (c) Non-locality of the susceptibility.

bulk dielectric constant  $\varepsilon$  [e.g. 33]. In particular, *rolling up a graphene sheet should not change the local polarisability*. By introducing cylindrical coordinates  $\boldsymbol{\rho} \equiv (\rho, \varphi, \mathfrak{z})$ , we can easily map each point on the cylinder  $\boldsymbol{\rho}$  to a point on the sheet  $\mathbf{r}(\boldsymbol{\rho})$  (see fig. 6.5a). The microscopic polarisability  $\pi_{\text{CNT}}$  and  $\pi_{\text{s}}$  of a nanotube and a sheet are then related by

$$\pi_{\text{CNT}}(\boldsymbol{\rho}\boldsymbol{\rho}') \rho' \stackrel{\text{ZF}}{=} \pi_{\text{s}}(\mathbf{r}(\boldsymbol{\rho}), \mathbf{r}(\boldsymbol{\rho}')) \mathcal{R}, \quad \mathbf{r}(\boldsymbol{\rho}) = \frac{\varphi}{2\pi} \mathbf{C} + \frac{\mathfrak{z}}{T} \mathbf{T} + (\rho - \mathcal{R}) \mathbf{e}_z, \quad (6.10)$$

where  $\mathcal{R} = \frac{1}{2\pi} C$  corresponds to the tube radius. This equation can be obtained starting from the definition of the response function in cylindrical and Cartesian coordinates, and using the mapping  $\mathbf{r}(\boldsymbol{\rho})$  between the two (see appendix A.4.2).

Similar to our approach in graphene, we will use a Fourier expansion along the translationally invariant directions (angle  $\varphi$ , tube axis  $\mathfrak{z}$ ). The Fourier transformed polarisabilities of graphene and the nanotube are related by [see eq. (A.60)]

$$\pi_{\text{CNT}}(ll'pp'; \rho\rho') \rho' \stackrel{\text{ZF}}{=} \pi_{\text{s}}(\bar{\mathbf{q}}\bar{\mathbf{q}}'; zz'), \quad \bar{\mathbf{q}} = \bar{\mathbf{q}}(lp) = l \frac{2\pi\mathbf{C}}{C^2} + p \frac{\mathbf{T}}{T}, \quad z = \rho - \mathcal{R}. \quad (6.11)$$

This equation is the basis for all following calculations in this chapter. It can be understood as an extension of eq. (6.5) for the microscopic dielectric function or, equivalently, as an application of the zone-folding model to the polarisability of the system. The great advantage of the zone-folding model is that we do not have to calculate the polarisability of the full tube with several 10–100 atoms in the unit cell directly. Instead, an *ab-initio* calculation for an isolated graphene sheet with a 2 atom basis is sufficient, which corresponds to the use of a reduced unit cell of the tube. Note, however, that

1. the response function  $\pi_{\text{s}}$  is actually *not* the response function of graphene, but of an artificial graphene ribbon of width  $C = 2\pi\mathcal{R}$  with periodic boundary conditions. Any integral over the Brillouin zone of graphene, like for the independent-particle polarisability  $\chi^0$ , becomes a sum over the discrete set of lines shown in fig. 6.2a.

2. this approach is limited to sufficiently large tubes ( $d \gtrsim 1$  nm). Indeed, the non-locality range  $z_c$  of the response function perpendicular to the sheet must be much smaller than the tube radius  $\mathcal{R}$ , i. e.,  $\pi_s(\mathbf{r}\mathbf{r}') \neq 0$  only for  $|z| + |z'| < z_c \ll \mathcal{R}$ .

If, instead, the tube is very small ( $d < 1$  nm), one has to go beyond the zone-folding model and full *ab-initio* calculations become necessary. For achiral tubes, the linear-angular unit cell is sufficiently small to perform a standard supercell calculation. For chiral tubes, like the (6, 4) tube, one has to switch to the reduced unit cell and a special *ab-initio* code that is adapted for helical systems has to be used [186].

In this thesis, we consider large tubes for which the zone-folding model is sufficiently accurate. *We show that the microscopic dielectric properties of a SWCNT can be obtained from a very simple ab-initio calculation for bulk graphite by a post-processing procedure.*

### 6.3.2 Dyson Equation for Nanotubes

In the next step, we calculate the susceptibility  $\chi_{\text{CNT}}$ . Expressing the Dyson eq. (1.11) in cylindrical coordinates and performing a Fourier transform (A.50) in  $\varphi$  and  $\mathfrak{z}$ , we get

$$\begin{aligned} \chi_{\text{CNT}}(\boldsymbol{\xi}\boldsymbol{\xi}'; \varrho\varrho') &= \pi_{\text{CNT}}(\boldsymbol{\xi}\boldsymbol{\xi}'; \varrho\varrho') + \\ &+ \sum_{\boldsymbol{\xi}''} \int d\varrho_1 d\varrho_2 \varrho_1 \varrho_2 \pi_{\text{CNT}}(\boldsymbol{\xi}\boldsymbol{\xi}''; \varrho_1\varrho_2) v(\boldsymbol{\xi}''; \varrho_1\varrho_2) \chi_{\text{CNT}}(\boldsymbol{\xi}''\boldsymbol{\xi}'; \varrho_2\varrho'). \end{aligned} \quad (6.12)$$

Here, we have introduced the helical momentum transfer  $\boldsymbol{\xi} \equiv (l, p)$  to label the normal mode excitations of the cylinder. Its angular part  $l$  is an integer corresponding to the number of oscillation periods along the circumference, while  $p$  denotes the on-axis momentum. A charge oscillation with helical momentum  $\boldsymbol{\xi}$  can be always associated with a plane-wave oscillation on the curved surface with in-plane momentum  $\bar{\mathbf{q}}$  [see eq. (6.11) and fig. 6.5b]. For the microscopic dielectric function (1.10), we obtain

$$\varepsilon_{\text{CNT}}(\boldsymbol{\xi}\boldsymbol{\xi}'; \varrho\varrho') = \frac{1}{\varrho} \delta(\varrho - \varrho') \delta_{ll'} \delta_{pp'} - \int d\varrho_1 \varrho_1 v(\boldsymbol{\xi}; \varrho_1) \pi_{\text{CNT}}(\boldsymbol{\xi}\boldsymbol{\xi}'; \varrho_1\varrho') \quad (6.13)$$

and a similar expression for the inverse microscopic dielectric function  $\varepsilon^{-1} = \hat{1} + v\chi$ .

### Coulomb Potential

Using cylindrical coordinates, the Coulomb potential reads [11]

$$v(\boldsymbol{\xi}''; \varrho_1\varrho_2) = \frac{e^2}{\varepsilon_0} I_l(|p''|\rho_{<}) K_l(|p''|\rho_{>}), \quad \rho_{\gtrless} = \frac{\max}{\min}(\varrho_1, \varrho_2). \quad (6.14)$$

This expression can be derived by expanding  $1/|\mathbf{r} - \mathbf{r}'|$  in terms of the modified Bessel functions  $K_l$  and  $I_l$  [see eq. (A.71)] and performing the Fourier transform in  $\varphi$  and  $z$ . Physically,  $v$  corresponds to the potential of a charged cylinder surface, where  $\varrho_2$  denotes the radius of the cylinder and  $\boldsymbol{\xi}'' = (l'', p'')$  is the helical momentum of the charge oscillation on the surface. The dependence of the induced potential on the radial coordinate  $\varrho_1$  is shown in fig. 6.6 for different helical momenta  $\boldsymbol{\xi}''$ .

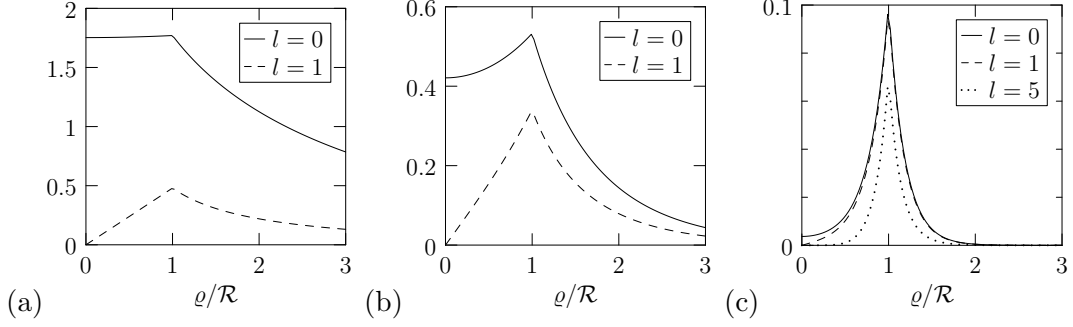


**Fig. 6.6:** Behaviour of the Coulomb potential  $\frac{\epsilon_0}{\epsilon} v(lp; q, q')$  for fixed radius  $q' = \mathcal{R}$  and increasing on-axis momentum transfers from left to right: (a)  $p = 0.2/\mathcal{R}$ , (b)  $p = 1/\mathcal{R}$ , and (c)  $p = 5/\mathcal{R}$ .

Two limiting cases can be distinguished: For small helical momentum ( $p\mathcal{R} \ll 1$ ,  $l$  small) the Coulomb potential is long ranged and has a broad maximum at the tube radius  $q \approx \mathcal{R}$ . In contrast, it shows a short range behaviour for large helical momentum ( $p\mathcal{R} \gg 1$ ). This corresponds to the fact that the electrostatic interaction between a test electron and the charge oscillation on the cylinder vanishes, when the distance to the tube surface becomes larger than the wavelength of the helical charge oscillation. Note that the exponential decay of the 2D Coulomb potential (5.28) is recovered in the limit of large tubes (see appendix A.4.5).

### 6.3.3 Local-Response Approximation

In continuation of the discussion in section 5.4.1, we find that both the polarisability  $\pi_{\text{CNT}}$  and the susceptibility  $\chi_{\text{CNT}}$  of the tube are localised along the radial direction

$$\chi_{\text{CNT}}(\varrho, \varrho') \approx 0, \quad \text{for } |\varrho - \mathcal{R}| \gg \lambda, \text{ or } |\varrho' - \mathcal{R}| \gg \lambda. \quad (6.15)$$

Note, however, that only the polarisability  $\pi_{\text{CNT}}$  is local along the circumference and the zone-folding model (6.10) cannot be applied for the susceptibility. Indeed,  $\chi_{\text{CNT}}$  includes the long-range Coulomb interaction and opposite walls of the cylinder can interact with each other. This leads to a non-local behaviour of  $\chi_{\text{CNT}}$  in  $\varphi$  and  $\mathfrak{z}$  (see fig. 6.5c).

Using eq. (6.15), we can now proceed in complete analogy to section 5.4.2 and simplify the Dyson equation within the local-response approximation. Due to the locality of  $\pi_{\text{CNT}}$  and  $\chi_{\text{CNT}}$  along  $\varrho$ , we restrict the integration in eq. (6.12) to a small range  $|\varrho_{1,2} - \mathcal{R}| \lesssim \lambda$ . For small momentum transfers  $\xi''$  and sufficiently large tubes  $\lambda \ll \mathcal{R}$ , the Coulomb interaction  $v(\xi''; \varrho_1 \varrho_2) \approx v(\xi''; \mathcal{R}\mathcal{R})$  is nearly constant in this range. If we further neglect the coupling between different helical excitations  $\chi_{\text{CNT}}(\xi\xi') \approx \chi_{\text{CNT}}(\xi)\delta_{\xi\xi'}$ , the Dyson equation decouples as in eq. (5.30). Compared to graphene, this corresponds to the neglect of in-plane crystal local-field effects inside the rolled sheet.

Introducing the *cylinder polarisation function*

$$\bar{\pi}_{\text{CNT}}(\boldsymbol{\xi}) \equiv \int d\varrho d\varrho' \varrho\varrho' \pi_{\text{CNT}}(\boldsymbol{\xi}\boldsymbol{\xi}; \varrho\varrho') \quad (6.16)$$

and analogously the *cylinder susceptibility*  $\bar{\chi}_{\text{CNT}}$ , we finally obtain the Dyson equation

$$\bar{\chi}_{\text{CNT}} \stackrel{\text{LRA}}{\approx} \bar{\pi}_{\text{CNT}} + \bar{\pi}_{\text{CNT}} v_{\text{CNT}} \bar{\chi}_{\text{CNT}}, \quad v_{\text{CNT}}(lp) = \frac{e^2}{\varepsilon_0} I_l(|p|\mathcal{R}) K_l(|p|\mathcal{R}). \quad (6.17)$$

Again, this equation can be solved by introducing two scalar effective dielectric functions

$$\bar{\varepsilon}_{\text{CNT}}(\boldsymbol{\xi}) \equiv 1 - v_{\text{CNT}}(\boldsymbol{\xi}) \bar{\pi}_{\text{CNT}}(\boldsymbol{\xi}), \quad \bar{\varepsilon}_{\text{CNT}}^{-1}(\boldsymbol{\xi}) \equiv 1 + v_{\text{CNT}}(\boldsymbol{\xi}) \bar{\chi}_{\text{CNT}}(\boldsymbol{\xi}), \quad (6.18)$$

which are inverse to each other by virtue of eq. (6.17). Thus, we have rederived expression (6.9) that was used in our tight-binding calculation.

### Ab-Initio Calculations in ZF+LRA

With the definitions (5.31) and (6.16) of the sheet and cylinder polarisation functions, we can now rewrite the zone-folding model (6.11) for the effective response functions:

$$\bar{\pi}_{\text{CNT}}(\boldsymbol{\xi}) \stackrel{\text{ZF}}{=} \mathcal{R} \bar{\pi}_s(\bar{\boldsymbol{q}}(\boldsymbol{\xi})), \quad (6.19)$$

where we assumed that the tube is large enough  $\mathcal{R} \gg z_c$ , so that  $\varrho = \mathcal{R} + z \approx \mathcal{R}$ . In random phase approximation ( $\pi = \chi^0$ ), this equation is equivalent to the zone-folding approximation for the wave functions and corresponding matrix elements eq. (6.8) which was already used in the tight-binding calculation. In analogy to the LRA method II for graphene (see p. 98), we can now calculate the dielectric function  $\bar{\varepsilon}_{\text{CNT}}(lp)$  of the nanotube from first-principles within the local-response approximation and the zone-folding model:

#### Procedure IV: ZF+LRA method

1. Starting point is the *ab-initio* calculation (in RPA) of the macroscopic polarisability  $\pi_d = \chi_d^0(\bar{\boldsymbol{q}}\bar{\boldsymbol{q}}; q_z=0=q'_z)$  for a graphene stack with small interlayer distance  $d = 2d_0$  (see file `outnlf.mdf`). The in-plane momentum  $\bar{\boldsymbol{q}} = \bar{\boldsymbol{q}}(lp)$  is given by eq. (6.11). Due to the quantisation along the circumference, a special  $k$ -point mesh has to be used in this calculation. It consists of the  $N$  parallel line segments shown in fig. 6.2a which are sampled with  $N_z$   $k$ -points each.
2. Within the local-response approximation and the zone-folding model, we obtain the cylinder polarisability as  $\bar{\pi}_{\text{CNT}}(lp) = \mathcal{R} d \pi_d(\bar{\boldsymbol{q}}(lp))$  [eq. (5.31),(6.19)].
3. We solve the scalar Dyson eq. (6.17) for the cylinder susceptibility  $\bar{\chi}_{\text{CNT}}(lp)$  and calculate the corresponding dielectric function  $\bar{\varepsilon}_{\text{CNT}}^{-1}(lp)$  from eq. (6.18).

In figure 6.7, we show the resulting spectra of a (9,9) nanotube for increasing angular momentum  $l$  and fixed on-axis momentum transfer  $p$  (solid lines). The dielectric

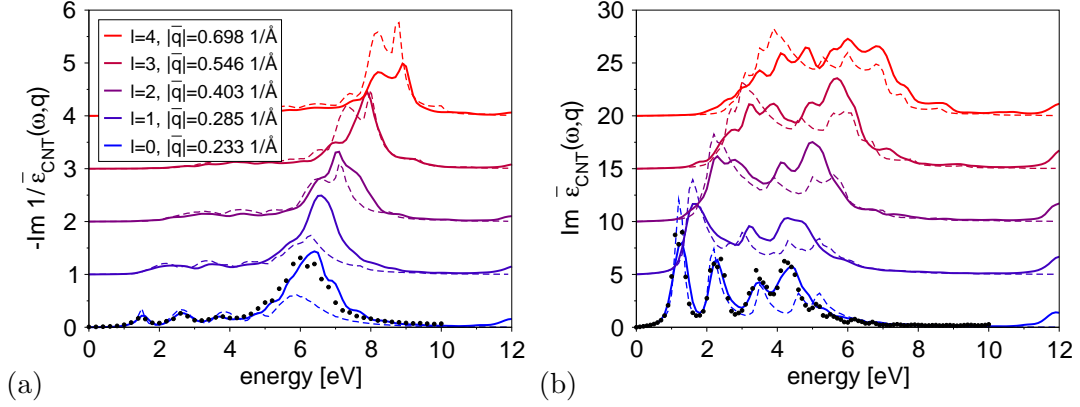


**Fig. 6.7:** Dielectric response of a (9,9) nanotube for on-axis momentum  $p = 0.23 \text{ \AA}^{-1}$  and different angular momenta  $l$ . (a) The loss function  $-\text{Im} \bar{\epsilon}_{\text{CNT}}^{-1}(lp)$  and (b) the dielectric function  $\text{Im} \bar{\epsilon}_{\text{CNT}}(lp)$  of the cylinder was calculated using the tight-binding (dashed lines) or the ZF+LRA method (solid lines). The latter uses an *ab-initio* calculation for graphene with momentum  $\bar{q}$ . Black dots show a full *ab-initio* calculation of the SWCNT for comparison (see also fig. 6.8).

function  $\text{Im} \bar{\epsilon}_{\text{CNT}}(lp) \propto \text{Im} \chi_d^0$  (right panel) has several distinct peaks which correspond to van-Hove singularities in the one-dimensional density of states for the nanotube. They are a direct consequence of the quantisation in  $k$ -space and vanish in the limit of large nanotubes (dense cutting lines in the Brillouin zone of graphene). The loss function  $-\text{Im} \bar{\epsilon}_{\text{CNT}}^{-1}(lp)$  (left panel) shows a dominant peak that corresponds to the  $\pi$ -plasmon excitation in graphene. With increasing angular momentum  $l$ , the peak shifts to higher energies. This fact is easily understood from the plasmon dispersion in graphene with increasing in-plane momentum  $\bar{q}(lp)$  (see fig. 5.12 for comparison). Of course, the local-response approximation is limited to small momentum transfers as we have discussed in section 5.4.3 for two-dimensional systems.

*How does the ZF+LRA method compare to other calculations?* First, the tight-binding calculations for the SWCNT (dashed lines), that have been described in section 5.2.2, lead to qualitatively very similar results. Both the shape of the spectra and the dispersion of the peaks are in good agreement. In our *ab-initio* ZF+LRA calculations, however, we correctly calculate the matrix elements and no fitting parameters are included.

Second, for the  $l = 0$  mode, we can compare our results with an *ab-initio* calculation of the full (9,9) nanotube (black dots) [187]. The good agreement, including the position and intensity of the van-Hove peaks, validates the use of the zone-folding model even for rather small tubes ( $\mathcal{R} = 6.1 \text{ \AA}$ ). We extend this comparison in the following section.

Third, this approach is much faster than a full *ab-initio* calculation. The computational cost is reduced to few *ab-initio* calculations (see first step) for the polarisability of a dense graphene stack which takes only few minutes each.

### 6.3.4 Angular-Resolved EELS

So far, we have only considered the loss function of the tube in dependence of the helical momentum  $\xi$  which corresponds to a normal mode excitation. In a real experiment, the external perturbation is generally a superposition of several normal modes  $\xi$  with different weights  $C_{lp}$ . For example, a plane wave  $e^{i\mathbf{q}\mathbf{r}}$  perturbation can be expanded in Bessel functions using the Jacobi-Anger relation (A.70),

$$e^{i\mathbf{q}\mathbf{r}} = \sum_{l=-\infty}^{\infty} C_{lp} e^{i(l\varphi + p\beta)}, \quad C_{lp} = i^l J_l(q_{\perp}\varrho) \delta_{p,q_{\parallel}}, \quad (6.20)$$

where  $q_{\perp}$  and  $q_{\parallel}$  denote the perpendicular and on-axis part of the momentum transfer  $\mathbf{q}$  with respect to the tube, respectively. The exponential  $\exp[i(l\varphi + p\beta)]$  corresponds to a normal mode excitation of the tube with helical momentum  $\xi = (l, p)$ . An example is shown in fig. 6.5b. Each of these modes will induce a (surface) charge oscillation on the cylinder, eventually with a different helical momentum  $\xi'$ . Its amplitude is given by the tube response function  $\varepsilon_{\text{CNT}}^{-1}(\xi\xi'; \varrho'\varrho)$ . The total energy-loss is then calculated from the work done by the induced charges in the external field which finally leads us to an expression that formally resembles eq. (6.6).

#### Loss Function in Cartesian Coordinates

In the following, a more formal and rigorous derivation will be given. In eq (1.22), we have seen that the energy-loss probability for the scattering of electrons in the broad-beam geometry is described by the loss function  $-\text{Im} \varepsilon_{\text{CNT}}^{-1}(\mathbf{q}\mathbf{q})$ , where  $\mathbf{q} = \mathbf{q}_{\perp} + q_{\parallel}\mathbf{e}_3$  is given in Cartesian coordinates. The relation with the microscopic response function  $\varepsilon_{\text{CNT}}^{-1}(\xi\xi'; \varrho'\varrho)$  of the nanotube is derived in appendix A.4.1. For a nanotube in a normalisation box of volume  $V = L_1L_2L_3 \equiv \pi\mathcal{R}_{\text{max}}^2L_3$  we have with eq. (A.53)

$$\varepsilon_{\text{CNT}}^{-1}(\mathbf{q}\mathbf{q}) = \frac{2}{\mathcal{R}_{\text{max}}^2} \sum_{l,l'} \int_0^{\mathcal{R}_{\text{max}}} d\varrho d\varrho' \varrho\varrho' (-ie^{i\phi})^{l-l'} J_l(q_{\perp}\varrho) J_{l'}(q_{\perp}\varrho') \varepsilon_{\text{CNT}}^{-1}(ll'q_{\parallel}q_{\parallel}; \varrho\varrho') \quad (6.21)$$

We have assumed that the box is sufficiently large such that  $\varepsilon_{\text{CNT}}^{-1}$  vanishes for  $\varrho \approx \mathcal{R}_{\text{max}}$ . Using the symmetry of the nanotube, one can show that  $l - l'$  must be a multiple of  $N$ , where  $N$  gives the number of hexagons in the unit cell of the tube [see eq. (A.62)].

Because  $\varepsilon_{\text{CNT}}^{-1} = \hat{1} + v_{3\text{D}}\chi_{\text{CNT}}$  contains the long-range Coulomb potential, it is much more convenient to consider the analogous equation for the susceptibility  $\chi_{\text{CNT}}$  which is localised along the radial direction. Thus, we can simplify this expression within the LRA: First, we assume that the Bessel function is nearly constant  $J_l(q_{\perp}\varrho) \approx J_l(q_{\perp}\mathcal{R})$  in the range where  $\chi_{\text{CNT}}$  is non-zero [see eq. (6.15)]. Second, we neglect all off-diagonal terms  $l \neq l'$  which is exact only for a homogeneous cylinder. Then, we find with eq. (6.16)

$$\chi_{\text{CNT}}(\mathbf{q}\mathbf{q}) \stackrel{\text{LRA}}{\approx} \frac{2\pi}{A} \sum_l J_l^2(q_{\perp}\mathcal{R}) \bar{\chi}_{\text{CNT}}(lq_{\parallel}), \quad (6.22)$$

where  $A = L_1 L_2 = \pi \mathcal{R}_{\max}^2$  is the normalisation area for the supercell of the nanotube. An equivalent equation holds for  $\pi_{\text{CNT}}$ . The energy-loss function for AR-EELS reads

$$-\text{Im} \varepsilon_{\text{CNT}}^{-1}(\mathbf{q}) = -v_{3\text{D}}(\mathbf{q}) \text{Im} \chi_{\text{CNT}}(\mathbf{q}\mathbf{q}) \stackrel{\text{LRA}}{\approx} - \sum_{l=-\infty}^{\infty} C_l^2(\mathbf{q}) \text{Im} \bar{\varepsilon}_{\text{CNT}}^{-1}(lq_{\parallel}), \quad (6.23)$$

$$C_l^2(\mathbf{q}) = \frac{2\pi}{A} \frac{v_{3\text{D}}(\mathbf{q})}{v_{\text{CNT}}(lq_{\parallel})} J_l^2(q_{\perp} \mathcal{R}),$$

where  $C_l$  denotes the probe factor of the external electron [compare with eq. (6.6)]. For achiral nanotubes, we can restrict the summation to non-negative  $l$  values: Due to the additional mirror symmetry and the perpendicular rotation axis, the dielectric function  $\bar{\varepsilon}_{\text{CNT}}^{-1}(l, q_{\parallel}) = \bar{\varepsilon}_{\text{CNT}}^{-1}(-l, q_{\parallel})$  is symmetric in  $l$  and  $C_l^2 = C_{-l}^2$  by means of eq. (A.65).

Equivalently, we find for the dielectric function in independent-particle approximation:

$$\varepsilon_{\text{CNT}}^{\text{NLF}}(\mathbf{q}) = 1 - v_{3\text{D}}(\mathbf{q}) \pi_{\text{CNT}}(\mathbf{q}\mathbf{q}) \stackrel{\text{LRA}}{\approx} 1 - \sum_{l=-\infty}^{\infty} C_l^2(\mathbf{q}) [1 - \bar{\varepsilon}_{\text{CNT}}(lq_{\parallel})], \quad (6.24)$$

which corresponds to the dielectric response calculated in random phase approximation and neglecting crystal local-field effects [see eq. (1.16)]. This quantity is much more simple to calculate than the loss spectrum  $\text{Im} \varepsilon_{\text{CNT}}^{-1}(\mathbf{q})$  as it does not include the long-range Coulomb interaction. Nevertheless, we can check the validity of the zone-folding approximation and the decomposition of the external plane-wave perturbation in cylindrical waves by comparing  $\varepsilon_{\text{CNT}}^{\text{NLF}}(\mathbf{q})$  with the full *ab-initio* results for the tubes (outnlf.mdf file).

### 6.3.5 Ab-initio Calculations for the CNT(9,9)

Putting everything together, we can calculate AR-EEL spectra of a nanotube for arbitrary directions of the momentum transfer starting from a tight-binding or an *ab-initio* calculation for graphene. In particular, we can now compare directly with *ab-initio* calculations for the full SWCNT [188, 189].

These reference calculations have been performed in our group by X. Lopez-Lozano and C. Giorgetti [187]. The largest tube that has been considered is a (9,9) nanotube in a hexagonal unit cell with an intertube distance of 8 Å. The interaction between the replicas should be negligible for the loss spectra when the momentum transfer  $\mathbf{q}$  is large enough. A lower limit of  $q > 0.3 \text{ \AA}^{-1}$  can be estimated from the minimal interlayer distance for isolated graphene (see table 5.2). The corresponding calculation parameters are shown in the panel above.

Instead of these computationally very demanding simulations, in this thesis we use eq. (6.24) and (6.23) to calculate the response function  $\varepsilon_{\text{CNT}}^{\text{NLF}}(\mathbf{q})$  and the AR-EEL spectrum  $-\text{Im} \varepsilon_{\text{CNT}}^{-1}(\mathbf{q})$  of the tube. The

# CNT(9,9) ref
# geometry
a' : 38.17 Bohr
c' : 4.622 Bohr
# ground state
ngkpt: 4 4 22
ecut : 25 Ha
# dp (rpa calc)
npwfn: 4997
nbands: 252
npwmat: 97

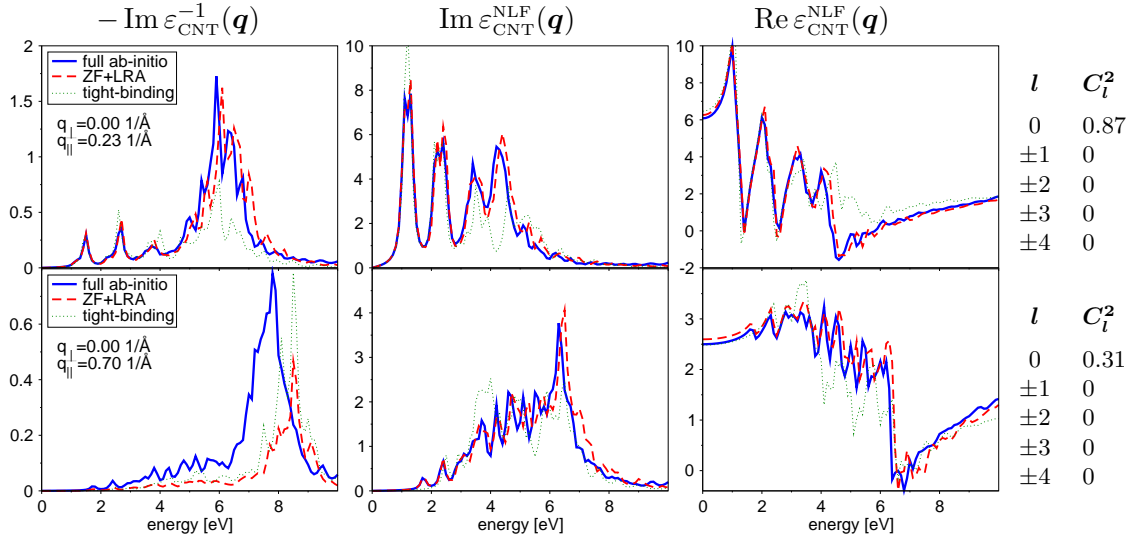


**Fig. 6.8:** AR-EEL spectra (left) and dielectric function  $\varepsilon_{\text{CNT}}^{\text{NLF}}(\mathbf{q}) = \varepsilon_{\text{CNT}}(\mathbf{q}\mathbf{q})$  (middle+right) of the (9,9) nanotube for two momentum transfers along the tube axis. We compare full *ab-initio* calculations (solid, [187]) with the ZF+LRA method IV (dashed, see text) and the tight-binding results (dotted). The weights  $C_l^2(\mathbf{q})$  for the contributing modes are indicated at the right.

cylinder response function  $\bar{\varepsilon}_{\text{CNT}}^{-1}(lq_{\parallel})$  is obtained using either the tight-binding method<sup>5</sup> or the ZF+LRA approach IV. Both methods work with the two-atom unit cell and are therefore much faster. For a direct comparison with the reference calculations, we use the same number of  $k$ -points  $N_z = 22$  along the tube axis (adding more points will slightly smoothen the spectra, see section 3.3.3). The results of the three methods are compared for (a) a momentum transfer  $\mathbf{q}$  along the tube axis, (b) perpendicular to the axis, and (c) in a diagonal direction (see fig. 6.8–6.10).

**(a) Excitation along the axis:** We start with the simple case of on-axis momentum transfer. The link with the in-plane excitations in graphene seems to be rather obvious. It has been already discussed in section 6.1, where we found a good agreement between the plasmon dispersion in graphene and AR-EELS experiments on large SWCNTs.

However, we are now able to go beyond this phenomenological description. Formally, the weights  $C_l^2(q_{\perp} = 0)$  vanish for all  $l \neq 0$  [see eq. (A.66)]. The loss function is exclusively given by the contribution  $-\text{Im } v_{3\text{D}} \bar{\chi}_{\text{CNT}}(0, q_{\parallel})$  of the  $l = 0$  mode, i. e., an oscillation along the tube axis. It differs from the loss function in graphene  $-\text{Im } v_{3\text{D}} \bar{\chi}_{\text{S}}$  in two important points: First, the quantisation effects in the tube lead to additional peaks in the polarisability  $\bar{\pi}_{\text{CNT}}$  and second, the effective Coulomb potential in the Dyson equation is not the same for the tube (6.17) and the sheet (5.32).

Although these differences vanish for large tubes, they become clearly visible for the (9,9) nanotube. Figure 6.8 shows the AR-EEL spectra (left) and the dielectric function

<sup>5</sup>Nearest-neighbour tight-binding calculation using the parameters  $\gamma_0 = -2.5$  eV,  $s_0 = 0$ ,  $\epsilon_0 = 2.4$ .

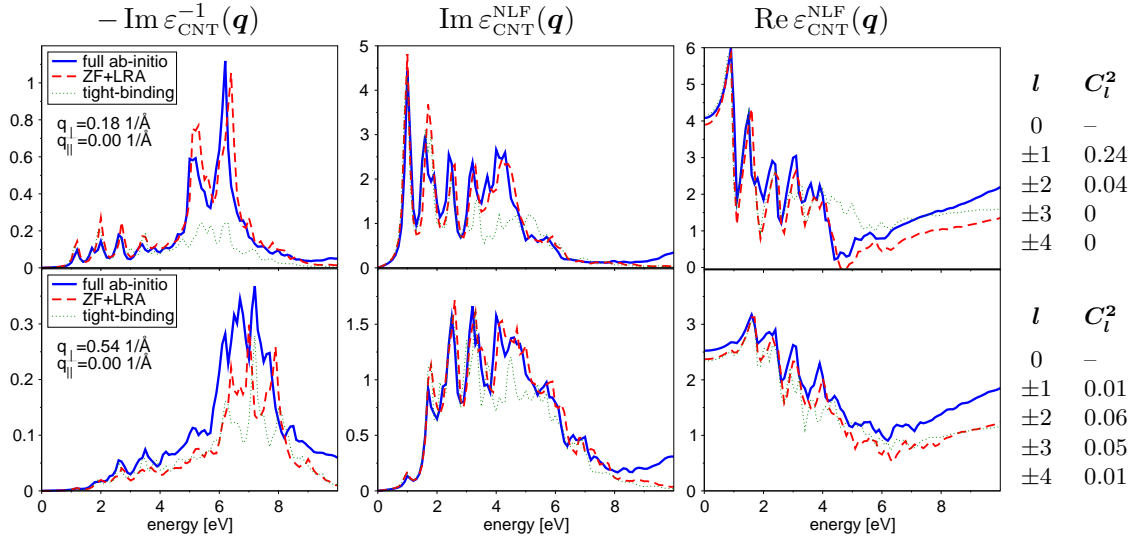


**Fig. 6.9:** Same as fig. 6.8 for momentum transfers perpendicular to the tube axis.

$\varepsilon_{\text{CNT}}^{\text{NLF}}(\mathbf{q})$  (middle+right) for small (top) and large (bottom) on-axis momentum transfers. Regarding the latter, the reference calculations (solid line) and the ZF+LRA results (dashed) are in perfect agreement. No further scaling has to be applied, when the unit-cell size of the tube calculation<sup>6</sup> is correctly taken into account in eq. (6.24) by the corresponding normalisation area  $A = \frac{\sqrt{3}}{2}(a')^2 = 353 \text{ \AA}$ . In contrast, the AR-EEL spectra start to differ at high momentum transfers. The reason is the failure of the local-response approximation which has been used in the scalar Dyson equation (6.17). This problem was extensively discussed in section 5.5 for the two-dimensional case (compare with fig. 5.12). For large momentum transfers, one has to go beyond the LRA and include the radial dependence of the polarisability  $\pi_{\text{CNT}}$ . The tight-binding calculations (dotted lines) are in qualitative agreement with the *ab-initio* calculations, except for the intensities of the loss function.

**(b) Excitation perpendicular to the axis:** Now we consider the case of perpendicular momentum transfers shown in figure 6.9. Depending on the size of  $q_{\perp}$ , several  $l$  modes will be excited by the external perturbation and the total spectrum is a sum of several tube response functions with different weights  $C_l^2$  (see table at the right). The  $l = 0$  mode cannot be excited for  $q_{\parallel} = 0$ . It corresponds to an oscillation with infinite wavelength and would therefore violate the charge conservation in the tube. Again, we find a very good agreement for the dielectric function  $\varepsilon_{\text{CNT}}^{\text{NLF}}(\mathbf{q})$ , and slight deviations for the AR-EEL spectrum for large momentum transfers due to the failure of the LRA. Also the tight-binding calculations give reasonable results.

<sup>6</sup>The nanotubes were arranged in a triangular lattice with inter-tube distance  $a'$ .

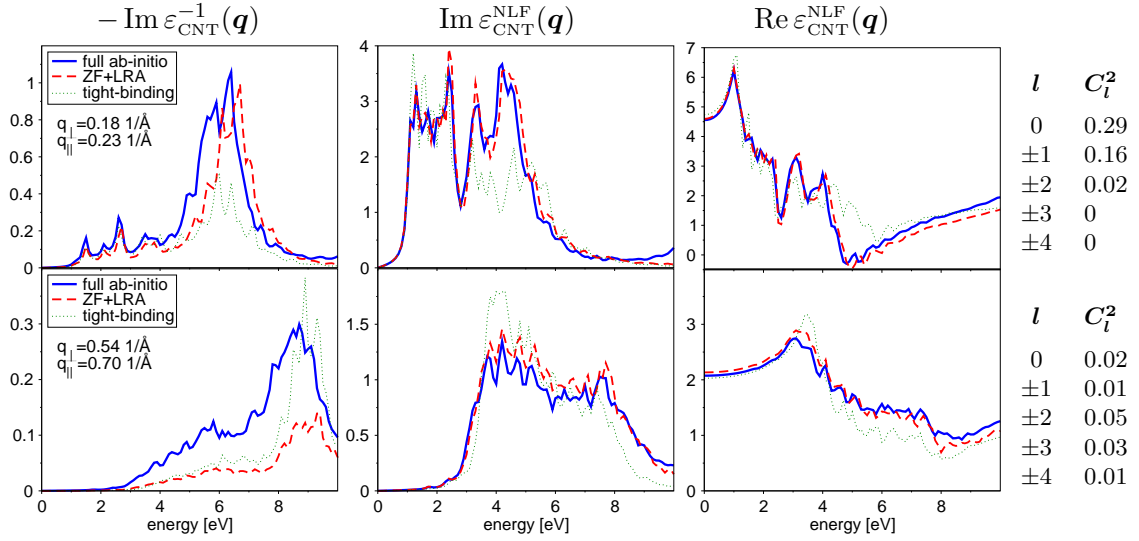


**Fig. 6.10:** Same as fig. 6.8 for momentum transfers in arbitrary direction.

**(c) Excitation in arbitrary direction:** Finally, we use a momentum transfer that is neither on-axis, nor perpendicular (see fig. 6.10). Concerning  $\varepsilon_{\text{CNT}}^{\text{NLF}}(\mathbf{q})$ , the reference calculation is again well reproduced by the ZF+LRA method, while the deviations in the loss spectrum become more important (note that  $q$  is also larger than in the previous cases). The results in the top panel are actually a sum of the  $l = 0$  and  $\pm 1$  cylinder response functions shown in fig. 6.7. As a result, the van-Hove singularities in  $\bar{\varepsilon}_{\text{CNT}}(\boldsymbol{\xi})$  are more and more masked for increasing  $q_{\perp}$  component by the superposition of several excited  $l$  modes. The same behaviour can be observed in the tight-binding results.

## Conclusions

- The polarisability of a SWCNT can be reproduced from the polarisability of a graphene-ribbon with periodic boundary conditions. This validates the use of the zone-folding model even for the dielectric properties of single-wall nanotubes with diameters larger than 1 nm.
- Within the local-response approximation we can efficiently calculate the loss function of an isolated nanotube with diameters larger than 1 Å. For small momentum transfers  $|\mathbf{q}| \lesssim 0.2 \text{ \AA}^{-1}$ , the results reproduce full *ab-initio* calculations of the tube.
- For larger momentum transfers  $q_{\parallel}$  or  $q_{\perp}$ , however, the local-response approximation fails. The variation of the polarisability along the radial direction has to be taken into account to overcome this problem.
- Our tight-binding calculations give reasonable results for the dielectric function  $\varepsilon_{\text{CNT}}^{\text{NLF}}(\mathbf{q})$ . The resulting AR-EEL spectra of a tube reproduce the full *ab-initio* calculations qualitatively and can be used to study trends. The peak positions and intensities, however, are generally not reliable in nearest-neighbour tight-binding.

## 6.4 Anisotropic Excitations in SWCNTs

The presented ZF+LRA method does not only constitute a great improvement in terms of computation time—it can be also very useful for the physical interpretation of AR-EEL spectra of single-wall carbon nanotubes. In particular for very small tubes, these spectra often consist of several peaks which show a complicated dispersion with increasing momentum transfer and strongly depend on the orientation of the tube. Many aspects of this complex behaviour can be understood in terms of the normal modes of the tube [see eq. (6.23)] and their relation with in-plane excitations in graphene [see eq. (6.19)].

In this section, we consider AR-EEL spectra of carbon nanotubes and investigate several trends using our tight-binding calculations. The code, which has been implemented for this purpose, is briefly described in appendix C.1 and C.3. Comparative *ab-initio* calculations for the (9,9) tube have confirmed our findings [187]. Note, however, that only  $\pi$  electrons are explicitly taken into account and the energy scale depends on  $\gamma_0$ . In the following, we use the tight-binding parameters  $\gamma_0 = -2.5$  eV,  $s_0 = 0$ , and  $\epsilon_0 = 2.4$ .

### 6.4.1 Plasmon Dispersion

We are interested in the following questions: *Which information about the nanotubes are accessible via AR-EELS measurements? How does the dispersion of the  $\pi$ -plasmon excitation depend on the direction of the momentum transfer  $\mathbf{q}$ ? What is the influence of the tube radius? Do AR-EELS spectra contain signatures of the tube chirality?*

#### Directional Dependence

First, we consider the plasmon dispersion in a (9,9) nanotube for a momentum transfer  $\mathbf{q} = q_{\parallel} \mathbf{e}_3$  along the tube axis (see fig. 6.11a). Only  $l = 0$  modes will be excited in this case. Following eq. (6.11), this mode can be associated to a plane-wave excitation in the unrolled graphene ribbon with an in-plane momentum  $\bar{\mathbf{q}} = q_{\parallel} \mathbf{T}/T$ . The dispersion of the plasmon peak to higher energies can be directly related to the in-plane plasmon dispersion in graphene. Indeed, this is the formal derivation of the model used in the motivation of this chapter (see section 6.1).

*How do the loss spectra change for increasing perpendicular momentum transfer?* One might argue that the tube acts essentially as a quantum dot in perpendicular direction. In this case, the excitations are considered to be localised and should not disperse in energy with increasing momentum. However, this is not the case for the (9,9) nanotube.

In figure 6.11b, we clearly see a dispersion of the peak structure to higher energies with increasing perpendicular momentum. In order to understand this behaviour, we have to consider the evolution of the weights  $C_l^2(q_{\perp})$ . Due to the properties of the Bessel function  $J_l(q_{\perp} \mathcal{R})$  (see appendix A.4.3), modes with higher angular momentum  $l$  will be excited for increasing perpendicular momentum. For fixed  $q_{\perp}$ , the maximum of  $J_l$  is roughly found at  $l_0 = \lfloor q_{\perp} \mathcal{R} \rfloor$ . The contribution of the  $\pm l_0$  modes to the total spectrum is indicated by the shaded area. Larger  $l$  modes are associated with a larger in-plane momentum  $\bar{\mathbf{q}} = 2\pi l \mathbf{C}/C^2$  in the unrolled graphene sheet. The peaks in the loss function

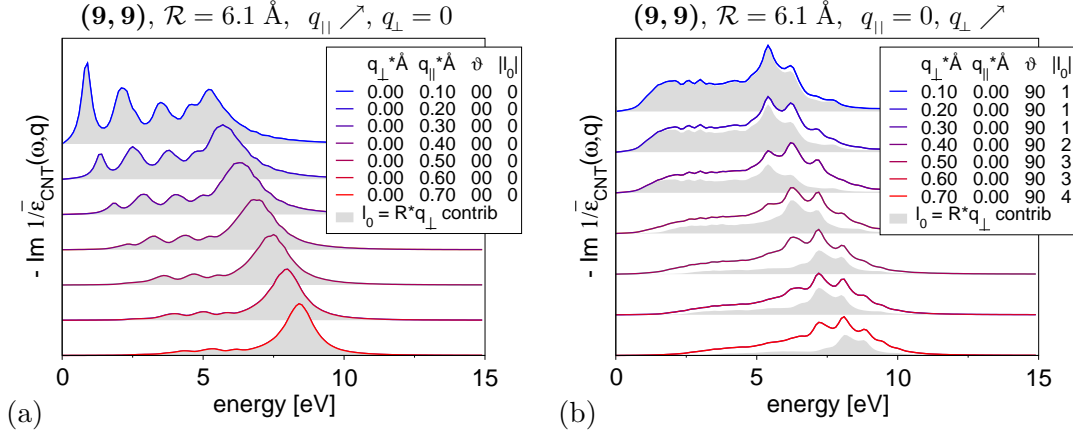


**Fig. 6.11:** Tight-binding calculations for the plasmon dispersion in the (9,9) nanotube. The loss function for several momentum transfers (a) parallel and (b) perpendicular to the tube axis are shown. The shaded area corresponds to the contribution of the  $l_0 = \lfloor q_{\perp} \mathcal{R} \rfloor$  mode in eq. (6.23).

will therefore depend on  $q_{\perp}$  and shift to higher energies with increasing perpendicular momentum transfer.

*Why are the modes close to  $l_0$  most important for the spectrum?* This formal finding can be also understood physically. The wavelength of the excitation with angular momentum  $l_0$  is given by  $\lambda = 2\pi\mathcal{R}/l_0 \approx 2\pi/q_{\perp}$ , i. e., exactly the wavelength of the external plane wave. We can depict this excitation as a cylindrical wave which is excited in the nanotube walls parallel to  $\mathbf{q}$ . Thus, the SWCNT must be considered as a quasi-two-dimensional system for large perpendicular momentum transfers  $q > 1/\mathcal{R}$ , i. e., when the wavelength of the perturbation is smaller than the diameter of the tube. In the optical limit  $q_{\perp}\mathcal{R} \ll 1$ , instead, the tube appears as one-dimensional system and the argumentation above for non-dispersing modes in perpendicular direction holds.

*How do the loss spectra change with the orientation of the momentum transfer?* Comparing the tight-binding results for parallel and perpendicular direction, we find that the dispersion is actually very similar (see fig. 6.11a and b). Indeed, the plasmon position is nearly unaffected by the orientation of  $\mathbf{q}$  because the response of graphene is probed for large momentum transfers (see discussion above). This finding is in agreement with recent IXS measurements on aligned SWCNTs [176].

A more detailed inspection (see also fig. 6.13) shows that the plasmon peak is generally broader for perpendicular momentum transfers because several  $l$  modes contribute. Additionally, one finds differences in the peaks at lower energies that are only visible for small tubes. However, for a reliable description of these features we have to go beyond the tight-binding approximation and *ab-initio* calculations are indispensable. Comparing fig. 6.8 and fig. 6.9, we can already estimate that the intensity is reduced by a factor of 2 for perpendicular momentum transfers in (9,9) SWCNTs (note the different scale). The direction of  $\mathbf{q}$  mainly influences the intensity of the loss function which is reduced by the depolarisation effect for perpendicular momentum transfers.

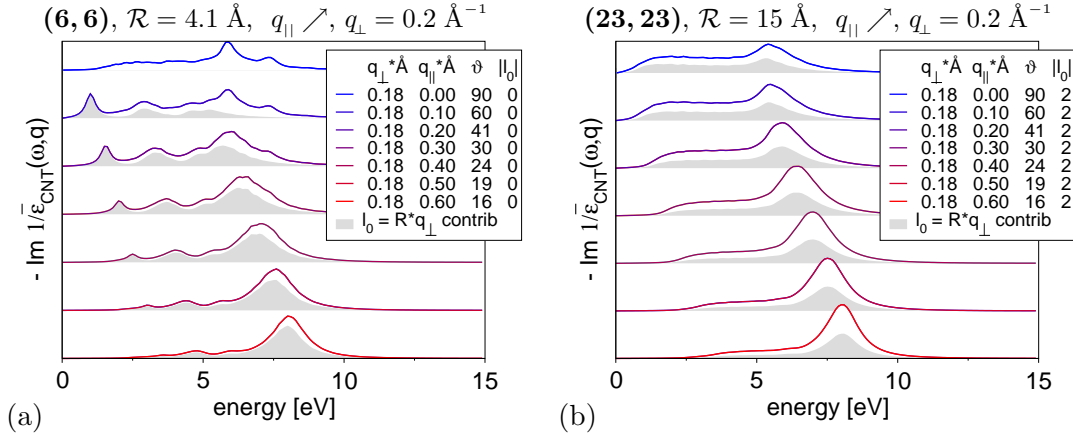


**Fig. 6.12:** Plasmon dispersion for a (a) small (6,6) and (b) large (23,23) nanotube.

### Diameter Dependence

Figure 6.12 compares the loss functions for a nanotube with (a) small and (b) large radius. In both cases, the dispersion with increasing on-axis momentum  $q_{\parallel}$  and fixed perpendicular component  $q_{\perp} = 0.18 \text{ \AA}^{-1}$  is shown. Note that  $\mathbf{q}$  changes from a perpendicular to an on-axis direction (see angle  $\vartheta$  with respect to the tube axis).

The loss function for the (6,6) nanotube in fig. 6.12a shows several dispersing peaks. The first three peaks can be attributed to the  $l = 0$  mode. They are due to the quantisation along the circumference which is especially important in small tubes. For diameters beyond 3 nm these quantisation effects completely vanish (see fig. 6.12b) and the spectra resemble very much our graphene results (see fig. 5.12a). Note that several modes contribute to the spectra which leads to a broadening of the  $\pi$  plasmon. The presence of the peaks at low energies is thus a signature of very small tubes (the relative intensities of these peaks is much smaller in full *ab-initio* calculations, see upper panel in fig. 6.10).

### Chirality Dependence

Finally, we consider the influence of the chirality of the tube. In figure 6.13, we compare the armchair (6,6) tube with a chiral (9,2) tube of comparable diameter. The direction  $\vartheta$  of the momentum transfer is changed for fixed modulus  $q$ . Comparing the two different chiralities, we find only very subtle differences both in perpendicular (top) and on-axis direction (bottom). It should be difficult to distinguish the two tubes using AR-EELS.

*Where does the chirality come into play?* Of course, the chirality can only influence the cylinder response function  $\bar{\epsilon}_{\text{CNT}}(\boldsymbol{\xi})$ , not the probe factor  $C_l^2$ . It enters in two ways: First, the direction of the associated momentum transfer  $\bar{\mathbf{q}}(\boldsymbol{\xi})$  in the unrolled graphene ribbon depends on the vectors  $\mathbf{T}$  and  $\mathbf{C}$  [see eq. (6.11)]. The chirality is therefore connected to the in-plane anisotropy of graphene which influences the  $\pi$ -plasmon dispersion only for very large momentum transfers  $\bar{q} > 0.6 \text{ \AA}^{-1}$  (see fig. 5.9b). Second, the line segments that constitute the Brillouin zone of the nanotube are parallel to the vector  $\mathbf{T}$  (see

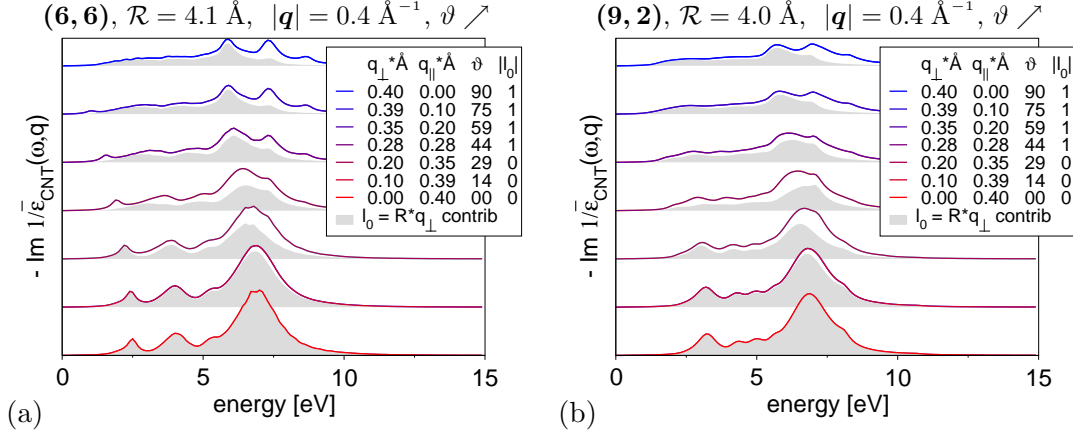


**Fig. 6.13:** Dependence of the loss function on the direction of the momentum transfer  $q = 0.4 \text{ \AA}^{-1}$ . We compare an (a) armchair and (b) chiral nanotube with similar radius  $\mathcal{R} \approx 4 \text{ \AA}$ .

fig. 6.2). As the band structure of graphene is anisotropic, the exact position of the van-Hove peaks can change with the chirality of the tube.

### 6.4.2 Decomposition of Spectra

Finally, we come back to the discussion of the absorption and AR-EELS experiments on aligned nanotubes (see fig. 6.3, [157, 161]). The questions arise, if the spectra can be decomposed into on-axis and perpendicular contributions and if the energy of the ‘on-axis’  $\pi$  plasmon is determined by the total momentum transfer  $q$  or just the component  $q_{\parallel}$  along the tube axis. To investigate the decomposition, let us consider again eq. (6.22)

$$\chi_{\text{CNT}}(\mathbf{q}\mathbf{q}) \stackrel{\text{LRA}}{\approx} \frac{2\pi}{A} \left( J_0^2(q_{\perp} \mathcal{R}) \bar{\chi}_{\text{CNT}}(0, q_{\parallel}) + \sum_{l \neq 0} J_l^2(q_{\perp} \mathcal{R}) \bar{\chi}_{\text{CNT}}(l, q_{\parallel}) \right), \quad (6.25)$$

For a momentum transfer exactly parallel  $q_{\parallel} \mathbf{e}_3$  or perpendicular  $\mathbf{q}_{\perp}$  to the axis, we have:

$$\chi_{\text{CNT}}(\mathbf{q}_{\parallel} \mathbf{q}_{\parallel}) \stackrel{\text{LRA}}{\approx} \frac{2\pi}{A} \bar{\chi}_{\text{CNT}}(0, q_{\parallel}), \quad \chi_{\text{CNT}}(\mathbf{q}_{\perp} \mathbf{q}_{\perp}) \stackrel{\text{LRA}}{\approx} \frac{2\pi}{A} \sum_{l \neq 0} J_l^2(q_{\perp} \mathcal{R}) \bar{\chi}_{\text{CNT}}(l, 0), \quad (6.26)$$

because  $J_0(0) = 1$  and the  $l=0$  mode can not be excited in the latter case due to charge conservation. Comparing the two terms in eq. (6.25) with the expressions in eq. (6.26), we see that the spectra can be only decomposed if  $\bar{\chi}_{\text{CNT}}(l, q_{\parallel}) \approx \bar{\chi}_{\text{CNT}}(l, 0)$ , i. e., when  $q_{\parallel}$  is small. In this case, the loss function for arbitrary momentum transfer  $\mathbf{q}$  can be written as a linear combination of the loss functions for the *projections* of  $\mathbf{q}$  parallel and perpendicular to the axis:

$$\text{Im } \varepsilon_{\text{CNT}}^{-1}(\mathbf{q}\mathbf{q}) \approx J_0^2(q_{\perp} \mathcal{R}) (q_{\parallel}^2/q^2) \text{Im } \varepsilon_{\text{CNT}}^{-1}(\mathbf{q}_{\parallel} \mathbf{q}_{\parallel}) + (q_{\perp}^2/q^2) \text{Im } \varepsilon_{\text{CNT}}^{-1}(\mathbf{q}_{\perp} \mathbf{q}_{\perp}). \quad (6.27)$$

A similar equation can be derived for the dielectric function  $\text{Im } \varepsilon_{\text{CNT}}(\mathbf{q}\mathbf{q})$ .

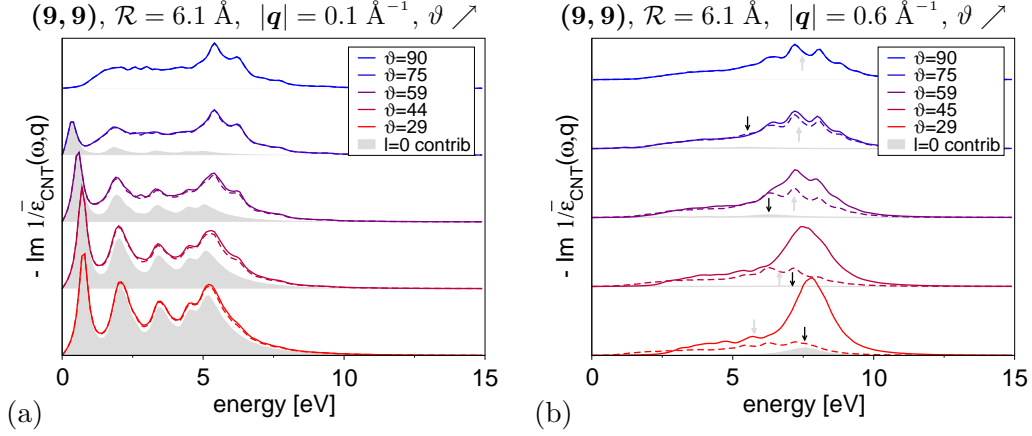


**Fig. 6.14:** Loss function of a (9,9) tube (solid) and the sum of perpendicular and parallel contribution (dashed) for (a) small  $q = 0.1 \text{ \AA}^{-1}$  and (b) large  $q = 0.6 \text{ \AA}^{-1}$  and different orientations  $\vartheta$ .

### Electron Energy-Loss Spectroscopy

In fig. 6.14, we now consider the decomposition of AR-EEL spectra for two different momentum transfers  $q = 0.1 \text{ \AA}^{-1}$  (left) and  $q = 0.6 \text{ \AA}^{-1}$  (right). Solid lines show the loss function for several momentum transfers  $\mathbf{q}$  with different orientation  $\vartheta$  and constant modulus. The contribution of the  $l = 0$  mode (shaded area) corresponds to the first term in eq. (6.27). Dashed lines show the loss function calculated from eq. (6.27) assuming that  $\bar{\chi}_{\text{CNT}}(l, q_{\parallel}) \approx \bar{\chi}_{\text{CNT}}(l, 0)$ . For small momentum transfers  $q = 0.1 \text{ \AA}^{-1}$  (fig. 6.14a) the loss function for  $\mathbf{q}$  is perfectly reproduced. As expected, the decomposition fails for larger momentum transfers  $q = 0.6 \text{ \AA}^{-1}$  (fig. 6.14b). Additionally, the  $\pi$  plasmon for the total momentum  $\mathbf{q} = \mathbf{q}_{\parallel} + \mathbf{q}_{\perp}$  is found at higher energy than in the loss functions for the projected moments  $\mathbf{q}_{\parallel}$  (black arrows) and  $\mathbf{q}_{\perp}$  (grey arrows). Indeed, we have already seen that the peak position is determined by the modulus of the momentum transfer, not its projection along the axis (see fig. 6.13). In conclusion, *the decomposition of the loss function in parallel and perpendicular contributions is only meaningful for small momentum transfers*. For large  $q$ , instead, one can use the decomposition (6.22) in terms of different angular momenta  $l$ .

### Optical Absorption

In absorption experiments, one measures  $\text{Im } \varepsilon(\mathbf{q}\mathbf{q})$  for very small  $q\mathcal{R} \ll 1$ . Because the decomposition of  $\varepsilon^{-1}$  in eq. (6.27) also holds for the dielectric function  $\varepsilon$ , we obtain

$$\text{Im } \varepsilon_{\text{CNT}}(\mathbf{q} \rightarrow 0) \approx \cos^2(\vartheta) \text{Im } \varepsilon_{\text{CNT}}^{\parallel} + \sin^2(\vartheta) \text{Im } \varepsilon_{\text{CNT}}^{\perp}, \quad (6.28)$$

where  $\vartheta$  denotes the angle between the polarisation vector  $\mathbf{q}$  and the tube axis, and we have used the limit  $J_0(x) \xrightarrow{x \rightarrow 0} 1$  for the Bessel function. For instance, we can apply this simple formula to the absorption measurements of Murakami *et al.* [161].

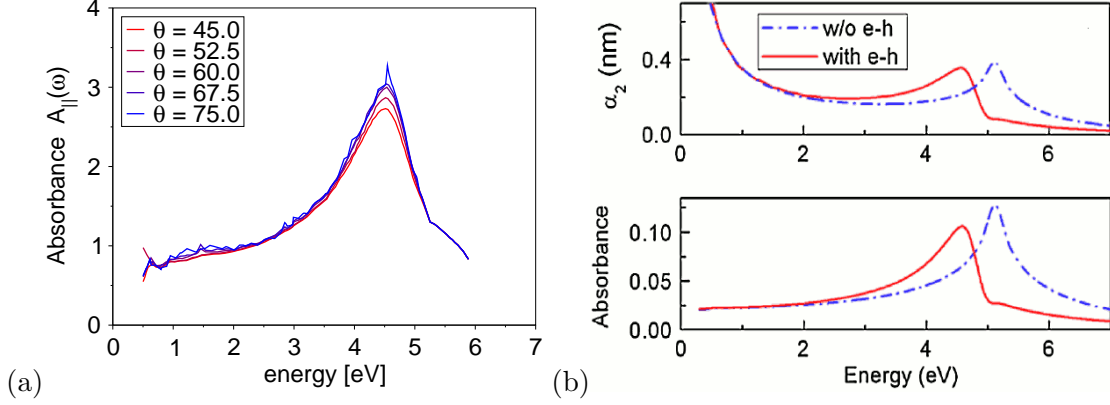


**Fig. 6.15:** Decomposition for the X-ray absorption measurements on isolated nanotubes of Murakami *et al.* [161]. We compare (a) the on-axis contribution  $A_{||}$  to the absorbance of the tubes which is calculated from the experimental data shown in fig. 6.3a with (b) the absorbance of graphene obtained from a Bethe-Salpeter calculation by Yang *et al.* [159] (Reproduced from [159], © 2009 by The American Physical Society).

Figure 6.15a shows the on-axis contribution  $\varepsilon_{\text{CNT}}^{\parallel}$  that we have calculated from the data shown in fig. 6.3a ( $\varepsilon_{\text{CNT}}^{\perp}$  is the lowest spectrum) by inverting eq. (6.28). From the zone-folding argument (6.19), we expect that this on-axis component ( $l = 0$ ) corresponds to the in-plane absorption in graphene. Indeed, the resemblance with the Bethe-Salpeter calculations for isolated graphene sheets [159] is striking (see fig. 6.15b). This is another example of the close connection between excitations in single-wall carbon nanotubes and graphene.

### Independent-Particle Polarisability

For a qualitative understanding of the excitation spectra, it is often useful to work in the independent-particle picture. The polarisability  $\chi_{\text{CNT}}^0(\mathbf{q}\mathbf{q})$  is then given as a sum over all transitions between the valence and conduction bands in the one-dimensional Brillouin zone of the nanotube (see fig. 6.2b). Depending on the particular momentum transfer  $\mathbf{q}$  many of these transitions are very weak or even forbidden due to the symmetry properties of the tube. These selection rules can be naturally derived from the expansion (6.22) of  $\chi_{\text{CNT}}^0(\mathbf{q}\mathbf{q})$  in terms of the normal-mode contributions  $\bar{\chi}_{\text{CNT}}^0(lp)$ .

To this end, let us first consider the sum-over-states expression for  $\bar{\chi}_{\text{CNT}}^0(lp)$ . The formalism is greatly simplified if we use the mapping from the nanotube to graphene in eq. (6.11) and work with the momentum  $\bar{\mathbf{q}}(l, p)$  in the quasi two-dimensional Brillouin zone of the tube (see fig. 6.2a). This corresponds to the use of helical coordinates instead of the linear-angular coordinates  $l$  and  $p$  (see section 6.1). The cylinder polarisability  $\bar{\chi}_{\text{CNT}}^0(lp)$  is then given by eq. (3.14) for  $\mathbf{G} = \mathbf{G}' = \mathbf{0}$ , where the wave vectors  $\mathbf{k}$  and  $\mathbf{q}_r$  are replaced by the helical wave vectors  $\bar{\mathbf{k}}(j, k)$  and  $\bar{\mathbf{q}}(l, p)$ , respectively. The summation runs over the  $N$  discrete lines of the Brillouin zone of the tube and only transitions between the helical wave vectors  $\bar{\mathbf{k}} - \bar{\mathbf{q}}$  and  $\bar{\mathbf{k}}$  are allowed.

If we neglect Umklapp effects, this corresponds to transitions between the bands labelled by  $j - l$  and  $j$  and on-axis moments  $k - p$  and  $k$ . In other words,  $\bar{\chi}_{\text{CNT}}^0(lp)$  includes only transitions with  $\Delta j = l$  and  $\Delta k = p$ . Following eq. (6.22), the contribution of  $\bar{\chi}_{\text{CNT}}^0(lp)$  to the full polarisability  $\chi_{\text{CNT}}^0(\mathbf{q}\mathbf{q})$  is determined by the weighting factors  $J_l^2(q_{\perp}\mathcal{R})$ . For on-axis momentum transfers  $\mathbf{q} = q_{\parallel}\mathbf{e}_3$ , all weighting factors vanish, except for the  $l = 0$  mode. As a consequence, only transitions between valence and conduction bands with the same label  $j$  will contribute, i. e.,

$$\mathbf{q} = q_{\parallel}\mathbf{e}_3 : \quad \Delta j = 0 \quad (\text{without Umklapp}) \quad (6.29)$$

For perpendicular momentum transfers  $\mathbf{q} = \mathbf{q}_{\perp}$ , the  $l = 0$  mode is forbidden by charge conservation. If  $q$  is sufficiently small, only the  $l = \pm 1$  modes contribute in eq. (6.22) and we find for perpendicular polarisation

$$\mathbf{q} = \mathbf{q}_{\perp} : \quad \Delta j = \pm 1 \quad (\text{without Umklapp}) \quad (6.30)$$

These are exactly the well-known selection rules for SWCNTs [146]. For larger momentum transfers, these rules become more complicated. First, several  $l$  modes will contribute to the polarisation and second, we have to take into account Umklapp effects. *The use of helical coordinates, i. e., the momentum  $\bar{\mathbf{q}}(l, p)$  in the quasi two-dimensional Brillouin zone of the tube, greatly simplifies the analysis of transitions in SWCNTs [172].*

## 6.5 Zone-Folding for the Microscopic Dielectric Function

As we have seen in the discussion of section 6.3.5, the LRA-method is limited to small momentum transfers  $\mathbf{q}$ . In order to calculate the dielectric response for large  $q$ , we have to account for the nonlocal corrections (spatial dispersion) and the inhomogeneity of the system (in-plane LFE). To this end, the full *microscopic* polarisability  $\pi(\mathbf{q}\mathbf{q}', \omega)$  will be used in the following calculations. The necessary formalism has been already derived in section 6.3.1 and 6.3.2: First, we apply the zone-folding for the polarisability of graphene using eq. (6.11). Second, the full Dyson eq. (6.12) is solved in real space. And finally, the AR-EEL spectrum for a given momentum transfer  $\mathbf{q}^0 = \mathbf{q}_{\perp}^0 + q_{\parallel}^0\mathbf{e}_3$  is calculated by the summation over all angular momentum contributions in eq. (6.21).

### Symmetry Considerations

It is important to note that  $\varepsilon_{\text{CNT}}^{-1}(ll', q_{\parallel}^0 q_{\parallel}^0; \varrho\varrho')$  vanishes for many combinations of  $l$  and  $l'$  due to the screw symmetries of the tube. These symmetries have not been taken into account in the derivation of eq. (6.21) as we have used the angular and on-axis momentum  $l$  and  $p$ , i. e., the linear-angular unit cell of the tube. If we switch to helical coordinates  $\bar{\mathbf{q}}(l, p)$  as described above, we implicitly use a reduced unit cell of the tube which contains only two atoms. The screw symmetries of the tube give rise to the ‘Bragg’ condition  $\bar{\mathbf{q}} - \bar{\mathbf{q}}' = \bar{\mathbf{G}}$ , where  $\bar{\mathbf{G}}$  denotes a reciprocal lattice vector in the unrolled graphene sheet. Only modes with the same reduced momentum  $\bar{\mathbf{q}}_{\text{r}}$  can interact.<sup>7</sup>

<sup>7</sup> This simple rule becomes formally much more complicated if we use  $l$  and  $p$  coordinates [see eq. (A.62)]. Indeed, we find that  $\varepsilon_{\text{CNT}}^{-1}(ll', q_{\parallel}^0 q_{\parallel}^0; \varrho\varrho')$  vanishes if  $l - l'$  is not a multiple  $N = 2(n^2 + m^2 + nm)/d_R$ .

## Implementation

During this thesis, I have developed and implemented this zone-folding method as a post-processing tool for the DP-code (see `zf_method.py`, tab. C.2). The AR-EEL spectrum of a SWCNT for a momentum transfer  $\mathbf{q}^0 = \mathbf{q}_\perp^0 + q_\parallel^0 \mathbf{e}_3$  is calculated from a previous *ab-initio* calculation of the polarisability of a periodic graphene ribbon in six steps:

### Procedure V: Zone-folding method

1. We start from an *ab-initio* calculation (in RPA) of the *microscopic* polarisability  $\pi_d = \chi_d^0(\mathbf{q} + \mathbf{G}, \mathbf{q} + \mathbf{G}')$  of a graphene stack with small interlayer distance  $d = 2d_0$  (see file `chi0.dat`) for  $N$  different in-plane momentum transfers  $\bar{\mathbf{q}}(lq_\parallel^0)$  with  $l = 0, \dots, N-1$ . A special  $k$ -point grid of  $N$  equidistant lines is used.
2. Using a Fourier transform in  $G_z$  and  $G'_z$ , we calculate  $\pi_d(\bar{\mathbf{q}} + \bar{\mathbf{G}}, \bar{\mathbf{q}} + \bar{\mathbf{G}}'; zz')$  (see fig. 5.15a). The real-space grid extends from  $z = -d_0$  to  $z = d_0$  and is sampled by  $N_z$  points which is exactly the number of  $\mathbf{G}$  vectors along the  $z$ -direction. Eventually, the real-space sampling  $\Delta_z = 2d_0/N_z$  is increased by a Fourier interpolation (we just have to add zeros in reciprocal space).
3. We apply the zone-folding (6.11) in order to obtain  $\pi_{\text{CNT}}(\boldsymbol{\xi}\boldsymbol{\xi}'; \varrho\varrho')$ . The resulting real-space grid extends from  $\varrho = 0$  to  $\mathcal{R}_{\text{max}}$  and has the same sampling interval  $\Delta_\varrho = \Delta_z$ . The  $z = 0$  component is centred at the radius  $\mathcal{R}$ .
4. The microscopic dielectric function  $\varepsilon_{\text{CNT}}(\boldsymbol{\xi}\boldsymbol{\xi}'; \varrho\varrho')$  is obtained by a convolution of  $\pi_{\text{CNT}}(\boldsymbol{\xi}\boldsymbol{\xi}'; \varrho\varrho')$  with the Coulomb potential  $v(\boldsymbol{\xi}; \varrho\varrho')$  [see eq. (6.13)].
5. By inversion<sup>8</sup> of  $\varepsilon_{\text{CNT}}(\boldsymbol{\xi}\boldsymbol{\xi}'; \varrho\varrho')$ , we implicitly solve the Dyson eq. (6.12). As in the Coulomb-cutoff method III, the Coulomb potential is intrinsically cut-off at the borders of the real-space grid (correct or converge the parameter  $\mathcal{R}_{\text{max}}$ ).
6. The AR-EEL spectrum  $-\text{Im} \varepsilon_{\text{CNT}}^{-1}(\mathbf{q}^0 \mathbf{q}^0)$  is calculated from eq. (6.21). Also off-diagonal terms  $\varepsilon_{\text{CNT}}^{-1}(\boldsymbol{\xi}\boldsymbol{\xi}'; \varrho\varrho')$  contribute as the external plane wave is decomposed in several coherent cylinder waves (see two-beam case in section 2.3.1).

Step 1 and 6 are the same as in the ZF+LRA method IV (see p. 125 and appendix C.2) except that we now have to consider the full microscopic response matrix  $\chi_{\mathbf{G}\mathbf{G}'}^0$  of the graphene ribbon instead of just the macroscopic component  $\chi_{\mathbf{0}\mathbf{0}}^0$ . Steps 2,4, and 5 are analogous to the Coulomb-cutoff method III for graphene (see p. 102) where the Dyson equation for the susceptibility was solved in real space.

Obviously, this procedure is much more involved than the ZF+LRA-method IV, but it is also much faster than a full *ab-initio* calculation of the tube in a large supercell. In principle, we can study arbitrary chiralities and rather large tubes. Due to the cutoff, we obtain results for an ideally isolated tube.

<sup>8</sup> Due to the screw symmetries of the system, the  $N$  polarisabilities from step 1 with different (reduced) in-plane momentum  $\bar{\mathbf{q}}(lq_\parallel^0)$  cannot mix and the inversion can be performed independently.

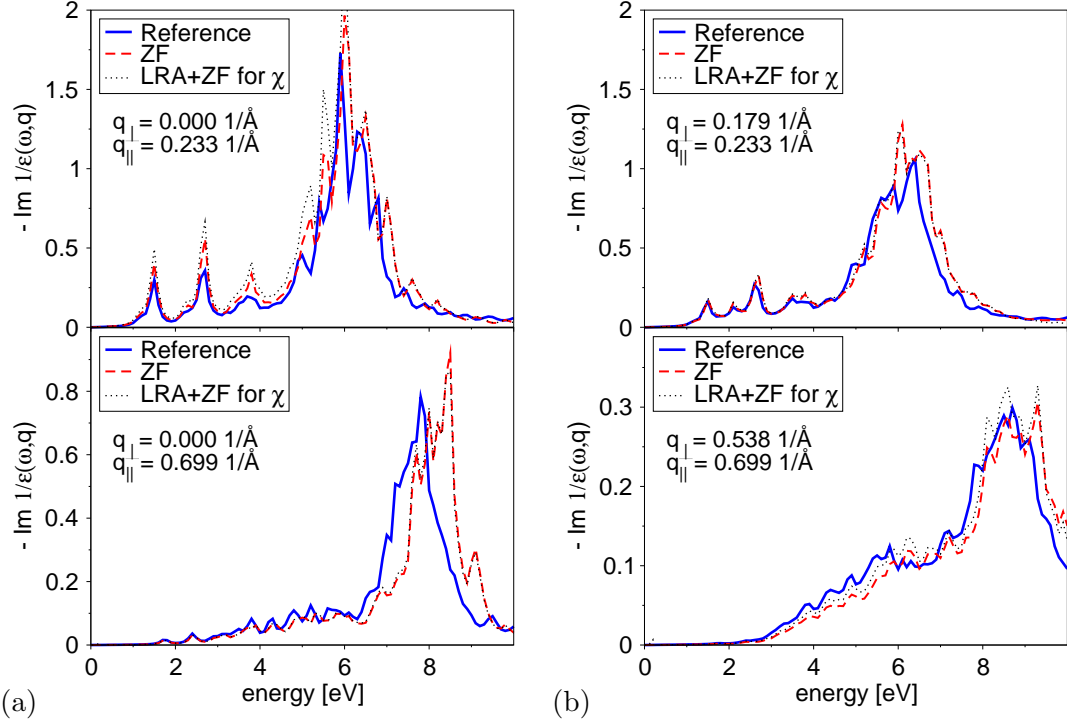


**Fig. 6.16:** Dielectric response of a (9,9) tube for (a) on-axis momentum transfer and (b) arbitrary direction of  $\mathbf{q}^0$  with small (top) and large magnitude (bottom). We compare full *ab-initio* calculations (solid, [187]) with the ZF results including (dashed lines) or excluding contributions of in-plane LFE (dotted lines). Compare with ZF+LRA results shown in fig. 6.8 and 6.10.

### Comparison with Ab-Initio Results

We have applied the zone-folding method **V** to calculate the AR-EEL spectra of a (9,9) nanotube for different momentum transfers  $\mathbf{q}^0$  (see fig. 6.16). For small momentum transfer (top), the zone-folding method (red dashed line) reproduces the full *ab-initio* reference calculations of C. Giorgetti and X. Lopez-Lozano [187] (solid blue line). Note that the intensity is correctly predicted, if the difference in the normalisation volume for the two calculations is properly taken into account. Also for large momentum transfer (bottom), the spectra are clearly improved with respect to our ZF+LRA results shown in fig. 6.8a and fig. 6.10a. Note that the zone-folding method includes both the nonlocal corrections of the polarisability and the in-plane local-field effects in the cylinder.

The deviation of the spectrum for large on-axis momentum (see fig. 6.16a, bottom) needs further investigation. In this case, only the  $l = 0$  mode contributes which should be close to the in-plane spectrum of graphene. A test calculation for on-axis momentum transfers and a very large (90,90) tube exactly reproduces the expected graphene limit. Indeed, the Coulomb potential of the tube converges towards the Coulomb potential of the sheet for  $\mathcal{R} \rightarrow \infty$  (see appendix A.4.5). In this limit, the zone-folding method **V** for tubes becomes equivalent to the Cutoff-method **III** for graphene.

## LRA for the Susceptibility

We expect that the graphene limit of the tube is also reached for large momentum transfers  $q^0 \gg 1/\mathcal{R}$ , i. e., when modes with large angular momentum  $l$  or on-axis momentum  $p$  become dominant in the AR-EEL spectra of the tube. In this case, the Coulomb potential (6.14) in the Dyson eq. (6.12) of the tube becomes very local in radial direction (see fig. 6.6c) and decays exponentially like the Coulomb term for the sheet (5.28). We might expect that the effects of the Coulomb potential in the nanotube and the sheet are comparable and that the susceptibility of the tube  $\chi_{\text{CNT}}$  can be related to the susceptibility of the sheet  $\bar{\chi}(\bar{\mathbf{q}})$  within the zone-folding approximation [compare with eq. (6.11)].

In order to verify this statement, we have applied the LRA+ZF method IV (see p. 125) directly for the susceptibility  $\bar{\chi}(\bar{\mathbf{q}})$  of the sheet.

### Procedure VI: ZF+LRA method for $\chi$

1. Starting point is the *macroscopic* component  $\chi_d(\bar{\mathbf{q}}\bar{\mathbf{q}}, q_z = 0 = q'_z)$  of the susceptibility for a stack of graphene ribbons with sufficiently large interlayer distance  $d$  such that the sheets do not interact. It can be obtained from a stack with small interlayer distance, e. g., by using the interpolation method I. A special  $k$ -point mesh according to the tube has to be used (see fig. 6.2a).
2. Within the local-response approximation and the zone-folding model, the tube susceptibility is obtained from  $\bar{\chi}_{\text{CNT}}(lp) = \mathcal{R} d \chi_d(\bar{\mathbf{q}}(lp))$  [see eq. (5.31), (6.19)].
3. The loss spectrum is calculated from eq. (6.23) as sum over several  $l$  modes.

On the one hand, this method is computationally very efficient. Using the methods developed in the previous chapter 5, the first step becomes quite fast. The following two steps only involve scalar response functions and can be performed in a few seconds. On the other hand, the method implies the following strong assumptions: (i) The influence of the Coulomb potential in the Dyson equation is comparable for the tube and the sheet, i. e., we can compare the decay perpendicular to the wall/sheet and the in-plane local-field effects in the two systems. (ii) The contribution of non-diagonal terms  $l \neq l'$  in the expression for the AR-EEL spectrum is negligible [see eq. (6.21)].

It is therefore most astonishing that the ZF+LRA method VI for  $\chi$  (see dotted lines in fig. 6.16) gives nearly identical results as the zone-folding method V for  $\pi$  (red dashed lines) for the AR-EEL spectra of the (9,9) tube. This has two important consequences: First, it shows that the zone-folding model can be also applied for the sheet susceptibility  $\bar{\chi}$  as long as the external plane-wave perturbation has a sufficiently short wavelength ( $\mathcal{R}q^0 \gg 1$ ). And second, we might conclude that the discrepancy between the zone-folding calculations and full *ab-initio* calculations (blue solid lines) for large on-axis momentum is due to curvature effects which are neglected both in method V and VI.

*The stunning agreement between the full ab-initio calculations and our zone-folding method clearly validates the formalism developed in this chapter and the use of graphene to understand excitations in SWCNTs.*

## Conclusion

In this chapter, I studied the collective excitations of single-wall carbon nanotubes. In particular, the dynamic structure factor  $S(\mathbf{q}, \omega)$  of an isolated tube has been calculated from first principles for different directions of the momentum transfer  $\hbar\mathbf{q}$ .

Usually, full *ab-initio* calculations for the excited properties of an isolated tube are numerically very demanding and become even unfeasible for large tubes with hundreds of electrons per unit cell. I have developed and implemented a building-block approach to overcome these limitations: Combining effective-medium theory and *ab-initio* calculations, we describe the collective excitations in nanostructures (like carbon nanotubes) starting from the microscopic polarisability of their building blocks (graphene). To this end, Maxwell's equations are solved using the full frequency- and momentum-dependent microscopic dielectric function  $\varepsilon(\mathbf{q}, \mathbf{q}', \omega)$  of graphene. The latter can be efficiently calculated from first principles using the methods discussed in the previous chapter 5.

Very good agreement with full *ab-initio* calculations is then obtained for the energy-loss spectra of graphene and single-wall carbon nanotubes while the computational effort is reduced by at least one order of magnitude. This opens the way to study electronic excitations for systems which are too large for a full *ab-initio* treatment, and too small for a reasonable description within the dielectric formalism.

I applied the building-block approach to study the directional dependence of angular-resolved electron energy-loss spectra of single-wall carbon nanotubes. The dispersion of the plasmon peaks in the valence-loss region is understood in terms of the normal mode excitations of the tube. Two regimes can be distinguished:

In the limit of a large wave length  $2\pi/q \gg \mathcal{R}$  of the external plane-wave perturbation, the nanotube reacts like a one-dimensional system and the response can be decomposed into an on-axis and perpendicular contribution. The latter is generally strongly reduced due to the depolarisation effect. Within the zone-folding model, we found that the loss function of the tube is closely related to the in-plane response in graphene.

For small wave length  $2\pi/q \ll \mathcal{R}$ , however, the tube behaves like a quasi-two dimensional system. The external perturbation excites several helical charge oscillations on the cylinder surface which are characterised by the helical momentum  $\xi$ . The orientation of the momentum transfer  $\mathbf{q}$  influences the intensity of the different induced  $\xi$  modes. Typically, charge oscillations with a wave length of the order of  $2\pi/q$  are dominant. Within the zone-folding model, each helical mode on the tube can be associated with an in-plane excitation of the unrolled sheet. This allows us to understand the loss spectra of single-wall carbon nanotubes in terms of the collective excitations in periodic graphene ribbons.

# 7 Towards Spatially-Resolved EELS

In this last chapter, we give an outlook on the calculation of spatially-resolved electron energy-loss spectra for atomically thin nanostructures, namely graphene and single-wall carbon nanotubes. We assume that all scattered electrons are collected by the detector such that the semi-classical approach can be applied (see section 2.5.3). Consequently, we can directly use the methods that have been developed in the previous chapters for the calculation of the angular-resolved loss spectra—we only have to replace the external plane-wave perturbation by a delta function in space.

Within this approach, we first consider the influence of nonlocal corrections, i. e., the  $\mathbf{q}$ -dependence of the dielectric function  $\varepsilon(\mathbf{q}, \omega)$  of the target. Second, we briefly discuss the possibility to describe atomically-resolved electron energy-loss spectra using the full microscopic dielectric response function  $\varepsilon(\mathbf{q}, \mathbf{q}', \omega)$  of the target. And finally, we present some open questions that might be investigated in continuation of this thesis.

## 7.1 Near-Field EELS for a Graphene Layer

In this section, we consider the energy-loss for an electron beam passing parallel to an isolated graphene sheet. This model system allows us to study the delocalisation of the loss signal and the importance of spatial dispersion in the target response.

Already 30 years ago, local dielectric theory has been used to calculate the energy-loss of a swift electron for thin slabs and interfaces [30, 190], and in particular for thin slabs of graphite [179]. Nonlocal effects have been discussed, e. g., in the context of a metal surface, using a model dielectric function [191, 192]. In this section, we consider the local and nonlocal response of an atomically thin graphene layer, where the dielectric response is calculated from first principles. First, we rederive the energy-loss probability for this geometry in close analogy to section 1.3.3. And second, we discuss our numerical results.

### 7.1.1 Electron Energy-Loss Probability

We consider an electron that moves with constant velocity  $v$  on a straight line parallel to an isolated graphene sheet (see fig. 7.1a). The sheet shall be located in the  $xy$ -plane while the electron moves parallel to the  $y$ -axis at a distance  $b$ . The charge density reads

$$\begin{aligned}\rho^e(\mathbf{r}, t) &= -e \delta(x - a) \delta(y - vt) \delta(z - b), \\ \rho^e(\bar{\mathbf{q}}; z, \omega) &= -2\pi e \delta(\omega - q_y v) \delta(z - b) e^{-iq_x a}, \quad \bar{\mathbf{q}} = (q_x, q_y),\end{aligned}\tag{7.1}$$

where the in-plane coordinates have been Fourier transformed like in chapter 5. With the corresponding Coulomb potential (5.28) we obtain for the external potential

$$\varphi^e(\bar{\mathbf{q}}; z, \omega) = \int dz' \frac{1}{\epsilon^2} v(\bar{\mathbf{q}}; z, z') \rho^e(\bar{\mathbf{q}}; z') = -\frac{2\pi}{eV} v_{2D}(\bar{\mathbf{q}}) e^{-|\bar{\mathbf{q}}||z-b|-iq_x a} \delta\left(\frac{\omega}{v} - q_y\right). \quad (7.2)$$

Note that the on-axis momentum  $\hbar q_y = \hbar\omega/v$  is fixed by the energy loss  $\hbar\omega$  and the velocity  $v$  of the external electron, while  $\varphi^e$  decays exponentially with increasing  $q_x$ .

In a second step, we calculate the total energy that is lost by the electron. It corresponds to the work that is needed to bring the induced charge  $\rho^i$  from infinity in the external potential  $\varphi^e$ . As in the derivation for eq. (1.20), we find for the loss probability

$$P(\mathbf{b}, \omega) = \frac{2}{(2\pi)^3} \text{Im} \int d\bar{\mathbf{q}} \int dz [\varphi^e(\bar{\mathbf{q}}; z, \omega)]^* \rho^i(\bar{\mathbf{q}}; z, \omega). \quad (7.3)$$

The induced charge is given via the susceptibility (1.7). Due to the translation symmetry of the graphene crystal, the susceptibility is a function of the reduced momentum transfer  $\bar{\mathbf{q}}_r$  and a matrix in the in-plane reciprocal lattice vectors  $\bar{\mathbf{G}}$ . We have

$$P(\mathbf{b}, \omega) = \frac{e^2}{4\pi^3} \text{Im} \sum_{\bar{\mathbf{G}}, \bar{\mathbf{G}}'} \int_{\text{BZ}} d\bar{\mathbf{q}}_r \int dz dz' [\varphi^e(\bar{\mathbf{q}}_r + \bar{\mathbf{G}}; z, \omega)]^* \chi_{\bar{\mathbf{G}}\bar{\mathbf{G}}'}(\bar{\mathbf{q}}_r; z, z', \omega) \varphi^e(\bar{\mathbf{q}}_r + \bar{\mathbf{G}}'; z', \omega). \quad (7.4)$$

### Local-Response Approximation

We have seen in section 5.4.2 that the susceptibility  $\chi(z, z')$  is very localised in direction perpendicular to the sheet. Consequently, the integration in eq. (7.4) can be restricted to a very small range  $|z^{(\prime)}| \lesssim \lambda$ . For large impact parameters  $b \gg \lambda$ , the exponential  $e^{-|\bar{\mathbf{q}}||z-b|}$  and thus the external potential  $\varphi^e(z)$  is nearly constant in this region [see eq. (7.2)]. Additionally, the same exponential acts as a cutoff for large wave vectors  $\bar{q} \gtrsim 1/b$ . Restricting to momentum transfers inside the first Brillouin zone, only diagonal terms in the response  $\chi_{00}(\bar{\mathbf{q}}_r)$  contribute in eq. (7.4). With these two assumptions, the energy-loss probability then simplifies to

$$P(\mathbf{b}, \omega) \stackrel{\text{LRA}}{\approx} \frac{e^2}{4\pi^3} \int_{\text{BZ}} d\bar{\mathbf{q}}_r |\varphi^e(\bar{\mathbf{q}}_r; z=0, \omega)|^2 \iint dz dz' \text{Im} \chi_{00}(\bar{\mathbf{q}}_r; z, z', \omega), \quad (7.5)$$

where the second integral actually corresponds to the slab susceptibility  $\bar{\chi}(\bar{\mathbf{q}}_r)$  [see eq. (5.31)]. So far we have only assumed that the *external* potential is slowly varying along  $z$ , i. e., we have used the local-response approximation for the Coulomb interaction between the external electron and the graphene layer. The *induced* potential instead has microscopic components which might contribute to the macroscopic response  $\chi_{00}$  of the graphene sheet. Indeed, we have seen in section 5.4 that the local-response approximation for the Dyson eq. (5.27) can be only applied for small momentum transfers  $\bar{\mathbf{q}}_r < 0.1 \text{ \AA}^{-1}$ . For large  $\bar{\mathbf{q}}_r$ , the response of the graphene sheet has to be calculated from a full *ab-initio* calculation.

With the external potential  $\varphi^e$  from eq. (7.2) we finally find (we drop the index in  $\bar{\mathbf{q}}_r$ )

$$P(\mathbf{b}, \omega) \stackrel{\text{LRA}}{\approx} \frac{e^4}{4\pi\epsilon_0^2 v^2} \int dq_x \frac{e^{-2\bar{q}b}}{\bar{q}^2} \text{Im} \bar{\chi}(\bar{\mathbf{q}}, \omega) = -\frac{e^4 L_z}{4\epsilon_0^2 v^2} \int dq_x C(b, \omega; q_x) S(\bar{\mathbf{q}}, \omega). \quad (7.6)$$

which has been rewritten in terms of the dynamic structure factor  $S(\bar{\mathbf{q}}, \omega)$  using the definition (5.31) of  $\bar{\chi}$  and the fluctuation-dissipation theorem (2.48). Thus, the expression for the energy-loss at impact parameter  $b$  is decomposed into a material specific part  $S(\bar{\mathbf{q}}, \omega)$  which corresponds to the quantity measured in AR-EELS and a probe factor  $C$  that describes the experimental conditions for the incident electron:

$$C(b, \omega; q_x) = (1/\bar{q}^2) e^{-2\bar{q}b}, \quad \bar{q}b = \sqrt{(q_x b)^2 + \zeta^2}, \quad \zeta = \frac{b\omega}{v}. \quad (7.7)$$

It basically acts as a low-pass filter for the integration over the in-plane momentum component  $q_x$ . For a better understanding of eq. (7.6), it is useful to study the behaviour of  $S$  and  $C$  for some limiting cases.

### Dynamic Structure Factor

In order to integrate over  $q_x$ , the  $\bar{\mathbf{q}}$ -dependent response  $S(\bar{\mathbf{q}}) \propto \text{Im} \bar{\chi}(\bar{\mathbf{q}})$  of the graphene sheet has to be known. Following chapter 5, we can distinguish three ranges:

- In the optical limit  $\bar{q} \rightarrow 0$ , the influence of the Coulomb potential vanishes and we have  $\bar{\chi} = \bar{\pi}$  (see section 5.4.2). In RPA, this corresponds to the independent-particle polarisability and the spectra can be understood by the sum-over-states expression (3.14). As  $\bar{\pi} \propto \bar{q}^2$ , the divergence of the probe factor  $C$  is compensated.
- For wave vectors  $\bar{q} \lesssim 0.1 \text{ \AA}^{-1}$ , two observations are important: First, the local-response approximation can be applied for the Dyson eq. (5.27) and we obtain a scalar equation (5.32) that connects the slab susceptibility  $\bar{\chi}(\bar{\mathbf{q}})$  with the slab polarisability  $\bar{\pi}(\bar{\mathbf{q}})$ . Second, the susceptibility changes rapidly with  $\bar{\mathbf{q}}$  (compare the graphene spectra in the lower and middle panel of fig. 5.8b), while the scaled polarisability  $v\pi$  is nearly unchanged (see fig. 5.8c). Together, we obtain an analytic expression for the  $\bar{\mathbf{q}}$ -dependence of the dynamic structure factor

$$S(\bar{\mathbf{q}}, \omega) \approx -\frac{1}{\pi L_z} \text{Im} \frac{\bar{q}^2 \bar{\Pi}(\omega)}{1 - v_{2D}(\bar{\mathbf{q}}) \bar{q}^2 \bar{\Pi}(\omega)}, \quad \bar{\Pi}(\omega) = \lim_{\bar{\mathbf{q}} \rightarrow \mathbf{0}} \bar{q}^{-2} \bar{\pi}(\bar{\mathbf{q}}, \omega). \quad (7.8)$$

This approach is also used in dielectric theory when non-local effects (spatial dispersion) are neglected. The material is then described by a  $\bar{\mathbf{q}}$ -independent bulk dielectric function  $\epsilon(\omega)$  (which is directly related to  $\bar{\Pi}$ ), but the response of the target (described by  $S$ ) becomes  $\bar{\mathbf{q}}$ -dependent due to the Coulomb interaction.

- For larger momentum transfers  $\bar{q} \gtrsim 0.1 \text{ \AA}^{-1}$ , both  $\bar{\pi}$  and  $\bar{\chi}$  depend on  $\bar{\mathbf{q}}$ , i. e., spatial dispersion becomes important. The dynamic structure factor  $S(\bar{\mathbf{q}})$  can be calculated from a full *ab-initio* calculation, using the interpolation method I (p. 92), or the empirical LRA- $\beta$  method (see section 5.5.1).

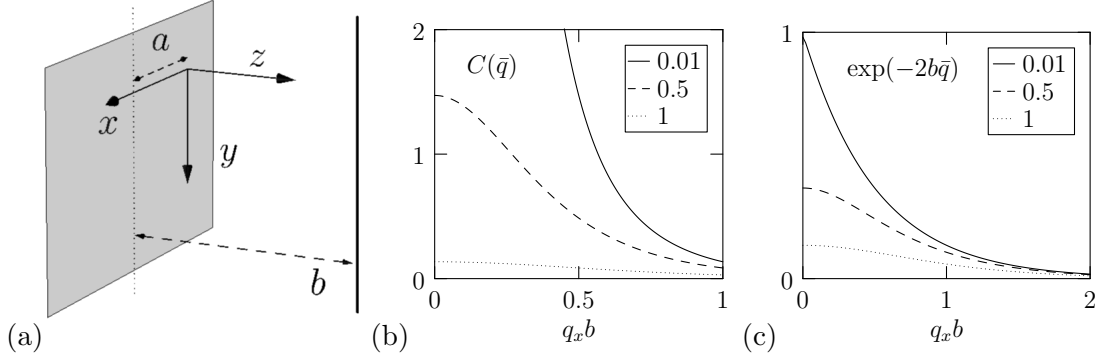


**Fig. 7.1:** (a) Geometry for the SR-EELS calculation in a planar sheet. (b) Probe factor  $C(q_x)$  for three different parameters  $\zeta = \frac{b\omega}{v}$  [see eq. (7.7)]. (c) Exponential  $e^{-2\bar{q}b}$  for the same parameters.

### Probe Factor

The probe factor  $C(b, \omega; q_x)$  given in eq. (7.7) rapidly decays for large momentum transfers  $q_x$  (see fig. 7.1b). As the factor  $\bar{q}^{-2}$  is compensated by the dynamic structure factor  $S(\bar{q}) \propto q^2$ , we only have to investigate the exponential  $e^{-2\bar{q}b}$  (see fig. 7.1c). Its behaviour strongly depends on the impact parameter  $b$  and the on-axis wave vector  $q_y = \omega/v$ . Introducing the adiabatic parameter<sup>1</sup>  $\zeta = b\omega/v$ , one can distinguish two cases:

- For small  $\zeta < 0.1$ , the exponential  $e^{-2\bar{q}b} \approx e^{-2q_x b}$  becomes independent of  $\omega$  and  $v$  and the integration (7.6) will be limited to small  $q_x \lesssim 2/b$ .
- For larger  $\zeta > 0.1$ , the exponential  $e^{-2\bar{q}b} \approx e^{-2\zeta}$  is rather small and approximately constant for  $q_x \ll \zeta/b$ . It decays exponentially only for larger  $q_x$  values.

For instance, in an electron microscope, the acceleration voltage is typically of the order of 100 keV. In this case, one has  $\beta = v/c = 0.55$  and  $1/v \approx 0.001 \text{ \AA}^{-1}/\text{eV}$ , i. e., an energy loss of 10 eV is associated with an on-axis momentum transfer  $\omega/v$  of  $0.01 \text{ \AA}^{-1}$ . For impact parameters  $b \lesssim 10 \text{ \AA}$  we are clearly in the first case, i. e., the exact velocity  $v$  and energy transfer  $\omega$  does not influence the resulting loss spectrum. The second case will be important for large energy loss (in particular for core-loss spectroscopy) or low velocities  $v$ .

### 7.1.2 Numerical Simulations

In this section, we present the numerical results obtained from the semi-classical approach described above. We proceed in three steps: First, the response of the graphene sheet is calculated from the dielectric response in the  $q \rightarrow 0$  limit using eq. (7.8). Second, nonlocal effects (spatial dispersion) are included in the description of the target. Third, we briefly discuss the microscopic dielectric approach which becomes necessary for the description of atomically-resolved spectra.

<sup>1</sup>If relativistic effects are included, the velocity  $v$  is replaced by  $\gamma v$ , where  $\gamma = [1 - (v/c)^2]^{-1/2}$  [11].

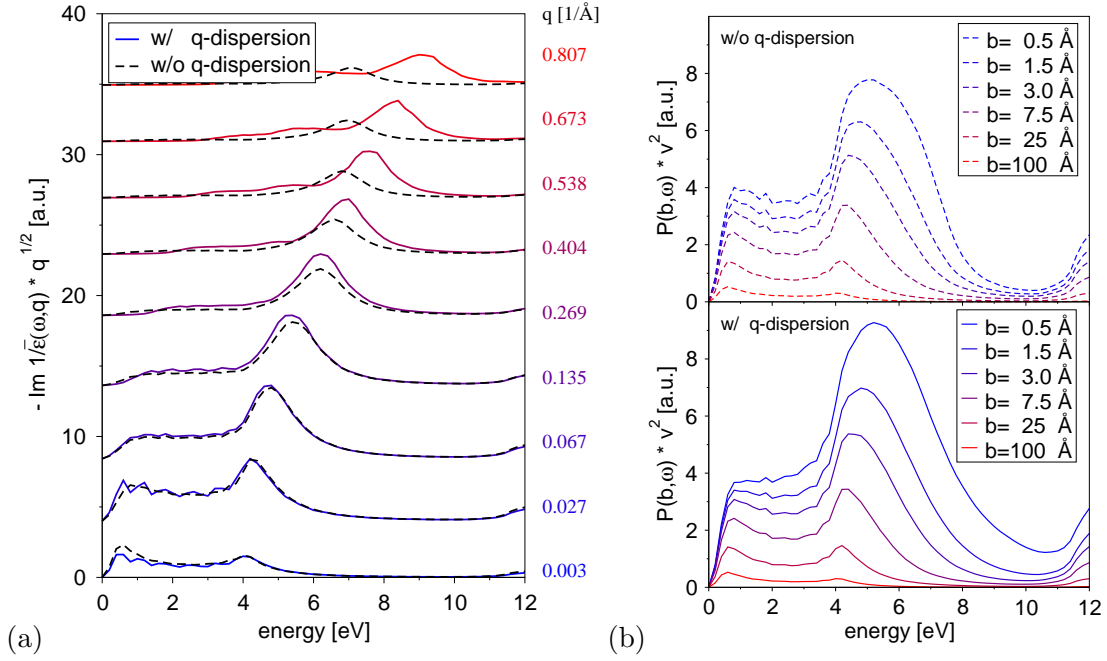


**Fig. 7.2:** Electron energy-loss spectra for a graphene sheet with and without nonlocal effects. (a) Angular-resolved EELS  $-\text{Im } \bar{\epsilon}^{-1}(\bar{\mathbf{q}}) \propto \pi L_z v(\bar{\mathbf{q}}) S(\bar{\mathbf{q}})$  for different in-plane momentum transfers  $\bar{q}$ . The spectra have been shifted along the ordinate. (b) Spatially-resolved EELS for several impact parameters  $b$  [see eq. (7.6)]. In (a) and (b), the dynamic structure factor  $S(\bar{\mathbf{q}})$  of graphene is calculated in a local approximation [eq. (7.8), dashed] or by full *ab-initio* calculations (solid).

### Local Dielectric Response

We start from an *ab-initio* calculation of the polarisability  $\pi(\bar{\mathbf{q}} \rightarrow \mathbf{0}, \omega)$  of a graphene stack with doubled interlayer distance for small momentum transfer  $\bar{q} = 0.067 \text{ \AA}^{-1}$ . The momentum-dependent dynamic structure factor  $S(\bar{\mathbf{q}}, \omega)$  of the graphene sheet is then calculated from eq. (7.8), i. e., we assume that the local-response approximation is valid and we neglect the  $\bar{\mathbf{q}}$ -dependence of the polarisability. In fig. 7.2a, we compare the results of this local approximation (dashed lines) with our full *ab-initio* calculations for the response of graphene in a sufficiently large supercell (solid lines). Interestingly, non-local effects start to become important for these angular-resolved energy-loss spectra only for large momentum transfers  $\bar{q} > 0.1 \text{ \AA}^{-1}$ .

In order to calculate the spatially-resolved electron energy-loss probability  $P(b, \omega)$ , the integration over  $q_x$  in eq. (7.6) is performed numerically by calculating the sum

$$P(\mathbf{b}, \omega) = -\frac{e^4 L_z}{4\epsilon_0^2 v^2} \sum_n S(\Delta \mathbf{q} \cdot (n + \frac{1}{2}) \mathbf{e}_x + \frac{\omega}{v} \mathbf{e}_y, \omega) \int_{\Delta \mathbf{q} \cdot n}^{\Delta \mathbf{q} \cdot (n+1)} dq_x C(b, \omega; q_x), \quad (7.9)$$

which is found to be converged for a step size of  $\Delta q = 0.005 \text{ \AA}^{-1}$ . The resulting spectra for different impact parameters  $b$  ranging from  $0.5 \text{ \AA}$  up to  $100 \text{ \AA}$  are shown in the upper

panel of fig. 7.2b. At very large distances from the sheet, the exponential  $e^{-2\bar{q}b}$  in eq. (7.7) rapidly decays and thus only the smallest  $q_x$  values contribute to the integration. Indeed, the spectrum at  $b = 100 \text{ \AA}$  is nearly identical to the AR-EELS spectrum for vanishing momentum transfer in fig. 7.2a. Because the latter is closely related to the in-plane dielectric function  $\text{Im } \varepsilon_{\perp}(\omega)$  of graphite (see section 5.4.2), the loss probability at large distances from the graphene sheet corresponds to the absorption spectrum in graphite. Dielectric theory for an electron moving parallel to an infinitesimally thin slab of graphite predicts an energy loss  $P(\omega) \propto \text{Im } \varepsilon_{\perp}(\omega) - \text{Im } \varepsilon_{\parallel}^{-1}(\omega)$  [179, p. 3]. This differs from our result in the second term which corresponds to out-of-plane excitations.

With decreasing distance  $b$  between the electron trajectory and the graphene sheet, the probe factor  $C$  increases and larger  $|q_x|$  contribute to the integration. As a consequence, both the shape and the intensity of the loss spectrum change considerably with  $b$  (see fig. 7.2b, top). In particular, the  $\pi$ -plasmon peak is broadened and shifts to higher energies.

### Nonlocal Effects in the Target Response

For very small distances  $b = 0.5 \text{ \AA}$ , momentum transfers up to  $|q_x| = 0.7 \text{ \AA}^{-1}$  contribute. Therefore, we have to include nonlocal effects (spatial dispersion) in the response of the graphene sheet by taking into account the full  $\bar{q}$ -dependence of the polarisability  $\pi(\bar{q}, \omega)$ . To this end, we start from our *ab-initio* calculations of the dynamic structure factor  $S(\bar{q}, \omega) = -\frac{1}{\pi} \text{Im } \chi(\bar{q}, \omega)$  for graphene which have been presented in section 5.3.2. The results for momentum transfers  $\bar{q}$  up to  $0.8 \text{ \AA}^{-1}$  along the  $\Gamma\text{M}$  direction are shown in fig. 7.2a (solid lines). As we need a dense grid of  $q_x$  values, we have used a new interpolation method for spectra that has been developed by Weissker *et al.* [193] and which I have implemented in Python during my thesis. It allows us to calculate  $S(\bar{q}, \omega)$  at arbitrary momentum transfers  $\bar{q}$  up to  $1 \text{ \AA}^{-1}$  and we can repeat the numerical integration in eq. (7.9) including the full nonlocal response of the target.

The results of these calculations are shown in the lower panel of fig. 7.2b. For distances larger than  $b > 5 \text{ \AA}$  the influence of nonlocal corrections is found to be negligible. This is in good agreement with previous model calculations for metal interfaces [191, 192]. Only at very small distances, sufficiently large  $|q_x|$  values contribute in the integration of eq. (7.9) and nonlocal effects become noticeable. They increase the loss probability especially for larger energies  $\hbar\omega > 5 \text{ eV}$ . Finally, fig. 7.3 shows the decay of the loss probability  $P(b, \omega)$  with increasing impact parameter  $b$ . The EELS signal decays within 2–10  $\text{\AA}$  depending on the energy  $\hbar\omega$  of the excitation.

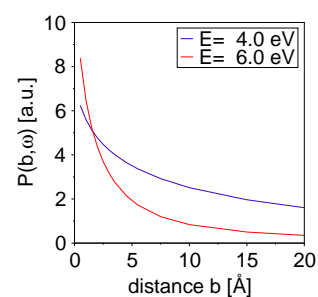


**Fig. 7.3:** delocalisation of the loss signal in graphene

### Towards Atomic Resolution

Remembering the phase problem of electron microscopy (see section 2.3.1), we know that only the off-diagonal elements of the mixed dynamic form factor  $S(\mathbf{q}, \mathbf{q}', \omega)$  con-

tain spatially-resolved information about the target. But so far, only the diagonal part  $S(\mathbf{q}, \mathbf{q}, \omega)$  has been included in our calculations. Off-diagonal contributions have been completely neglected in eq. (7.6). Within the local-response approximation,  $S(\bar{\mathbf{q}}, \bar{\mathbf{q}}; q_z, q'_z)$  becomes constant for all  $q_z$  and  $q'_z$ , i. e., the sheet is described as an effective homogeneous, infinitely thin slab. Any in-plane modulation of the electron charge or the extension of the orbitals perpendicular to the sheet are certainly not included in this description, even if we take spatial dispersion into account, i. e., the  $\bar{\mathbf{q}}$ -dependence of the response function.

In order to include the atomic modulation, we should start from the general expression (7.4) which contains the full microscopic response function  $\chi(\bar{\mathbf{q}}, \bar{\mathbf{q}}'; z, z', \omega)$ . This quantity can be calculated efficiently with the Coulomb-cutoff method III that has been developed in chapter 5 for the isolated graphene sheet (see p. 102). Note that this step has to be performed for all  $\bar{\mathbf{q}}_r$  values in the first Brillouin zone of the sheet with  $\bar{q}_y = \omega/v$ . The lateral position  $a$  of the electron beam only enters via the phase factor  $e^{i(G_x - G'_x)a}$ , i. e., only off-diagonal elements  $\chi_{\bar{\mathbf{G}}\bar{\mathbf{G}}'}$  contribute to the spatially-resolved signal and we expect that the wing elements  $\chi_{\bar{\mathbf{0}}\bar{\mathbf{G}}'}$  and  $\chi_{\bar{\mathbf{G}}\bar{\mathbf{0}}}$  are most important because  $e^{-|\bar{\mathbf{q}}||z-b|}$  in eq. (7.2) rapidly vanishes for large momentum  $|\bar{\mathbf{q}}|$ . Deviations from the results obtained within the local-response approximation can be only expected for very small distances  $b < 1 \text{ \AA}$  from the sheet. Unfortunately, these calculations have not yet been performed.

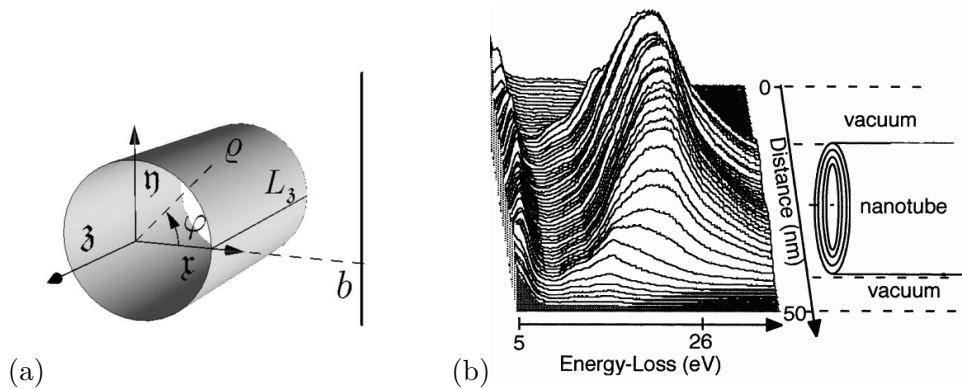


**Fig. 7.4:** (a) Geometry of the STEM measurements scanning across an isolated nanotube. (b) Experimental valence EEL spectra for an isolated multi-wall carbon nanotube (Reprinted from [173], Journal of Electron Spectroscopy © 2001, with permission from Elsevier).

## 7.2 Near-Field EELS for Carbon Nanotubes

For isolated nanotubes it has been actually possible to perform near-field electron energy-loss experiments. Using a scanning transmission electron microscope (STEM), Stéphan *et al.* [173] have been able to record a series of energy-loss spectra for different positions  $b$  scanning across a multi-wall carbon nanotube (see fig. 7.4). Similar experiments have been performed even for isolated single-wall carbon nanotubes with a radius of 6 and 11 Å [174].

The authors have used local dielectric theory to explain the STEM experiments on single- and multi-wall carbon nanotubes starting from the anisotropic polarisability of bulk graphite [178]. However, if we want to study the fine structures in the valence-loss spectra of single-wall carbon nanotubes, like the van-Hove singularities, we have to go beyond the description of the material with a bulk polarisability. In this section, we will briefly outline how the building-block approach (see chapter 6) can be used to calculate spatially-resolved energy-loss spectra starting from *ab-initio* calculations.

### 7.2.1 Dielectric Theory for Single-Wall Carbon Nanotubes

In analogy to the case of the graphene sheet considered above, we use a semi-classical approach to calculate the electron energy-loss probability for a fast electron passing by an isolated single-wall carbon nanotube. We closely follow the calculations of Bertsch *et al.* [194] and Taverna *et al.* [178] who have used a local, anisotropic dielectric function (derived from graphite) in order to describe the response of the tube.

The energy-loss probability for the nanotube is obtained in three steps, calculating (i) the external potential  $\varphi^e$ , (ii) the induced charge density of the system due to this external perturbation, and (iii) the associated energy loss. In contrast to the derivation of section 7.1.1, we will work in cylindrical coordinates in order to use the symmetry of the system.

## External Field

Consider an electron moving with constant velocity  $v$  on a straight line perpendicular to a single-wall nanotube (see fig. 7.4a). We assume that the impact parameter  $b$  is larger than the tube radius  $\mathcal{R}$ , i. e., the electron does not intersect the cylinder. The coordinate system is chosen such that the electron moves parallel to the  $\boldsymbol{\eta}$ -axis and the tube is located at the  $\boldsymbol{z}$ -axis. The charge density and the potential of the external electron reads

$$\rho^e(\mathbf{r}, t) = -e\delta(\mathbf{r} - b\mathbf{e}_x - vt\mathbf{e}_\eta), \quad \varphi^e(\mathbf{r}, t) = \frac{1}{e^2}v\rho^e = \frac{-e}{4\pi\epsilon_0} \frac{1}{|\mathbf{r} - b\mathbf{e}_x - vt\mathbf{e}_\eta|}. \quad (7.10)$$

As in the previous chapter 6, we switch to cylindrical coordinates  $\boldsymbol{\varrho} = (\varrho, \varphi, \boldsymbol{z})$  and perform a Fourier transform along the translationally invariant directions  $\varphi$  and  $\boldsymbol{z}$  (see appendix A.4.1). Following Bertsch *et al.* [194], one obtains

$$\varphi^e(\boldsymbol{\xi}; \varrho, \omega) = -\frac{e}{\epsilon_0} \frac{\pi}{v} I_l(|p|\varrho) \tilde{C}(\boldsymbol{\xi}, \omega), \quad \boldsymbol{\xi} = (p, l), \quad (7.11)$$

where  $I_l$  is the modified Bessel function (see appendix A.4.3) and  $\tilde{C}$  is given by

$$\tilde{C}(\boldsymbol{\xi}; \omega) = \frac{1}{q_{\text{eff}}} \left( \frac{q_{\text{eff}} + (\omega/v)}{p} \right)^l e^{-bq_{\text{eff}}}, \quad q_{\text{eff}}^2 = p^2 + (\omega/v)^2. \quad (7.12)$$

The momentum  $q_{\text{eff}}$  comprises the momentum component  $p$  along the tube axis and the one along the trajectory of the electron  $\omega/v$ .

## Energy Loss

In a second step, we rewrite the expression in eq. (1.21) for the energy-loss function  $P(\mathbf{b}, \omega)$  in cylindrical coordinates. The energy loss is given by the energy of the induced charge  $\rho^i$  inside the external potential  $\varphi^e$ . In analogy to the derivation above, we find

$$P(\mathbf{b}, \omega) = \frac{2}{(2\pi)^2 L_3} \text{Im} \sum_{\boldsymbol{\xi}} \int d\varrho \varrho [\varphi^e(\boldsymbol{\xi}; \varrho, \omega)]^* \rho^i(\boldsymbol{\xi}; \varrho, \omega). \quad (7.13)$$

With the susceptibility (1.7), we finally have

$$P(\mathbf{b}, \omega) = \frac{e^2}{2\pi^2 L_3} \text{Im} \sum_{\boldsymbol{\xi}\boldsymbol{\xi}' } \int d\varrho d\varrho' \varrho \varrho' [\varphi^e(\boldsymbol{\xi}; \varrho, \omega)]^* \chi(\boldsymbol{\xi}, \boldsymbol{\xi}'; \varrho, \varrho', \omega) \varphi^e(\boldsymbol{\xi}'; \varrho', \omega). \quad (7.14)$$

## Local-Response Approximation

As we have discussed in section 6.3.3, the response of the tube  $\chi_{\text{CNT}}(\varrho, \varrho')$  is very localised along the radius and the integration in eq. (7.14) can be restricted to a very small range  $|\varrho^{(\prime)} - \mathcal{R}| \lesssim \lambda$ . Assuming that the external potential  $\varphi^e(\boldsymbol{\varrho})$  is constant in this region and neglecting in-plane local-field effects, we have

$$\begin{aligned}
P(\mathbf{b}, \omega) &\stackrel{\text{LRA}}{\approx} \frac{e^2}{2\pi^2 L_z} \sum_{\xi} |\varphi^e(\xi; \mathcal{R}, \omega)|^2 \text{Im} \bar{\chi}_{\text{CNT}}(\xi, \omega) \\
&\stackrel{\text{LRA}}{\approx} \frac{e^4}{2L_z \varepsilon_0^2 v^2} \sum_{\xi} I_l^2(|p|\mathcal{R}) \tilde{C}^2(\xi, \omega) \text{Im} \bar{\chi}_{\text{CNT}}(\xi, \omega).
\end{aligned} \tag{7.15}$$

Due to the rather complicated behaviour of the modified Bessel function  $I_l^2$ , it is much more difficult to estimate the most important contributions to this sum. Nevertheless, the prefactor decays again exponentially for large  $p$ . Using  $I_l(x) \xrightarrow{x \rightarrow \infty} \frac{e^x}{\sqrt{2\pi x}}$ , we have

$$I_l(|p|\mathcal{R}) \cdot \tilde{C}(lp, \omega) \xrightarrow{p \rightarrow \infty} \frac{e^{p\mathcal{R}}}{\sqrt{2\pi p\mathcal{R}}} \cdot \frac{e^{-pb}}{p} \propto p^{-3/2} e^{-p(b-\mathcal{R})}. \tag{7.16}$$

Additionally,  $I_l(x)$  decreases with increasing angular momentum  $l$  and the summation in eq. (7.15) is essentially restricted to small helical momentum  $\xi$ .

## 7.2.2 Outlook

Although the corresponding numerical simulations have not yet been performed, we can already give an estimation for the results using our experience with the graphene sheet:

### Influence of Nonlocal Corrections

On the one hand, we could include nonlocal corrections (spatial dispersion) by using the  $\xi$ -dependent polarisability  $\bar{\pi}_{\text{CNT}}(\xi, \omega)$  to describe the nanotube. From the graphene results, we can estimate that these corrections become only important for very small impact parameters  $b - \mathcal{R} \lesssim 5 \text{ \AA}$ . Similar results have been obtained by Aizpurua [195], who studied the influence of nonlocal corrections for cylindrical cavities in metals using a model dielectric function.

### Graphite Response

On the other hand, we could try to use the local-response approximation to explain why the dielectric model of Taverna *et al.* [178] also gives quite reasonable results for single-wall carbon nanotubes. In dielectric theory, the nanotube is approximated as a hollow cylinder of bulk graphite with a thickness of about  $1 \text{ \AA}$  (see fig. 6.4a). Like in the case of the graphene sheet (see previous section), the loss function for an infinitely thin cylinder approaches  $P \propto \text{Im} \varepsilon_{\perp} - \text{Im} \varepsilon_{\parallel}^{-1}$ , where the in-plane absorption spectrum of graphite  $\text{Im} \varepsilon_{\perp}$  is thought to be dominant [174, 178].

In our calculations using the local-response approximation we arrive at the same conclusion in two steps: First, with the exponential decay of the probe factor  $C$  [see eq. (7.16)] only small helical momenta contribute to the energy-loss spectrum for large impact parameters  $b$ . And second, for a graphene sheet we have found that the influence of the long-rang part of the Coulomb potential vanishes in the optical limit  $q \rightarrow 0$  and consequently the loss function of graphene nearly coincides with the in-plane absorption  $\text{Im} \varepsilon_{\perp}$  of graphite (see section 5.4.2). We can expect a similar behaviour for the tubes.

### 7.3 Microscopic Charge Oscillations

So far, we considered the simulation of experimental energy-loss spectra in a transmission electron microscope. As we have seen in chapter 2, these spectra include information about the mixed dynamic form factor  $S(\mathbf{q}, \mathbf{q}', \omega)$ , or equivalently, the microscopic dielectric response  $\chi(\mathbf{q}, \mathbf{q}', \omega)$  of the target. However, it is difficult to extract these information directly from experiment where generally only integrated quantities are measured.

Much more details on the physical properties of the target can be obtained by combining electron energy-loss spectroscopy and corresponding *ab-initio* calculations. On the one hand, the calculations can be used to study the origin of the features observed in experiment. Several examples can be found in the previous chapters, like the explanation of the angular anomaly of the dynamic structure factor in crystals (see chapter 4), or the linear plasmon dispersion in single-wall carbon nanotubes (see section 5.3.3).

On the other hand, *ab-initio* calculations allow us to study physical properties that are not directly accessible to experimental observation. For instance, we can visualise the microscopic charge oscillations inside the material that are induced by an external perturbation. This will be the subject of this section.

#### Response to a Perturbing Plane Wave

We consider the perturbation of the target by the scattering of an external plane electron wave (broad-beam geometry). An electron that transfers a momentum  $\hbar\tilde{\mathbf{q}}$  and an energy  $\hbar\tilde{\omega}$  to the target can be associated with a plane wave perturbation

$$\varphi^e(\mathbf{r}, t) = \varphi_0^e e^{-i(\tilde{\omega}t - \tilde{\mathbf{q}}\mathbf{r})}, \quad \varphi^e(\mathbf{q}', \omega') = 2\pi V \varphi_0^e \delta(\mathbf{q}' - \tilde{\mathbf{q}}) \delta(\omega' - \tilde{\omega}). \quad (7.17)$$

In a crystal, the corresponding induced charge density is then given by [see eq. (A.36)]

$$\rho_{\mathbf{G}}^i(\mathbf{q}_r, \omega) = \sum_{\mathbf{G}'} e^2 \chi_{\mathbf{G}\mathbf{G}'}(\mathbf{q}_r, \omega) \varphi_{\mathbf{G}'}^e(\mathbf{q}_r, \omega), \quad (7.18)$$

and we obtain for the microscopic charge oscillation in real space [see eq. (A.40)]

$$\rho^i(\mathbf{r}, t) = e^2 \varphi_0^e e^{-i\tilde{\omega}t} \sum_{\mathbf{G}} e^{i(\tilde{\mathbf{q}}_r + \mathbf{G})\mathbf{r}} \chi_{\mathbf{G}\tilde{\mathbf{G}}}(\tilde{\mathbf{q}}_r, \omega), \quad \tilde{\mathbf{q}} = \tilde{\mathbf{q}}_r + \tilde{\mathbf{G}}. \quad (7.19)$$

Note that only the real part  $\text{Re} \rho^i(\mathbf{r}, t)$  has a physical meaning. It oscillates with the frequency  $\tilde{\omega}$  of the external perturbation and can be calculated from the  $\tilde{\mathbf{G}}$ th column of the susceptibility matrix  $\chi_{\mathbf{G}\mathbf{G}'}$  by a simple Fourier transform.

#### Charge Oscillations in Graphite

As an example, we considered bulk graphite which is perturbed by a plane wave with in-plane wave vector  $\tilde{\mathbf{q}} = 0.74 \text{ \AA}^{-1}$  along the  $\Gamma\text{M}$  direction. Figure 7.5 shows a snapshot of the induced charge oscillation at time  $t = 0$  for two different frequencies  $\tilde{\omega}$  which correspond to the excitation energies of the  $\pi$  and  $\pi + \sigma$  plasmon, respectively. The

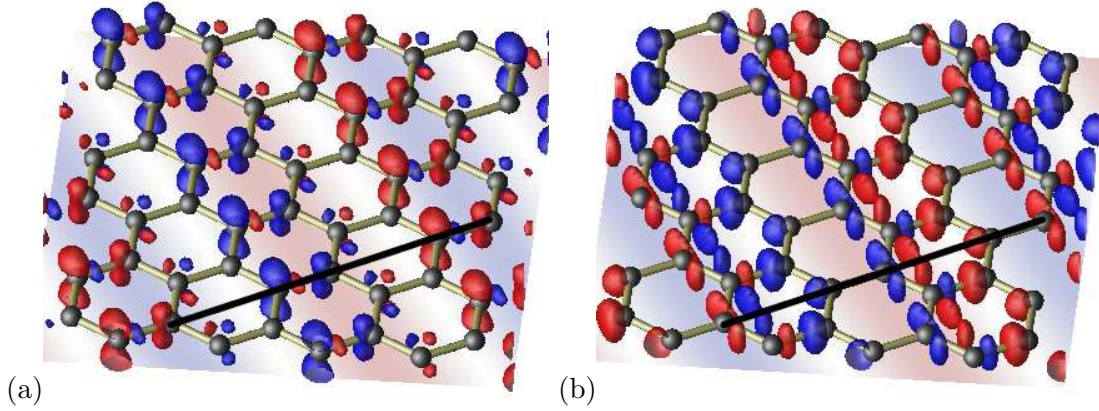


**Fig. 7.5:** Induced density in graphite due to a plane-wave perturbation  $\varphi^e(\mathbf{r}t) \propto e^{-i(\tilde{\omega}t - \tilde{\mathbf{q}}\mathbf{r})}$  with wave vector  $|\tilde{\mathbf{q}}| = 0.74 \text{ \AA}^{-1}$  and (a) energy  $\hbar\omega = 9\text{eV}$  ( $\pi$  plasmon) or (b) energy  $\hbar\omega = 30\text{eV}$  ( $\pi + \sigma$  plasmon). The direction and wave length  $\lambda = 8.5\text{\AA}$  of the external plane wave is indicated by the black line. The blue and red colour of the isosurface corresponds to a positive and negative charge density variation, respectively. The resolution is  $0.8\text{\AA}$ .

induced charge density is clearly periodic with the wave length  $\lambda = 2\pi/\tilde{q}$  of the external perturbation (black line) Moreover, one clearly recognises the two lobes of the  $\pi$  orbitals for  $\tilde{\omega} = 9 \text{ eV}$  (see fig. 7.5a). At larger energies  $\tilde{\omega} = 30 \text{ eV}$  (see fig. 7.5b) the charges between two carbon atoms oscillate. Comparing with the partial ground-state density shown in fig. 5.2e, this can be associated to an oscillation of the  $\sigma$  electrons. *Consequently, we can identify the electrons that contribute to the response by looking at the spatial distribution of the microscopic induced charge density.*

### Time-Dependent Charge Oscillations

In the framework of the master thesis of Giulia Pegolotti [196], we have considered the time-dependence of the microscopic charge oscillation. For the plane-wave perturbation (7.17), the induced charge follows the external plane-wave potential with an energy-dependent phase shift that can be understood from a classical spring model.

Additionally to this periodic perturbation, a delta-pulse in time has been investigated (see [196] for details). In principle, one can also calculate the density oscillations for arbitrary external perturbations like that of an electron flying on a straight line through the crystal. Similar calculations have been considered recently in literature [197–199], but often include only the diagonal part of the mixed dynamic form factor.

## 7.4 Open Questions and Outlook

In this chapter, we have investigated spatially-resolved electron energy-loss experiments starting from first principles. So far, an isolated graphene sheet and the influence of spatial-dispersion effects have been studied. The extension to experimentally accessible systems, like single-wall carbon nanotubes, has been discussed.

Building upon this work, many interesting physical questions can be studied. As an outlook, several possible directions for further investigations are outlined in the following:

### **Spatially-Resolved EELS from Ab-Initio**

In continuation of our work, it could be interesting to systematically improve the local dielectric approach [10] using the methods developed in the previous chapters: First, the influence of nonlocal corrections (spatial dispersion) might be studied for different geometries and experimental situations. Second, the full microscopic dielectric function  $\varepsilon(\mathbf{q}, \mathbf{q}', \omega)$  could be used for the description of the system. It includes all information of the microscopic response at the atomic level and allows us, in principle, to describe atomically resolved experiments. Finally, one might go beyond the semi-classical dielectric approach that was used in this chapter. For instance, the influence of different collection apertures on the spatial resolution could be studied also for valence EELS experiments. Therefore, the full quantum-mechanical scattering approach has to be used (see chapter 2).

### **Complex Systems**

Clearly the methods developed in this thesis can be also applied for other materials than carbon systems. For example, one could easily repeat our studies for monolayer systems with different elemental composition (like boron-nitride sheets and nanotubes). Moreover, one might consider doped systems (shift in the Fermi level) or even sheets and nanotubes with defects. In the latter case, larger unit cells become necessary and, e. g., the Coulomb cutoff method III or the building-block approach for the nanotubes can be of great use to keep the numerical calculations affordable.

### **Connection with Local Dielectric Theory**

In the limits of the local-response approximation, we should be able to connect the macroscopic dielectric theory (see section 1.2.1) with the microscopic approach that is used in this thesis. However, a direct connection between the corresponding response functions is not immediately clear. For instance, the slab response functions introduced in eq. (5.31) always respond to the potential  $\varphi(\bar{\mathbf{q}}, z)$  instead of the corresponding field  $\mathbf{E}(\bar{\mathbf{q}}, z) = -(iq_x, iq_y, \partial_z)^T \varphi(\bar{\mathbf{q}}, z)$ .

This should be also considered in the discussion of bulk and surface plasmons. These two excitations can be clearly defined in the macroscopic dielectric approach (see section 1.2.1). In the microscopic formalism, instead, we cannot define a sharp boundary at the microscopic level and a distinction between these two excitations is less obvious.

### **Plasmons in Crystals**

Already the definition of a volume plasmon becomes more complicated in the microscopic dielectric formalism. Following our discussion in section 4.2, collective excitations in

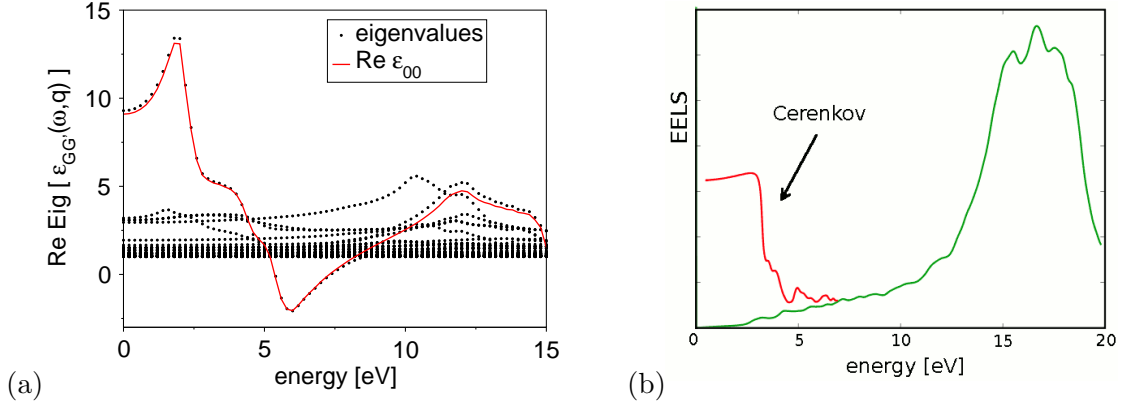


**Fig. 7.6:** (a) Eigenvalues (dots) of the dielectric matrix  $\varepsilon_{\mathbf{G}\mathbf{G}'}(\mathbf{q}_r, \omega)$  of graphite for an in-plane momentum transfer  $\mathbf{q}_r = 0.4 \text{ \AA}^{-1}$ . For comparison, the head element  $\varepsilon_{00}(\mathbf{q}_r, \omega)$  is shown (solid line). (b) Electron energy-loss spectrum for silicon with (red) and without (green) Čerenkov losses (for 200 keV electrons). Momentum transfers  $|\mathbf{q}| < 0.013 \text{ \AA}^{-1}$  are integrated ( $\Delta\vartheta = 0.05 \text{ mrad}$ ).

crystals form a set of plasmon bands which are defined by  $\det |\varepsilon_{\mathbf{G}\mathbf{G}'}(\mathbf{q}_r, \omega)| = 0$ .<sup>2</sup> Starting from our *ab-initio* calculations, we can directly study the plasmon-band structure and the contribution of the microscopic modes. For example, fig. 7.6a shows the eigenvalues of the matrix  $\varepsilon_{\mathbf{G}\mathbf{G}'}(\mathbf{q}_r, \omega)$  compared to the head element  $\varepsilon_{00}$  for bulk graphite. One of the eigenvalues becomes approximately 0 at 7.8 eV (also the imaginary part is then small). The corresponding eigenvector characterises the plasmon mode. Indeed, the charge oscillation that is associated with the plasmon resonance could be also visualised in real space (compare with fig. 7.5).

### Relativistic Effects in EELS

In this thesis, relativistic effects have been completely neglected in the description of electron scattering. Nevertheless, electrons that are accelerated to kinetic energies of about 100 eV have a velocity close to the speed of light ( $0.55c$ ) and retardation effects can become noticeable. For instance, Čerenkov losses can be observed if the velocity becomes superior to the speed of light in the material. In silicon, they can considerably increase the loss probability at low energies  $\hbar\omega < 5 \text{ eV}$  for small momentum transfers  $\mathbf{q} \rightarrow 0$  [201]. Within the dielectric formalism, Čerenkov losses for electrons passing through thin slabs can be described by the Kröger formula [38]. The resulting loss spectra for silicon are shown in fig. 7.6b for an on-axis detector with an opening angle of  $\vartheta = 0.05 \text{ mrad}$ . Jouffrey *et al.* [202] and Sorini *et al.* [54] have considered relativistic effects in the quantum-mechanical scattering approach. And finally, we might also wonder if transverse local-field effects might play a role in electron energy-loss experiments [130].

<sup>2</sup>Moreover, the characterisation of a plasmon as a longitudinal normal mode of the system becomes problematic in crystals. Transverse and longitudinal fields are generally coupled and the normal modes should be classified by their symmetry properties [200].

# Summary

In this thesis, I have tried to answer the following questions:

*Why can the loss spectrum become strongly anisotropic at large momentum transfers ?*

The mixed dynamic form factor  $S(\mathbf{q}, \mathbf{q}', \omega)$ , or equivalently the microscopic dielectric function, is a key quantity for the understanding of spatially-resolved electron energy-loss spectroscopy (EELS). In particular, large momentum transfers beyond the first Brillouin zone should play an important role for atomic-resolution experiments. I found that near certain Bragg reflections, the energy-loss function can be changed drastically by a very small variation in  $\mathbf{q}$ . A detailed analysis reveals that this discontinuity is caused by crystal local-field effects and can be explained in terms of a two-plasmon-band model. To verify our prediction, I have proposed inelastic X-ray scattering (IXS) measurements on graphite and silicon. These experiments have clearly confirmed the predicted anomalous angular dependence.

*How does the dimensionality of a system affect its electronic response ?*

In order to answer this question, I have studied collective excitations of carbon systems with different dimensionality both numerically and analytically. The momentum-dependent electron energy-loss function of graphite, graphene, and single-wall carbon nanotubes (SWCNT) were calculated from first principles within the random phase approximation using (time-dependent) density-functional theory. I have shown that the microscopic components of the induced Hartree potential strongly influence the electronic response in low-dimensional systems. This is due to the confinement of the electrons as we can understand from a simple dielectric model.

*What can we learn from graphene about excitations in SWCNTs ?*

A comparison of EELS measurements on isolated SWCNTs and our graphene calculations revealed that the linear  $\pi$  plasmon dispersion along the axis can be explained by the excitation spectrum of graphene. This connection is less obvious for arbitrary directions of the momentum transfer. To this end, I have combined the ideas of effective medium theory with *ab-initio* calculations to describe the dielectric response of SWCNTs starting from the microscopic polarisability  $\varepsilon(\mathbf{q}, \mathbf{q}', \omega)$  of graphene (zone-folding method). The results are shown to be very similar to a full *ab-initio* calculation. Besides an important gain in calculation time (only a few hours instead of several days are needed), this method allows us to give a clear interpretation of the energy-loss spectra of SWCNTs in terms of the excitations in graphene.

*Which electrons take part in a collective excitation ?*

*Ab-initio* calculations yield a detailed analysis of microscopic quantities. We visualise the time-dependent microscopic charge oscillations induced by an external plane-wave

perturbation that correspond to a plasmon excitation in an EELS experiment. We can identify the electrons that take part in the oscillation by looking at the spatial distribution of the induced charge density. For graphite, contributions from  $\pi$  and  $\sigma$  electrons have been distinguished, depending on the energy of the perturbation.

*How can we use ab-initio calculations for the prediction of spatially-resolved EELS in the valence-loss region ?*

Finally, I apply the methods that I have developed during the course of this thesis for an *ab-initio* simulation of spatially-resolved electron energy-loss spectra of atomically thin nanostructures. First, I consider the loss spectrum of an electron moving parallel to a graphene sheet including non-local effects in the response of the system. Second, I give an outlook how to use the zone-folding method to calculate spatially-resolved energy-loss spectra of single-wall carbon nanotubes starting from the polarisability of graphene within a microscopic dielectric formalism.

The main original results of my work can be summarised in five points:

- A discontinuous behaviour of the dynamic form factor at certain Bragg reflections has been predicted, explained in terms of crystal local-field effects, and verified by inelastic X-ray scattering experiments.
- Combining effective-medium theory and *ab-initio* calculations, a new method has been developed to describe collective excitations of nanostructures (like carbon nanotubes) starting from the polarisability of their building blocks (graphene).
- The linear dispersion of the on-axis  $\pi$  plasmon in isolated SWCNTs has been explained with the excitation spectrum of graphene. In general, electron energy-loss spectra of SWCNTs for arbitrary momentum transfers are understood by a summation of normal-mode excitations.
- By visualising microscopic charge oscillations in real space, it is possible to determine which electrons contribute to the excitation.
- First studies for *ab-initio* calculations of spatially-resolved EELS are presented.

The following methods have been used:

- First-principles RPA calculations of the momentum-resolved and frequency-dependent dynamic structure factor  $S(\mathbf{q}, \mathbf{q}', \omega)$  are performed using the DP-code [102]. The electronic ground state is calculated in DFT-LDA (local-density approximation) with ABINIT [100], using a plane-wave basis set and norm-conserving pseudopotentials.
- New codes have been developed, in particular, a nearest-neighbour tight-binding method for graphene and SWCNTs and a zone-folding method for the calculation of SWCNT spectra starting from the polarisability of graphene. These codes are briefly described and will be made available.

**Part III**

**Appendices**



# A Theoretical Supplements

## A.1 Time-Dependent Perturbation Theory

We recall the fundamentals of time-dependent perturbation theory [203]. Starting from the solution of the Schrödinger equation for a time-independent Hamiltonian  $H_0$

$$H_0 |\Psi_n^0\rangle = E_n |\Psi_n^0\rangle, \quad |\Psi_n^0(t)\rangle = e^{-\frac{i}{\hbar} E_n(t-t_0)} |\Psi_n^0\rangle, \quad (\text{A.1})$$

we would like to find an (approximate) solution of a slightly perturbed system

$$i\hbar\partial_t |\Psi(t)\rangle = (H_0 + H') |\Psi(t)\rangle, \quad |\Psi(t_0)\rangle = |\Psi_i^0\rangle. \quad (\text{A.2})$$

We assume that the system is initially found in the unperturbed eigenstate  $|\Psi_i^0\rangle$  at time  $t_0$  and the time-dependent perturbation  $H'$  is small. For the following, it is convenient to switch to the interaction picture (Dirac picture). The unitary transformation

$$U_0 = e^{-\frac{i}{\hbar} H_0(t-t_0)}, \quad |\Psi_D(t)\rangle = U_0^+ |\Psi(t)\rangle, \quad H'_D(t) = U_0^+ H' U_0, \quad (\text{A.3})$$

removes the trivial time-dependence associated with  $H_0$  from eq. (A.2) and we obtain:

$$i\hbar\partial_t |\Psi_D(t)\rangle = H'_D |\Psi_D(t)\rangle, \quad |\Psi_D(t_0)\rangle = |\Psi_i^0\rangle. \quad (\text{A.4})$$

This differential equation can be recast into an integral equation by introducing the time-evolution operator  $U'_D$ . It connects the solution at time  $t$  with the initial state at  $t_0$

$$i\hbar\partial_t U'_D(t, t_0) = H'_D U'_D(t, t_0), \quad |\Psi_D(t)\rangle = U'_D(t, t_0) |\Psi_i^0\rangle. \quad (\text{A.5})$$

The boundary condition requires that  $U'_D(t_0, t_0) = \hat{1}$ . By formal integration we obtain

$$U'_D(t, t_0) = \hat{1} + \frac{1}{i\hbar} \int_{t_0}^t dt_1 H'_D(t_1) U'_D(t_1, t_0). \quad (\text{A.6})$$

This implicit integral equation can be expanded into a series of  $H'_D$ :

$$U'_D(t, t_0) = \hat{1} + \frac{1}{i\hbar} \int_{t_0}^t dt_1 H'_D(t_1) + \frac{1}{(i\hbar)^2} \int_{t_0}^t \int_{t_0}^{t_1} dt_1 dt_2 H'_D(t_1) H'_D(t_2) + \dots \quad (\text{A.7})$$

This *Dyson series* is central to perturbation theory. If the interaction is sufficiently small, i. e.  $(t - t_0)\langle H'_D \rangle_t \ll 1$ , we can restrict the series to few elements. Within first-order perturbation theory we keep only the linear term in  $H'_D$ .

### A.1.1 Adiabatically-Switched Periodic Perturbation

One important application of time-dependent perturbation theory is the calculation of transition probabilities in a system that is subject to a periodic perturbation. To avoid effects from a sudden turn-on, we use an adiabatic switching with vanishing  $\eta$

$$H'(t) = e^{+\eta t} e^{-i\omega t} V, \quad \lim_{t_0 \rightarrow -\infty} H'(t_0) = 0. \quad (\text{A.8})$$

Note that the order of the limiting process is crucial: for fixed  $t$  we let  $t_0 \rightarrow -\infty$  first, and take the limit  $\eta \rightarrow 0$  afterwards. Using eq. (A.7) to first-order, we can approximate the transition probability between unperturbed states  $|\Psi_i^0\rangle$  at  $t_0$  and  $U_0(t)|\Psi_f^0\rangle$  at  $t$  as

$$w_{i \rightarrow f}^{(1)}(t) = \left| \langle \Psi_f^0 | U_D^{(1)}(t, t_0) | \Psi_i^0 \rangle \right|^2 = \left| \frac{1}{\hbar} \int_{t_0}^t dt_1 e^{i\omega_0(t_1 - t_0)} \langle \Psi_f^0 | H'(t_1) | \Psi_i^0 \rangle \right|^2 \quad (\text{A.9})$$

$$\xrightarrow{t_0 \rightarrow -\infty} \frac{1}{\hbar^2} \frac{e^{2\eta t}}{\eta^2 + (\omega_0 - \omega)^2} \left| \langle \Psi_f^0 | V | \Psi_i^0 \rangle \right|^2, \quad \hbar\omega_0 = E_f^0 - E_i^0.$$

We have used eq. (A.3) and assumed that the final state differs from the initial one. With the known limit of the Lorentzian function  $\lim_{\eta \rightarrow 0} \frac{\eta}{\eta^2 + x^2} = \pi\delta(x)$ , we finally obtain in the limit  $\eta \rightarrow 0$  the transition rate in first-order perturbation theory

$$\Gamma_{i \rightarrow f}^{(1)} = \partial_t w_{i \rightarrow f}^{(1)} = \frac{2\pi}{\hbar} \left| \langle \Psi_f^0 | V | \Psi_i^0 \rangle \right|^2 \delta(E_f^0 - E_i^0 - \hbar\omega). \quad (\text{A.10})$$

This equation is the well known *Fermi Golden Rule*.

### A.1.2 Linear Response Theory

Often, one is interested in the evolution of the observable  $f(t) = \langle \Psi(t) | F | \Psi(t) \rangle$  due to a perturbation  $H'$ . Applying the Dyson series (A.7) for  $U_D'$ , we have up to first order

$$f(t) = \langle \Psi_D(t) | F_D(t) | \Psi_D(t) \rangle = \langle \Psi_i^0 | U_D^{+'}(t, t_0) F_D(t) U_D'(t, t_0) | \Psi_i^0 \rangle \quad (\text{A.11})$$

$$= \langle \Psi_i^0 | F_D(t) | \Psi_i^0 \rangle - \frac{1}{i\hbar} \int_{t_0}^t dt' \langle \Psi_i^0 | [H_D'(t'), F_D(t)]_- | \Psi_i^0 \rangle + \dots$$

The perturbation is generally given by a time-dependent function  $g(t)$  which couples to the system via an operator  $G$  (e. g. the potential  $\varphi$  and density operator  $n$ , respectively)

$$H'(t) = g(t)G, \quad H_D'(t) = g(t)G_D(t), \quad (\text{A.12})$$

where  $g(t < t_0) = 0$ . The first-order fluctuation  $\tilde{f}$  of the observable is then given by

$$\tilde{f}(t) = f(t) - \langle \Psi_i^0 | F_D(t) | \Psi_i^0 \rangle \approx \int_{-\infty}^{\infty} dt' \mathfrak{R}(t, t') g(t'), \quad (\text{A.13})$$

$$\mathfrak{R}(t, t') = \frac{\delta f(t)}{\delta g(t')} = \frac{1}{i\hbar} \Theta(t - t') \langle \Psi_i^0 | [F_D(t), G_D(t')]_- | \Psi_i^0 \rangle.$$

The function  $\mathfrak{R}(t, t')$  is the (*retarded*) *linear response function* [77]. It describes the response at time  $t$  of a system, that has been perturbed by an impulse  $g(t) = \delta(t - t')$  at time  $t'$ . The step function  $\Theta$  ensures causality, i. e., the fact that the answer always follows the perturbation in time. By using the cyclic properties of the expectation value  $\langle\langle \cdot \rangle\rangle_0 \equiv \langle \Psi_i^0 | \cdot | \Psi_i^0 \rangle$ , we find that the response does only depend on the time *difference*

$$\begin{aligned} \langle\langle F_D(t)G_D(t') \rangle\rangle_0 &= \langle\langle U_0^+(t, t_0)FU_0(t, t_0)U_0^+(t', t_0)GU_0(t', t_0) \rangle\rangle_0 \\ &= \langle\langle U_0(t', t_0)U_0(t_0, t)FU_0(t - t' + t_0, t_0)G \rangle\rangle_0 \\ &= \langle\langle F_D(t - t' + t_0)G_D(t_0) \rangle\rangle_0 \end{aligned} \quad (\text{A.14})$$

With the fluctuation operators  $\tilde{F}$  and  $\tilde{G}$ ,

$$\tilde{F} \equiv F - \langle\langle F \rangle\rangle_0, \quad \langle\langle \tilde{F}\tilde{G} \rangle\rangle_0 = \langle\langle FG \rangle\rangle_0 - \langle\langle F \rangle\rangle_0 \langle\langle G \rangle\rangle_0, \quad (\text{A.15})$$

we can finally rewrite the response function (A.13) as

$$\mathfrak{R}(t, t') = \frac{1}{i\hbar} \Theta(t - t') \langle\langle [\tilde{F}(t), \tilde{G}(t')]_- \rangle\rangle_0 = \frac{1}{\hbar} G^{\text{ret}}(t, t'). \quad (\text{A.16})$$

A Fourier transform in  $t - t'$  leads to the spectral representation [204]

$$\mathfrak{R}(E) = \sum_{n \neq i} \left\{ \frac{\langle \Psi_i^0 | \tilde{F} | \Psi_n^0 \rangle \langle \Psi_n^0 | \tilde{G} | \Psi_i^0 \rangle}{E - (E_n - E_i) + i\eta} - \frac{\langle \Psi_i^0 | \tilde{G} | \Psi_n^0 \rangle \langle \Psi_n^0 | \tilde{F} | \Psi_i^0 \rangle}{E + (E_n - E_i) + i\eta} \right\}, \quad (\text{A.17})$$

where we have inserted a complete set of states  $\sum_n |\Psi_n^0\rangle \langle \Psi_n^0|$  and used the following representation of the step function  $\Theta(t - t') = \lim_{\eta \rightarrow 0} \frac{i}{2\pi} \int_{-\infty}^{\infty} dE e^{-iE(t-t')/\hbar} [E + i\eta]^{-1}$ .

### Density Response Function

An important example is the change in the charge density  $\rho$  of the system due to an external scalar perturbation  $\varphi^e$ . The observable  $F$  corresponds to the charge density operator  $\hat{\rho}(\mathbf{r}) = -e\hat{n}(\mathbf{r})$ . The interaction Hamiltonian reads  $H'(t) = \int d\mathbf{r} \hat{\rho}(\mathbf{r})\varphi^e(\mathbf{r}t)$ , i. e.,  $G$  is an integral operator that acts on  $g(t) = \varphi^e(t)$ . Consequently, eq. (A.13) becomes

$$\tilde{\rho}(\mathbf{r}t) \equiv \rho^i(\mathbf{r}t) \approx \int dt' \int d\mathbf{r}' e^2 \chi(\mathbf{r}t, \mathbf{r}'t') \varphi^e(\mathbf{r}'t'), \quad (\text{A.18})$$

where we have introduced the (*retarded*) *density response function* or *susceptibility*

$$e^2 \chi(\mathbf{r}\mathbf{r}', \tau) = \frac{\delta \rho^i(\mathbf{r}t)}{\delta \varphi^e(\mathbf{r}'t')} = \frac{1}{i\hbar} \Theta(t - t') \langle\langle [\tilde{\rho}(\mathbf{r}t), \tilde{\rho}^+(\mathbf{r}'t')]_- \rangle\rangle_0. \quad (\text{A.19})$$

Analogously, we have in Fourier space

$$\chi(\mathbf{q}\mathbf{q}', \tau) = \frac{1}{e^2} \frac{\delta \rho^i(\mathbf{q}t)}{\delta \varphi^e(\mathbf{q}'t')} = \frac{1}{i\hbar} \Theta(t - t') \langle\langle [\tilde{n}(\mathbf{q}t), \tilde{n}^+(\mathbf{q}'t')]_- \rangle\rangle_0. \quad (\text{A.20})$$

### A.1.3 Relation to Scattering Theory

The formalism of time-dependent perturbation theory is closely related to the time-dependent approach to scattering theory (see, e. g., [203, 205]). We therefore consider that  $H_0$  denotes the free Hamiltonian of target and scattering particle, and  $H'$  the interaction between the two. The latter should vanish at  $t_0 \rightarrow \pm\infty$ , i. e., when the scattering particle is far away. We can include this boundary condition by using an adiabatic switching of a constant interaction potential  $V$  similar to eq. (A.8).

The scattering operator  $S$  and the corresponding scattering matrix  $S_{fi}$  is then connected to the evolution operator in the limit of infinite times

$$S = \lim_{t_0 \rightarrow -\infty} \lim_{t \rightarrow \infty} U'_D(t, t_0), \quad S_{fi} = \langle \Psi_f^0 | U'_D(\infty, -\infty) | \Psi_i^0 \rangle. \quad (\text{A.21})$$

Together with the integral equation (A.6), one eventually arrives at the Lippmann-Schwinger-Equation for the scattering state  $|\Psi_i^+\rangle$  [205]:

$$|\Psi_i^+\rangle = |\Psi_i^0\rangle + \frac{1}{E_i - H_0 + i\eta} V |\Psi_i^+\rangle \quad (\text{A.22})$$

Within the first Born approximation, one approximates  $|\Psi_i^+\rangle$  by  $|\Psi_i^0\rangle$  on the right-hand side of the previous equation which leads us to the same transition probability as found in eq. (A.10) previously (for  $\omega = 0$ ).

## A.2 Continuous Fourier Transformation

### A.2.1 One-Particle Functions

We use the following notation for the Fourier transform (FT) of a one-particle function  $f$ :

$$\begin{aligned} f(t) &= (2\pi)^{-1} \int d\omega \tilde{f}(\omega) e^{-i\omega t} & \longleftrightarrow & \quad \mathcal{F}_\omega f = \tilde{f}(\omega) = \int dt f(t) e^{+i\omega t} \\ f(t) &= (2\pi\hbar)^{-1} \int dE \tilde{f}(E) e^{-iEt/\hbar} & \longleftrightarrow & \quad \mathcal{F}_E f = \tilde{f}(E) = \int dt f(t) e^{+iEt/\hbar} \quad (\text{A.23}) \\ f(\mathbf{r}) &= (2\pi)^{-3} \int d\mathbf{q} \tilde{f}(\mathbf{q}) e^{+i\mathbf{q}\mathbf{r}} & \longleftrightarrow & \quad \mathcal{F}_\mathbf{q} f = \tilde{f}(\mathbf{q}) = \int d\mathbf{r} f(\mathbf{r}) e^{-i\mathbf{q}\mathbf{r}} \end{aligned}$$

Examples are the Fourier transform of a constant, the delta-distribution, the Heaviside step function, and the Coulomb potential:

$$\delta(t) = (2\pi)^{-1} \int d\omega e^{-i\omega t}, \quad \longleftrightarrow \quad \delta(\omega) = (2\pi)^{-1} \int dt e^{i\omega t}, \quad (\text{A.24})$$

$$\delta(\mathbf{r}) = (2\pi)^{-3} \int d\mathbf{q} e^{+i\mathbf{q}\mathbf{r}}, \quad \longleftrightarrow \quad \delta(\mathbf{q}) = (2\pi)^{-3} \int d\mathbf{r} e^{-i\mathbf{q}\mathbf{r}}, \quad (\text{A.25})$$

$$\Theta(t) = \begin{cases} 1 & \text{for } t > 0 \\ 0 & \text{for } t < 0 \end{cases} \quad \longleftrightarrow \quad \tilde{\Theta}(\omega) = \frac{i}{\omega + i0^+} = \pi\delta(\omega) + i\mathcal{P}\frac{1}{\omega}, \quad (\text{A.26})$$

$$v(\mathbf{r}) = \frac{e^2}{4\pi\epsilon_0} \frac{1}{|\mathbf{r}|} \quad \longleftrightarrow \quad \tilde{v}(\mathbf{q}) = \frac{e^2}{\epsilon_0} \frac{1}{q^2}. \quad (\text{A.27})$$

For the FT of a product of one-particle functions, the convolution theorem holds:

$$\mathcal{F}[f \cdot g](\mathbf{q}) = (2\pi)^{-3}[\mathcal{F}f * \mathcal{F}g](\mathbf{q}) \equiv (2\pi)^{-3} \int d\mathbf{q}' \tilde{f}(\mathbf{q} - \mathbf{q}') \tilde{g}(\mathbf{q}'), \quad (\text{A.28})$$

$$\mathcal{F}^{-1}[\mathcal{F}f \cdot \mathcal{F}g](\mathbf{r}) = [f * g](\mathbf{r}) \equiv \int d\mathbf{r}' f(\mathbf{r} - \mathbf{r}') g(\mathbf{r}'), \quad (\text{A.29})$$

which can be verified using the definitions above. Note the asymmetry in the prefactor.

## A.2.2 Response Functions

The most general linear mapping between two one-particle functions  $f(\mathbf{r})$  and  $g(\mathbf{r}')$  is given by an integral operator containing the linear response function  $\mathfrak{R}(\mathbf{r}, \mathbf{r}')$ :

$$f(\mathbf{r}) = \int d\mathbf{r}' \mathfrak{R}(\mathbf{r}, \mathbf{r}') g(\mathbf{r}') \quad \longleftrightarrow \quad \tilde{f}(\mathbf{q}) = \int d\mathbf{q}' \tilde{\mathfrak{R}}(\mathbf{q}, \mathbf{q}') \tilde{g}(\mathbf{q}'). \quad (\text{A.30})$$

In Fourier space,  $\tilde{\mathfrak{R}}$  is the corresponding mapping between  $\tilde{f}$  and  $\tilde{g}$ . Using eq. (A.23), we find the connection between  $\mathfrak{R}$  and  $\tilde{\mathfrak{R}}$  (Fourier transform of a response function)

$$\tilde{\mathfrak{R}}(\mathbf{q}\omega, \mathbf{q}'\omega') = (2\pi)^{-4} \int d\mathbf{r} dt \int d\mathbf{r}' dt' e^{+i(\omega t - \mathbf{q}\mathbf{r})} \mathfrak{R}(\mathbf{r}t, \mathbf{r}'t') e^{-i(\omega't' - \mathbf{q}'\mathbf{r}')} \quad (\text{A.31})$$

and analogously the back-transformation with the *same* prefactor. Physically a response function  $\mathfrak{R}$  gives the response  $f$  of a linear system to an external perturbation  $g$ , e. g., the induced polarisation due to an external electric field. The complexity of the general case in eq. (A.30) can be often reduced by the symmetry of the system or due to locality.

### local, inhomogeneous:

If the response  $f(\mathbf{r})$  depends only on the perturbation  $g(\mathbf{r}')$  at the same position  $\mathbf{r} = \mathbf{r}'$ , the response function  $\mathfrak{R}$  is local in space and we have with eq. (A.28)

$$f(\mathbf{r}) = \mathfrak{R}(\mathbf{r}) \cdot g(\mathbf{r}) \quad \longleftrightarrow \quad \tilde{f}(\mathbf{q}) = [\tilde{\mathfrak{R}} * \tilde{g}](\mathbf{q}) = \int d\mathbf{q}' \tilde{\mathfrak{R}}(\mathbf{q} - \mathbf{q}') \tilde{g}(\mathbf{q}'), \quad (\text{A.32})$$

where  $\tilde{\mathfrak{R}}(\mathbf{q})$  is the Fourier transform (A.23) of the one-particle function  $\mathfrak{R}(\mathbf{r})$ . Comparing with (A.30), the relation with the general response function is given by

$$\mathfrak{R}(\mathbf{r}, \mathbf{r}') = \mathfrak{R}(\mathbf{r}) \delta(\mathbf{r} - \mathbf{r}') \quad \longleftrightarrow \quad \tilde{\mathfrak{R}}(\mathbf{q}, \mathbf{q}') = \tilde{\mathfrak{R}}(\mathbf{q} - \mathbf{q}'). \quad (\text{A.33})$$

### non-local, homogeneous: $\mathfrak{R}(\mathbf{r}, \mathbf{r}') = \mathfrak{R}(\mathbf{r} + \mathbf{r}'', \mathbf{r}' + \mathbf{r}'')$

The response  $f(\mathbf{r})$  depends on the perturbation  $g(\mathbf{r}')$  at all positions  $\mathbf{r}'$ , but the system is invariant under any translation  $\mathbf{r}''$ . The response only depends on the distance  $\mathbf{r} - \mathbf{r}'$ :

$$f(\mathbf{r}) = \int d\mathbf{r}' \mathfrak{R}(\mathbf{r} - \mathbf{r}') g(\mathbf{r}') = [\mathfrak{R} * g](\mathbf{r}) \quad \longleftrightarrow \quad \tilde{f}(\mathbf{q}) = \tilde{\mathfrak{R}}(\mathbf{q}) \cdot \tilde{g}(\mathbf{q}). \quad (\text{A.34})$$

The different  $\mathbf{q}$ -modes do not mix in Fourier space. Analogous to eq. (A.33), we have

$$\mathfrak{R}(\mathbf{r}, \mathbf{r}') = \mathfrak{R}(\mathbf{r} - \mathbf{r}') \quad \longleftrightarrow \quad \tilde{\mathfrak{R}}(\mathbf{q}, \mathbf{q}') = \tilde{\mathfrak{R}}(\mathbf{q}) \delta(\mathbf{q} - \mathbf{q}'). \quad (\text{A.35})$$

**crystal symmetry:**  $\mathfrak{R}(\mathbf{r}, \mathbf{r}') = \mathfrak{R}(\mathbf{r} + \mathbf{R}'', \mathbf{r}' + \mathbf{R}'')$

A crystal is invariant under translations by any lattice vector  $\mathbf{R}''$ . By dividing the space into unit cells  $\Omega_{\mathbf{R}}$  at position  $\mathbf{R}$  and correspondingly the momentum  $\mathbf{q} = \mathbf{q}_r + \mathbf{G}$  in a reduced vector  $\mathbf{q}_r$  in the first Brillouin zone and a reciprocal lattice vector  $\mathbf{G}$ , one has

$$f(\mathbf{r} + \mathbf{R}) = \sum_{\mathbf{R}'} \int_{\Omega_0} d\mathbf{r}' \mathfrak{R}(\mathbf{r} + \mathbf{R}, \mathbf{r}' + \mathbf{R}') g(\mathbf{r}' + \mathbf{R}') \longleftrightarrow \tilde{f}(\mathbf{q}_r + \mathbf{G}) = \sum_{\mathbf{G}'} \tilde{\mathfrak{R}}(\mathbf{q}_r + \mathbf{G}, \mathbf{q}_r + \mathbf{G}') \tilde{g}(\mathbf{q}_r + \mathbf{G}'), \quad (\text{A.36})$$

which can be also written in matrix notation as

$$\begin{pmatrix} \tilde{f}_{\mathbf{G}} \end{pmatrix} = \begin{pmatrix} \tilde{\mathfrak{R}}_{\mathbf{G}\mathbf{G}'} \end{pmatrix} \begin{pmatrix} \tilde{g}_{\mathbf{G}'} \end{pmatrix}, \quad \tilde{\mathfrak{R}}_{\mathbf{G}\mathbf{G}'}(\mathbf{q}_r) \equiv \tilde{\mathfrak{R}}(\mathbf{q}_r + \mathbf{G}, \mathbf{q}_r + \mathbf{G}'). \quad (\text{A.37})$$

The reduced momentum  $\mathbf{q}_r$  is the *same* for  $\tilde{f}$  and  $\tilde{g}$ . In a system with crystal symmetry, only modes that differ by a reciprocal lattice vector  $\mathbf{G}$  are mixed which is taken into account by the matrix notation. The homogeneous system of eq. (A.34) is recovered if the matrix  $\tilde{\mathfrak{R}}(\mathbf{q}) = \tilde{\mathfrak{R}}_{\mathbf{G}\mathbf{G}'}(\mathbf{q}_r) \delta_{\mathbf{G}\mathbf{G}'}$  is diagonal.

### A.2.3 Symmetries of the Response Function

In general, any geometric transformation  $\{D; \boldsymbol{\tau}\}$  of the response function in real space with the rotation  $D$  and translation  $\boldsymbol{\tau}$

$$\{D; \boldsymbol{\tau}\} \mathfrak{R}(\mathbf{r}, \mathbf{r}') \equiv \mathfrak{R}(\{D; \boldsymbol{\tau}\}^{-1} \mathbf{r}, \{D; \boldsymbol{\tau}\}^{-1} \mathbf{r}'). \quad (\text{A.38})$$

is related with the following transformation in reciprocal space

$$\{D; \boldsymbol{\tau}\} \mathfrak{R}(\mathbf{q}, \mathbf{q}') \equiv \mathfrak{R}(D^{-1} \mathbf{q}, D^{-1} \mathbf{q}') e^{-i(\mathbf{q} - \mathbf{q}') \boldsymbol{\tau}}. \quad (\text{A.39})$$

## A.3 Discrete Fourier Series

### A.3.1 Born-van-Kármán Periodicity

In order to avoid mathematical problems with infinite systems and to allow a numerical treatment, one often introduces periodic boundary conditions within a large box  $V$ . These *Born-van-Kármán* boundary conditions apply to all (wave)functions of the system. The Fourier transform of a periodic one-particle function  $f(\mathbf{r})$  is given by the Fourier series:

$$f(\mathbf{r}) = \frac{1}{V} \sum_{\mathbf{q}} \tilde{f}(\mathbf{q}) e^{+i\mathbf{q}\mathbf{r}} \longleftrightarrow \tilde{f}(\mathbf{q}) = \int_V d\mathbf{r} f(\mathbf{r}) e^{-i\mathbf{q}\mathbf{r}}, \quad (\text{A.40})$$

where the  $\mathbf{q}$  vectors are now restricted to discrete values. Each component  $\alpha = 1, 2, 3$  is given by  $q_\alpha = (2\pi/L_\alpha)p_\alpha$ , where  $p_\alpha$  is a number and  $L_\alpha$  is the length of the box along direction  $\mathbf{e}_\alpha$ , leading to a volume  $V = L_1L_2L_3$ . In analogy to eq. (A.25), one has

$$\delta(\mathbf{r}) = \frac{1}{V} \sum_{\mathbf{q}} e^{+i\mathbf{q}\mathbf{r}}, \quad \delta_{\mathbf{q}\mathbf{q}'} = \frac{1}{V} \int_V d\mathbf{r} e^{-i(\mathbf{q}-\mathbf{q}')\mathbf{r}}, \quad (\text{A.41})$$

and we find for the response function  $\tilde{f}(\mathbf{q}) = \sum_{\mathbf{q}'} \tilde{\mathfrak{R}}(\mathbf{q}, \mathbf{q}')g(\mathbf{q}')$ :

$$\tilde{\mathfrak{R}}(\mathbf{q}\omega, \mathbf{q}'\omega') = \frac{1}{2\pi V} \int_V d\mathbf{r} dt \int_V d\mathbf{r}' dt' e^{+i(\omega t - \mathbf{q}\mathbf{r})} \mathfrak{R}(\mathbf{r}t, \mathbf{r}'t') e^{-i(\omega't' - \mathbf{q}'\mathbf{r}')}. \quad (\text{A.42})$$

### A.3.2 Real-Space Sampling

For a numerical treatment, we also have to discretise the real-space variable  $\mathbf{r}$  [e. g. 206]. Without loss of generality, we consider only the one-dimensional case. The periodic complex function  $f : [0, L) \rightarrow \mathbb{C}$  is numerically represented by  $N$  complex numbers  $f_i = f(z_i)$  at the sampling points  $z_i = i \cdot \Delta z$  for  $i = 0, 1, \dots, N-1$ . In the limit  $\Delta z \rightarrow 0$  we can approximate the integration in eq. (A.40) by the summation

$$\tilde{f}(q_p) \approx \Delta z \sum_i f_i e^{-iq_p z_i}, \quad q_p = p \cdot \frac{2\pi}{L}, \quad p = 0, \pm 1, \dots, \pm \lfloor \frac{N}{2} \rfloor. \quad (\text{A.43})$$

Note, that  $\tilde{f}(q_p)$  becomes periodic  $\tilde{f}(q_p) = \tilde{f}(q_p + 2\pi/\Delta z)$  in frequency  $q$  within this approximation. One can introduce the discrete Fourier transformation  $FT : \mathbb{C}^N \rightarrow \mathbb{C}^N$

$$f_i = \frac{1}{N} \sum_p \tilde{f}_p e^{+iq_p z_i} \quad \longleftrightarrow \quad \tilde{f}_p = FT f_i = \sum_i f_i e^{-iq_p z_i}, \quad (\text{A.44})$$

which is related to the continuous Fourier transform (A.40) by

$$f(z_i) = f(i \cdot \Delta z) = f_i, \quad \tilde{f}(q_p) = \tilde{f}(p \cdot \frac{2\pi}{L}) \approx \Delta z \tilde{f}_p. \quad (\text{A.45})$$

Analogous to the continuous case, we find for the two-particle function  $f_i = \sum_{i'} \mathfrak{R}_{ii'} g_{i'}$ :

$$\mathfrak{R}_{ii'} = \frac{1}{N} \sum_{qq'} e^{+iq_p z_i} \tilde{\mathfrak{R}}_{qq'} e^{-iq'_p z'_i} \quad \longleftrightarrow \quad \tilde{\mathfrak{R}}_{pp'} = \frac{1}{N} \sum_{ii'} e^{-iq_p z_i} \mathfrak{R}_{ii'} e^{+iq'_p z'_i}, \quad (\text{A.46})$$

$$\mathfrak{R}(z_i, z'_i) \approx \mathfrak{R}_{ii'} / \Delta z, \quad \tilde{\mathfrak{R}}(q_p, q'_p) \approx \tilde{\mathfrak{R}}_{pp'}. \quad (\text{A.47})$$

In a formally similar way, we obtain the discretisation for the delta distributions

$$\delta(z - z') \rightarrow \delta_{ii'} / \Delta z, \quad \delta(q - q') \rightarrow \delta_{pp'} \quad (\text{A.48})$$

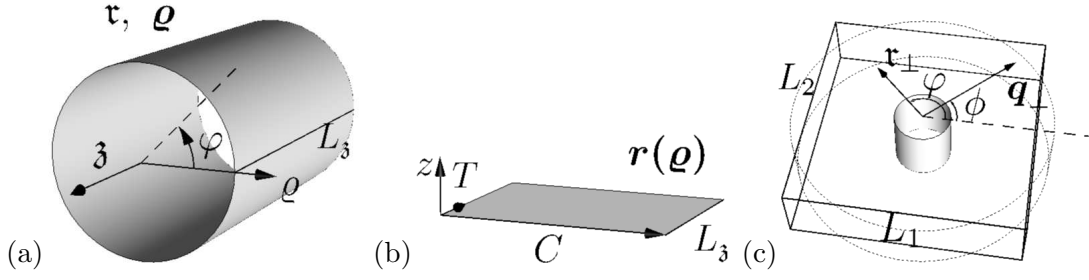


**Fig. A.1:** The geometry of the (a) cylinder and (b) the unrolled sheet (see also section 6.1). (c) Normalisation volume for the Fourier transform.

## A.4 Response in Cylindrical Systems

### A.4.1 Cylindrical Coordinates

Let  $\mathbf{r} = (x, y, z)$  be the position vector in the tube coordinate system (see fig. A.1a). In cylindrical coordinates  $\boldsymbol{\rho} \equiv (\rho, \varphi, z)$ , the volume element  $d^3\mathbf{r}$  and the delta function read

$$d^3\mathbf{r} = dx dy dz = \rho d\rho d\varphi dz \equiv \rho d\boldsymbol{\rho}, \quad \delta(\mathbf{r}) = \frac{1}{\rho} \delta(\rho) \delta(\varphi) \delta(z). \quad (\text{A.49})$$

### Fourier Transform in Cylindrical Coordinates

We use the following definition of the discrete Fourier transform of  $f(\rho, \varphi, z)$  in  $\varphi$  and  $z$ :

$$f(\boldsymbol{\rho}) = f(\rho, \varphi, z) = \frac{1}{2\pi L_z} \sum_{lp} \tilde{f}(lp; \rho) e^{+il\varphi} e^{+ipz}, \quad (\text{A.50})$$

$$\tilde{f}(\boldsymbol{\xi}; \rho) = \tilde{f}(lp; \rho) = \int_0^{2\pi} d\varphi \int_0^{L_z} dz f(\rho, \varphi, z) e^{-il\varphi} e^{-ipz}, \quad \boldsymbol{\xi} = (l, p)$$

in accordance with eq. (A.40). Analogously to eq. (A.31) we find for the response function

$$\tilde{f}(\boldsymbol{\xi}; \rho) = \sum_{\boldsymbol{\xi}'} \int d\rho' \rho' \tilde{\mathfrak{R}}(\boldsymbol{\xi}\boldsymbol{\xi}'; \rho\rho') \tilde{g}(\boldsymbol{\xi}'; \rho') \quad (\text{A.51})$$

$$\tilde{\mathfrak{R}}(\boldsymbol{\xi}\boldsymbol{\xi}'; \rho\rho') = \frac{1}{2\pi L_z} \int_0^{2\pi} d\varphi d\varphi' \int_0^{L_z} dz dz' e^{-i(l\varphi+pz)} \mathfrak{R}(\rho\rho') e^{+i(l'\varphi'+p'z')} \quad (\text{A.52})$$

### Relation with Cartesian Fourier Transform

In order to calculate the AR-EELS spectrum for a cylindrical system, we investigate the connection of  $\mathfrak{R}(\boldsymbol{\xi}\boldsymbol{\xi}'; \rho\rho')$  with the Fourier transform  $\mathfrak{R}(\mathbf{q}\mathbf{q}')$  in Cartesian coordinates. Starting from the definition (A.42) of the Fourier transform in a normalisation box of volume  $V_{\text{CNT}} = L_1 L_2 L_3$  (see fig. A.1c), we decompose the momentum  $\mathbf{q} = \mathbf{q}_\perp + q_\parallel \mathbf{e}_3$  in a

perpendicular and on-axis component and express all quantities in cylindrical coordinates

$$\tilde{\mathfrak{X}}(\mathbf{q}\mathbf{q}') = \frac{1}{V_{\text{CNT}} V_{\text{CNT}}} \iint d\boldsymbol{\varrho} d\boldsymbol{\varrho}' \varrho \varrho' e^{-i\mathbf{q}_{\perp} \cdot \mathbf{r}_{\perp} - i\mathbf{q}_{\parallel} \mathfrak{z}} \mathfrak{X}(\boldsymbol{\varrho}\boldsymbol{\varrho}') e^{+i\mathbf{q}'_{\perp} \cdot \mathbf{r}'_{\perp} + i\mathbf{q}'_{\parallel} \mathfrak{z}'}$$

If the normalisation box is large such that  $\mathfrak{X}(\boldsymbol{\varrho}, \boldsymbol{\varrho}')$  vanishes at the border of the supercell (no interaction between periodic replicas), we can replace the rectangular by a cylindrical normalisation box of the same volume  $\pi \mathcal{R}_{\text{max}}^2 L_3 = L_1 L_2 L_3$ . Expanding

$$e^{i\mathbf{q}_{\perp} \cdot \mathbf{r}_{\perp}} = e^{i q_{\perp} \varrho \cos(\varphi - \phi)} \stackrel{\text{(A.70)}}{=} \sum_l i^l J_l(q_{\perp} \varrho) e^{il(\varphi - \phi)}$$

we finally obtain with the Fourier transform in cylindrical coordinates (A.52)

$$\tilde{\mathfrak{X}}(\mathbf{q}\mathbf{q}') = \frac{2}{\mathcal{R}_{\text{max}}^2} \sum_{l, l'} \int_0^{\mathcal{R}_{\text{max}}} d\varrho d\varrho' \varrho \varrho' (-i)^l (i)^{l'} e^{+il\phi} e^{-il'\phi'} J_l(q_{\perp} \varrho) J_{l'}(q'_{\perp} \varrho') \tilde{\mathfrak{X}}(ll', q_{\parallel} q'_{\parallel}; \varrho \varrho'). \quad (\text{A.53})$$

#### A.4.2 Zone-Folding

Within the zone-folding approximation (ZF), we transfer the properties of an isolated graphene sheet to a cylinder. Formally, this can be expressed by a mapping  $\boldsymbol{\varrho} \rightarrow \mathbf{r}(\boldsymbol{\varrho})$  between cylinder and graphene coordinates (see fig. A.1a and b). For a scalar function, we have [note that  $\mathbf{r}(\boldsymbol{\varrho})$  and  $\mathbf{r}(\boldsymbol{\varrho})$  denote the position in the tube and sheet, respectively]

$$f_{\text{CNT}}(\boldsymbol{\varrho}) \stackrel{\text{ZF}}{=} f_s(\mathbf{r}(\boldsymbol{\varrho})), \quad \mathbf{r}(\boldsymbol{\varrho}) = (x, y, z) = \frac{\varphi}{2\pi} \mathbf{C} + \frac{\mathfrak{z}}{T} \mathbf{T} + (\varrho - \mathcal{R}) \mathbf{e}_z, \quad (\text{A.54})$$

where  $f_s(\mathbf{r})$  is a scalar function for the sheet in Cartesian coordinates and  $f_{\text{CNT}}(\boldsymbol{\varrho})$  the corresponding scalar function of the tube in cylindrical coordinates. Of course, the sheet function has to be periodic  $f_s(\mathbf{r}) = f_s(\mathbf{r} + \mathbf{C})$  along the circumference and sufficiently localised perpendicular to the sheet, i. e.,  $f_s(\mathbf{r}) \neq 0$  only for  $|z| < z_c \ll \mathcal{R}$ . In contrast to eq. (A.49), the volume element in the coordinate system of the sheet is given by

$$d^3 \mathbf{r} = dx dy dz = \mathcal{R} d\varrho d\varphi d\mathfrak{z} = \mathcal{R} d\boldsymbol{\varrho}. \quad (\text{A.55})$$

This follows directly from the transformation in eq. (A.54) if we choose the  $x$ -axis of the sheet along  $\mathbf{C}$ . Then we have  $\frac{\partial x}{\partial \varphi} = \frac{C}{2\pi} = \mathcal{R}$ ,  $\frac{\partial y}{\partial \mathfrak{z}} = 1$ , and  $\frac{\partial z}{\partial \varrho} = 1$ .

#### Zone-Folding in Reciprocal Space

As in section 5.4, we perform a 2D-Fourier transform only for the in-plane quantities  $\bar{\mathbf{r}} = \bar{\mathbf{r}}(\varphi, \mathfrak{z}) = \frac{\varphi}{2\pi} \mathbf{C} + \frac{\mathfrak{z}}{T} \mathbf{T}$ . With the area  $A_s = 2\pi L_3 \mathcal{R}$  of the unrolled sheet, we find

$$\tilde{f}_s(\bar{\mathbf{q}}; z) = \int_{A_s} d\bar{\mathbf{r}} f_s(\bar{\mathbf{r}}, z) e^{-i\bar{\mathbf{q}} \cdot \bar{\mathbf{r}}} \stackrel{\text{(A.55)}}{=} \int_0^{2\pi} d\varphi \int_0^{L_3} d\mathfrak{z} \mathcal{R} f_s(\bar{\mathbf{r}}(\varphi, \mathfrak{z}), z) e^{-i\bar{\mathbf{q}} \cdot \bar{\mathbf{r}}(\varphi, \mathfrak{z})} \quad (\text{A.56})$$

With the definitions (see section 6.1)

$$l \equiv \mathbf{C} \cdot \bar{\mathbf{q}} / (2\pi), \quad p \equiv \bar{\mathbf{q}} \cdot \mathbf{T} / T, \quad \bar{\mathbf{q}} = 2\pi l \mathbf{C} / C^2 + p \mathbf{T} / T, \quad \varrho = z + \mathcal{R}, \quad (\text{A.57})$$

we have  $e^{-i\bar{\mathbf{q}}\mathbf{r}(\varphi, \delta)} = e^{-i(l\varphi + p\delta)}$ . A comparison of eq. (A.50) and (A.56) leads us to

$$\mathcal{R} \tilde{f}_{\text{CNT}}(\boldsymbol{\xi}; \varrho) \stackrel{\text{ZF}}{=} \tilde{f}_s(\bar{\mathbf{q}}; z), \quad \boldsymbol{\xi} = (l, p). \quad (\text{A.58})$$

### Zone-Folding for the Response Function

What does this mean for the response function  $\mathfrak{R}_{\text{CNT}}(\boldsymbol{\varrho}\boldsymbol{\varrho}')$ ? In real space, we have

$$f_{\text{CNT}}(\boldsymbol{\varrho}) \stackrel{\text{ZF}}{=} f_s(\mathbf{r}) = \int_V d\mathbf{r}' \mathfrak{R}_s(\mathbf{r}, \mathbf{r}') g_s(\mathbf{r}') \stackrel{(\text{A.55})}{=} \int_V d\boldsymbol{\varrho}' \mathcal{R} \mathfrak{R}_s(\mathbf{r}(\boldsymbol{\varrho}), \mathbf{r}(\boldsymbol{\varrho}')) g_{\text{CNT}}(\boldsymbol{\varrho}')$$

and thus by comparison with the definition of the response function of the tube

$$\boldsymbol{\varrho}' \mathfrak{R}_{\text{CNT}}(\boldsymbol{\varrho}\boldsymbol{\varrho}') \stackrel{\text{ZF}}{=} \mathcal{R} \mathfrak{R}_s(\mathbf{r}(\boldsymbol{\varrho}), \mathbf{r}(\boldsymbol{\varrho}')). \quad (\text{A.59})$$

Analogously, we obtain from eq (A.58) in reciprocal space

$$\begin{aligned} \mathcal{R} \tilde{f}_{\text{CNT}}(\boldsymbol{\xi}; \varrho) = \tilde{f}_s(\bar{\mathbf{q}}; z) &= \sum_{\bar{\mathbf{q}}'} \int_{-z_c}^{z_c} dz' \tilde{\mathfrak{R}}_s(\bar{\mathbf{q}}\bar{\mathbf{q}}'; zz') \tilde{g}_s(\bar{\mathbf{q}}'; z') \\ &= \sum_{\boldsymbol{\xi}'} \int_{\mathcal{R}-z_c}^{\mathcal{R}+z_c} d\boldsymbol{\varrho}' \mathcal{R} \tilde{\mathfrak{R}}_s(\bar{\mathbf{q}}(\boldsymbol{\xi})\bar{\mathbf{q}}(\boldsymbol{\xi}'); z(\boldsymbol{\varrho})z(\boldsymbol{\varrho}')) \tilde{g}_{\text{CNT}}(\boldsymbol{\xi}'; \boldsymbol{\varrho}') \end{aligned}$$

and thus by comparison with eq. (A.51)

$$\boldsymbol{\varrho}' \tilde{\mathfrak{R}}_{\text{CNT}}(\boldsymbol{\xi}\boldsymbol{\xi}'; \boldsymbol{\varrho}\boldsymbol{\varrho}') \stackrel{\text{ZF}}{=} \tilde{\mathfrak{R}}_s(\bar{\mathbf{q}}\bar{\mathbf{q}}'; zz'). \quad (\text{A.60})$$

Equivalently, we can arrive at this equation by a Fourier transform of eq. (A.59). The factor  $\mathcal{R}$  on the right-hand side is then compensated by the different normalisation areas  $A_s = 2\pi L_3 \mathcal{R}$  and  $A_{\text{CNT}} = 2\pi L_3$  in the Fourier transformations of the sheet and the tube.

As in the case of scalar functions, the zone-folding approach is limited to response functions that are periodic  $\mathfrak{R}_s(\mathbf{r}\mathbf{r}') = \mathfrak{R}_s(\mathbf{r} + \mathbf{C}, \mathbf{r}' + \mathbf{C})$  and local in perpendicular direction, i. e.,  $\mathfrak{R}_s(\mathbf{r}\mathbf{r}') = 0$  if  $|z| > z_c$  or  $|z'| > z_c$ . The model is applicable for the polarisability  $\pi_{\text{CNT}}$  of large tubes  $\mathcal{R} \gg z_c$ .

### Symmetry Considerations

Due to the crystal symmetry in the graphene sheet, the Fourier transform  $\tilde{\mathfrak{R}}_s(\bar{\mathbf{q}}\bar{\mathbf{q}}'; zz')$  is only non-zero if the Bragg condition  $\bar{\mathbf{q}} - \bar{\mathbf{q}}' = \bar{\mathbf{G}}$  is fulfilled [see eq. (A.36)]. By virtue of eq. (A.60) and (A.57) this must also hold for the cylinder response function:

$$\tilde{\mathfrak{R}}_{\text{CNT}}(ll', pp'; \boldsymbol{\varrho}\boldsymbol{\varrho}') \neq 0 \quad \iff \quad \exists \bar{\mathbf{G}} : \frac{2\pi}{C^2}(l - l')\mathbf{C} + \frac{2\pi}{T^2}(p - p')\mathbf{T} = \bar{\mathbf{G}}, \quad (\text{A.61})$$

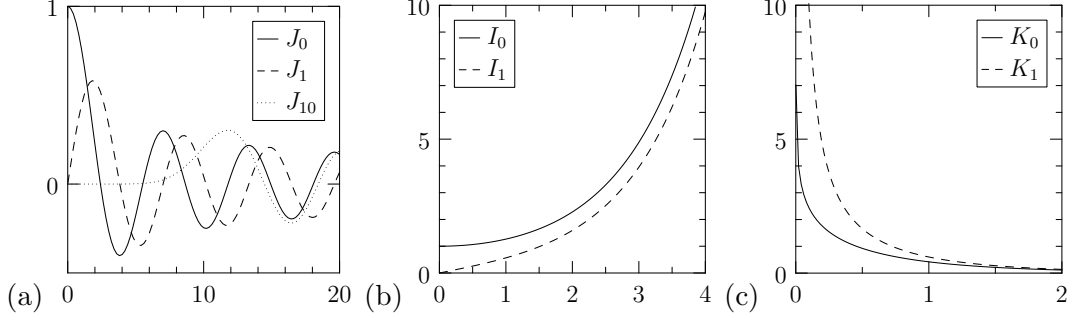


**Fig. A.2:** Behaviour of the (modified) Bessel functions (a)  $J_n(x)$ , (b)  $I_n(x)$ , and (c)  $K_n(x)$ .

Multiplying the reciprocal lattice vector  $\bar{\mathbf{G}}$  of graphene with  $N\mathbf{S} = \mathbf{C} - M\mathbf{T}$ , we find

$$(l - l') - M(p - p') = N\mathbf{S}\bar{\mathbf{G}}/(2\pi) = Nj, \quad j \in \mathbb{N}, \quad (\text{A.62})$$

where  $\mathbf{S}$  denotes the symmetry vector (6.2),  $N = 2(n^2 + m^2 + nm)/d_R$  is the number of graphene unit cells in the tube cell, and  $M = m\bar{p} - n\bar{q}$  is the number of primitive translations  $\mathbf{T}$  in  $N\mathbf{S}$  [4]. Two important conclusions follow from this equation:

- The difference  $l - l'$  must be a multiple of  $d = \text{gcd}(N, M)$  which corresponds to the number of pure rotations  $C_d$  present in the tube (see table 6.1). For chiral tubes, we find  $d = \text{gcd}(n, m)$  and for achiral tubes ( $m = n$  or  $m = 0$ ) we have  $d = n$ .
- For  $p = p'$ , the difference  $l - l'$  must be a multiple of  $N$ . Thus, expression (6.21) is largely simplified and  $i^{(l-l')} = \pm 1$  must be always real ( $N$  is an even number).

Additionally to the pure rotations, we can make use of the two-fold rotation axis perpendicular to the tube. If we choose the  $\mathbf{x}$ -axis along this rotation axis, the system remains unchanged under the transformation  $(\varrho, \varphi, \mathfrak{z}) \rightarrow (\varrho, -\varphi, -\mathfrak{z})$ . In reciprocal space we thus have [see eq. (A.39)]

$$\tilde{\mathfrak{R}}_{\text{CNT}}(ll', pp'; \varrho\varrho', \omega) = \tilde{\mathfrak{R}}_{\text{CNT}}(-l-l', -p-p'; \varrho\varrho', \omega). \quad (\text{A.63})$$

### A.4.3 Bessel Functions

Rewriting the Laplace equation  $\Delta\Phi(\mathbf{r}) = 0$  in cylindrical coordinates, the radial part takes the form of a Bessel differential equation which reads in standard form as [e.g. 11]

$$z^2\partial_z^2 w + z\partial_z w + (z^2 - \nu^2)w = 0, \quad w = w(z), \quad z \in \mathbb{C}, \quad \nu \in \mathbb{R}. \quad (\text{A.64})$$

The solutions are called *Bessel functions* of the first kind  $J_\nu(z)$ . Due to the symmetry

$$J_\nu(-z) = (-1)^\nu J_\nu(z), \quad J_{-n}(z) = (-1)^n J_n(z), \quad n \in \mathbb{Z}, \quad (\text{A.65})$$

the two solutions  $J_\nu$  and  $J_{-\nu}$  are independent only for non-integer  $\nu$ <sup>1</sup>. The Bessel functions show a damped oscillatory behaviour for  $|z| \gg 1$  (see figure A.2a). Their exact asymptotic behaviour is given by [207]:

$$J_\nu(z) \xrightarrow{|z| \rightarrow 0} \frac{1}{\Gamma(\nu + 1)} \left(\frac{z}{2}\right)^\nu + \mathcal{O}(z^{\nu+2}) \quad (\text{A.66})$$

$$J_\nu(z) \xrightarrow{|z| \rightarrow \infty} \sqrt{2/(\pi z)} \cos\left(z - \frac{1}{4}\pi - \frac{1}{2}\nu\pi\right) + \mathcal{O}\left(|z|^{-1}\right), \quad \text{if } |\arg z| < \pi. \quad (\text{A.67})$$

For real arguments  $J_\nu(x)$ , the crossover between these two behaviours is approximately found at  $x \approx \nu$ . For smaller  $x < \nu - 1$ , the Bessel function  $J_\nu(x)$  is essentially zero. It takes its global maximum at  $\bar{x}_\nu$  which is found at values slightly larger than  $\nu$ , e. g.,  $\bar{x}_0 = 0$ ,  $\bar{x}_1 = 1.8$ ,  $\bar{x}_2 = 3.1$ ,  $\bar{x}_3 = 4.2$ ,  $\bar{x}_4 = 5.3$ ,  $\bar{x}_5 = 6.4$ ,  $\bar{x}_{10} = 11.8$ . And finally, the Bessel function  $J_\nu(x)$  starts to oscillate with a period of  $2\pi$  for  $x \gg \nu$ .

The *modified Bessel functions*  $I_\nu(z)$  and  $K_\nu(z)$  are linear independent solutions of

$$z^2 \partial_z^2 w + z \partial_z w - (z^2 + \nu^2)w = 0, \quad w = w(z), \quad z \in \mathbb{C}, \quad \nu \in \mathbb{R}. \quad (\text{A.68})$$

Both are symmetric in the index  $\nu$

$$K_{-\nu}(z) = K_\nu(z), \quad I_{-n}(z) = I_n(z), \quad n \in \mathbb{Z}, \quad (\text{A.69})$$

and have an opposite asymptotic behaviour. For small  $|z| \ll 1$ ,  $I_{\nu>0}(z) \rightarrow 0$  vanishes and  $I_0(z) \rightarrow 1$ , while the function  $K_\nu$  diverges. At large  $|z| \gg 1$ ,  $I_\nu(z)$  diverges exponentially, and  $K_\nu(z)$  vanishes exponentially (see fig. A.2b and c).

#### A.4.4 Expansions in terms of Bessel Functions

Using Bessel functions, any plane wave can be expressed in cylindrical coordinates [207]

$$e^{i\mathbf{k} \cdot \mathbf{r}} = e^{ik\rho \cos \varphi} = \sum_{m=-\infty}^{\infty} i^m J_m(k\rho) e^{im\varphi}. \quad (\text{A.70})$$

This equation is known as the Jacobi-Anger expansion. The modified Bessel functions appear in the expansion of the Green function (Coulomb potential) [11, p. 118]

$$\frac{1}{|\mathbf{r} - \mathbf{r}'|} = \frac{1}{\pi} \sum_{m=-\infty}^{\infty} \int_{-\infty}^{\infty} dk e^{im(\varphi - \varphi')} e^{ik(z - z')} I_m(|k|\varrho_<) K_m(|k|\varrho_>) \quad (\text{A.71})$$

$$= \frac{1}{2} \sum_{m=-\infty}^{\infty} \int_{-\infty}^{\infty} dk e^{im(\varphi - \varphi')} e^{-|k||z - z'|} J_m(|k|\varrho) J_m(|k|\varrho'), \quad (\text{A.72})$$

where  $\varrho_< = \min\{\varrho, \varrho'\}$  and  $\varrho_> = \max\{\varrho, \varrho'\}$  denote the smaller and larger radius.

---

<sup>1</sup>Another linear independent solution is given by the Neumann function.

#### A.4.5 Coulomb Potential of the CNT

The Coulomb potential in cylindrical coordinates can be derived by expanding  $\frac{e^2}{4\pi\epsilon_0} \frac{1}{|\mathbf{r}-\mathbf{r}'|}$  in terms of the modified Bessel functions  $K_l$  and  $I_l$  [see eq. (A.71)] and performing the Fourier transform in  $\varphi$  and  $z$  [see eq. (A.50)]

$$v(lp, l'p'; \varrho_1 \varrho_2) = v(lp; \varrho_1 \varrho_2) \delta_{ll'} \delta_{pp'}, \quad v(lp; \varrho_1 \varrho_2) = \frac{e^2}{\epsilon_0} I_l(|p|\varrho_<) K_l(|p|\varrho_>). \quad (\text{A.73})$$

The Graphene limit is obtained, if we let the radius  $\mathcal{R} \rightarrow \infty$  while  $\varrho_1 = \mathcal{R} + d_1$  and  $\varrho_2 = \mathcal{R} + d_2$  with fixed  $d_1 < 0$  and  $d_2 > 0$ . For  $l = 0$ , one has

$$I_0(|p''|\varrho_1) K_0(|p''|\varrho_2) \xrightarrow{\mathcal{R} \rightarrow \infty} \frac{1}{2|p''|\mathcal{R}} e^{-|p''||d_1-d_2|}, \quad (\text{A.74})$$

which becomes the same as  $v_{2D}/\mathcal{R}$ .

To check the consistency of our equations, we formally rederive the Fourier representation of the Coulomb potential  $v(\mathbf{q}) = \frac{e^2}{\epsilon_0 q^2}$  by applying eq. (A.53). Switching to a continuous Fourier transform, i. e., letting  $\mathcal{R}_{\max} \rightarrow \infty$  and  $\pi \mathcal{R}_{\max}^2 = V \rightarrow (2\pi)^2$ , we have

$$v(\mathbf{q}\mathbf{q}') = \frac{e^2}{\epsilon_0} \frac{\delta_{pp'}}{2\pi} \sum_l \iint_0^\infty d\varrho d\varrho' \varrho \varrho' e^{+il(\phi-\phi')} J_l(\bar{q}\varrho) J_l(\bar{q}'\varrho') v(lp; \varrho\varrho'). \quad (\text{A.75})$$

Considering only the integration in  $\varrho$ , the integrand is known to decay exponentially if the on-axis momentum  $p$  does not vanish. One finds for  $\bar{q} > 0$  and  $|p| > 0$

$$\int_0^{\mathcal{R}_{\max}} d\varrho \varrho J_l(\bar{q}\varrho) I_l(|p|\varrho_<) K_l(|p|\varrho_>) \xrightarrow[\varrho' \text{ fixed}]{\mathcal{R}_{\max} \rightarrow \infty} \frac{1}{\bar{q}^2 + p^2} J_l(\bar{q}\varrho') \quad (\text{A.76})$$

and thus

$$v(\mathbf{q}\mathbf{q}') = \frac{e^2}{\epsilon_0} \frac{\delta_{pp'}}{\bar{q}^2 + p^2} \frac{1}{2\pi} \sum_l e^{+il(\phi-\phi')} \int_0^\infty d\varrho' \varrho' J_l(\bar{q}\varrho') J_l(\bar{q}'\varrho') \quad (\text{A.77})$$

$$= \frac{e^2}{\epsilon_0} \frac{1}{q^2} \delta_{pp'} \delta(\phi - \phi') \frac{1}{\bar{q}} \delta(\bar{q} - \bar{q}') = \frac{e^2}{\epsilon_0 q^2} \delta_{pp'} \delta^{(2)}(\bar{\mathbf{q}} - \bar{\mathbf{q}}'), \quad (\text{A.78})$$

where we have used eq. (A.41) and the orthogonality relation for the Bessel functions [11]

$$\frac{\delta(k - k')}{k} = \int_0^\infty d\varrho \varrho J_n(k\varrho) J_n(k'\varrho). \quad (\text{A.79})$$

## A.5 Algebra of the Dielectric Matrix

### A.5.1 Block inversion

The  $n \times n$ -matrix  $M$  and its inverse  $M^{-1}$  shall be both divided into four block matrices

$$M = \begin{pmatrix} P & Q \\ R & S \end{pmatrix}, \quad M^{-1} = \begin{pmatrix} A & B \\ C & D \end{pmatrix} \quad (\text{A.80})$$

The separated blocks are then related with each other as

$$A = (P - QS^{-1}R)^{-1}, \quad (\text{A.81})$$

$$B = -A(QS^{-1}), \quad C = -(S^{-1}R)A, \quad (\text{A.82})$$

$$D = S^{-1} + (S^{-1}R)A(QS^{-1}), \quad (\text{A.83})$$

which follows from the definition  $MM^{-1} = \hat{1}$ . For block diagonal matrices ( $Q = R = 0$ ), we have  $A = P^{-1}$ .

# B Microscopic Dielectric Theory

In the following, we consider the excitation of a crystal by external fields within the framework of a semi-classical dielectric theory. The external perturbation is treated in a purely classical way, while the material is described by a response function that has to be determined from a quantum-mechanical calculation. We will discuss (1) the role of longitudinal and transverse components (2) the ambiguity of the definition of the microscopic dielectric function for large momentum transfers  $\mathbf{q} > 0$ . (3) the relation between microscopic and macroscopic quantities.

## B.1 Dielectric Theory

### B.1.1 Microscopic Maxwell Equations

The microscopic Maxwell equations (MW) read in SI-notation<sup>1</sup> [208]:

$$\boxed{\begin{array}{ll} (i) & \nabla \cdot \mathbf{B} = 0 \\ (iii) & \nabla \times \mathbf{E} + \partial_t \mathbf{B} = 0 \end{array} \quad \begin{array}{ll} (ii) & \nabla \times \mathbf{B} - \frac{1}{c^2} \partial_t \mathbf{E} = \mu_0 \mathbf{j} \\ (iv) & \nabla \cdot \mathbf{E} = \rho / \varepsilon_0 \end{array}} \quad (\text{B.1})$$

The microscopic electric field  $\mathbf{E}$  and magnetic field  $\mathbf{B}$  are generated by the charge and current densities  $\rho$  and  $\mathbf{j}$ , respectively. They are intimately connected by the *continuity equation* (in real and reciprocal space, see appendix A.2):

$$\nabla \cdot \mathbf{j} + \partial_t \rho = 0, \quad \longleftrightarrow \quad \mathbf{q} \cdot \mathbf{j} = \omega \rho. \quad (\text{B.2})$$

Note that all quantities are to be understood as being statistical averages of the corresponding quantum mechanical operators, i. e.,  $\mathbf{E} = \text{Sp}\{\hat{\rho} \hat{\mathbf{E}}\}$  [121].

### Potentials

The homogeneous equations (i) and (iii) are automatically fulfilled by introducing the potentials  $\mathbf{B} = \nabla \times \mathbf{A}$  and  $\mathbf{E} = -\nabla \varphi - \partial_t \mathbf{A}$ . Using the *Coulomb-gauge* ( $\nabla \cdot \mathbf{A} = 0$ ), the inhomogeneous Maxwell equations (ii) and (iv) can be written as

$$\square \mathbf{A} = \mu_0 \mathbf{j}_T, \quad \Delta \varphi = -\frac{1}{\varepsilon_0} \rho, \quad \square \equiv \left( \frac{1}{c^2} \partial_t^2 - \Delta \right). \quad (\text{B.3})$$

Here, the current density  $\mathbf{j}$  has been separated into a transverse part  $\mathbf{q} \cdot \mathbf{j}_T = 0$  and a longitudinal part  $\mathbf{q} \times \mathbf{j}_L = \mathbf{0}$  that is related to the density  $\mathbf{q} \cdot \mathbf{j}_L = \omega \rho$  by eq. (B.2).

<sup>1</sup>Using CGS-notation, one has to replace  $\varepsilon_0 = \frac{1}{4\pi}$  and  $\mu_0 = \frac{4\pi}{c^2}$  in any of the following equations.

## Wave Equation

Eliminating  $\mathbf{B}$  in the Maxwell eq. (B.1,ii), one arrives at the *wave equation* which directly links the electric field  $\mathbf{E}$  to its sources  $\mathbf{j}$

$$\nabla \times (\nabla \times \mathbf{E}) + \left(\frac{1}{c}\partial_t\right)^2 \mathbf{E} = -\mu_0 \partial_t \mathbf{j}. \quad (\text{B.4})$$

The inversion of this equation by means of the Greens function operator  $\mathcal{O}^{-1}$  gives

$$\mathbf{E} = -\mu_0 \mathcal{O}^{-1} \partial_t \mathbf{j}, \quad \mathcal{O} \equiv \nabla \times (\nabla \times \cdot) + \left(\frac{1}{c}\partial_t\right)^2. \quad (\text{B.5})$$

## Separation of Charges

In order to describe the interaction of charged particles or electromagnetic radiation with a solid, one should start from Maxwell equations that include all internal and external sources. The static charge density  $\rho^0$  accounts for all electrons and nuclei of the unperturbed solid in the ground state. When *external* sources  $\rho^e$  are added to the system, the (internal) *total* charge density  $\rho^t = \rho - \rho^e$  will differ from  $\rho^0$  by the *induced* charges  $\rho^i$ , i.e.,  $\rho = \rho^0 + \rho^e + \rho^i$ . The current density  $\mathbf{j}$  and the fields  $\mathbf{E}$  and  $\mathbf{B}$  are split up analogously. Because of linearity, the Maxwell equations (B.1) and the continuity equation (B.2) will hold for each of the subsystems. Therefore, one can separate the static charge density  $\rho^0$  from the problem and consider Maxwell equations that contain only the changes  $\rho^t$  due to the perturbation [51]. Further,  $\rho^t = \rho^e + \rho^i$  is divided into external and internal charges by assuming that a clear distinction is possible at any time. This excludes, e.g., exchange and correlation effects between the external electrons and the electrons inside the solid (test-particle case).

### B.1.2 Response Functions

To close the set of equations (B.1), one still needs a so called *material equation* relating the induced current  $\mathbf{j}^i$  with the external one  $\mathbf{j}^e$ . In most cases, the perturbation is small and we can restrict ourselves to a *linear* relation. The most general linear relation between two fields is given by:

$$F_\alpha^i(\mathbf{r}t) = \int d\mathbf{r}' \int dt' \mathfrak{R}^{\alpha\beta}(\mathbf{r}, \mathbf{r}'; t - t') F_\beta^e(\mathbf{r}'t'), \quad \text{or shorter: } \mathbf{F}^i = \mathfrak{R} \mathbf{F}^e. \quad (\text{B.6})$$

Of course, the linear operator  $\mathfrak{R}$  has to be homogeneous in time (see appendix A.2.2). Several relations are used in literature [209]

$$\begin{aligned} (a) \quad & \text{internal conductivity } \sigma : & \mathbf{j}^i &= \sigma \mathbf{E}^t \\ (b) \quad & \text{external conductivity } \sigma^e : & \mathbf{j}^i &= \sigma^e \mathbf{E}^e \\ (c) \quad & \text{polarisability } \pi : & \partial_t \mathbf{j}^i &= \pi \mathbf{E}^t \\ (d) \quad & \text{susceptibility } \chi : & \partial_t \mathbf{j}^i &= \chi \mathbf{E}^e \\ (e) \quad & \text{micr. dielectric function } \varepsilon : & \mathbf{E}^e &= \varepsilon \mathbf{E}^t \end{aligned} \quad (\text{B.7})$$

and only one of these is necessary to close the Maxwell eq. (B.1). Of course the different functions are intimately related with each other. But there are several differences [121]:

First, only (b) and (d) should be called *response function*, because they are the only quantities that describe the response to an *external* field which can be varied arbitrarily. Only in this case, Kramers-Kronig relations and sum rules strictly hold. The other quantities, which will be called *generalised response functions* for clarity, may obey such relations only in certain limits (e. g., for long wavelength  $q \rightarrow 0$ ).

Second, several definitions for the microscopic dielectric function are used in literature, which are the same in the optical limit  $\mathbf{q} \rightarrow \mathbf{0}$  but differ for non-zero momentum transfers. We will consider this point in detail in section B.2.

### B.1.3 Longitudinal and Transverse Fields

Due to the structure of the Maxwell equations, it is useful to separate all fields into a irrotational (curl-free) and solenoidal (divergence-free) component. For plane waves, this corresponds to a polarisation parallel (e.g., plasmons) or perpendicular (e.g., photons) to the direction of propagation, respectively. By introducing the following projectors [51]

$$\begin{aligned} P_L &= \frac{\mathbf{q}(\mathbf{q})}{q^2} = \frac{q_\alpha q_\beta}{q^2}, & P_T &= -\frac{\mathbf{q} \times (\mathbf{q} \times \cdot)}{q^2} = \delta_{\alpha\beta} - \frac{q_\alpha q_\beta}{q^2}, \\ P_L^2 &= P_L, & P_T^2 &= P_T, & P_L P_T &= 0 = P_T P_L, & P_L + P_T &= \hat{1}, \end{aligned} \quad (\text{B.8})$$

any vector field can be divided into its longitudinal (curl-free) and transverse (divergence-free) components. For example, one has in Fourier space,

$$\mathbf{E}(\mathbf{q}) = (P_L + P_T)\mathbf{E} = \mathbf{E}_L + \mathbf{E}_T = \frac{1}{q^2}\mathbf{q}(\mathbf{E} \cdot \mathbf{q}) - \frac{1}{q^2}\mathbf{q} \times (\mathbf{q} \times \mathbf{E}).$$

Using the Coulomb gauge, the Maxwell equations (B.1) can be separated, too. Indeed, the vector potential  $\mathbf{A}$  determines exactly the transverse components, and the scalar potential  $\varphi$  the longitudinal components of the  $\mathbf{E}$  and  $\mathbf{B}$  fields.

### Longitudinal and Transverse Green-Function

Accordingly, the operators  $\mathcal{O}$  and  $\mathcal{O}^{-1}$  can be Fourier transformed

$$\mathcal{O}(\mathbf{r}t) = \nabla \times (\nabla \times \cdot) + \left(\frac{1}{c}\partial_t\right)^2 \quad \longleftrightarrow \quad \mathcal{O}(\mathbf{q}\omega) = q^2 P_T - \frac{\omega^2}{c^2} \hat{1},$$

and divided into their longitudinal and transverse components (see [209, 210]):

$$\mathcal{O}(\mathbf{q}\omega) = -\frac{\omega^2}{c^2} P_L - \frac{\omega^2 - c^2 q^2}{c^2} P_T, \quad \mathcal{O}^{-1}(\mathbf{q}\omega) = -\frac{c^2}{\omega^2} \left[ P_L + \frac{1}{1 - (q/q_0)^2} P_T \right]. \quad (\text{B.9})$$

Here,  $q_0 \equiv \omega/c$  is the wave vector of light with frequency  $\omega$  in vacuum. One can now distinguish three cases:

- $\mathbf{q} \gg \mathbf{q}_0$  :  $\mathcal{O}^{-1} \approx \mathcal{O}_L^{-1}$ . The transverse component is negligible. In particular, this holds for all microscopic fields in crystals with wave vectors  $\mathbf{q} = \mathbf{k} + \mathbf{G}$  outside the first Brillouin zone (like crystal local fields).

- $\mathbf{q} \ll \mathbf{q}_0$  : Both, the longitudinal, and the transverse part are important.
- $\mathbf{q} \approx \mathbf{q}_0$  :  $\mathcal{O}^{-1} \approx \mathcal{O}_T^{-1}$ . The transverse component diverges for  $q = q_0$ . In this case, modes with wave vector  $\mathbf{q}$  obey the dispersion law of light in vacuum and can escape from the solid (Čerenkov radiation).

### B.1.4 Macroscopic Maxwell Equations

In the optical limit, i. e., when the wavelength  $\lambda$  of the perturbation is much larger than the size of the unit cell  $a$ , one usually introduces the phenomenological macroscopic Maxwell equations. Microscopic effects like the crystal local-field effects are then incorporated into the macroscopic dielectric function and need careful consideration.

#### Spatial Averages

The macroscopic Maxwell equations are usually derived from the microscopic Maxwell equations (B.1) by averaging all microscopic quantities within a mesoscopic volume  $\lambda^3 \gg V \gg a^3$  using a convolution with any function  $\phi$  that vanishes outside of  $V$  [11, 211]:

$$\langle F \rangle(\mathbf{r}, t) \equiv \phi(\mathbf{r}) * F(\mathbf{r}, t) = \int d\mathbf{r}' \phi(\mathbf{r} - \mathbf{r}') F(\mathbf{r}', t). \quad (\text{B.10})$$

Bound charges  $\rho^b$ , that stay within a microscopic volume  $a^3$  in spite of the external perturbation, do not contribute to the averaged total charge density  $\langle \rho^t \rangle$ . However, as they can act as microscopic electric and magnetic dipoles, they give rise to a macroscopic polarisation  $\langle \mathbf{P} \rangle$  and magnetisation  $\langle \mathbf{M} \rangle^2$ ,

$$-\nabla \cdot \langle \mathbf{P} \rangle = \langle \rho^b \rangle, \quad \nabla \times \langle \mathbf{M} \rangle + \partial_t \langle \mathbf{P} \rangle = \langle \mathbf{j}^b \rangle. \quad (\text{B.11})$$

An example for bound charges might be the core electrons of the atoms. Free charges  $\rho^f$  instead which can move inside the crystal, like the conduction electrons of a metal, are retained in the macroscopic Maxwell equations which finally read [208]

(i)	$\nabla \cdot \langle \mathbf{B} \rangle = 0$	(ii)	$\nabla \times \langle \mathbf{H} \rangle - \partial_t \langle \mathbf{D} \rangle = \langle \mathbf{j}^e \rangle + \langle \mathbf{j}^f \rangle$	(B.12)
(iii)	$\nabla \times \langle \mathbf{E} \rangle + \partial_t \langle \mathbf{B} \rangle = 0$	(iv)	$\nabla \cdot \langle \mathbf{D} \rangle = \langle \rho^e \rangle + \langle \rho^f \rangle$	
$\langle \mathbf{H} \rangle = \frac{1}{\mu_0} \langle \mathbf{B} \rangle - \langle \mathbf{M} \rangle,$		$\langle \mathbf{D} \rangle = \epsilon_0 \langle \mathbf{E} \rangle + \langle \mathbf{P} \rangle.$		

#### Macroscopic Dielectric Function

The *macroscopic dielectric function*  $\epsilon_M$  is then defined as  $\langle \mathbf{D} \rangle = \epsilon_0 \epsilon_M \langle \mathbf{E} \rangle$ , i. e.,

$$\langle D_\alpha \rangle(\mathbf{r}, t) = \int d\mathbf{r}' \int dt' \epsilon_0 \epsilon_M^{\alpha\beta}(\mathbf{r} - \mathbf{r}', t - t') \langle E_\beta \rangle(\mathbf{r}', t'). \quad (\text{B.13})$$

<sup>2</sup>  $\mathbf{P}$  and  $\mathbf{M}$  are introduced as the sum over all microscopic dipoles  $\mathbf{p}_n$  and  $\mathbf{m}_n$ , i. e.  $\mathbf{P} = \sum_n \mathbf{p}_n \delta(\mathbf{r} - \mathbf{r}_n)$ .

As the averaged crystal is homogeneous in space, the dielectric function only depends on the distance  $\mathbf{r} - \mathbf{r}'$  [see eq. (A.35)]. In most cases, the response is very localised, i. e., a perturbation at  $\mathbf{r}'$  will only affect points  $\mathbf{r}$  at a distance that is very small compared to the wavelength  $\lambda$  of the excitation. The Fourier transform  $\varepsilon_M(\mathbf{q}, \omega)$  is then a very smooth function of  $q = 2\pi/\lambda$  and can be therefore expanded as [46]

$$\varepsilon_M^{\alpha\beta}(\mathbf{q}, \omega) = \hat{\varepsilon}_M^{\alpha\beta}(\omega) + \hat{\gamma}^{\alpha\beta\eta}(\omega)q_\eta + \hat{\alpha}^{\alpha\beta\eta\nu}(\omega)q_\eta q_\nu + \dots, \quad (\text{B.14})$$

where  $\hat{\gamma} = [\nabla_{\mathbf{q}}\varepsilon_M(\mathbf{q}, \omega)]_{\mathbf{q}=\mathbf{0}}$  is a rank-three,  $\hat{\alpha}$  a rank-four tensor, and so on. These terms constitute the non-local corrections to the local, macroscopic dielectric matrix  $\hat{\varepsilon}_M(\omega)$ . They account for the *spatial-dispersion* in the material and are responsible for effects like the intrinsic birefringence in cubic crystals.

Note, however, that the derivation of the macroscopic Maxwell eq. (B.12) and the definition of  $\varepsilon_M$  is justified *only* in case of a long wavelength  $\lambda \gg a$  compared to the lattice constant  $a$ . Otherwise, the separation of bound and free charges becomes ambiguous, and thus the definition of  $\langle \mathbf{P} \rangle$  and  $\langle \mathbf{M} \rangle$  (see next section). Additionally, the equations are not Lorentz-invariant and thus only valid in the rest frame of the crystal.

## B.2 Ambiguity of the Microscopic Dielectric Function

With the advance in solid state physics and the possibility to actually calculate microscopic charge-density fluctuations for real materials (e. g., using density functional theory), one is interested in generalising the macroscopic dielectric function, which was introduced above, for the microscopic Maxwell equations.

### B.2.1 Generalisation of the Dielectric Function

Of course, the distinction between bound and free charges becomes obsolete on microscopic distances and one has to choose a different method [209]. The starting point is to split the induced current  $\mathbf{j}^i$  into a microscopic polarisation  $\mathbf{P}$  and a microscopic magnetisation  $\mathbf{M}$  in formal analogy to eq. (B.11)

$$\rho^i = \nabla \cdot \mathbf{P}, \quad \mathbf{j}^i = \partial_t \mathbf{P} + \nabla \times \mathbf{M}. \quad (\text{B.15})$$

The microscopic Maxwell equations (B.1) then assume a form, that is very similar to the macroscopic Maxwell equations (B.12), except that all quantities are now microscopic:

(i) $\nabla \cdot \mathbf{B}^t = 0$	(ii) $\nabla \times \mathbf{H} - \partial_t \mathbf{D} = \mathbf{j}^e$
(iii) $\nabla \times \mathbf{E}^t + \partial_t \mathbf{B}^t = 0$	(iv) $\nabla \cdot \mathbf{D} = \rho^e$
$\mathbf{H} = \frac{1}{\mu_0} \mathbf{B}^t - \mathbf{M}$	$\mathbf{D} = \varepsilon_0 \mathbf{E}^t + \mathbf{P}.$

(B.16)

Analogously to eq. (B.13) we might now define a microscopic  $\varepsilon$  as  $\mathbf{D} = \varepsilon_0 \varepsilon \mathbf{E}^t$ , i. e.,

$$D_\alpha(\mathbf{r}, t) = \int d\mathbf{r}' \int dt' \varepsilon_0 \varepsilon^{\alpha\beta}(\mathbf{r}, \mathbf{r}', t-t') E_\beta^t(\mathbf{r}', t'). \quad (\text{B.17})$$

Of course, the crystal is not homogeneous and we have to retain the full dependence on  $\mathbf{r}$  and  $\mathbf{r}'$ . The problem with this definition is, that the splitting and hence the microscopic fields  $\mathbf{P}$  and  $\mathbf{M}$  are not uniquely defined. Indeed, one can always perform the following transformation without changing the induced current  $\mathbf{j}^i$  and the physics of the system

$$\tilde{\mathbf{P}} = \mathbf{P} - \nabla \times \mathbf{L}, \quad \tilde{\mathbf{M}} = \mathbf{M} + \partial_t \mathbf{L}, \quad \text{for arb. } \mathbf{L}(\mathbf{r}, t). \quad (\text{B.18})$$

Also  $\mathbf{D}$  and  $\mathbf{H}$  will transform accordingly and are not unique ( $\tilde{\mathbf{H}} = \mathbf{H} + \mathbf{M} - \dot{\tilde{\mathbf{M}}}$ ),

$$\tilde{\mathbf{D}} = \mathbf{D} - \nabla \times \mathbf{L}, \quad \tilde{\mathbf{H}} = \mathbf{H} - \partial_t \mathbf{L}. \quad (\text{B.19})$$

The microscopic dielectric function is therefore only defined up to an arbitrary field  $\mathbf{L}$ :

$$(\mathbf{D} - i\mathbf{q} \times \mathbf{L}) = \varepsilon_0 \tilde{\varepsilon} \mathbf{E}^t. \quad (\text{B.20})$$

This ambiguity vanishes in the optical limit  $\mathbf{q} \rightarrow 0$ , where the microscopic and macroscopic definitions coincide. Note that only the transverse part of  $\mathbf{D}$  is affected by the choice of  $\mathbf{L}$ . Hence the longitudinal contractions  $\tilde{\varepsilon}_{LL}$  and  $\tilde{\varepsilon}_{LT}$  of the dielectric function are uniquely defined. Contrarily, the inverse dielectric function  $\tilde{\varepsilon}_{LL}^{-1}$  at large  $\mathbf{q}$  is only uniquely defined in homogeneous media. For the proof, we rewrite equation (B.20) as

$$\varepsilon_0^{-1} \begin{pmatrix} \varepsilon_{LL}^{-1} & \varepsilon_{LT}^{-1} \\ \varepsilon_{TL}^{-1} & \varepsilon_{TT}^{-1} \end{pmatrix} \begin{pmatrix} D_L \\ D_T \end{pmatrix} = \begin{pmatrix} E_L^t \\ E_T^t \end{pmatrix} \stackrel{!}{=} \varepsilon_0^{-1} \begin{pmatrix} \tilde{\varepsilon}_{LL}^{-1} & \tilde{\varepsilon}_{LT}^{-1} \\ \tilde{\varepsilon}_{TL}^{-1} & \tilde{\varepsilon}_{TT}^{-1} \end{pmatrix} \begin{pmatrix} D_L \\ D_T - L'_T \end{pmatrix}, \quad \mathbf{L}' \equiv i\mathbf{q} \times \mathbf{L},$$

Assuming that  $\varepsilon_{LL}^{-1} = \tilde{\varepsilon}_{LL}^{-1}$  does not depend on  $\mathbf{L}$ , one has  $\varepsilon_{LT}^{-1} D_T = \tilde{\varepsilon}_{LT}^{-1} [D_T - L'_T]$ , which contradicts the requirement of  $\tilde{\varepsilon}_{LT}^{-1}$  to be linear (e. g., let  $D_T$  be  $\lambda D_T$ ). In homogeneous systems, this contradiction vanishes because  $\varepsilon_{LT}^{-1} = 0$ .

*But in general, one has to specify the choice of  $\mathbf{L}$  used in the definition of the microscopic dielectric function.* Two different definitions are commonly used in literature:

**(a) Separation of Charges:  $\mathbf{D} = \varepsilon_0 \mathbf{E}^e$**

A natural choice is to separate all quantities in the microscopic Maxwell eq. (B.1) in external and induced contributions. In consistency with eq. (B.15) one defines

$$\mathbf{P} = -\varepsilon_0 \mathbf{E}^i, \quad \mathbf{M} = \mathbf{B}^i / \mu_0, \quad (\text{B.21})$$

as the fields generated by the subsystem of induced charges. It follows that

$$\mathbf{D} = \varepsilon_0 \mathbf{E}^t + \mathbf{P} = \varepsilon_0 \mathbf{E}^e, \quad \mathbf{H} = \mathbf{B}^t / \mu_0 - \mathbf{M} = \mathbf{B}^e / \mu_0, \quad (\text{B.22})$$

are the fields originating from the external charges. The microscopic dielectric function, according to eq. (B.20), relates the two subsystems

$$\mathbf{E}^e = \varepsilon \mathbf{E}^t, \quad \mathbf{E}^t = \varepsilon^{-1} \mathbf{E}^e. \quad (\text{B.23})$$

This choice will be particularly useful, if we want to determine the macroscopic response  $\mathbf{E}^t$  to a macroscopic external perturbation  $\mathbf{E}^e$ . In this thesis, we will mainly refer to this definition of  $\varepsilon$ . It is also used, e. g., by the references [49, 121, 209], and [51, p. 181,  $\Theta$ ].

**(b) Vanishing Magnetisation:  $\tilde{\mathbf{M}} = \mathbf{0}$**

Another common choice is to remove the magnetisation from all equations by setting  $\partial_t \mathbf{L} = -\mathbf{M}$ . The magnetic response is then incorporated into the  $\tilde{\mathbf{D}}$  and  $\tilde{\mathbf{H}}$ -field, and hence into the dielectric function  $\tilde{\varepsilon}$ , while  $\tilde{\mu} = \hat{1}$ . It follows from eq. (B.15) and (B.16)

$$\partial_t \tilde{\mathbf{P}} = \mathbf{j}^i, \quad \tilde{\mathbf{M}} = \mathbf{0}, \quad \partial_t \tilde{\mathbf{D}} = \mathbf{j}^i + \varepsilon_0 \partial_t \mathbf{E}^t, \quad \tilde{\mathbf{H}} = \mathbf{B}^t / \mu_0; \quad (\text{B.24})$$

and one has, according to eq. (B.20),

$$\tilde{\mathbf{D}} = \varepsilon_0 \tilde{\varepsilon} \mathbf{E}^t, \quad \varepsilon_0 \mathbf{E}^t = \tilde{\varepsilon}^{-1} \tilde{\mathbf{D}}. \quad (\text{B.25})$$

Examples for references that use this definition include [212], [51, p. 177, pseudo dielectric tensor  $\varepsilon$ ], [213], [28]. The main advantage is clearly the formal equivalence with the macroscopic definition (B.13). Nevertheless, the averaging is indeed more complicated than for definition (a), because both,  $\tilde{\mathbf{D}}$  and  $\mathbf{E}^t$  are microscopic fields.

### B.2.2 Relation to Other Response Functions

The susceptibility  $\chi$  and polarisability  $\pi$  are directly connected with the induced current  $\mathbf{j}^i$  and are thus uniquely defined. In order to derive their relation with  $\varepsilon^{-1}$ , we use

$$\varepsilon^{-1} \mathbf{E}^e \stackrel{(\text{B.23})}{=} \mathbf{E}^t = \mathbf{E}^e + \mathbf{E}^i \stackrel{(\text{B.5})}{=} \mathbf{E}^e - \mu_0 \mathcal{O}^{-1} \partial_t \mathbf{j}^i \stackrel{(\text{B.7})}{=} (\hat{1} - \mu_0 \mathcal{O}^{-1} \chi) \mathbf{E}^e, \quad (\text{B.26})$$

A similar equation holds for  $\varepsilon$  and we find

$$\varepsilon = \hat{1} + \mu_0 \mathcal{O}^{-1} \pi, \quad \varepsilon^{-1} = \hat{1} - \mu_0 \mathcal{O}^{-1} \chi. \quad (\text{B.27})$$

To obtain the corresponding relation to the dielectric function  $\tilde{\varepsilon}$ , we consider

$$\varepsilon_0 \partial_t^2 \tilde{\varepsilon} \mathbf{E}^t \stackrel{(\text{B.25})}{=} \partial_t^2 \tilde{\mathbf{D}} \stackrel{(\text{B.24})}{=} \partial_t \mathbf{j}^i + \varepsilon_0 \partial_t^2 \mathbf{E}^t \stackrel{(\text{B.7})}{=} (\pi + \varepsilon_0 \partial_t^2) \mathbf{E}^t. \quad (\text{B.28})$$

Thus, we find (using a Fourier transform)

$$\varepsilon_0 \partial_t^2 \tilde{\varepsilon} = \varepsilon_0 \partial_t^2 + \pi \quad \longleftrightarrow \quad \tilde{\varepsilon} = \hat{1} - \mu_0 \frac{c^2}{\omega^2} \pi. \quad (\text{B.29})$$

### B.2.3 Difference between $\varepsilon$ and $\tilde{\varepsilon}$

From eq. (B.27) and (B.29) we immediately find in Fourier space ( $q_0 = \omega/c$ )

$$-\frac{c^2}{\omega^2} \mathcal{O}(\varepsilon - \hat{1}) = (\tilde{\varepsilon} - \hat{1}), \quad \left[ -\frac{c^2}{\omega^2} \mathcal{O} = \hat{1} - (q/q_0)^2 P_T \right]. \quad (\text{B.30})$$

and a projection to the subspace of longitudinal waves gives a relation between  $\varepsilon$  and  $\tilde{\varepsilon}$ :

$$\varepsilon_{\text{LL}} = \tilde{\varepsilon}_{\text{LL}}, \quad \varepsilon_{\text{LT}} = \tilde{\varepsilon}_{\text{LT}}, \quad (\text{B.31})$$

$$\left[ \hat{1}_T - \left(\frac{q}{q_0}\right)^2 P_T \right] (\varepsilon_{\text{TT}} - \hat{1}_T) = (\tilde{\varepsilon}_{\text{TT}} - \hat{1}_T), \quad \left[ \hat{1}_T - \left(\frac{q}{q_0}\right)^2 P_T \right] \varepsilon_{\text{TL}} = \tilde{\varepsilon}_{\text{TL}}. \quad (\text{B.32})$$

As we have already seen earlier in eq. (B.20), we find that  $\varepsilon$  and  $\tilde{\varepsilon}$  coincide for their longitudinal projections  $\varepsilon_{\text{LL}}$  and  $\varepsilon_{\text{LT}}$ , or in the limit  $q \rightarrow 0$ .

One can derive similar equations for the field  $\mathbf{D}$  and  $\tilde{\mathbf{D}}$ . With

$$\tilde{\mathbf{D}} \stackrel{\text{(B.19)}}{=} \mathbf{D} - i\mathbf{q} \times \frac{1}{i\omega} \mathbf{M} \stackrel{\text{(B.21)}}{=} \varepsilon_0 \mathbf{E}^e - \mathbf{q} \times \frac{1}{\mu_0 \omega} \mathbf{B}^i = \varepsilon_0 \mathbf{E}^e - \frac{1}{\mu_0 \omega^2} \mathbf{q} \times (\mathbf{q} \times \mathbf{E}^i),$$

where the Maxwell eq. (B.1(iii)) has been used in the last step, one has

$$\tilde{D}_{\text{L}} = D_{\text{L}} = \varepsilon_0 \mathbf{E}_{\text{L}}^e, \quad \tilde{D}_{\text{T}} = D_{\text{T}} + \frac{1}{\mu_0} \frac{q^2}{\omega^2} \mathbf{E}_{\text{T}}^i. \quad (\text{B.33})$$

## B.3 Connecting Microscopic and Macroscopic Quantities

### B.3.1 Full Hamiltonian

First, the connection between the microscopic and macroscopic dielectric function is recalled. One starts from the relation between the microscopic fields  $\mathbf{E}^e$  and  $\mathbf{E}^t$

$$\mathbf{E}^t = \mathbf{E}^e + \mathbf{E}^i = (\hat{1} - \mu_0 \mathcal{O}^{-1} \chi) \mathbf{E}^e = \varepsilon^{-1} \mathbf{E}^e, \quad (\text{B.34})$$

where  $\mathcal{O}^{-1}$  is the Greens function of the vacuum. Assuming a *macroscopic* external field  $\mathbf{E}^e = \langle \mathbf{E}^e \rangle$ , one can define a macroscopic dielectric function  $\langle\langle \varepsilon \rangle\rangle$  relating  $\langle \mathbf{E}^e \rangle$  and  $\langle \mathbf{E}^t \rangle$ :

$$\langle \mathbf{E}^e \rangle = \langle\langle \varepsilon \rangle\rangle \langle \mathbf{E}^t \rangle, \quad \langle\langle \varepsilon \rangle\rangle = [\hat{1} - \mu_0 \langle\langle \mathcal{O}^{-1} \chi \rangle\rangle]^{-1} = [\langle\langle \varepsilon^{-1} \rangle\rangle]^{-1}. \quad (\text{B.35})$$

Similarly, with

$$\langle \partial_t \mathbf{j}^i \rangle = \langle\langle \chi \rangle\rangle \langle \mathbf{E}^e \rangle = \langle\langle \chi \rangle\rangle \langle\langle \varepsilon \rangle\rangle \langle \mathbf{E}^t \rangle \quad (\text{B.36})$$

one introduces the macroscopic dielectric function  $\langle\langle \tilde{\varepsilon} \rangle\rangle$  relating  $\langle \mathbf{j}^i \rangle$  and  $\langle \mathbf{E}^t \rangle$

$$\langle \partial_t \mathbf{j}^i \rangle = \varepsilon_0 [\langle\langle \tilde{\varepsilon} \rangle\rangle - \hat{1}] \langle \partial_t^2 \mathbf{E}^t \rangle, \quad \langle\langle \tilde{\varepsilon} \rangle\rangle = \hat{1} - \frac{1}{\varepsilon_0 \omega^2} \langle\langle \chi \rangle\rangle [\hat{1} - \mu_0 \langle\langle \mathcal{O}^{-1} \chi \rangle\rangle]^{-1}. \quad (\text{B.37})$$

### B.3.2 Coulomb Hamiltonian

Del Sole and Fiorino [212] argued, that in the formalism of TDDFT the transverse part of the induced field  $\mathbf{E}_{\text{T}}^i$  has to be treated like an additional external perturbation. They introduced the perturbing field  $\mathbf{E}^p = \mathbf{E}^e + \mathbf{E}_{\text{T}}^i = \mathbf{E}^t - \mathbf{E}_{\text{L}}^i$  and defined a new response function, the *quasi-susceptibility*

$$\partial_t \mathbf{j}^i = \chi^p \mathbf{E}^p \quad (\text{B.38})$$

which is supposed to be calculated in TDDFT instead of the full susceptibility  $\chi$ . Compared with the argumentation above, the perturbing field is considered to be purely classical (i.e. determined by the Maxwell equations), while the exchange-correlation part is neglected  $\mathbf{A}_{\text{XC}} = \mathbf{0}$ .

Analogously to eq. (B.34) one starts from the relations connecting the microscopic perturbing field  $\mathbf{E}^p$  with the fields  $\mathbf{E}^t$  and  $\mathbf{E}^e$ :

$$\mathbf{E}^t = \mathbf{E}^p + \mathbf{E}_L^i = (\hat{1} - \mu_0 \mathcal{O}_L^{-1} \chi^p) \mathbf{E}^p, \quad (\text{B.39})$$

$$\mathbf{E}^e = \mathbf{E}^p - \mathbf{E}_T^i = (\hat{1} + \mu_0 \mathcal{O}_T^{-1} \chi^p) \mathbf{E}^p. \quad (\text{B.40})$$

For a purely *macroscopic* perturbing potential  $\mathbf{E}^p = \langle \mathbf{E}^p \rangle$  one can again introduce the macroscopic dielectric function  $\langle\langle \varepsilon \rangle\rangle$  which relates  $\langle \mathbf{E}^e \rangle$  and  $\langle \mathbf{E}^t \rangle$  as

$$\langle \mathbf{E}^e \rangle = \langle\langle \varepsilon \rangle\rangle \langle \mathbf{E}^t \rangle, \quad \langle\langle \varepsilon \rangle\rangle = [\hat{1} + \mu_0 \langle\langle \mathcal{O}_T^{-1} \chi^p \rangle\rangle] [\hat{1} - \mu_0 \langle\langle \mathcal{O}_L^{-1} \chi^p \rangle\rangle]^{-1}. \quad (\text{B.41})$$

Analogously to eq. (B.36) one finds

$$\langle \partial_t \mathbf{j}^i \rangle = \langle\langle \chi^p \rangle\rangle \langle \mathbf{E}^p \rangle = \langle\langle \chi^p \rangle\rangle [\hat{1} - \mu_0 \langle\langle \mathcal{O}_L^{-1} \chi^p \rangle\rangle]^{-1} \langle \mathbf{E}^t \rangle \quad (\text{B.42})$$

for introducing the macroscopic dielectric function  $\langle\langle \tilde{\varepsilon} \rangle\rangle$  as

$$\langle \partial_t \mathbf{j}^i \rangle = \varepsilon_0 [\langle\langle \tilde{\varepsilon} \rangle\rangle - \hat{1}] \langle \partial_t^2 \mathbf{E}^t \rangle, \quad \langle\langle \tilde{\varepsilon} \rangle\rangle = \hat{1} - \frac{1}{\varepsilon_0 \omega^2} \langle\langle \chi^p \rangle\rangle [\hat{1} - \mu_0 \langle\langle \mathcal{O}_L^{-1} \chi^p \rangle\rangle]^{-1}. \quad (\text{B.43})$$

We can directly compare our results with the findings of [212]. Instead of the susceptibility  $\chi^p$ , they use the quasi-polarisability  $\alpha^p$ , which is defined by  $\tilde{\mathbf{P}} = \alpha^p \mathbf{E}^p$ . With

$$\partial_t^2 \tilde{\mathbf{P}} = \partial_t^2 \alpha^p \mathbf{E}^p = \partial_t \mathbf{j}^i = \chi^p \mathbf{E}^p, \quad \iff \quad -\omega^2 \alpha^p = \chi^p, \quad (\text{B.44})$$

one finds that eq. (B.43) and Del Sole and Fiorino [212], eq. (22) differ only by a change in notation:

$$\chi^p \rightarrow -\omega^2 \tilde{\alpha}, \quad \mathcal{O}_L^{-1} \chi^p \rightarrow c^2 \frac{q}{q} \tilde{\alpha}_{L \rightarrow}, \quad \langle\langle \tilde{\alpha} \rangle\rangle = [\tilde{\alpha}]_{\mathbf{0}, \mathbf{0}} \quad \langle\langle \tilde{\varepsilon} \rangle\rangle \rightarrow \overset{\leftarrow}{\epsilon}_M, \quad (\text{B.45})$$

and a switch to the CGI-system by letting  $\varepsilon_0 = 1/4\pi$ , and  $\mu_0 = 4\pi/c^2$ .

### B.3.3 Normal Modes

In medium described by the dielectric function  $\varepsilon$  (or equivalently  $\tilde{\varepsilon}$ ), one usually rewrites the wave equation (B.4) in the following way (in Fourier space and real space):

$$i\omega \mu_0 \mathbf{j}^e = \mathcal{O} \mathbf{E}^e = \mathcal{O} \varepsilon \mathbf{E}^t \quad \iff \quad \nabla \times [\nabla \times (\varepsilon \mathbf{E}^t)] + \frac{1}{c^2} \partial_t^2 (\varepsilon \mathbf{E}^t) = -\mu_0 \partial_t \mathbf{j}^e, \quad (\text{B.46})$$

or, using eq. (B.30), one obtains for  $\tilde{\varepsilon}$ :

$$i\omega \mu_0 \mathbf{j}^e = q^2 P_T \mathbf{E}^t - \frac{\omega^2}{c^2} \tilde{\varepsilon} \mathbf{E}^t \quad \iff \quad \nabla \times [\nabla \times \mathbf{E}^t] + \frac{1}{c^2} \partial_t^2 (\tilde{\varepsilon} \mathbf{E}^t) = -\mu_0 \partial_t \mathbf{j}^e. \quad (\text{B.47})$$

The solutions of the homogeneous equations, i.e. without any external perturbation  $\mathbf{j}^e = \mathbf{0}$ , are the *normal modes* or resonances of the medium. Their dispersion is given by the zeros of the determinant

$$\det[\mathcal{O}(q\omega)\varepsilon(q\omega)] \stackrel{!}{=} 0, \quad \det[q^2 P_T - \frac{\omega^2}{c^2} \tilde{\varepsilon}] \stackrel{!}{=} 0. \quad (\text{B.48})$$



# C Code Development

Our aim is the numerical calculation of AR-EEL spectra for graphene, graphite, and single-wall carbon nanotubes. In this section, I give a brief overview of the `Python`-codes that I have developed for this purpose (see table C.2, p. 193). References to the names of the relevant files and routines are indicated at the outer margin in the online version. The source code can be found at <http://etsf.polytechnique.fr/People/Ralf/Codes> and a more technical documentation can be extracted from each file using `pydoc`. If not stated differently, atomic units will be used in the following.

## C.1 Tight-Binding for Carbon Materials

The tight-binding approximation for graphene has been described in section 5.2.2 for nearest-neighbour interaction. In file `tight_binding.py`, I have implemented the corresponding equations to calculate the dielectric function  $\bar{\epsilon}(\bar{\mathbf{q}}, \omega)$  and  $\bar{\epsilon}_{\text{CNT}}(lp, \omega)$  of a graphene sheet and a single-wall carbon nanotube, respectively.

tight\_binding.py

### C.1.1 Graphene and Graphite

The tight-binding calculation for graphene is implemented in the `class TB_Graphene` and closely follows the work of Lin *et al.* [148] and Shung [147]. We use the parameters

class  
TB\_Graphene

$$a = 4.632 \text{ Bohr}, \quad E_0 = 0 \text{ eV}, \quad \gamma_0 = -2.84 \text{ eV}, \quad s_0 = 0.07, \quad \varepsilon_\sigma = 2.4. \quad (\text{C.1})$$

First, the geometry factor (5.11) is calculated. With the nearest neighbours (see fig. 5.5c)

\_\_g()

$$\mathbf{t}_1 = \frac{a}{3}(\sqrt{3}, 0)^T, \quad \mathbf{t}_2 = \frac{a}{3}(-\sqrt{3}/2, 3/2)^T, \quad \mathbf{t}_3 = \frac{a}{3}(-\sqrt{3}/2, -3/2)^T, \quad (\text{C.2})$$

and using Cartesian coordinates for  $\mathbf{k} = (k_x, k_y)$ , one finds

$$g(k_x, k_y) = e^{ik_x a/\sqrt{3}} + 2e^{-ik_x a/(2\sqrt{3})} \cos(k_y a/2). \quad (\text{C.3})$$

The tight-binding energy  $E_{n\mathbf{k}}$  is calculated from eq. (5.14), and the  $\mathbf{q}$ -dependent matrix elements  $\tilde{\rho}_{\mathbf{k}}^{nn'}$  are readily given by eq. (5.17) and (5.19). Note that even if the overlap  $s_0$  is included in the energies  $E_{n\mathbf{k}}$ , it is always neglected in the calculation of  $\tilde{\rho}_{\mathbf{k}}^{nn'}$ .

energy()  
rhotw()

Second, the graphene polarisability  $\bar{\chi}^0$  is computed by a summation over all  $\mathbf{k}$ -points of the grid `kgrid_cc`. By default, a Monkhorst-Pack grid of  $N_k \times N_k$  equally spaced  $\mathbf{k}$ -points is used. In the case of undoped graphene at zero temperature, only *interband* transitions between valence and conduction states contribute. Equation (3.14) and (5.31) then give

chi0()

$$\bar{\chi}^0(\mathbf{q}, \omega) = \frac{2}{A} \sum_{\mathbf{k}} \tilde{\rho}_{\mathbf{k}}^{vc}(\mathbf{q}) [\tilde{\rho}_{\mathbf{k}}^{vc}(\mathbf{q})]^* \frac{E_{c\mathbf{v}\mathbf{k}} - E_{v\mathbf{c}\mathbf{k}}}{(\hbar\omega + E_{v\mathbf{c}\mathbf{k}} + i\eta)(\hbar\omega + E_{c\mathbf{v}\mathbf{k}} + i\eta)}, \quad (\text{C.4})$$

where  $E_{v\mathbf{c}\mathbf{k}} = E_{v\mathbf{k}-\mathbf{q}} - E_{c\mathbf{k}}$  denotes the energy of the resonant, and  $E_{c\mathbf{v}\mathbf{k}} = E_{c\mathbf{k}-\mathbf{q}} - E_{v\mathbf{k}}$  the energy of the corresponding anti-resonant transition. The normalisation volume  $L_z/V$  is given by the area  $A$  of the graphene sheet in the normalisation box, i. e.  $A = N_k^2 A_{\text{cell}}$  given in Bohr<sup>2</sup>. All energies have to be converted to atomic units (Ha). For doped graphene with a Fermi level  $E_F \neq 0$ , expression (3.14) is calculated for *interband* and *intra*band contributions separately. The occupation numbers at  $T = 0$  K are given by the step function  $f_{n\mathbf{k}} = \Theta(E_F - E_{n\mathbf{k}})$ .

Finally, the two-dimensional macroscopic dielectric function  $\bar{\varepsilon}$  is calculated (see eq. 5.20). Compared to DP,  $\bar{\varepsilon}$  corresponds to the macroscopic dielectric function for in-plane momentum transfer  $\bar{\mathbf{q}}$  which is calculated in RPA neglecting all LFE. In contrast,  $-\text{Im}\{1/\bar{\varepsilon}\}$  corresponds to the EELS spectrum which is calculated within the local-response approximation, i. e., taking into account crystal LFE along the direction perpendicular to the plane.

### Comparison with Lin *et al.* [148]

To test the implementation, we reproduce the results of Lin *et al.* [148], who calculated the dielectric function  $\varepsilon_M$  of graphite for different in-plane momenta  $\bar{\mathbf{q}}$ . In contrast to isolated graphene, the interaction between the different layers of graphite has to be taken into account which leads to a modified Coulomb potential [148, eq. (7b)]

$$v_{\text{Graphite}}(\bar{\mathbf{q}}, q_z = 0) = v_{2\text{D}}(\bar{\mathbf{q}})S(\bar{\mathbf{q}}), \quad S(\bar{\mathbf{q}}) = \sinh(\bar{q}d_0) \cosh(\bar{q}d_0), \quad (\text{C.5})$$

where  $d_0$  denotes the graphite interlayer distance. Additionally, a correction of  $\chi^0$ , which was proposed by Mermin for finite broadening  $\eta$ , has been used [148, eq. (4)]

$$\chi_{\text{corr}}^0(\mathbf{q}, \omega) = \frac{\omega + i\eta}{\omega + i\eta[\chi^0(\mathbf{q}, \omega)/\chi^0(\mathbf{q}, 0)]} \chi^0(\mathbf{q}, \omega). \quad (\text{C.6})$$

Using the same parameters as Lin *et al.*, i. e.,  $a = 4.6478$  Bohr,  $\gamma_0 = -2.5$  eV,  $s_0 = 0$ ,  $\varepsilon_\sigma = 2.4$ , and  $\eta = 0.1$  eV, we exactly reproduce their results. Figure C.1 shows, for instance,  $\text{Im}\bar{\varepsilon}_M$  of graphite for different in-plane momenta  $\bar{\mathbf{q}}$  along the  $\Gamma\text{K}$  direction, and  $\text{Im}\bar{\varepsilon}$  of intercalated graphite for  $\bar{\mathbf{q}}$  along  $\Gamma\text{M}$ .

### C.1.2 Single-Wall Carbon Nanotubes

As we have seen in section 6.2.2, the wave functions and energies of the tube can be directly obtained from graphene within the zone-folding model [see eq. (6.7)]. To this end, general tube parameters (like  $\mathbf{C}$ ,  $\mathbf{T}$ , and  $\mathbf{R}$ ) are implemented in the class `CNT()` following the notation of Saito *et al.* [4]. The `zone_folding` module provides functions for the mapping between graphene and tube coordinates in real and reciprocal space [see eq. (6.10) and (6.11)] as well as the construction of the corresponding unit cells.

cnt.py

zone\_folding.py

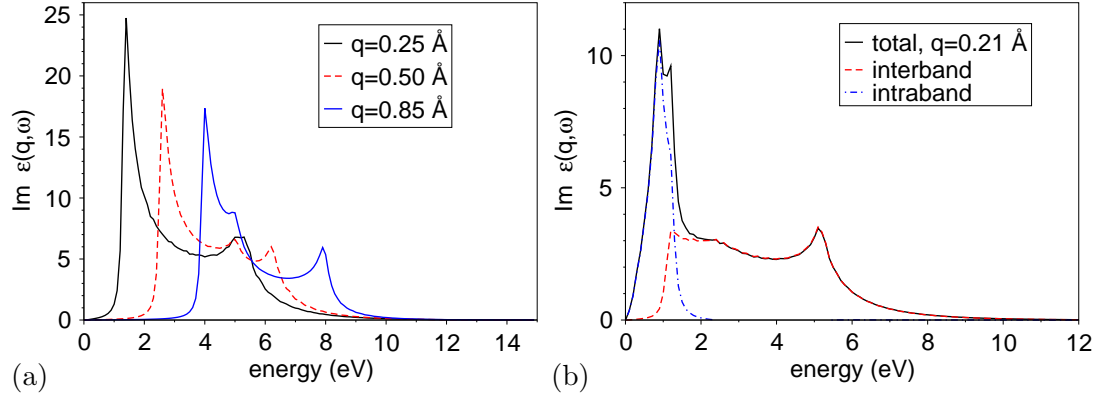


**Fig. C.1:** (a) The dielectric function  $\bar{\epsilon}$  of undoped graphite ( $d_0 = 3.35 \text{ \AA}$ ,  $E_F = 0 \text{ eV}$ ) for different in-plane momenta  $\bar{q}$  along the  $\Gamma K$  direction. Compare with [148, fig. 3(d)]. (b) The dielectric function  $\bar{\epsilon}$  of an stage-1 intercalated graphite compound ( $d_0 = 9.42 \text{ \AA}$ ,  $E_F = 0.75 \text{ eV}$ ) for an in-plane momentum  $\bar{q}$  along  $\Gamma M$ . Compare with [148, fig. 7(b)].

The independent-particle polarisability of the tube can be obtained from the corresponding tight-binding expression (C.4) for graphene if the wave vectors  $\mathbf{k}$  and  $\mathbf{q}$  are substituted by  $\boldsymbol{\kappa} = (j, k)$  and  $\boldsymbol{\xi} = (l, p)$ , respectively:

$$\bar{\chi}_{\text{CNT}}^0(lp, \omega) = \frac{2}{\bar{A}} \sum_{j=0}^{N-1} \sum_k \frac{(E_{jk}^{cv} - E_{jk}^{vc})}{(\hbar\omega + E_{jk}^{vc} + i\eta)(\hbar\omega + E_{jk}^{cv} + i\eta)} \bar{\rho}_{jk}^{vc}(lp) [\bar{\rho}_{jk}^{vc}(lp)]^* \quad (\text{C.7})$$

where  $E_{jk}^{nn'} = E_{n, j-l, k-p} - E_{n', j, k}$  denotes the energy of the transition  $n' \rightarrow n$  and

$$\bar{\rho}_{jk}^{nn'}(lp) = \langle n', j-l, k-p | e^{-il\varphi} e^{-ipz} | n, j, k \rangle. \quad (\text{C.8})$$

The summation in eq. (C.7) runs over the quasi two-dimensional Brillouin zone of the tube (see fig. 6.2a). Umklapp processes are correctly taken into account as we work directly with the helical wave vector  $\bar{\mathbf{q}}(l, p)$  and  $\bar{\mathbf{k}}(j, k)$  [see eq. (6.11)]. This corresponds to the use of helical coordinates instead of the linear-angular coordinates (see section 6.1).

All energies have to be converted to atomic units (Ha) and the normalisation volume  $\bar{A} = 1/(2\pi N_k T)$  is directly related to the area of the unrolled graphene ribbon  $\mathcal{R}\bar{A} = 2\pi \mathcal{R}L_z = CTN_z = A_{\text{cell}}NN_k$ . The expression becomes equivalent to the polarisability of the graphene sheet in the limit of very large tubes, i. e., when the cutting lines in the Brillouin zone of the tube become sufficiently dense.

### Comparison with Lin *et al.* [181]

Figure 6.4b shows the results of the tight-binding calculation for the loss function  $-\text{Im} \bar{\epsilon}_{\text{CNT}}^{-1}$  of a (23, 0) SWCNT. The on-axis momentum is chosen as  $p = 0.2 \text{ \AA}^{-1}$  and different angular momenta  $l$  are shown. We reproduce exactly the results shown in Fig. 2a of Lin *et al.* [181].

tight\_binding.py  
class TB\_CNT

ex\_cnt()

## C.2 Local-Response Approximation

The presented tight-binding method is fast but not very accurate and relies on several fit parameters. To avoid these drawbacks, I have used the DP code to calculate the two-dimensional polarisability  $\bar{\chi}^0$  of graphene from first-principles. The response  $\bar{\chi}$  of graphene and carbon nanotubes can be then calculated by the following post-processing:

### C.2.1 Graphene

Within the local-response approximation (see section 5.4), the susceptibility  $\bar{\chi}$  of the graphene sheet is obtained from  $\bar{\chi}^0$  by solving the Dyson equation for an effective homogeneous, infinitely thin slab [see eq. (5.32)]. The corresponding LRA method II (see page 98) has been implemented in class `LRA_Graphene` (see file `lra_graphene.py`). During initialisation, the polarisability  $\chi_d^0(\bar{\mathbf{q}})$  for different in-plane momentum transfers  $\bar{\mathbf{q}}$  is read from the given list of `outnlf.mdf` files using the `dp_mdf` module. The member functions `chi0`, `chi`, `eps`, and `epsi` return the corresponding sheet polarisability, sheet susceptibility, and two-dimensional (inverse) dielectric function [see eq. (5.31)] for a given momentum  $\bar{\mathbf{q}}$  in Cartesian coordinates. If the parameter `lambda` is specified at the initialisation of the object, the LRA- $\beta$  method is used (see section 5.5.1). Typical values for the decay length are  $\lambda = 1.5 \text{ \AA}$  for the  $\pi$  plasmon and  $\lambda = 0.8 \text{ \AA}$  for the  $\pi + \sigma$  plasmon which have been obtained from a best fit to full RPA *ab-initio* calculations (see fig. 5.13b and 5.18a).

For very small momentum transfers  $|\bar{\mathbf{q}}| < 0.1 \text{ \AA}^{-1}$  the two-dimensional dielectric function  $\bar{\epsilon}(\bar{\mathbf{q}}, \omega) \approx \bar{\epsilon}(\bar{\mathbf{q}} \rightarrow \bar{\mathbf{0}}, \omega)$  is found to be independent of the momentum transfer  $\bar{\mathbf{q}}$ . It has to be calculated only once and we can obtain the susceptibility at *any* other small momentum transfer  $\bar{\mathbf{q}}$  from eq. (7.8). This corresponds to the neglect of spatial dispersion effects (see fig. 7.2a) and has been implemented in class `LRA_Graphene_nondispersive`.

### C.2.2 Single-Wall Carbon Nanotubes

The response of a single-wall carbon nanotube is calculated analogously by solving the Dyson equation for an effective homogeneous, infinitely thin cylinder [see eq. (6.17)]. The corresponding LRA+ZF method IV (see page 125), is very similar to the LRA method II for graphene described above. However, there are two important differences:

1. We have to take into account the periodicity of the Kohn-Sham wave functions along the circumference of the tube. Within the zone-folding model, we have to calculate the polarisability of a *periodic graphene ribbon* instead of an infinite graphene layer. Thus, for each  $(n, m)$  tube one has to create a new `kss`-file with ABINIT, where the  $k$ -point set is given by  $N$  parallel line segments that constitute the two-dimensional Brillouin zone of the unrolled tube (see fig. 6.2a). The list of  $k$  points is created by the function `BZ_to_abinit(CNT, Nk, shiftk)`, where `CNT` is an instance of the `CNT`-class (see `cnt.py`) describing the geometry of the tube, `Nk` denotes the number of  $k$  points per line segment, and `shiftk` their shift along the tube axis.

Second, the macroscopic component of the polarisability  $\chi_d^0(\bar{\mathbf{q}})$  has to be calculated with the DP-code, where  $\bar{\mathbf{q}}(l, p)$  is related to the angular and on-axis momentum

transfer  $l$  and  $p$  in the tube via eq. (6.11). Function `to_DP()` creates a list of  $\bar{\mathbf{q}}$  vectors for the DP input file for different  $l$  and  $p$  values (see `prepare_AbInitio.py`).

`to_DP()`

2. The effective Dyson equation (6.17) for a tube has to be solved. This has been implemented in the class `LRA_CNT` (see `lra_cnt.py`) which has the same member functions as `LRA_Graphene`. The cylinder polarisability, susceptibility, and (inverse) dielectric function is calculated for a given  $l$  and  $p$  using the LRA or LRA- $\beta$  method.

`lra_cnt.py`

`class LRA_CNT`

As example, we compare the results of the ZF+LRA and tight-binding method for the cylinder response functions  $-\text{Im} \bar{\varepsilon}_{\text{CNT}}^{-1}(lp)$  and  $\text{Im} \bar{\varepsilon}_{\text{CNT}}(l, p)$  of a (9, 9) tube in fig. 6.7.

### C.3 AR-EELS for SWCNT

So far, we have calculated the response  $\bar{\varepsilon}_{\text{CNT}}(l, p)$  of the tube to a helical-wave perturbation. Now want to go a step further and determine the AR-EEL spectrum of the tube, i. e., the response to a plane-wave perturbation with wave vector  $\mathbf{q}^0 = \mathbf{q}_\perp^0 + q_\parallel^0 \mathbf{e}_3$ . To this end, we have to perform a weighted sum over several spectra  $-\text{Im} \bar{\varepsilon}_{\text{CNT}}^{-1}(l, p)$  for different angular moments  $l$  and fixed on-axis momentum  $p = q_\parallel^0$  [see eq. (6.23)]. The summation is performed by the function `tube_2_plane_wave(CNT, q_cc, chiCNT)` which expects a `CNT`-object defining the geometry of the tube, a 3D vector `q_cc` specifying  $\mathbf{q}^0$ , and a pointer to a function `chiCNT(p, l)` which returns  $\bar{\chi}_{\text{CNT}}(l, p)$  for any  $l$  and  $p$ . For chiral tubes, the summation runs from  $-l_{\text{max}}$  to  $l_{\text{max}}$ . For achiral tubes, we can restrict the summation to non-negative  $l$  because of the additional mirror symmetry along  $\mathbf{z}$  and the symmetry relation (A.63). Note, that the mode with  $l = 0$  and  $p = 0$  can not be excited—it corresponds to a uniform increase or decrease of the charge density and thus violates charge conservation. The  $l = 0$  mode must be therefore skipped if  $\mathbf{q}^0$  is oriented exactly perpendicular to the tube axis. In order to compare directly with supercell calculations for the full tube, one has to specify the in-plane area  $A$  of the cell. In our case  $A = \frac{\sqrt{3}}{2} a^2$ , as the tubes are arranged in a triangular lattice with lattice constant  $a$ .

`ar_eels.py`

`tube2planewave()`

`lmax`

The cylinder susceptibility  $\bar{\chi}_{\text{CNT}}(l, p)$  can be calculated either within the tight-binding or local-response approximation (see section C.1 and C.2). Examples for the calculation of the AR-EELS spectra like in fig. 6.13 and 6.10 are included at the end of the files `ar_eels.py` and `lra_cnt.py`, respectively (execute these files with Python).

1. `prepare_AbInitio.py`: create input files for AbInit and DP
2. `AbInit`: create KSS-file for graphene ribbon corresponding to `CNT(n, m)`
3. `DP`: create `outnlf.mdf` files for several  $p$  and  $l$  momenta,  $|l| \leq l_{\text{max}}$
4. `lra_cnt.py` + `ar_eels.py`:
  - construct `LRA_CNT`-object for list of `outnlf.mdf` files
  - calculate AR-EELS spectrum for the tube

**Tab. C.1:** Workflow for an AR-EEL spectrum of a  $(n, m)$  tube using the LRA+ZF method.

## C.4 From Graphite to Graphene

### C.4.1 Interpolation Method

The different steps of the interpolation method **I** have been outlined on page 92. Due to the strong localisation of the independent-particle polarisability  $\chi^0(z, z')$  (see section 5.4.1), the Fourier transformed quantity  $\chi^0(G_z, G'_z)$  is nearly constant and can be easily interpolated. Two methods have been implemented in file `interpolate_chi0.py`:

- First, we have implemented a cubic-spline interpolation. As  $\chi^0$  is complex in reciprocal space, the real and imaginary part of  $\chi^0$  are interpolated independently.
- Second, we used two Fourier transforms in order to increase the interlayer distance in real space. To this end, we first calculate  $\chi^0(z, z')$  from  $\chi^0(G_z, G'_z)$  by applying a two-dimensional, inverse Fourier transform (see fig. C.2). Second, we increase the size of the super cell in real space by a given factor  $N$  (see fig. C.3b) and fill the unknown values with 0 (no response). Third, the Fourier transformation back to reciprocal space yields an interpolated  $\tilde{\chi}^0(G_z, G'_z)$  where the interlayer distance is increased by the factor  $N$  (see fig. C.3a).

Working in real space, the Fourier interpolation has a clear physical meaning: assuming that the polarisability is localised (see section 5.4.1), we just have to add an additional region with zeros (no response) for larger systems. This padding technique has been already proposed to calculate the Hartree energy of finite systems [214] and, more generally, is related to the interpolation in image processing. Indeed, a discrete set of data points can be interpolated by Fourier transforming the sample, adding high frequency coefficients which are assumed to be zero, and applying the back transform.

Note that the Fourier interpolation has some advantages compared to the cubic-spline interpolation: First, it is numerically more stable and slightly faster. Second, it does not depend on the phase of  $\chi^0$ . Indeed, in order to interpolate real and imaginary part independently, we have to assume that both are smooth functions. But already a simple translation of the layers with respect to the origin will introduce phase oscillations in reciprocal space and the cubic-spline method will break down.

Figure C.4a shows the in-plane loss spectrum of a graphene stack with interlayer distance  $d = 16d_0$ . We compare a full *ab-initio* calculation with the result from the interpolation method starting from the polarisability of a graphene stack with  $d = 2d_0$ . If we use the Fourier-interpolation method, we exactly reproduce the *ab-initio* results, while the cubic-spline interpolation fails in this case. Indeed, the origin was shifted along  $z$ -direction and both, the real and imaginary part of  $\chi^0$  strongly oscillate.

### C.4.2 Coulomb-cutoff method

The Coulomb-cutoff method **III** has been described on page 102 and implemented in file `realspace_chi0.py`. Figure C.4b shows the loss function of a graphene stack with  $d = 4d_0$ , i. e., the sheets are still interacting at a momentum transfer  $\bar{q} = 0.27 \text{ \AA}^{-1}$ . Comparing full *ab-initio* calculations (black solid) and the results of the Coulomb-cutoff method

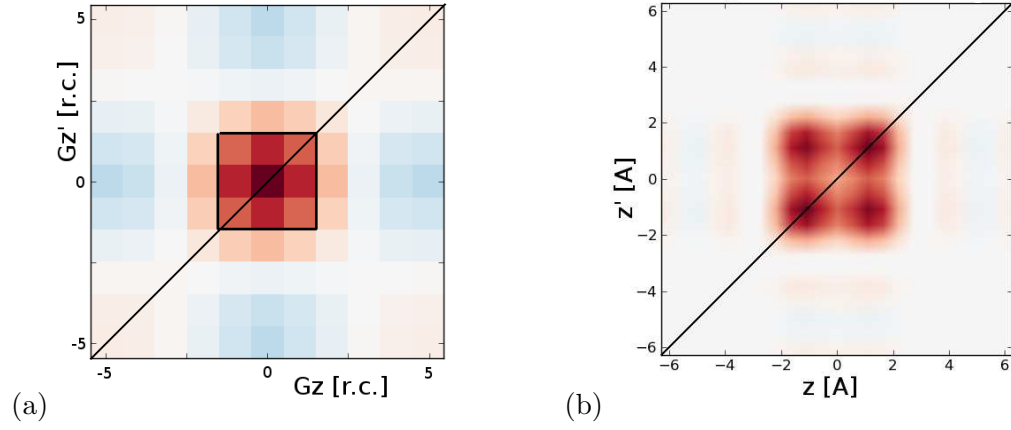


**Fig. C.2:** Independent-particle polarisability for a graphene stack with doubled interlayer distance  $d = 2d_0$ . (a) First, in reciprocal space  $\text{Im} \chi^0(\bar{q}\bar{q}'; G_z G'_z)$  and (b) second, in real space  $\text{Im} \chi^0(\bar{q}\bar{q}'; z z')$ . The other parameters are fixed as  $\bar{q} = \bar{q}' = 0.27 \text{\AA}^{-1}$ ,  $\omega = 4 \text{eV}$ .

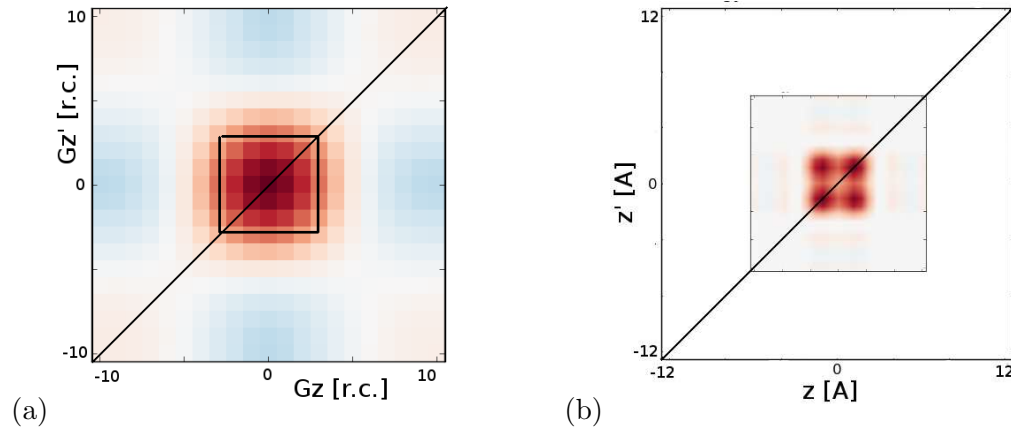


**Fig. C.3:** (b) We increase the size of the supercell in real space and add zero's at the border. (a) The Fourier transform of this modified quantity is than an interpolated version of fig C.2a.

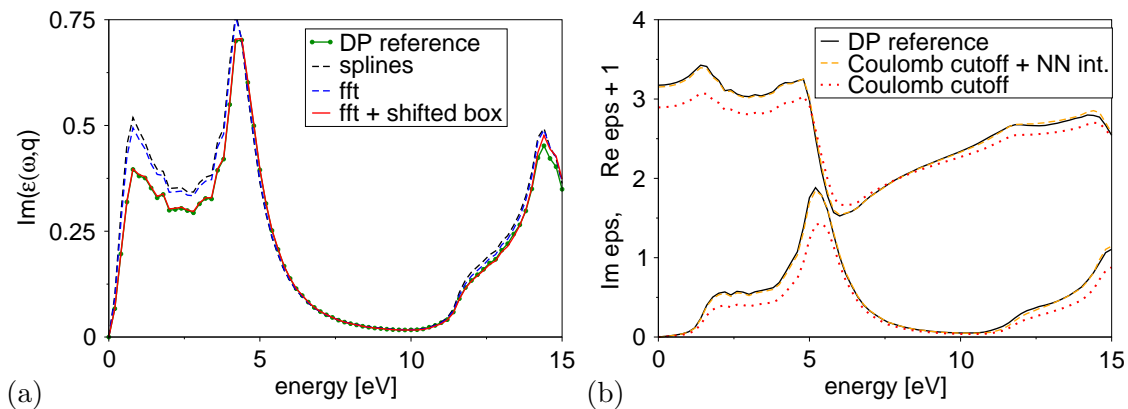


**Fig. C.4:** (a) Energy-loss function of a graphene stack with interlayer distance  $d = 16d_0$  and in-plane momentum  $\bar{q} = 0.07 \text{ \AA}^{-1}$ . (b) Loss function for a graphene stack with  $d = 4d_0$  and in-plane momentum  $\bar{q} = 0.27 \text{ \AA}^{-1}$ . See text for further details.

(red dots) starting from a graphene stack with  $d = 2d_0$  shows a slight difference in the spectra. This difference completely vanishes, if we take into account the interaction between neighbouring sheets in the Coulomb-cutoff method by using eq. (5.44).

Alternatively to the solution of the Dyson equation in real space, one can also work in reciprocal space using a modified Coulomb potential  $v_{\text{cut}}$  which is either cut-off at a distance  $R$  (see, e.g., [168–170]) or modified to simulate a larger interlayer distance  $D$  using a step-like Coulomb potential (see file `modified_coulomb_cutoff.py` and `modified_coulomb_varyd.py`, respectively). As there is no Fourier transform and zero-padding involved, this approach is even faster and simpler to implement than the proposed Coulomb-cutoff method III. For thick slabs, like in the case of surface calculations, one should use a combined approach of zero-padding and Coulomb cutoff in reciprocal space [214].

## Conclusions

We have seen that both the Fourier-interpolation method and the Coulomb-cutoff method reproduce exactly the full *ab-initio* calculations for the in-plane loss spectra of graphene stacks. The interpolation method actually calculates the susceptibility of an infinite stack of graphene layers with increased distance. The Coulomb-cutoff method, instead, calculates the susceptibility of an isolated layer of graphene. Interactions can be re-introduced using the building-block approach.

The following table summarises all codes that I have implemented during my thesis.

package	module	description
<b>CNT</b>	<code>cnt</code>	Basic parameters for graphene and SWCNTs.
	<code>zone_folding</code>	Connection between graphene and the SWCNT within the zone-folding model.
	<code>tight_binding</code>	Electronic structure and response of graphene and SWCNTs using nearest-neighbour tight-binding.
	<code>ar_eels</code>	Calculate AR-EELS of a tube by expanding the external plane-wave perturbation into Bessel functions.
<b>3Dto2D</b>	<code>lra_graphene</code>	Calculate slab response function of graphene from graphite within the local-response approximation. $\rightarrow$ <i>Implements LRA method II (see p. 98)</i> .
	<code>interpolate_chi0</code>	Increase interlayer distance of graphite via a fft / cspline interpolation of the microscopic pol. $\chi_{GG'}^0$ . $\rightarrow$ <i>Implements Interpolation method I (see p. 92)</i> .
	<code>modified_coulomb</code>	Increase interlayer distance with a modified Coulomb potential ( <code>varyd</code> ) or by applying a cutoff ( <code>cutoff</code> ).
	<code>realspace_chi0</code>	Calculate the response of a 2D system from the bulk polarisability by solving the Dyson eq. in real space. $\rightarrow$ <i>Implements Coulomb-cutoff method III (p. 102)</i> .
<b>3DtoCNT</b>	<code>prepare_AbInitio</code>	Create input-files for the <i>ab-initio</i> calculations of the unrolled SWCNT (ABINIT and DP).
	<code>lra_cnt</code>	Calculation of the cylinder response function of a SWCNT within the local-response approximation. $\rightarrow$ <i>Implements ZF+LRA method IV (see p. 125)</i> .
	<code>zf_method</code>	Calculate the response of a tube from the polarisability of graphite by solving the Dyson eq. in real space. $\rightarrow$ <i>Implements Zone-folding method V (see p. 139)</i> .
<b>DPio</b>	<code>SRcommon</code>	General definitions like index grids ( <code>RegularVGrid</code> ).
	<code>SRplot</code>	Plotting for 2D-arrays depending on two parameters.
	<code>dp_chi0</code>	Read full $\chi^0$ from DP-output file <code>chi0.dat</code> .
	<code>dp_mdf</code>	Read DP-output file <code>out(n)lf.mdf</code> (header+data).
	<code>dp_log</code>	Read DP-logfile (k-points and energies).

**Tab. C.2:** Overview of the Python modules. See <http://etsf.polytechnique.fr/People/Ralf/Codes> or the local SVN repository for the latest version of the source code.



# Acknowledgements

I would like to thank everyone who has guided and accompanied my way during the last three years.

First of all I would like to thank my supervisors **Lucia Reining** and **Christine Giorgetti** for creating a very stimulating working atmosphere, for conceding the freedom to develop my own ideas, and for their availability and guidance whenever it was necessary.

I also thank the whole group of the LSI for a very enjoyable, generous, and collaborative environment. In particular, **Hannes Hübener** for the numerous physical and non-physical discussions that I enjoyed a lot; **Gaelle Bruant** for her open-hearted welcome and for sharing a disproportionate interest in climbing tiny rocks; **Hansi Weißker** for his sense of humour; **Andrea Cucca**; and all the members of the Theoretical Spectroscopy Group in Palaiseau.

Further, I would like to thank my theoretical and experimental collaborators from whom I learned a lot and I was pleased to work with. In particular, **Christian Kramberger** and **Thomas Pichler** for many discussions on their SWCNT experiments; **Nozomu Hiraoka** for the experimental verification of our predictions on the angular anomaly in Graphite at the SPring8 in Taiwan; **Simo Huotari** for inviting me to participate in the measurements at the ESRF Synchrotron in Grenoble; **Alberto Zobelli** and the members of the LPS at Orsay for interesting discussions on electron microscopy.

I am grateful to the referees of my thesis, **Peter Schattschneider** and **Luc Henrard** for their time and interest in my work. And I thank the C’Nano IDF for financial support.

And finally, I want to express my deep gratitude to my parents and Katja for their unconditional and continuous support.

*Merci!*



## Bibliography

- [1] R. Lay, ed.: *Texte zum naturwissenschaftlichen Weltbild*, pp. 55–71 (München, 1976).
- [2] J. D. Joannopoulos, S. G. Johnson, J. N. Winn, *et al.*: *Photonic Crystals: Molding the Flow of Light* (Princeton University Press, 2008), 2nd ed.
- [3] C. Delerue and M. Lannoo: *Nanostructures: Theory and Modelling*. (Springer, 2004).
- [4] R. Saito, G. Dresselhaus, and M. S. Dresselhaus: *Physical Properties of Carbon Nanotubes* (Imperial College Press, 1998).
- [5] A. K. Geim and K. S. Novoselov: *Nat Mater*, **6**, 183 (2007).
- [6] E. Ruska: *Rev. Mod. Phys.*, **59**, 627 (1987).
- [7] P. Forbes: *The Gecko's Foot: Bio-inspiration: Engineering New Materials from Nature* (W. W. Norton, 2006).
- [8] M. Haider, S. Uhlemann, E. Schwan, *et al.*: *Nature*, **392**, 768 (1998).
- [9] R. F. Egerton: *Reports on Progress in Physics*, **72**, 016502 (2009).
- [10] F. J. García de Abajo: *Rev. Mod. Phys.*, **82**, 209 (2010).
- [11] J. D. Jackson: *Classical Electrodynamics* (Wiley, 1998).
- [12] W. Kohn: *Rev. Mod. Phys.*, **71**, 1253 (1999).
- [13] E. Runge and E. K. U. Gross: *Phys. Rev. Lett.*, **52**, 997 (1984).
- [14] J.-C. Charlier, X. Blase, and S. Roche: *Rev. Mod. Phys.*, **79**, 677 (2007).
- [15] D. A. Muller: *Nat Mater*, **8**, 263 (2009).
- [16] C.-L. Jia, S.-B. Mi, K. Urban, *et al.*: *Nat Mater*, **7**, 57 (2008).
- [17] R. F. Egerton: *Physical principles of electron microscopy: an introduction to TEM, SEM, and AEM* (Springer, 2005).
- [18] K. Urban: *Nat Mater*, **8**, 260 (2009).
- [19] I. Arslan and N. D. Browning: *Microscopy Research and Technique*, **69**, 330 (2006).

- [20] R. Erni and N. D. Browning: *Ultramicroscopy*, **104**, 176 (2005).
- [21] D. A. Muller, L. F. Kourkoutis, M. Murfitt, *et al.*: *Science*, **319**, 1073 (2008).
- [22] J. Park, S. Heo, J.-G. Chung, *et al.*: *Ultramicroscopy*, **109**, 1183 (2009).
- [23] J. Nelayah, M. Kociak, O. Stéphan, *et al.*: *Nat Phys*, **3**, 348 (2007).
- [24] P. E. Batson: *Micron*, **39**, 648 (2008).
- [25] D. A. Muller and J. Silcox: *Ultramicroscopy*, **59**, 195 (1995).
- [26] H. Rose: *Ultramicroscopy*, **110**, 488 (2010).
- [27] P. Schattschneider and W. S. M. Werner: *Journal of Electron Spectroscopy and Related Phenomena*, **143**, 83 (2005).
- [28] F. J. García de Abajo and M. Kociak: *Phys. Rev. Lett.*, **100**, 106804 (2008).
- [29] A. Howie: *Micron*, **34**, 121 (2003).
- [30] Z. L. Wang: *Micron*, **27**, 265 (1996).
- [31] D. A. Muller, T. Sorsch, S. Moccio, *et al.*: *Nature*, **399**, 758 (1999).
- [32] M. Couillard, A. Yurtsever, and D. A. Muller: *Phys. Rev. B*, **77**, 085318 (2008).
- [33] J. M. Pitarke, V. M. Silkin, E. V. Chulkov, *et al.*: *Reports on Progress in Physics*, **70**, 1 (2007).
- [34] W. L. Barnes, A. Dereux, and T. W. Ebbesen: *Nature*, **424**, 824 (2003).
- [35] R. H. Ritchie: *Phys. Rev.*, **106**, 874 (1957).
- [36] G. Gumbs and N. J. M. Horing: *Phys. Rev. B*, **43**, 2119 (1991).
- [37] T. Stöckli, Z. L. Wang, J.-M. Bonard, *et al.*: *Phil. Mag. B*, **79**, 1531 (1999).
- [38] E. Kröger: *Zeitschrift für Physik A Hadrons and Nuclei*, **216**, 115 (1968).
- [39] A. L. Fetter: *Annals of Physics*, **81**, 367 (1973).
- [40] F. J. García de Abajo and A. Howie: *Phys. Rev. Lett.*, **80**, 5180 (1998).
- [41] F. J. García de Abajo and A. Howie: *Phys. Rev. B*, **65**, 115418 (2002).
- [42] R. Fuchs: *Phys. Rev. B*, **11**, 1732 (1975).
- [43] H. A. Lorentz: *The Theory of Electrons*, vol. 39 (B.G. Teubner, Leipzig, 1909).
- [44] B. T. Draine and P. J. Flatau: *Journal of the Optical Society of America A*, **11**, 1491 (1994).

- [45] B. T. Draine and P. J. Flatau: *J. Opt. Soc. Am. A*, **25**, 2693 (2008).
- [46] V. M. Agranovich and V. L. Ginzburg: *Spatial Dispersion in Crystal Optics and the Theory of Excitons* (Wiley, 1966).
- [47] I. Newton: *Opticks or a treatise of the reflections, refractions, inflections and colours of light* (London, 1704).
- [48] M. Born and E. Wolf: *Principles of Optics: Electromagnetic Theory of Propagation, Interference and Diffraction of Light* (Cambridge University Press, 1999), 7th ed.
- [49] S. L. Adler: *Phys. Rev.*, **126**, 413 (1962).
- [50] N. Wiser: *Phys. Rev.*, **129**, 62 (1963).
- [51] H. Stolz: *Einführung in die Vielelektronentheorie der Kristalle* (Akademie-Verlag, Berlin, 1974).
- [52] P. Nozières and D. Pines: *Phys. Rev.*, **113**, 1254 (1959).
- [53] P. Schattschneider, C. Hébert, H. Franco, *et al.*: *Phys. Rev. B*, **72**, 045142 (2005).
- [54] A. P. Sorini, J. J. Rehr, and Z. H. Levine: *Phys. Rev. B*, **77**, 115126 (2008).
- [55] P. Schattschneider, M. Nelhiebel, H. Souchay, *et al.*: *Micron*, **31**, 333 (2000).
- [56] J. J. Sakurai: *Modern Quantum Mechanics* (Addison-Wesley, 1994).
- [57] P. Schattschneider: *Fundamentals of Inelastic Electron Scattering* (Springer, Wien, 1986).
- [58] D. Pines: *Rev. Mod. Phys.*, **28**, 184 (1956).
- [59] A. Haug: *Theoretical solid state physics* (Pergamon Press, Oxford, 1972).
- [60] R. v. Baltz: In B. DiBartolo, ed., *Spectroscopy and Dynamics of Collective Excitations in Solids*, vol. 356 of *Nato ASI Series B* (Plenum, 1997).
- [61] H. Kohl and H. Rose: *Theory of Image Formation by Inelastically Scattered Electrons in the Electron Microscope*, vol. 65, chap. 3, pp. 173–227 (Academic Press, 1985).
- [62] H. Kohl: *Ultramicroscopy*, **11**, 53 (1983).
- [63] Y. Kainuma: *Acta Crystallographica*, **8**, 247 (1955).
- [64] H. Lichte and B. Freitag: *Ultramicroscopy*, **81**, 177 (2000).
- [65] P. Schattschneider, S. Rubino, C. Hébert, *et al.*: *Nature*, **441**, 486 (2006).

- [66] R. H. Ritchie and A. Howie: *Phil. Mag. A*, **58** **5**, 753 (1988).
- [67] D. L. Misell, G. W. Stroke, and M. Halioua: *Journal of Physics D*, **7**, L113 (1974).
- [68] H. Rose: *Ultramicroscopy*, **15**, 173 (1984).
- [69] D. V. Dyck, H. Lichte, and J. C. H. Spence: *Ultramicroscopy*, **81**, 187 (2000).
- [70] I. Campillo, J. M. Pitarke, and A. G. Eguiluz: *Phys. Rev. B*, **58**, 10307 (1998).
- [71] S. D. Findlay, P. Schattschneider, and L. J. Allen: *Ultramicroscopy*, **108**, 58 (2007).
- [72] W. Schülke: *Electron Dynamics by Inelastic X-Ray Scattering*. Oxford Series on Synchrotron Radiation (Oxford Univ. Press, Oxford, 2007).
- [73] M. von Laue: *Röntgenstrahl Interferenzen* (Akademische Verlagsgesellschaft, Frankfurt, 1960).
- [74] W. Schülke and A. Kaprolat: *Phys. Rev. Lett.*, **67**, 879 (1991).
- [75] L. van Hove: *Phys. Rev.*, **95**, 249 (1954).
- [76] S. Boffi: *Da Heisenberg a Landau*. Quaderni di Fisica Teorica (Bibliopolis, Napoli, 2004).
- [77] R. Kubo: *Reports of Progress in Physics*, **29**, 255 (1966).
- [78] E. Cosgriff, M. Oxley, L. Allen, *et al.*: *Ultramicroscopy*, **102**, 317 (2005).
- [79] F. Jensen: *Introduction to Computational Chemistry* (Wiley, Chichester, 1999).
- [80] W. M. C. Foulkes, L. Mitas, R. J. Needs, *et al.*: *Rev. Mod. Phys.*, **73**, 33 (2001).
- [81] A. Georges, G. Kotliar, W. Krauth, *et al.*: *Rev. Mod. Phys.*, **68**, 13 (1996).
- [82] A. L. Fetter and J. D. Walecka: *Quantum Theory of Many-Particle Systems* (Dover, New York, 2003).
- [83] S. Botti, A. Schindlmayr, R. D. Sole, *et al.*: *Reports on Progress in Physics*, **70**, 357 (2007).
- [84] R. M. Dreizler and E. K. U. Gross: *Density functional theory: an approach to the quantum many-body problem* (Springer, 1990).
- [85] K. Capelle: A bird's-eye view of density-functional theory (2006).
- [86] P. Hohenberg and W. Kohn: *Phys. Rev.*, **136**, B864 (1964).
- [87] W. Kohn and L. J. Sham: *Phys. Rev.*, **140**, A1133 (1965).
- [88] R. P. Feynman: *Statistical Mechanics* (Benjamin Publishing Company, Reading, 1972).

- [89] D. M. Ceperley and B. J. Alder: *Phys. Rev. Lett.*, **45**, 566 (1980).
- [90] J. P. Perdew and A. Zunger: *Phys. Rev. B*, **23**, 5048 (1981).
- [91] P. E. Trevisanutto, C. Giorgetti, L. Reining, *et al.*: *Phys. Rev. Lett.*, **101**, 226405 (2008).
- [92] C.-O. Almbladh and U. von Barth: *Phys. Rev. B*, **31**, 3231 (1985).
- [93] L. Hedin: *Phys. Rev.*, **139**, A796 (1965).
- [94] E. K. U. Gross and W. Kohn: *Phys. Rev. Lett.*, **55**, 2850 (1985).
- [95] A. Zangwill and P. Soven: *Phys. Rev. A*, **21**, 1561 (1980).
- [96] M. A. L. Marques, C. Ullrich, F. Nogueira, *et al.*, eds.: *Time-dependent Density Functional Theory*. Lecture Notes in Physics (Springer, Berlin, 2006).
- [97] R. van Leeuwen: *Phys. Rev. Lett.*, **80**, 1280 (1998).
- [98] R. van Leeuwen: *Phys. Rev. Lett.*, **82**, 3863 (1999).
- [99] H. Ehrenreich and M. H. Cohen: *Phys. Rev.*, **115**, 786 (1959).
- [100] X. Gonze, J. M. Beuken, R. Caracas, *et al.*: *Comp. Mat. Sci.*, **25**, 478 (2002).
- [101] X. Gonze, G. M. Rignanese, M. Verstraete, *et al.*: *Zeit. Kristallogr.*, **220**, 558 (2005).
- [102] V. Olevano, L. Reining, and F. Sottile: <http://www.dp-code.org/> (1998).
- [103] V. Olevano, M. Palumbo, G. Onida, *et al.*: *Phys. Rev. B*, **60**, 14224 (1999).
- [104] M. C. Payne, M. P. Teter, D. C. Allan, *et al.*: *Rev. Mod. Phys.*, **64**, 1045 (1992).
- [105] M. L. Cohen: *Science*, **234**, 549 (1986).
- [106] W. E. Pickett: *Computer Physics reports*, **9**, 115 (1989).
- [107] D. Vanderbilt: *Phys. Rev. B*, **41**, 7892 (1990).
- [108] N. Troullier and J. L. Martins: *Phys. Rev. B*, **43**, 1993 (1991).
- [109] D. R. Hamann, M. Schlüter, and C. Chiang: *Phys. Rev. Lett.*, **43**, 1494 (1979).
- [110] H. J. Monkhorst and J. D. Pack: *Phys. Rev. B*, **13**, 5188 (1976).
- [111] F. Fuchs, C. Rödl, A. Schleife, *et al.*: *Phys. Rev. B*, **78**, 085103 (2008).
- [112] A. G. Marinopoulos, L. Reining, A. Rubio, *et al.*: *Phys. Rev. B*, **69**, 245419 (2004).
- [113] Y. Q. Cai, P. C. Chow, O. D. Restrepo, *et al.*: *Phys. Rev. Lett.*, **97**, 176402 (2006).

- [114] K. Sturm, W. Schülke, and J. R. Schmitz: *Phys. Rev. Lett.*, **68**, 228 (1992).
- [115] E.-N. Foo and J. J. Hopfield: *Phys. Rev.*, **173**, 635 (1968).
- [116] K. Sturm and L. E. Oliveira: *Phys. Rev. B*, **30**, 4351 (1984).
- [117] E. Petri and A. Otto: *Phys. Rev. Lett.*, **34**, 1283 (1975).
- [118] M. Urner-Wille: *Journal of Physics D*, **10**, 49 (1977).
- [119] A. vom Felde, J. Sprösser-Prou, and J. Fink: *Phys. Rev. B*, **40**, 10181 (1989).
- [120] L. E. Oliveira and K. Sturm: *Phys. Rev. B*, **22**, 6283 (1980).
- [121] L. V. Keldysh: *Introduction*, chap. 1, pp. 1–40. Vol. 24 of [215] (1989).
- [122] W. Hanke: *Adv. Phys.*, **27**, 287 (1978).
- [123] K. Sturm and L. E. Oliveira: *Phys. Rev. B*, **22**, 6268 (1980).
- [124] K. C. Pandey, P. M. Platzman, P. Eisenberger, *et al.*: *Phys. Rev. B*, **9**, 5046 (1974).
- [125] K. Sturm: *Phys. Rev. Lett.*, **40**, 1599 (1978).
- [126] K. Sturm and W. Schülke: *Phys. Rev. B*, **46**, 7193 (1992).
- [127] A. G. Marinopoulos, L. Reining, V. Olevano, *et al.*: *Phys. Rev. Lett.*, **89**, 076402 (2002).
- [128] D. L. Johnson: *Phys. Rev. B*, **9**, 4475 (1974).
- [129] F. Bechstedt: *Phys. Stat. Sol. B*, **112**, 9 (1982).
- [130] R. Hambach: *Parameterfreie Untersuchung der elektronischen Struktur von graphitartigem Kohlenstoff*. Master's thesis, Friedrich-Schiller-Universität Jena (2007).
- [131] R. Hambach, C. Giorgetti, N. Hiraoka, *et al.*: *Phys. Rev. Lett.*, **101**, 266406 (2008).
- [132] H.-C. Weissker, J. Serrano, S. Huotari, *et al.*: *Phys. Rev. B*, **81**, 085104 (2010).
- [133] A. Fleszar and W. Hanke: *Phys. Rev. B*, **56**, 10228 (1997).
- [134] U. Fano: *Phys. Rev.*, **124**, 1866 (1961).
- [135] J. R. Trail and D. M. Bird: *Phys. Rev. B*, **60**, 7875 (1999).
- [136] T. Ando, A. B. Fowler, and F. Stern: *Rev. Mod. Phys.*, **54**, 437 (1982).
- [137] K. S. Novoselov, A. K. Geim, S. V. Morozov, *et al.*: *Science*, **306**, 666 (2004).

- [138] K. S. Novoselov, D. Jiang, F. Schedin, *et al.*: *Proceedings of the National Academy of Sciences of the United States of America*, **102**, 10451 (2005).
- [139] I. Forbeaux, J. M. Themlin, and J. M. Debever: *Phys. Rev. B*, **58**, 16396 (1998).
- [140] A. Fasolino, J. H. Los, and M. I. Katsnelson: *Nat Mater*, **6**, 858 (2007).
- [141] T. Eberlein, U. Bangert, R. R. Nair, *et al.*: *Phys. Rev. B*, **77**, 233406 (2008).
- [142] M. H. Gass, U. Bangert, A. L. Bleloch, *et al.*: *Nat Nano*, **3**, 676 (2008).
- [143] A. L. Fetter: *Ann. Phys. (NY)*, **88**, 1 (1974).
- [144] S. Reich, J. Maultzsch, C. Thomsen, *et al.*: *Phys. Rev. B*, **66**, 035412 (2002).
- [145] K. Zeppenfeld: *Z. Phys. A*, **243**, 229 (1971).
- [146] S. Reich, C. Thomsen, and J. Maultzsch: *Carbon Nanotubes, Basic Concepts and Physical Properties* (Wiley, 2004).
- [147] K. W. K. Shung: *Phys. Rev. B*, **34**, 979 (1986).
- [148] M. F. Lin, C. S. Huang, and D. S. Chuu: *Phys. Rev. B*, **55**, 13961 (1997).
- [149] P. R. Wallace: *Phys. Rev.*, **71**, 622 (1947).
- [150] C. Zener: *Phys. Rev.*, **36**, 51 (1930).
- [151] E. A. Taft and H. R. Philipp: *Phys. Rev.*, **138**, A197 (1965).
- [152] C. S. Huang, M. F. Lin, and D. S. Chuu: *Solid State Commun.*, **103**, 603 (1997).
- [153] T. Stauber, J. Schliemann, and N. M. R. Peres: *Phys. Rev. B*, **81**, 085409 (2010).
- [154] A. Hill, S. A. Mikhailov, and K. Ziegler: *Europhysics Letters*, **87**, 27005 (2009).
- [155] E. H. Hwang and S. Das Sarma: *Phys. Rev. B*, **75**, 205418 (2007).
- [156] R. E. Camley and D. L. Mills: *Phys. Rev. B*, **29**, 1695 (1984).
- [157] C. Kramberger, R. Hambach, C. Giorgetti, *et al.*: *Phys. Rev. Lett.*, **100**, 196803 (2008).
- [158] G. Onida, L. Reining, and A. Rubio: *Rev. Mod. Phys.*, **74**, 601 (2002).
- [159] L. Yang, J. Deslippe, C.-H. Park, *et al.*: *Phys. Rev. Lett.*, **103**, 186802 (2009).
- [160] P. E. Trevisanutto, M. Holzmann, M. Côté, *et al.*: *Phys. Rev. B*, **81**, 121405 (2010).
- [161] Y. Murakami, E. Einarsson, T. Edamura, *et al.*: *Phys. Rev. Lett.*, **94**, 087402 (2005).

- [162] A. Marini, R. Del Sole, and A. Rubio: *Phys. Rev. Lett.*, **91**, 256402 (2003).
- [163] H. M. Lawler, J. J. Rehr, F. Vila, *et al.*: *Phys. Rev. B*, **78**, 205108 (2008).
- [164] C. Hogan, M. Palummo, and R. D. Sole: *Comptes Rendus Physique*, **10**, 560 (2009).
- [165] W. Kohn: *Phys. Rev.*, **133**, A171 (1964).
- [166] C. Brouder, G. Panati, M. Calandra, *et al.*: *Phys. Rev. Lett.*, **98**, 046402 (2007).
- [167] D. A. Dahl and L. J. Sham: *Phys. Rev. B*, **16**, 651 (1977).
- [168] C. Hogan, R. Del Sole, and G. Onida: *Phys. Rev. B*, **68**, 035405 (2003).
- [169] C. A. Rozzi, D. Varsano, A. Marini, *et al.*: *Phys. Rev. B*, **73**, 205119 (2006).
- [170] S. Ismail-Beigi: *Phys. Rev. B*, **73**, 233103 (2006).
- [171] A. H. Castro Neto, F. Guinea, N. M. R. Peres, *et al.*: *Rev. Mod. Phys.*, **81**, 109 (2009).
- [172] E. B. Barros, A. Jorio, G. G. Samsonidze, *et al.*: *Physics Reports*, **431**, 261 (2006).
- [173] O. Stéphan, M. Kociak, L. Henrard, *et al.*: *Journal of Electron Spectroscopy and Related Phenomena*, **114-116**, 209 (2001).
- [174] O. Stéphan, D. Taverna, M. Kociak, *et al.*: *Phys. Rev. B*, **66**, 155422 (2002).
- [175] Y. Murakami, S. Chiashi, Y. Miyauchi, *et al.*: *Chem. Phys. Lett.*, **385**, 298 (2004).
- [176] C. Kramberger, E. Einarsson, S. Huotari, *et al.*: *Phys. Rev. B*, **81**, 205410 (2010).
- [177] J. M. Pitarke and A. Rivacoba: *Surface Science*, **377-379**, 294 (1997).
- [178] D. Taverna, M. Kociak, V. Charbois, *et al.*: *Phys. Rev. B*, **66**, 235419 (2002).
- [179] M. Kociak, O. Stéphan, L. Henrard, *et al.*: *Phys. Rev. Lett.*, **87**, 075501 (2001).
- [180] M. Kociak: *Supraconductivité et plasmons de surface dans les nanotubes*. Ph.D. thesis, Université Paris Sud, Orsay (2001).
- [181] M. F. Lin, D. S. Chuu, C. S. Huang, *et al.*: *Phys. Rev. B*, **53**, 15493 (1996).
- [182] M. F. Lin and D. S. Chuu: *Phys. Rev. B*, **57**, 10183 (1998).
- [183] P. Longe and S. M. Bose: *Phys. Rev. B*, **48**, 18239 (1993).
- [184] V. N. Popov and L. Henrard: *Phys. Rev. B*, **70**, 115407 (2004).
- [185] V. A. Margulis and E. E. Muryumin: *Physica B*, **405**, 1796 (2010).

- [186] E. Chang, G. Bussi, A. Ruini, *et al.*: *Phys. Rev. Lett.*, **92**, 196401 (2004).
- [187] X. Lopez-Lozano, C. Giorgetti, R. Hambach, *et al.*: Electronic Excitations in Single Wall Carbon Nanotubes. To be published (2011).
- [188] A. G. Marinopoulos, L. Wirtz, A. Marini, *et al.*: *Appl. Phys. A*, **78**, 1157 (2004).
- [189] A. G. Marinopoulos, L. Reining, and A. Rubio: *Phys. Rev. B*, **78**, 235428 (2008).
- [190] P. E. Batson: *Ultramicroscopy*, **11**, 299 (1983).
- [191] N. Zabala and P. M. Echenique: *Ultramicroscopy*, **32**, 327 (1990).
- [192] P. M. Echenique: *Phil. Mag. B*, **52** 1, 9 (1985).
- [193] H.-C. Weissker, R. Hambach, V. Olevano, *et al.*: *Phys. Rev. B*, **79**, 094102 (2009).
- [194] G. F. Bertsch, H. Esbensen, and B. W. Reed: *Phys. Rev. B*, **58**, 14031 (1998).
- [195] J. Aizpurua: *Coupling of electrons and electromagnetic surface modes in scanning transmission electron microscopy*. Ph.D. thesis, Universidad de Pais Vasco (1998).
- [196] G. Pegolotti: *Ab initio study of microscopic charge fluctuations in graphite*. Tesi di laurea specialistica, Universita degli Studi di Milano-Bicocca, Milano (2009).
- [197] I. Campillo and J. M. Pitarke: *Nuclear Instruments and Methods in Physics Research Section B*, **164-165**, 161 (2000).
- [198] P. Abbamonte, K. D. Finkelstein, M. D. Collins, *et al.*: *Phys. Rev. Lett.*, **92**, 237401 (2004).
- [199] P. Abbamonte, T. Graber, J. P. Reed, *et al.*: *Proceedings of the National Academy of Sciences*, **105**, 12159 (2008).
- [200] D. L. Johnson: *Phys. Rev. B*, **12**, 3428 (1975).
- [201] M. Stöger-Pollach, H. Franco, P. Schattschneider, *et al.*: *Micron*, **37**, 396 (2006).
- [202] B. Jouffrey, P. Schattschneider, and C. Hébert: *Ultramicroscopy*, **102**, 61 (2004).
- [203] W. Nolting: *Quantenmechanik - Methoden und Anwendungen*. Vol. 5.2 of [216] (2002).
- [204] W. Nolting: *Viel-Teilchen-Theorie*. Vol. 7 of [216] (2005).
- [205] B. A. Lippmann and J. Schwinger: *Phys. Rev.*, **79** (1950).
- [206] W. Press, B. Flannery, S. Teukolsky, *et al.*: *Numerical Recipes in C: The Art of Scientific Computing* (Cambridge University Press, 1992).

- [207] M. Abramowitz and I. A. Stegun: *Handbook of Mathematical Functions with Formulas, Graphs, and Mathematical Tables* (Dover, New York, 1964).
- [208] W. Nolting: *Elektrodynamik*. Vol. 3 of [216] (2002).
- [209] O. V. Dolgov and E. G. Maksimov: *The dielectric function of crystalline systems*, chap. 4, pp. 221–298. Vol. 24 of [215] (1989).
- [210] H. F. Arnoldus: *Journal of Modern Optics*, **50**, 755 (2003).
- [211] A. Wachter and H. Hoerber: *Repetitorium Theoretische Physik* (Springer Berlin, 1998).
- [212] R. Del Sole and E. Fiorino: *Phys. Rev. B*, **29**, 4631 (1984).
- [213] H. Hübener, E. Luppi, and V. Véniard: *Physica Status Solidi B*, **247**, 1984 (2010).
- [214] M. R. Jarvis, I. D. White, R. W. Godby, *et al.*: *Phys. Rev. B*, **56**, 14972 (1997).
- [215] L. V. Keldysh, D. A. Kirzhnits, and A. A. Maradudin, eds.: *The Dielectric Function of Condensed Systems*, vol. 24 of *Modern Problems in Condensed Matter Sciences* (North-Holland, Amsterdam, 1989).
- [216] W. Nolting: *Grundkurs Theoretische Physik* (Springer-Lehrbuch, Berlin, 2002).

# Index

- Bessel function ..... 171
  - modified ..... 172
- Born approximation ..... 18
- Born-Oppenheimer approximation 19,  
36
  
- characteristic angle ..... 22
- chiral vector ..... 113
- Coulomb-cutoff method ..... 102, 190
- cross section, differential 19, 21, 25, 27
- crystal local-field effects .... 15, 56, 87
- cutoff energy ..... 46
  
- delocalisation ..... 6, 148
- density response function ..... 29, 163
- dynamic structure factor ..... 21, 29
- Dyson equation ..... 13, 41, 56
  - cylindrical ..... 125
  - two-dimensional ..... 94
- Dyson series ..... 161
  
- electron energy-loss spectroscopy
  - angular-resolved ..... 19, 21, 27
  - spatially-resolved ..... 25, 31
  
- fluctuation-dissipation theorem .... 29
  
- inelastic X-ray scattering ... 26, 66, 72
- interpolation method ..... 92, 190
  
- local-density approximation ..... 38
  - adiabatic ..... 40, 42
- local-response approximation ..... 188
  - for graphene ..... 94
  - for nanotubes ..... 124
  - sr-eels ..... 144
- LRA method ..... 98
  
- mixed dynamic form factor . 23, 29, 53
- multiple scattering ..... 7
  
- polarisability ..... 13, 56, 93, 121, 190
  - cylinder ..... 125
  - independent-particle ..... 41
  - slab ..... 95
- pseudopotential ..... 44
  
- quantum numbers, helical ..... 116
  
- random phase approximation ..... 42
  
- small-angle approximation ..... 21
- supercell ..... 45, 84
- susceptibility ..... 13, 41, 56, 93, 163
- symmetry vector ..... 114
  
- tight binding ..... 78, 120, 185
  - interaction energy ..... 80
  - overlap integral ..... 80
- translational vector ..... 113
  
- Umklapp process ..... 116, 138
- unit cell, reduced ..... 115
  
- ZF+LRA method ..... 125, 141
- zone-folding method ..... 139
- zone-folding model
  - for bandstructure ..... 116
  - for polarisability ..... 121, 169